

A Measurement of the Diffractive Proton Structure Function at HERA

Timothy Christopher Nicholls

*Thesis submitted for the degree of
Doctor of Philosophy*

April 1997

School of Physics and Space Research
Faculty of Science
The University of Birmingham

Abstract

A measurement of the diffractive structure function of the proton, $F_2^{D(3)}(\beta, x_p, Q^2)$, is presented, based on an analysis of 1995 data from the HERA experiment H1. An extension of the accessible kinematic range in Q^2 and β has been achieved using the the upgraded backward region of the H1 detector.

A new backward calorimeter has been installed which increases the acceptance for scattered electrons up to polar angles of 178.6° for collisions where the interaction vertex is shifted by 70cm. The calorimeter is of a spaghetti (SPACAL) lead-fibre design, and is also required to provide timing information for the rejection of beam-induced backgrounds. A time-to-digital converter (TDC) system monitors the timing performance of SPACAL. Results from beam tests and early use in H1 are presented in this thesis and demonstrate that the required performance of the SPACAL and the TDC system has been achieved.

Diffractive deep-inelastic scattering events were selected by requiring the detection of an electron in SPACAL and an absence of hadronic activity in the forward region (pseudorapidity > 3.2). The cross section for the process $ep \rightarrow eXY$ with $M_Y < 1.6$ GeV has been measured, from which the structure function $F_2^{D(3)}(\beta, x_p, Q^2)$ has been determined in the region $0.3 < Q^2 < 12$ GeV², $0.005 < \beta < 0.8$ and $0.0001 < x_p < 0.075$. The results are consistent with the previous measurement in the region of overlap. A fit to the data of the form $F_2^{D(3)} = A(Q^2, \beta)x_p^{-n}$ shows a variation of n as a function of β , consistent with the previous measurement and demonstrating violation of factorisation of the diffractive structure function. At high β , n is observed to have a value of approximately 1.25. Tentative first evidence for a decrease of n with decreasing $\log(Q^2)$ is observed.

The author's contribution

The collaborative nature of experimental high-energy physics is such that a summary of my contribution to H1 and the work presented in this thesis is worthwhile.

The technical work on the SPACAL TDC system was undertaken by a small group of physicists and engineers from the UK. I was responsible for development of software to test the hardware during the prototyping and construction phase. I also wrote the applications used to verify the operation of the TDC devices. During the beam tests at CERN I worked to integrate the TDC system into the data acquisition system and was involved in the recording and analysis of the data taken. I participated in the installation and commissioning of SPACAL within H1 and the inclusion of the TDC readout in the calorimeter system.

The measurement of the diffractive structure function presented here was performed in collaboration with Christophe Royon, under the auspices of the H1 Diffractive Working Group. An analysis chain independent of that used for previous measurement was constructed, based on ntuple production code written by us, with contributions from a number of other people. The extraction and presentation of the structure function was enabled by a suite of code and macros also written by us.

A note on Units

In this thesis the natural system of units is used, in which $\hbar = c = 1$

This work was supported financially by the UK Particle Physics and Astronomy Research Council (PPARC).

Acknowledgements

I would like to thank Professors George Morrison and John Dowell for allowing me the opportunity of studying in the School of Physics and Space Research. I acknowledge the financial support of the UK taxpayer who, via PPARC, has funded me during the period of my studentship.

I am very grateful to my supervisor, John Dowell, for his help, advice and support throughout my time in the group. Special thanks go to him for allowing me to pursue the research topics that interested me most and for reading and commenting on draft versions of this thesis.

I would like to thank all the members of the Birmingham H1 Group for generating a stimulating and friendly environment in which to work. Ian Kenyon and John Garvey have been the source of much appreciated advice and discussion. Lee West and Paul Sutton are thanked for their persistent attempts to make me enjoy my times in Hamburg, a brave endeavour in which they were often successful! I am indebted to Paul “R is for Regge” Newman, for his friendship and help, particularly in reading and commenting on substantial parts of this thesis. Paul combines the ability to explain tough subjects lucidly with an extensive knowledge of everything you could possibly want to know about Regge theory (and plenty of things you probably never want to know about as well), and I have learnt a great deal just from sharing an office with him. Special thanks to Vicki Hudgson for her friendship over the last three and a half years, for suffering the trials of writing up at the same time as me, and for coveting my \LaTeX manual so relentlessly! Good luck to Kirstee Hewitt and Paul Thompson for their remaining time on H1. Thanks also to Pete Faulkner for his help with the H1 software at Brum.

I have crossed paths with many staff and students during my time in the Birmingham group, who I will not mention by name for fear of missing someone! I thank them all for their friendship, and apologise for the rather serious atmosphere in the H1 office over the last few months. As direct contemporaries of mine, Keith Norman and Dave Rigby get a special mention, in particular for joining the married club. A big thank you goes to Lawrie Lowe for answering my countless inane computing problems. Thanks also to the group secretary, Sue Griffiths, for her help.

On the SPACAL TDC project, I was fortunate to work with a fantastic group of people. Eric Eisenhandler gave me the best introduction to the world of HEP hardware and software development that I could have hoped for, and I thank him for this continued support. Murrough Landon was an invaluable source of help with the software aspects of

my work, and I am grateful to him for suffering beam test meetings with me and always remaining calm when instinct told me to run around in a blind panic. I am indebted to John Dowdell for his superb work in the management, design and construction of the TDC system; it was his skill and experience that made it a success and such a delight to work on. I am grateful to Brian Claxton for the loan of a mug at RAL and for not shouting when I broke things.

The physics analysis presented in this thesis would not have been possible without the help and support of Christophe Royon. He has worked with me and helped me at every stage, and I have learnt a great deal from him. Special thanks go to him for his patience and continued friendship. Thanks also to Michael Dirkmann for his contribution to the 1995 analysis efforts, and to the Diffractive Working Group for their support.

I would like to thank Jonathan Allday for first stimulating my interest in high energy physics at school through his raw enthusiasm and ability to communicate the subject. Thanks also to Pete Watkins for his support and encouragement during my time as a summer student and for convincing me that it was the right area to be in.

Thanks to my friends who made my time in Birmingham such a pleasant one, especially Pete Kightley who helped to make the traumas of finals and thesis writing bearable!

To all my family I send my love and thanks for their support and encouragement throughout my time as a student. Without them, I would never have been able to get this far. Finally, the biggest thank you must go to my wife, Sarah, for her unconditional love and support over the last few years. Not only has she endured my repeated trips abroad and antisocial behaviour during the writing of this thesis, but she was mad enough to marry me while it was all going on. Without her love and encouragement, all this would have been much harder to achieve.

This thesis is dedicated to my wife, Sarah

.... A white rabbit is pulled out of a top hat. Because it is an extremely large rabbit, the trick takes many billions of years. All mortals are born at the very tip of the rabbit's fine hairs, where they are in a position to wonder at the impossibility of the trick. But as they grow older they work themselves ever deeper into the fur. And there they stay. They become so comfortable they never risk crawling back up the fragile hairs again. Only some embark on this perilous expedition to the outermost reaches of language and existence. Some of them fall off, but others cling on desperately and yell at the people nestling deep in the snug softness

Sophie's World
Jostein Gaarder

Contents

Introduction	1
1 Physics at HERA	4
1.1 Deep-Inelastic Scattering	4
1.1.1 Deep-Inelastic Scattering Processes	4
1.1.2 Kinematics of Deep-Inelastic Scattering	5
1.1.3 The Inelastic Cross Section and Proton Structure Functions	6
1.1.4 Evidence for Scaling and the Quark Parton Model	8
1.1.5 Scaling Violations and the Role of QCD	9
1.1.6 Measurements of $F_2(x, Q^2)$ at HERA	10
1.2 Low x Phenomenology	12
1.2.1 The DGLAP Evolution Formalism	12
1.2.2 The BFKL Evolution Formalism	15
1.2.3 The GLR Equation	17
1.2.4 Measurement of the Gluon Density at Low x	17
1.2.5 The Low Q^2 Limit	18
1.2.6 Summary	20
1.3 Photoproduction	21

1.4	Beyond the Standard Model	22
2	Diffractive Deep-Inelastic Scattering	24
2.1	Hadron-Hadron Interactions and Regge Theory	24
2.2	The Pomeraňuk Trajectory	27
2.3	Diffraction in Deep-Inelastic Scattering	28
2.3.1	The Kinematics of Diffractive DIS	28
2.3.2	The Diffractive Structure Function	30
2.3.3	Models of the Pomeron in Diffractive DIS	31
2.4	Measurements of Diffractive DIS at HERA	34
2.5	Summary	39
3	The H1 Detector at HERA	40
3.1	The HERA Accelerator	40
3.2	Overview of the H1 Detector	42
3.3	Tracking	45
3.3.1	The Central Tracker	45
3.3.2	The Forward Tracker	47
3.3.3	The Backward Drift Chamber	48
3.4	Calorimetry	49
3.4.1	The Liquid Argon Calorimeter	49
3.4.2	The Tail Catcher	51
3.4.3	The Plug Calorimeter	51
3.5	Muon Detection	52

3.5.1	The Central Muon System	52
3.5.2	The Forward Muon Detector	53
3.6	The Luminosity System	54
3.7	The Very Forward Detectors	55
3.8	Time-of-Flight Detectors	56
3.9	Triggering and Data Acquisition	57
4	The SPACAL Calorimeter and TDC System	61
4.1	The SPACAL Calorimeter	61
4.1.1	Physics Motivation	61
4.1.2	SPACAL Construction	62
4.2	The SPACAL Electronics Chain	66
4.3	The SPACAL Trigger	69
4.3.1	The Inclusive Electron Trigger	70
4.3.2	The ToF/AToF Trigger	71
4.4	The SPACAL TDC System	71
4.4.1	The System Controller Module	75
4.4.2	The TDC and Histogrammer Module	77
4.4.3	Online Monitoring	83
4.4.4	Offline Reconstruction	84
5	Performance of SPACAL and the TDC System	87
5.1	SPACAL Electromagnetic Section Performance	87
5.2	SPACAL Hadronic Section Performance	92

5.3	Combined Performance	92
5.4	Inclusive Electron Trigger Performance	94
5.5	The TDC Pre-Prototype Module	97
5.6	Acceptance Testing of the TMCs	97
5.7	TDC Beam Test Results	99
5.8	Commissioning and use of the TDC System in H1	104
6	Event Reconstruction and Selection	114
6.1	Reconstruction of Kinematic Variables	114
6.2	Calibration of SPACAL	116
6.3	Final Electron Energy Reconstruction	118
6.4	Monte Carlo Models	118
6.5	Run Selection	119
6.6	DIS Event Selection	120
6.7	Selection of Diffractive Events	126
6.7.1	The η_{\max} Selection	126
6.7.2	Use of the Forward Subdetectors	128
6.7.3	Reconstruction of Forward Subdetector Signals	128
6.7.4	Forward Subdetector Response and Cuts	130
6.8	Comparison of Diffractive Data and Monte Carlo Samples	131
7	Measurement of the Diffractive Proton Structure Function	136
7.1	Definition of the Diffractive Structure Function	136
7.2	Extraction of the Measured Cross Section	137

7.3	Selection of Bins	140
7.4	Selection Efficiency	144
7.5	Systematic Errors	148
7.6	The Diffractive Proton Structure Function	149
7.7	Summary	155
A	Measured Values of $F_2^{D(3)}$	156
	Glossary	165
	References	167

List of Figures

1.1	The neutral current DIS process.	5
1.2	Measured values of $F_2(x, Q^2)$ from HERA and fixed target experiments. . .	11
1.3	Measured values of $F_2(x, Q^2)$ from H1, exploiting the upgraded 1995 detector. . .	11
1.4	Representation of splitting functions in DGLAP evolution.	13
1.5	QCD evolution ladder diagram for DIS low x	14
1.6	The gluon density $xg(x)$ from a NLO QCD fit.	18
1.7	A schematic illustration of the kinematic plane.	20
1.8	Examples of photoproduction processes.	22
2.1	Illustration of generalised s and t channel processes.	25
2.2	Chew-Frautschi plot of the ρ trajectory, $\alpha_\rho(t)$	26
2.3	A diffractive DIS process.	29
2.4	$x_P \cdot F_2^{D(3)}(\beta, Q^2, x_P)$ from analysis of 1994 data including phenomenological fit.	35
2.5	Variation of n as a function of a) β and b) Q^2	35
2.6	$x_P \cdot F_2^{D(3)}(\beta, Q^2, x_P)$ from analysis of 1994 data including fit with pomeron and meson contributions.	36
2.7	$\tilde{F}_2^D(\beta, Q^2)$ as a function of Q^2 and β	37
2.8	Parton momentum distributions from a QCD fit to \tilde{F}_2^D	38

3.1	Schematic layout of the HERA accelerator.	41
3.2	A cut-away view of the H1 detector.	43
3.3	Side view of the H1 tracking system.	46
3.4	An $r - \phi$ section of the central tracker.	47
3.5	Schematic depiction of the backward drift chamber (BDC).	49
3.6	Schematic view of the H1 calorimeters.	50
3.7	Schematic view of the Forward Muon Detector.	53
3.8	The layout of the luminosity system.	54
3.9	The three components of the trigger and data acquisition system.	59
4.1	An H1 SPACAL EM submodule.	63
4.2	Schematic side view of an H1 SPACAL EM supermodule.	64
4.3	Side view of part of the H1 detector showing the location of the SPACAL sections.	65
4.4	Block diagram of the SPACAL electronics chain.	66
4.5	Comparison of signal discrimination techniques.	68
4.6	Times-of-flight for SPACAL energy depositions.	72
4.7	Schematic layout of the SPACAL TDC System.	74
4.8	Block diagram of the SCM.	76
4.9	Block diagram of the THM.	78
4.10	Schematic of the TMC device.	79
4.11	VME memory mapping of the TMC registers.	81
4.12	Schematic of the TDC reconstruction mode SPTIME.	86
5.1	SPACAL EM section energy resolution.	89

5.2	SPACAL EM section spatial resolution.	89
5.3	Electromagnetic energy E_{em} distribution as a function of R_E	93
5.4	Performance of the IET processor at the CERN PS beam tests.	96
5.5	TMC single channel response to a delay-scanned test pulse input.	98
5.6	Energy-time correlation and resolution fit for TDC system.	100
5.7	Raw TDC time distributions for ToF/AToF selections.	100
5.8	TDC resolution dependence as a function of the HCLK correction factor.	102
5.9	TDC energy-time correlations and resolution fits.	103
5.10	Online histograms from a beam test run.	104
5.11	Raw timing distributions from the SRTE bank.	105
5.12	Fraction of SRTE time hits per bunch crossing, for four DSPPTR values.	105
5.13	Online TDC histograms from luminosity running.	107
5.14	Rate history for all cells in one ANBX during luminosity running.	107
5.15	SPACAL activity as a function of geometrical channel number.	109
5.16	Hit maps from the SNPU pile-up bank.	109
5.17	SPACAL energy spectra and TDC input efficiency.	111
5.18	SPACAL energy versus time plots.	111
5.19	Effect of offset correction of TDC data.	112
6.1	DJANGO and PHOJET comparisons for the DIS selection.	121
6.2	Effect of DIS cuts on reconstruction of electron candidate:	122
6.3	Shifted vertex data distributions for the DIS selection.	123
6.4	SVX kinematic peak and electron-tagger comparisons.	125
6.5	η_{\max} distribution for data and the DIS MC model (DJANGO).	127

6.6	Single particle detection efficiency from DJANGO.	127
6.7	Typical non-diffractive and diffractive DIS events.	129
6.8	Forward subdetector signals observed in random trigger events.	132
6.9	Comparison of the diffractive Monte Carlo with data.	133
6.10	Comparison of the diffractive Monte Carlo with data for electron kinematics.	135
6.11	Comparison of the diffractive Monte Carlo with data for sigma kinematics.	135
7.1	Resolution in the kinematic variables as a fraction of bin size.	142
7.2	The $x - Q^2$ kinematic plane, with diffractive candidate events.	143
7.3	Comparison of ZVTX efficiency in data and MC.	146
7.4	Efficiency of the DIS selection cuts as a function of Q^2	146
7.5	Efficiency of the DIS selection cuts as a function of $\log_{10}(x)$	147
7.6	Comparison of measured $F_2^{D(3)}$ points for electron and sigma methods.	150
7.7	Comparison of $x_P \cdot F_2^{D(3)}$ measured by the electron method with the 1994 measurement and fit parameterisation.	151
7.8	Comparison of $x_P \cdot F_2^{D(3)}$ measured by the sigma method with the 1994 measurement and fit parameterisation.	152
7.9	$x_P \cdot F_2^{D(3)}$ calculated using sigma kinematics with the phenomenological fits.	154
7.10	Result of the phenomenological fit to $F_2^{D(3)}$	155

List of Tables

4.1	H1 SPACAL Parameters.	63
4.2	SPACAL L1 triggers.	69
5.1	Results of SPACAL beam tests.	95
6.1	Fraction of random trigger events passing forward detector cuts.	132
7.1	Q^2 bin centres and boundaries.	141
7.2	$\log x$ bin centres and boundaries.	141
7.3	β bin centres and boundaries.	141

Introduction

Electron-hadron scattering experiments have played a vital role in the development of our understanding of the basic structure of matter. As stable, charged and point-like objects whose interactions are well understood, electrons are an ideal probe of more complex objects such as the proton.

High energy inelastic electron-proton scattering at the Stanford Linear Accelerator Centre (SLAC) presented the first evidence for substructure within the proton [1]. The inelastic cross section was observed to show a much weaker dependence on the four-momentum transfer squared, Q^2 , than the elastic cross section. This was interpreted as being due to the scattering of the electron from point-like objects within the proton.

Such Deep-Inelastic Scattering (DIS) interactions, where the electron probes the hadron via the exchange of a highly virtual photon, have provided the basis for the current model of hadron structure in which hadrons consist of quarks; spin-half, point-like particles with fractional electric charge. The quarks interact with one another via the strong force, which is mediated by the exchange of massless vector bosons known as gluons. DIS is therefore an important testing ground for the gauge theory of the strong force, Quantum Chromodynamics (QCD). The proton is conveniently understood in terms of structure functions, which are dependent on the spatial distribution of charged objects within the proton. The structure function $F_2(x, Q^2)$ is the most widely measured.

The most recent facility for the study of electron-proton collisions is the Hadron Electron Ring Accelerator (HERA), situated at the DESY Laboratory in Hamburg, Germany. Operational since 1992, HERA is the first accelerator to store beams of electrons and protons, which it collides at unprecedented energies. The very high centre of mass energy attainable with this machine allows the structure of the proton to be studied in entirely new kinematic regions, particularly at high Q^2 and low x , the Bjorken scaling variable. The HERA measurements extend the accessible region by several orders of magnitude in these variables.

The H1 experiment, one of a number situated at HERA, was designed to study electron-proton collisions in this new domain. Providing nearly total coverage around the collision point, H1 performs simultaneous measurement of the scattered electron and hadronic final state arising in DIS interactions. In the quest to extend the measurement to lower values of Q^2 and x , the H1 collaboration has upgraded during 1994/5 parts of its detector. Central to this upgrade programme was a new backward calorimeter and drift chamber designed to measure the scattered electron with good energy and spatial resolution, down to very small scattering angles ($\sim 2^\circ$). A spaghetti calorimeter (SPACAL), the active region of which consists of scintillating fibres embedded in a lead matrix, was chosen for its favourable performance and construction costs. A two section design was adopted, with electromagnetic and hadronic sections in order to detect DIS electrons and improve containment of hadronic energy in the backward region. In addition to replacing the previous backward calorimeter, SPACAL also displaced a time of flight (ToF) system which was vital in the rejection of proton beam-induced backgrounds, and therefore has to fulfil this role. The comparatively large number of channels (~ 1400) motivated the construction of a system to monitor the timing alignment and performance of the calorimeter and its electronics. This system provides time-to-digital conversion (TDC) of calorimeter signals with 1 ns precision using semi-custom devices, and sophisticated electronics to generate automatically information used to assess the timing performance of SPACAL. The design and implementation of the TDC system and, in a wider context, the performance of SPACAL, form a substantial part of this thesis.

At HERA, considerable interest has been generated by the observation of a class of DIS events in which rapidity gaps adjacent to the proton direction are observed [2, 3]. These events have been interpreted as arising from diffractive processes, in which no quantum numbers are exchanged between the interacting particles. Such processes are known to contribute significantly to high energy hadron-hadron interactions and are understood phenomenologically in terms of Regge theory. Here, strong interactions at low momentum transfers are described in terms of the exchange of virtual mesons. Elastic and total hadron-hadron cross sections are successfully described in this framework by the introduction of an exchange which has the quantum numbers of the vacuum, known as the pomeron.

In spite of the success of this approach, Regge theory has no predictive power about the possible partonic nature of the pomeron. This is one of the prime motivations for investigation of diffractive processes at HERA, where the hard scale provided by the virtual photon allows one to probe the structure of the pomeron. In the same way as the proton can be understood in terms of the structure function, $F_2(x, Q^2)$, a similar understanding of the pomeron can be gained by measuring the diffractive proton structure

function, $F_2^D(x, Q^2, x_p, t)$. This has been measured by the HERA experiments, and is providing new insights into the nature of the pomeron. In this thesis, an analysis is presented in which the new components of the H1 detector are exploited to extend the kinematic range of the measurement of F_2^D .

Chapter 1 presents an overview of the physics topics investigated at HERA, with particular emphasis on DIS, including relevant theoretical issues and recent results. In Chapter 2 diffractive physics is reviewed, including a discussion of Regge theory and its predictive power for diffractive DIS. The recent measurements at HERA of F_2^D are also presented. A description of the components comprising the H1 detector is given in Chapter 3. In Chapters 4 and 5 the motivation, implementation, testing and commissioning of the SPACAL calorimeter and TDC system is discussed. Results from beam tests are shown, demonstrating that both have attained the desired level of performance. The reconstruction and selection of DIS and diffractive events, using SPACAL to detect scattered electrons, is described in detail in Chapter 6. The measurement of F_2^D and comparison with previous H1 results is presented in Chapter 7.

Chapter 1

Physics at HERA

This chapter presents an overview of the physics topics relevant at HERA, with particular emphasis on deep-inelastic scattering (DIS). The formalism used for the measurement of DIS events is presented, and an introduction to structure functions given. The phenomenology of the low x regime, which is of particular interest, is discussed. Recent results from DIS measurements at HERA are presented and compared to theoretical models. A brief overview of some of the other physics topics relevant at HERA is given.

1.1 Deep-Inelastic Scattering

1.1.1 Deep-Inelastic Scattering Processes

Neutral current (NC) deep-inelastic scattering (DIS) is the process:

$$e + p \rightarrow e + X, \quad (1.1)$$

where X is an arbitrary hadronic final state. Such interactions are understood in terms of the exchange of single, neutral electroweak gauge bosons between the electron and some point-like object (generically termed a parton) in the proton. Figure 1.1 shows the process in lowest order QED, including the associated four-vectors.

The interaction proceeds via the exchange of either a photon or a Z^0 boson. However, since the propagator has a form $1/(Q^2 + M^2)$, where M is the mass of the boson, Z^0 exchange does not contribute significantly to the NC DIS cross section until the square of the four-momentum transferred approaches the mass of the Z^0 , $M_{Z^0}^2 \sim 10^4 \text{ GeV}^2$. Indeed, throughout the kinematic region where $Q^2 < 5000 \text{ GeV}^2$, Z^0 exchange does not contribute more than 5% to the NC cross section.

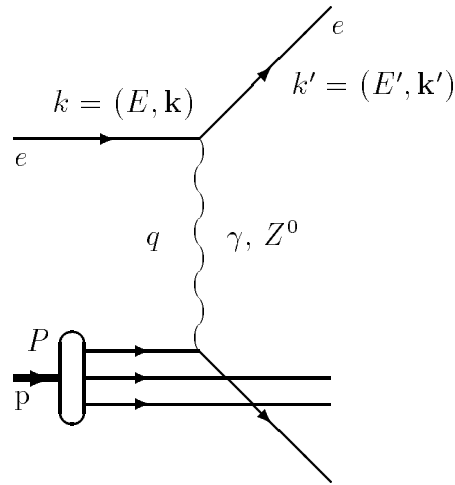


Figure 1.1: The neutral current DIS process. The four-momenta used in the definition of the DIS kinematics are shown.

Charged current (CC) DIS, in which the final state electron is replaced by a neutrino:

$$e + p \rightarrow \nu_e + X \quad (1.2)$$

proceeds via the exchange of a charged boson, W^\pm . The final state neutrino is unobserved, leading to a characteristic imbalance in the transverse momentum of the final state; this is the primary signature used for isolating CC from NC DIS. Again, the W^\pm is massive, and the propagator therefore suppresses the CC cross section except at very large momentum transfers.

1.1.2 Kinematics of Deep-Inelastic Scattering

The kinematics of DIS processes are characterised in terms of various combinations of the four-momenta of the initial and final state electron (k and k' respectively), the incoming proton (P) and the exchanged boson (q), as shown in Figure 1.1. The kinematic variables used to describe DIS are scalar products, or ratios of scalar products, of these four-vectors such that they are Lorentz invariant.

The centre of mass energy, \sqrt{s} , of the ep collision is defined by the four-momenta of the incoming electron and proton as:

$$\begin{aligned} s &= (k + P)^2 \\ &= m_e^2 + m_p^2 + 2k \cdot P \end{aligned} \quad (1.3)$$

$$\begin{aligned}
&= m_e^2 + m_p^2 + 2E_e E_p - 2\mathbf{k} \cdot \mathbf{P} \\
&\simeq 4E_e E_p
\end{aligned} \tag{1.4}$$

where E_e (m_e) and E_p (m_p) are the energies (masses) of the incident electron and proton respectively. In 1995 the beam energies were $E_e = 27.55$ GeV and $E_p = 820$ GeV, so that $s = 90364$ GeV². The negative square of the four-momentum transfer, Q^2 , which defines the virtuality of the exchanged boson, is defined as:

$$Q^2 = -q^2 = -(k - k')^2. \tag{1.5}$$

Note that the four-momentum of the boson, q , is such that $q^2 \leq 0$. Q^2 is therefore defined in such a way as to be always positive.

DIS is commonly described by the introduction of the dimensionless Bjorken variable x , defined as

$$x = \frac{Q^2}{2P \cdot q}. \tag{1.6}$$

In the infinite momentum frame of the proton, where the masses and transverse momenta of the partons may be neglected, x can be identified as the fraction of the momentum of the proton carried by the struck parton.

A second dimensionless scaling variable is also used frequently:

$$y = \frac{P \cdot q}{P \cdot k}. \tag{1.7}$$

y can be understood as the fractional energy loss of the electron in the rest frame of the proton. It also specifies the scattering angle of the electron in the electron-parton centre of mass frame, θ^* , according to the relation $y = (1 + \cos \theta^*)/2$.

Out of the three variables Q^2 , x and y , only two are independent. They are related via the expression

$$Q^2 \simeq sxy. \tag{1.8}$$

All three variables can therefore be determined by a measurement of any two, and a knowledge of the beam energies. The various methods of reconstruction of the kinematic variables from the final state of DIS interactions is described in more detail in Section 6.1.

1.1.3 The Inelastic Cross Section and Proton Structure Functions

The inclusive differential cross section for inelastic electron-proton scattering may be written, in lowest order QED, as

$$\frac{d^2 \sigma(ep \rightarrow eX)}{dE' d\Omega} = \frac{\alpha_{em}^2}{Q^4} \frac{E'}{E} L_{\mu\nu} W^{\mu\nu} \tag{1.9}$$

where E and E' are the initial and final state electron energies, as shown in Figure 1.1, $L_{\mu\nu}$ is the QED lepton tensor and $W_{\mu\nu}$ is the hadronic tensor, which parameterises an ignorance of the interaction occurring between the exchanged boson and the proton. Consideration of the requirements of Lorentz invariance and current conservation lead to the following expression for the cross section:

$$\frac{d^2\sigma(ep \rightarrow eX)}{dx dQ^2} = \frac{4\pi\alpha_{em}^2}{xQ^4} [xy^2 F_1(x, Q^2) + (1-y)F_2(x, Q^2)] \quad (1.10)$$

where $F_1(x, Q^2)$ and $F_2(x, Q^2)$ are structure functions which depend on the spatial distribution of charged objects within the proton. A formal derivation of Equation 1.10 can be found in [4, 5]. In order to describe fully neutral current DIS, a third structure function, $F_3(x, Q^2)$ is required, which takes account of the parity violating Z^0 exchange. This is neglected here for the reasons given in Section 1.1.1. A minimum of two structure functions are required since the photo-absorption cross section has two independent contributions, σ_T and σ_L , arising from transversely and longitudinally polarised photons respectively. It can be shown that $F_1(x, Q^2)$ describes σ_T and $F_2(x, Q^2)$ describes the sum $\sigma_T + \sigma_L$. Equation 1.10 can therefore be redefined in terms of just one structure function and the photo-absorption ratio, $R(x, Q^2)$, defined as

$$R(x, Q^2) = \frac{\sigma_L(x, Q^2)}{\sigma_T(x, Q^2)} = \frac{F_2(x, Q^2) - 2xF_1(x, Q^2)}{2xF_1(x, Q^2)} \quad (1.11)$$

giving

$$\frac{d^2\sigma(ep \rightarrow eX)}{dx dQ^2} = \frac{4\pi\alpha_{em}^2}{xQ^4} \left(1 - y + \frac{y^2}{2[1 + R(x, Q^2)]} \right) F_2(x, Q^2). \quad (1.12)$$

In order to measure separately $F_2(x, Q^2)$ and $R(x, Q^2)$ it is possible to exploit the differing dependence on y of their contributions to the cross section to determine the differential cross section at more than one centre of mass energies so that, at fixed x and Q^2 , s and therefore y are changed [6]. The same can be achieved at fixed beam energies by exploiting events with initial state QED radiation [7], which effectively have a reduced centre of mass energy. However, the experimental precision on the measurement of radiative events limits the sensitivity to R of such a technique.

An equivalent prescription, as used by H1, is to define a longitudinal structure function, F_L , such that

$$\frac{d^2\sigma(ep \rightarrow eX)}{dx dQ^2} = \frac{4\pi\alpha_{em}^2}{xQ^4} \left[\left(1 - y + \frac{y^2}{2} \right) F_2(x, Q^2) - \frac{y^2}{2} F_L(x, Q^2) \right] \quad (1.13)$$

and

$$R(x, Q^2) = \frac{F_L(x, Q^2)}{F_2(x, Q^2) - F_L(x, Q^2)}. \quad (1.14)$$

This formalism has the advantage that F_L is directly related to σ_L .

1.1.4 Evidence for Scaling and the Quark Parton Model

The DIS experiments performed at SLAC during the late 1960s [1] essentially observed that $F_2(x, Q^2)$ showed little dependence on Q^2 at fixed values of x . This behaviour is known as scale invariance [8] and was the basis for the interpretation of the structure of the proton in terms of the Quark Parton Model (QPM). In the QPM, the proton is considered to be composed of free, point-like fermions, namely quarks, the momentum distributions of which are described by parton density functions, $f_i(x)$. The normalisation of the density functions is, in this model, constrained by the momentum sum rule:

$$\sum_i \int_0^1 x f_i(x) dx = 1 \quad (1.15)$$

which sums over all types of quarks, i , in the proton. DIS processes are then understood in the QPM as incoherent elastic scattering of electrons from the charged quarks within the proton. The scattering takes place from point-like objects in the proton, and therefore the parton density functions should depend only on the dimensionless variable x . In particular, this implies that there should be no dependence on Q^2 at fixed x , as observed in the experiments [1]. By considering the DIS cross section in terms of the parton density functions $f_i(x)$, a relationship between them and the structure functions can be defined:

$$F_1 = \frac{1}{2} \sum_i e_i^2 f_i(x) \quad (1.16)$$

$$F_2 = x \sum_i e_i^2 f_i(x) \quad (1.17)$$

where e_i is the charge of the i -th species of parton. It can be seen from these expressions that there is a relationship between the two structure functions F_1 and F_2 :

$$F_2 = 2xF_1. \quad (1.18)$$

This is known as the Callan-Gross relationship [9], and is a consequence of the spin-half nature of the quarks. Indeed, the SLAC experiments provided evidence that the point-like partons within the proton were spin-half by establishing the validity of the Callan-Gross relationship [1]. Using this identity, we can substitute for F_2 in the expression for $R(x, Q^2)$, Equation 1.11, and notice that, if this relationship holds, R must be zero. Furthermore, we can see from Equations 1.14 and 1.18 that $F_L(x, Q^2)$ is the extent to which this identity is violated.

It is surprising that the QPM is able to provide a good description of DIS, given some of the assumptions that it contains. The concept that the partons within the proton do not interact is difficult to reconcile with the fact that quarks are never observed as free

particles, but always confined within hadrons, implying that there is a very strong interaction between them. This apparent anomaly can be understood in terms of the running of the strong coupling constant, α_s , a consequence of the nature of strong interaction. At low Q^2 , α_s is large, increasing the strength of the interaction between the quarks and confining them to a bound state. As Q^2 rises into the regime of the DIS measurements, α_s falls, and the quarks interact only weakly, a behaviour known as asymptotic freedom.

1.1.5 Scaling Violations and the Role of QCD

While scale invariance was observed to hold within errors in the region of the early DIS measurements, at $x \simeq 0.15$, variations of the structure function F_2 with $\log(Q^2)$ are observed at higher and lower values of x . Furthermore the momentum sum shown in Equation 1.15, was observed experimentally to be $\simeq 0.5$ [10], implying that other objects carry a significant fraction of the momentum of the proton.

These observations can be understood in terms of the field theory of the strong interaction, Quantum Chromodynamics (QCD). In QCD the quarks interact via the exchange of gluons. The non-Abelian nature of the strong interaction, which allows the gluons to interact with themselves, and therefore the coupling constant α_s to run, enables the quarks to appear free at sufficiently high Q^2 . The QPM model is therefore equivalent to zeroth order processes in QCD. When α_s is sufficiently small, strong interactions may be treated using perturbative QCD (pQCD), allowing higher order processes to be calculated. The scale at which this technique becomes applicable is usually taken to be $Q^2 \simeq 1 \text{ GeV}^2$, readily accessible at HERA. The study of proton structure, particularly $F_2(x, Q^2)$ is therefore an ideal testing ground for QCD.

Scaling violations can readily be interpreted in the framework of QCD. As Q^2 increases, the exchanged boson probes the proton with increasing spatial resolution, revealing finer details of the structure. The quarks within the proton interact with each other via exchange of gluons, and radiate gluons in a bremsstrahlung process, which can fluctuate to quark-antiquark pairs. High momentum quarks therefore lose momentum through these splitting processes and, as Q^2 increases, there is an increased probability of sampling a quark at low x , and a decreased probability at high x . Thus, at high x , $F_2(x, Q^2)$ decreases with increasing Q^2 and at low x the reverse happens.

Parton models have been developed [10] which admit the role of QCD as described above. In such models, the proton consists of three valence quarks, a sea of quark-antiquark pairs (at low x) and gluons which mediate the strong interaction between the quarks and

generate confinement. These give a good description of the x and Q^2 dependence of F_2 and therefore form the cornerstone of our understanding of the structure of the proton.

The non-zero value of $F_L(x, Q^2)$, and therefore of R , and the violation of the Callan-Gross relationship also has an interpretation in QCD. F_L is expected to acquire a value through the effects of gluon radiation.

1.1.6 Measurements of $F_2(x, Q^2)$ at HERA

$F_2(x, Q^2)$ is determined experimentally from a measurement of the differential DIS cross section, as given in Equation 1.10. This is the Born level cross section, and therefore takes no account of higher order QED processes. Radiative corrections are therefore applied to the measured cross section before extraction of $F_2(x, Q^2)$.

Using the 1994 data sample, $F_2(x, Q^2)$ has been measured [12] in the range $1.5 < Q^2 < 5000 \text{ GeV}^2$ and $3.2 \times 10^{-5} < x < 0.32$. This is shown in Figure 1.2a as a function of Q^2 at different values of x and in Figure 1.2b as a function of x at different values of Q^2 . The violation of scaling can clearly be seen in the former plot, with F_2 rising considerably as a function of $\log(Q^2)$ at low x , evolving to a slight fall with $\log(Q^2)$ at the highest value of x measured. The steep rise with decreasing x , becoming more prominent at high Q^2 can be seen in the latter plot. The results from the two HERA experiments are in good agreement, and represent a significant increase in the region of the kinematic plane explored. In addition, the HERA measurements are in good agreement with those of the fixed target experiments.

$F_2(x, Q^2)$ has been measured by H1 using 1995 shifted vertex data [13], exploiting the upgraded backward region, where the SPACAL calorimeter (see Chapter 4) enables detection of the scattered electron up to angles of $\theta = 178.6^\circ$. This measurement extends the kinematic region in which H1 has measured F_2 down to $Q^2 = 0.35 \text{ GeV}^2$ and $x = 6 \times 10^{-6}$. The results are shown in Figure 1.3 and are consistent with the 1994 measurement in the region where the two analyses overlap.

A measurement of the longitudinal proton structure function, F_L has been made by H1 with the 1994 data [11]. Since these data were taken at fixed beam energies, the standard technique for decoupling F_2 from F_L or R could not be used. Instead, a next-to-leading order QCD fit was used to evolve¹ the measurement of F_2 at low y values to high y , where the contribution of F_L to the NC DIS cross section is expected to be most significant, assuming F_L to be zero. By measuring the DIS cross section at high y (0.7) and subtracting

¹The DGLAP QCD evolution formalism was used for this, as described in Section 1.2.1.

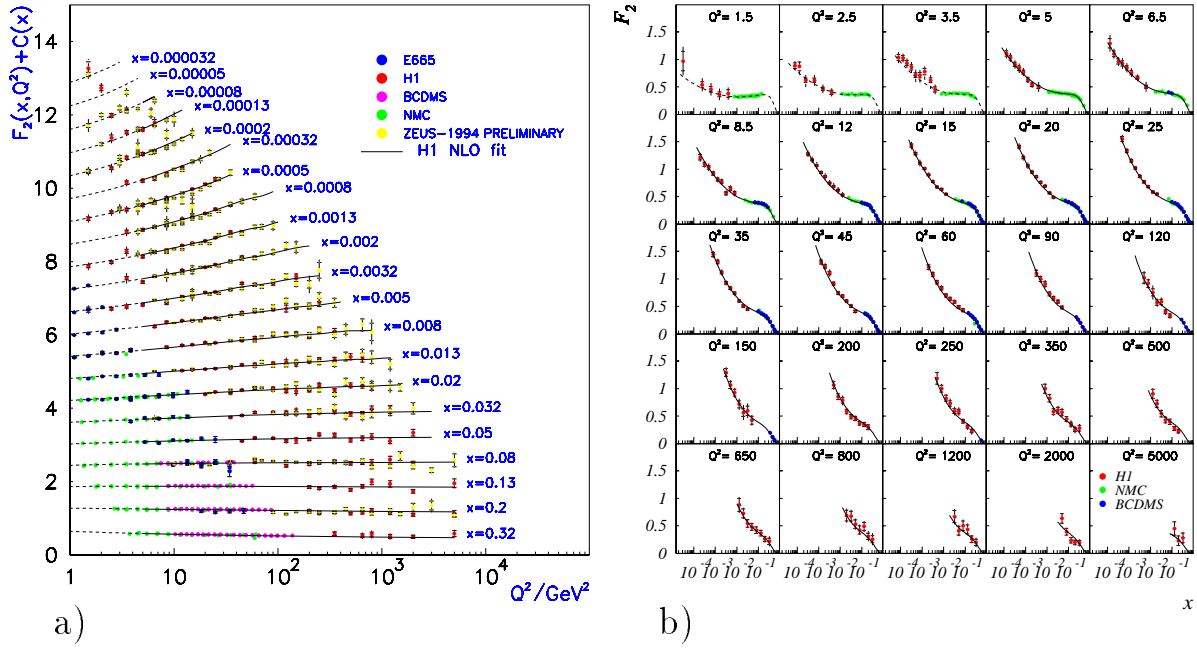


Figure 1.2: Measured values of $F_2(x, Q^2)$ from HERA and fixed target experiments, as a function of a) Q^2 and b) x . The curves are the result of a NLO QCD fit to the data by H1, described in [12]. The points in a) are displaced by an arbitrary amount for each value of x , for clarity.

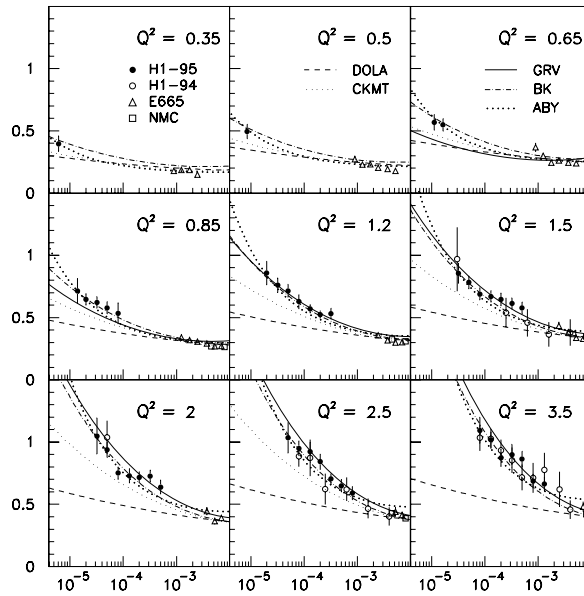


Figure 1.3: Measured values of $F_2(x, Q^2)$ from H1, exploiting the upgraded 1995 detector and therefore reaching substantially smaller Q^2 and x values than has previously been possible. Overlapping points from the earlier 1994 analysis and from fixed target experiments are also shown. The curves are different predictions for F_2 , described in the text and [13].

the evolved F_2 , F_L was determined. F_L was found to have an average value of $F_L = 0.52 \pm 0.03$ (stat) $^{+0.25}_{-0.22}$ (syst) at $Q^2 = 15.4 \text{ GeV}^2$ and $x = 2.43 \times 10^{-4}$. This result demonstrates that F_L , and therefore R , is inconsistent with zero.

1.2 Low x Phenomenology

Perhaps the most striking feature of the DIS measurements at HERA is the strong rise of F_2 at low x . This region has therefore generated a considerable amount of interest and experimental and theoretical activity [14, 15, 16, 17]. A significant effort has been made in attempting to understand the behaviour of F_2 in the low x region in terms of perturbative QCD. Different evolution schemes are used, discussed below, which differ in the treatment of terms in the perturbative QCD expansion of F_2 . This contains terms of the form $\alpha_s^n \ln^m Q^2$ and $\alpha_s^n \ln^m 1/x$ with all $m \leq n$, which are expected to dominate in different regions of the kinematic plane.

1.2.1 The DGLAP Evolution Formalism

In the kinematic region accessed by fixed target DIS experiments (relatively large x) the evolution equations of Dokshitzer, Gribov, Lipatov, Altarelli and Parisi (DGLAP) [18, 19] have been successful in describing the observed Q^2 dependence of the structure function. In this approach the parton density functions are separated into parts representing the valence quark (flavour non-singlet), sea quark (flavour singlet) and gluon distributions. These functions are determined from existing data at a reasonable starting scale, for instance $Q^2 = 4 \text{ GeV}^2$, where a perturbative approach is valid, and evolved to higher Q^2 by considering the QCD splitting processes, in which partons couple to others, such as those shown in Figure 1.4. The splitting functions, P_{ab} , represent the probability of the struck parton a , with momentum fraction x , originating from a parton b with momentum fraction y .

The momentum fraction of the non-singlet valence quarks coupling to the exchanged boson is modified from the starting scale by the gluon bremsstrahlung splitting process, $q \rightarrow qg$. The gluon distribution is derived from this process and from $g \rightarrow gg$. The singlet quark distribution is modified by gluon bremsstrahlung and the quark-antiquark pair production, $g \rightarrow q\bar{q}$. Considering contributions from all of these processes, the evolution at low x can be visualised in terms of ladder diagrams, such as that shown in Figure 1.5.

Given this scheme, the Q^2 evolution of the parton density functions for the non-singlet

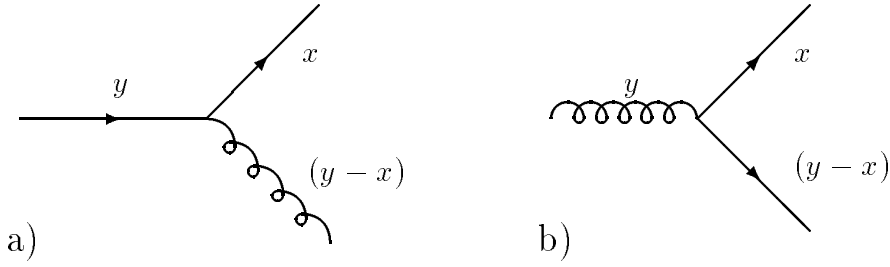


Figure 1.4: Representation of splitting functions in DGLAP evolution: a) $P_{qq}(x/y)$ and b) $P_{gg}(x/y)$.

quark, $q^{NS}(x, Q^2)$, the singlet quark, $q^S(x, Q^2)$, and the gluon, $g(x, Q^2)$ are given by the following three equations:

$$\frac{dq^{NS}(x, Q^2)}{d \ln Q^2} = \frac{\alpha_s(Q^2)}{2\pi} \int_x^1 \frac{dy}{y} \left[q^{NS}(y, Q^2) P_{qq} \left(\frac{x}{y} \right) \right] \quad (1.19)$$

$$\frac{dq^S(x, Q^2)}{d \ln Q^2} = \frac{\alpha_s(Q^2)}{2\pi} \int_x^1 \frac{dy}{y} \left[q^S(y, Q^2) P_{qq} \left(\frac{x}{y} \right) + g(y, Q^2) P_{qg} \left(\frac{x}{y} \right) \right] \quad (1.20)$$

$$\frac{dg(x, Q^2)}{d \ln Q^2} = \frac{\alpha_s(Q^2)}{2\pi} \int_x^1 \frac{dy}{y} \left[q^S(y, Q^2) P_{gq} \left(\frac{x}{y} \right) + g(y, Q^2) P_{gg} \left(\frac{x}{y} \right) \right] \quad (1.21)$$

The splitting functions, P_{nm} , have been calculated in next-to-leading order QCD, and the density functions are input from the starting scale in Q^2 . Solving these equations, from which F_2 can be calculated using Equation 1.17, leads to a prediction for the evolution of F_2 with Q^2 . The DGLAP formalism predicts that F_2 has a logarithmic dependence on Q^2 , falling with Q^2 at high x , and rising at low x . This behaviour is similar to the intuitive interpretation of the proton structure which was gained by admitting QCD radiation to the Quark Parton Model; with increasing Q^2 the virtual photon probes finer details of the structure.

The DGLAP formalism resums terms of the type $\alpha_s^n \ln^n Q^2$ (the leading log approximation in Q^2 , LLA(Q^2)). It is therefore valid only if the following constraints are satisfied:

$$\alpha_s \ll 1 \quad (1.22)$$

$$\ln \frac{1}{x} \ll \ln \frac{Q^2}{Q_0^2}. \quad (1.23)$$

Furthermore, the LLA(Q^2) method implies a strong ordering of the parton virtuality and a weak ordering in the momentum fraction in the ladder diagram shown in Figure 1.5:

$$Q^2 \gg k_{T_n}^2 \gg k_{T_{n-1}}^2 \gg \dots \gg k_{T_1}^2 \quad (1.24)$$

$$x \leq x_n \leq x_{n-1} \leq \dots \leq x_1. \quad (1.25)$$

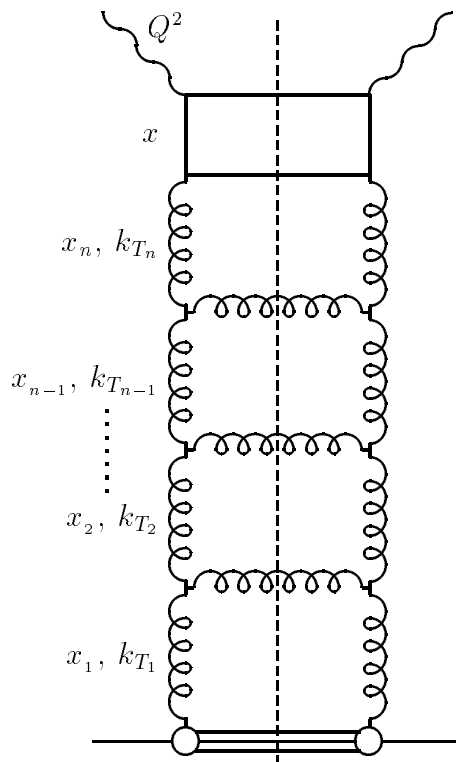


Figure 1.5: *QCD evolution ladder diagram for DIS low x for the DGLAP and BFKL formalisms. In DGLAP, the ladder can consist of both quarks and gluons. In the BFKL picture, the whole figure represents the squared amplitude from which the cross section is calculated; cutting down the dotted line reveals the diagram for the final state in the DIS process.*

This approximation is not necessarily reasonable in the low x region. DGLAP evolution is therefore only valid for large Q^2 and reasonably large x .

In spite of these restrictions, parameterisations of F_2 based on DGLAP evolution have been successful in describing the HERA data measured to date. The approach of Martin, Roberts and Stirling [20] has had notable success [12], providing that the input distributions at the starting scale ($Q_0^2 = 4 \text{ GeV}^2$) already rise with decreasing x .

A modified DGLAP approach, formulated by Glück, Reya and Vogt (GRV) [21, 22] has also been proven to describe the HERA data well. In this approach, all of the parton distributions are assumed to have a valence-like structure (vanishing as $x \rightarrow 0$) at a very low starting scale of $Q_0^2 = 0.34 \text{ GeV}^2$, and are then evolved to higher Q^2 using the DGLAP evolution equations. The determination of the input distributions at the starting scale uses fixed target data, and there is little freedom for adjustment in the HERA kinematic region. This approach has been criticised on the basis that, at the very low starting scale, α_s is large, placing the use of perturbative QCD into question.

The GRV calculation describes the H1 data well, even at low x [12]. This indicates that, in the low x regime, the sea quark distributions can be generated from the valence quark distributions at low Q^2 by QCD dynamics. In the low x region, the valence distribution does not play a significant role, and the singlet distribution is driven by that of the gluon, which rises rapidly with decreasing x (see Section 1.2.4). The 1995 H1 measurements of $F_2(x, Q^2)$ are consistent with GRV above $Q^2 = 1 \text{ GeV}^2$ but are systematically higher below this value [13]. This is unsurprising, given that higher twist effects become increasingly important at low Q^2 because α_s is large.

The success of the GRV approach indicates that predicting the behaviour of $F_2(x, Q^2)$ at low x and high Q^2 essentially requires an understanding of the gluon distribution alone. In this asymptotic region, Ball and Forte [23] have developed a convenient way of testing the behaviour of F_2 using two scaling variables of the form:

$$\sigma = \sqrt{\ln \frac{x_0}{x} \ln \frac{Q^2}{Q_0^2}} \quad (1.26)$$

$$\rho = \sqrt{\frac{\ln \frac{x_0}{x}}{\ln \frac{Q^2}{Q_0^2}}} \quad (1.27)$$

where the parameters x_0 and Q_0^2 are determined experimentally ($x_0 \simeq 0.1$, $Q_0^2 = 2.5 \text{ GeV}^2$). In these variables, the gluonic DGLAP evolution equation reduces to a two-dimensional wave equation which is analytically soluble. Given a gluon distribution at the starting scale which is soft, in the double asymptotic limit of large σ and ρ a rescaled structure function $R_F F_2$ is expected to be independent of ρ and σ and the function $\ln(R'_F F_2)$, should rise linearly with σ . R_F and R'_F are functions precisely specified in terms of ρ and σ . The H1 data are in good agreement with this approach, exhibiting the expected scaling properties to within errors [12].

1.2.2 The BFKL Evolution Formalism

We have seen that the DGLAP formalism has limited applicability across the kinematic domain and has no predictive power about the evolution of the structure function in x ; instead it relies on the x behaviour of the input distribution to reproduce the data. The DGLAP method does not deal with the terms $\alpha_s^n \ln^n(1/x)$ in the expansion of F_2 . In an approach which addresses these problems Balitski, Fadin, Kuraev and Lipatov (BFKL) [24, 25] treat these terms in a leading log ($1/x$) approximation (LLA($1/x$)) to provide an evolution in x . This method assumes that the low x region is dominated by the gluon splitting process, $g \rightarrow gg$ as in the diagrams shown in Figure 1.5. The strong ordering of the parton virtuality of the DGLAP evolution equations is relaxed, and a strong ordering

in x required:

$$Q^2 \geq k_{T_n}^2 \geq k_{T_{n-1}}^2 \geq \dots \geq K_{T_1}^2 \quad (1.28)$$

$$x \ll x_n \ll x_{n-1} \ll \dots \ll x_1 \quad (1.29)$$

The LLA($1/x$) approximation is valid in the region

$$\alpha_s \ll 1 \quad (1.30)$$

$$\ln \frac{Q^2}{Q_0^2} \ll \ln \frac{1}{x} \quad (1.31)$$

with $Q_0^2 \gtrsim 1 \text{ GeV}^2$; the BFKL formalism is therefore applicable to the region of low x and comparatively low Q^2 .

In the BFKL approach, the gluon density function is related to the non-integrated gluon distribution, $f(x, k^2)$, by

$$xg(x, Q^2) = \int_0^{Q^2} \frac{dk^2}{k^2} f(x, k^2) \quad (1.32)$$

Consideration of squared amplitudes, such as that shown in Figure 1.5, with all possible gluon insertions, leads to the BFKL equation, written for simplicity as:

$$x \frac{\partial f}{\partial x} \equiv K_L \otimes f \quad (1.33)$$

where the symbol \otimes implies integration over k_T . K_L is known as the Lipatov kernel, and represents summation over the terms $\alpha_s^n \ln^n(1/x)$ in the perturbative expansion. At fixed Q^2 , so that the variation of $\alpha_s(Q^2)$ may safely be neglected, the BFKL equation may be solved analytically. This leads to the prediction for $F_2(x, Q^2)$ in the low x regime that:

$$F_2(x, Q^2) \propto x^{-\lambda} \quad (1.34)$$

where

$$\lambda = \frac{12\alpha_s}{\pi} \ln 2 \sim 0.5 \quad (1.35)$$

The BFKL formalism therefore predicts the rise in the structure function with decreasing x , given the measured structure function at higher x and the same Q^2 .

At the present level of accuracy achieved by the HERA experiments, the DIS measurements are consistent with BFKL evolution, but are sufficiently well described by parameterisations based on DGLAP as not to require BFKL to play a significant role. Further measurements of F_2 may allow some discrimination to be made. In addition, other measurements, such as investigations of the final state in DIS [26], may be more sensitive to the dynamics of the low x region.

1.2.3 The GLR Equation

The rise of F_2 at low x cannot continue indefinitely, or unitarity would be violated. It is therefore assumed that some mechanism ultimately serves to damp the gluon distribution at large Q^2 , low x . One possibility is that, as $x \rightarrow 0$, the gluon density becomes so high that the recombination process, $gg \rightarrow g$, may become significant.

In this very low x region, where an understanding of the gluon distribution is clearly desirable, terms in the perturbative expansion of the form $\ln(Q^2)$ and $\ln(1/x)$ are both likely to be important. The approach of Gribov, Levin and Ryskin (GLR) [27] uses the double leading logarithm approximation (DLA) to treat both term types. This implies a strong ordering in both the parton virtuality, k_T^2 , and momentum fraction, x .

The GLR approach predicts, at large Q^2 and low x an asymptotic form for the gluon density:

$$xg(x) \sim e^{2 \left[\frac{3\alpha_s(Q^2)}{\pi} \ln\left(\frac{1}{x}\right) \ln\left(\frac{Q^2}{Q_0^2}\right) \right]^{\frac{1}{2}}} \quad (1.36)$$

The kinematic region accessible at HERA is not expected to be very sensitive to recombination effects and there has been no evidence for them as yet. For this reason, this formalism is presented for the sake of completeness only.

1.2.4 Measurement of the Gluon Density at Low x

We have seen that the structure of the proton at low x is driven by the gluon density in this region. A quantitative measurement of this quantity is therefore an important goal for the HERA experiments.

Since the photon does not couple directly to the gluons, the gluon density must be inferred from F_2 data. H1 has extracted the gluon density, $xg(x)$, at two values of Q^2 (5 and 20 GeV²) using a fit to the structure function F_2 [12]. The DGLAP evolution equations were solved in the next-to-leading order (NLO) approximation. Functional forms for the singlet, non-singlet and gluon density distributions were assumed, and $xg(x)$ extracted from a χ^2 fit to the measured $F_2(x, Q^2)$, additionally constrained by measurements from fixed target experiments. The fit result is shown in Figure 1.2b and found to be in excellent agreement with the data. Possible higher twist effects were avoided by excluding from the fit data in the range $Q^2 < 5$ GeV² ($Q^2 < 15$ GeV² for $x > 0.5$); the extension of the curves into these regions represents the evolution of the fit only. From the result of the fit, the gluon density was extracted, shown in Figure 1.6. The error bands are derived

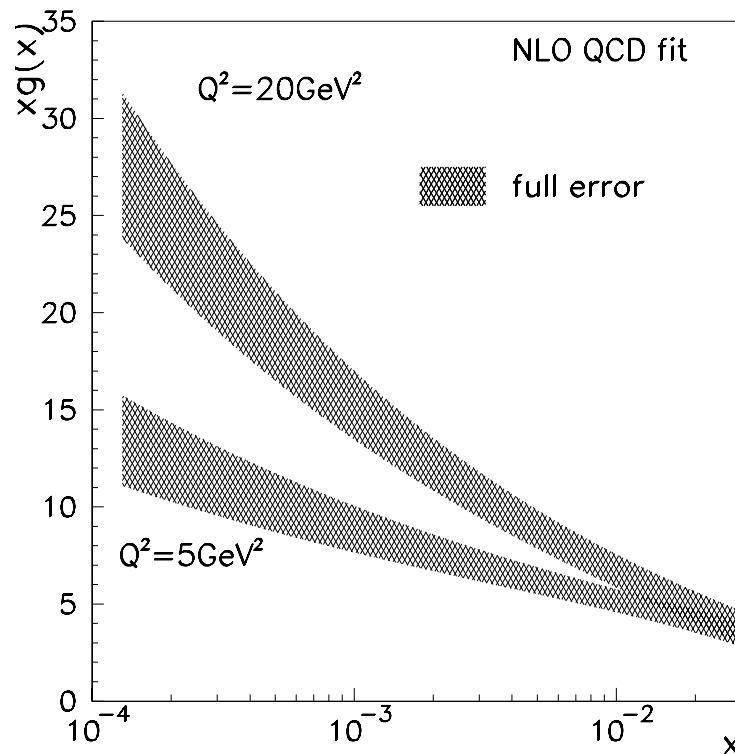


Figure 1.6: The gluon density $xg(x)$ at $Q^2 = 5 \text{ GeV}^2$ and $Q^2 = 20 \text{ GeV}^2$ extracted from H1 data with a NLO QCD fit.

from separate consideration of the statistical and systematic errors. The expected rise at low x is observed, becoming more significant with increasing Q^2 .

A complementary measurement of the gluon density has been made by the H1 collaboration from an analysis of photon-gluon fusion events [28], in which the process $\gamma^* g \rightarrow q\bar{q}$ occurs, leading to two jets in the final state. A dominant background to this process arises from QCD-Compton events, $\gamma^* q \rightarrow gq$, which was subtracted statistically. $xg(x)$ was then unfolded from the observed cross-section for two jet events and found to be in agreement, within errors, with the QCD fit measurement discussed above. The steep rise of the gluon density at low x is thus confirmed.

1.2.5 The Low Q^2 Limit

While the high Q^2 and low x regimes have motivated considerable activity at HERA, the low Q^2 region, where the transition between DIS and photoproduction occurs, is also of great interest. Whereas DIS can be considered as the scattering of virtual photons from partons in the target, photoproduction processes in the limit $Q^2 \rightarrow 0$ resemble hadron-hadron interactions, due to the fluctuation of the photon into a hadronic state before its interaction with the proton. A phenomenological description of this regime, which

is dominated by soft interactions between the hadronic photon and the proton, can be gained from the framework of Regge theory².

A distinct division between the two regimes, and therefore between the perturbatively calculable region of DIS and the non-perturbative region of photoproduction, is clearly unphysical. The use of Regge theory to describe the hadronic photon in photoproduction has therefore been extended into the low x , low Q^2 region of DIS. In such models, reggeon and pomeron exchange are used to describe the total photoproduction cross-section as a function of the invariant mass of the γp system, $W_{\gamma p}$, at fixed Q^2 which is then related to the proton structure function by the following expression:

$$\sigma_{\gamma p}^{tot}(W_{\gamma p}) \sim \lim_{Q^2 \rightarrow 0} \frac{4\pi^2 \alpha_{em}}{Q^2} F_2(x, Q^2). \quad (1.37)$$

The potential divergence at $Q^2 = 0$ implies that $F_2(x, Q^2 \rightarrow 0) \rightarrow 0$.

The Regge inspired model for F_2 at low Q^2 of Donnachie and Landshoff (DOLA) [29] assumes a soft pomeron with an intercept of $1 + \lambda \sim 1.08$ derived from fits to the total $p\bar{p}$ cross section, from which the dependence of F_2 with x ($F_2(x) \sim x^{-\lambda}$) is determined. The prediction of this model is compared with the low Q^2 measurement of $F_2(x, Q^2)$ from the 1995 H1 data [13] in Figure 1.3. The DOLA prediction can be seen to give an increasingly better description of the data as $Q^2 \rightarrow 0$.

The approach of Capella, Kiadalov, Merino and Tran Thanh Van (CKMT) [30] includes screening corrections and multi-pomeron exchange which mask an underlying “bare” pomeron and are assumed to decrease in significance as Q^2 increases. This gives rise to an “effective” pomeron intercept at $Q^2 = 0$ which tends towards the larger “bare” intercept as $Q^2 \rightarrow \infty$. Hence the structure function predicted by CKMT rises faster with decreasing x as Q^2 increases than that from the DOLA model. The CKMT prediction is therefore higher than that of DOLA, but still undershoots the data substantially as Q^2 increases (see Figure 1.3).

The total γp cross section is usually described with two contributions which correspond to pomeron and reggeon exchange:

$$\sigma_{\gamma p}^{tot}(W_{\gamma p}) = A_P W^{2(\alpha_P(0)-1)} + A_R W^{2(\alpha_R(0)-1)}. \quad (1.38)$$

In the Regge inspired model of Abramowicz, Levin, Levy and Maor (ALLM) [31], the valence and sea components of the structure function are identified with each of these terms, such that:

$$F_2(x, Q^2) = A_{sea} x^{1-\alpha_P(0)} + A_{val} x^{1-\alpha_R(0)} \quad (1.39)$$

²Regge theory is described in the context of diffraction in Chapter 2; some of the concepts used in this discussion are explained there.

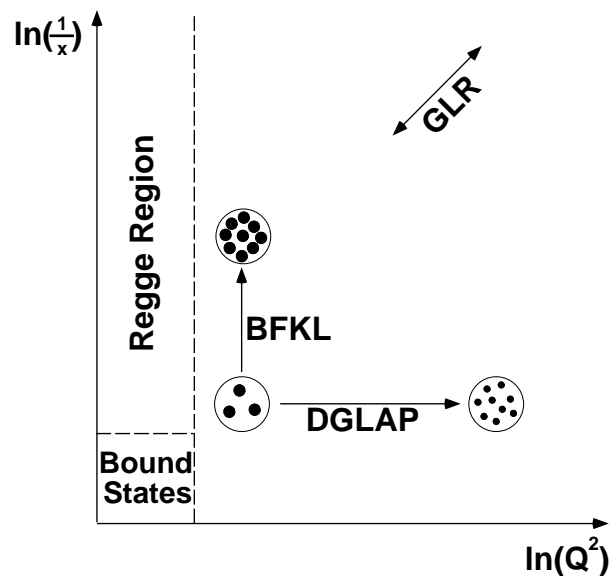


Figure 1.7: A schematic illustration of the kinematic plane, showing the regions of applicability of the various evolution schemes.

where $\alpha_P(0) = 1 + \lambda$ and $\alpha_R(0) \sim 0.5$. The exponent λ is then predicted to vary logarithmically with Q^2 , in the same way as in pQCD evolution at high Q^2 . The ALLM prediction is found to be below the data at low Q^2 , but is in reasonable agreement for $Q^2 > 2 \text{ GeV}^2$.

A further model compared with the 1995 data, not Regge inspired, is that of Badelek and Kwiecinski (BK) [32]. This combines the Vector Dominance Model (VDM), which considers the hadronic fluctuation of real photons to vector meson bound states, with a dynamical parton model similar to that of the GRV formalism having a starting scale at low Q^2 . This model has a smooth transition from the real photon limit ($Q^2 = 0$) to the region of pQCD applicability. As shown in Figure 1.3 this model is in good agreement across the entire Q^2 range of the measurement. The prediction of this model for the total photoproduction cross section has, however, been found to be too large in some regions.

1.2.6 Summary

A review has been given of the formalism used in attempting to describe the structure function of the proton. The phenomenology of the low x regime was presented, which is of particular interest at HERA. The structure function is driven by the gluon density in this region, and is found to rise sharply with decreasing x . This provides an ideal testing ground for the applicability of perturbative QCD treatments of proton structure. An overview of the approximations used to predict the evolution of the structure function

$F_2(x, Q^2)$ has been given, demonstrating the regions in which each is valid. This is summarised in Figure 1.7 (taken from [33]), which shows the kinematic region in $\ln(Q^2)$ and $\ln(1/x)$, the variables relevant to the perturbative expansion of $F_2(x, Q^2)$. The transitions from the region of validity of one approach to that of another are not well defined. Furthermore, the HERA data have shown that a number of methods can be used to describe the data well, even in regimes where their basic assumptions may not be legitimate.

$F_2(x, Q^2)$ has been measured over a very wide part of this plane. In the low Q^2 region the transition from DIS to photoproduction is of major interest. Regge and VDM inspired models have been shown to describe the qualitative behaviour of the data in this region, without complete success in the quantitative description of all aspects of DIS measurements. The extremely high Q^2 region is remarkably simple to describe by comparison, since $\alpha_s \rightarrow 0$ and perturbative expansions are quickly convergent. It is however, the searching ground for new physics and will be discussed in Section 1.4.

1.3 Photoproduction

In the region where $Q^2 \rightarrow 0$, the photon is nearly real and is observed to behave hadronically. As the ep differential cross-section contains a propagator of the form $1/Q^4$, collisions at HERA are dominated by such photoproduction interactions.

The total photoproduction cross section arises mainly from soft processes, which result in the production of low P_T final states. The Vector Dominance Model, in which the photon fluctuates to meson bound states with appropriate quantum numbers (e.g $\rho(770)$, $\omega(783)$, $\phi(1020)$ and $J/\psi(3097)$) describes this behaviour well [34].

High p_T (hard) interactions are also observed in photoproduction and are often subdivided into two classes. In direct processes, the photon interacts directly with a parton from the proton. The simplest example is the QCD-Compton interaction (Figure 1.8a), which leads to a final state containing, in addition to the proton remnant, two jets in the final state arising from the hadronisation of the quark and gluon. Another direct process is photon-gluon fusion (Figure 1.8b) where the photon interacts with a gluon from the proton via a $q\bar{q}$ pair. The final state is similar, containing jets initiated by the quark and antiquark. As mentioned in Section 1.2.4 a study of photon-gluon events can yield information on the gluon density of the proton. In addition, this is a major source of heavy-flavour production at HERA. Of particular interest is the production of $c\bar{c}$ pairs, which can form a bound state such as the J/ψ [35, 36]. Such events can have clean final state signatures, such as the decay mode $J/\psi \rightarrow \mu^+ \mu^-$.

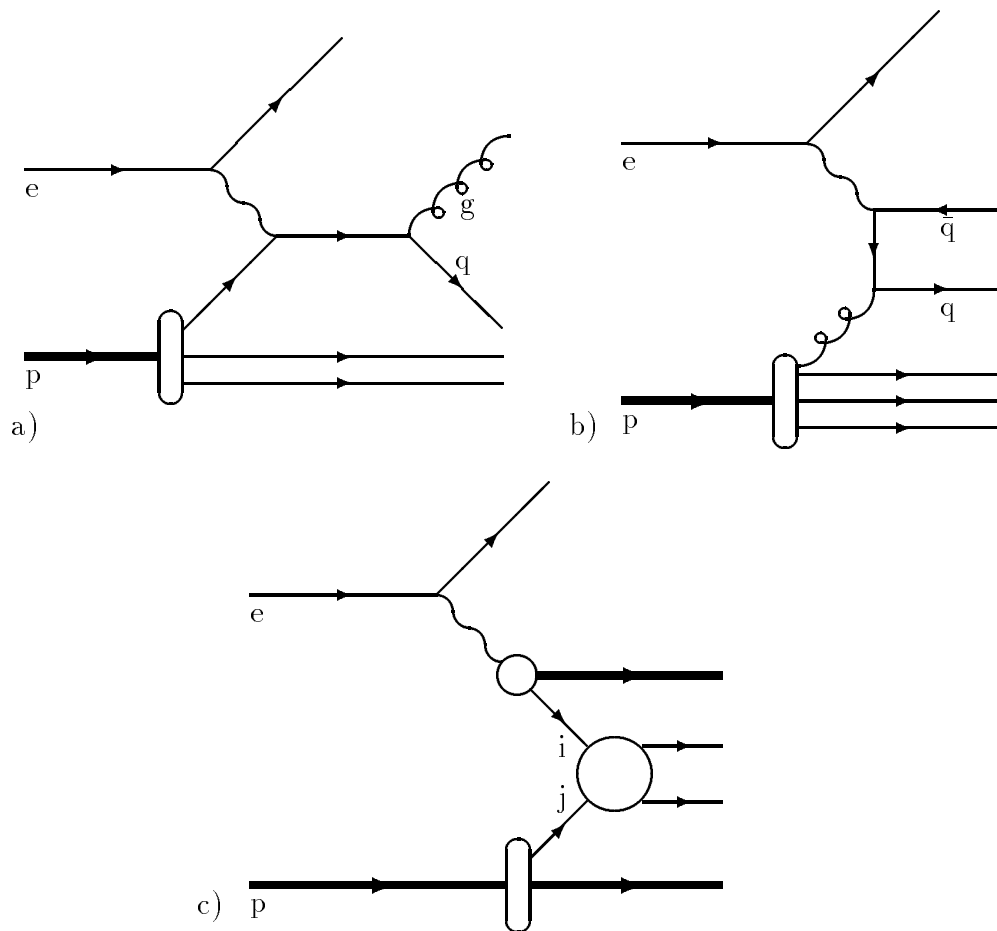


Figure 1.8: *Examples of photoproduction processes: direct a) QCD-Compton and b) photon-gluon fusion, and c) resolved.*

Resolved processes involve the interaction of the hadronic structure of the photon with that of the proton. However, the hard scale prevents the full development of a non-perturbative bound meson state, and the VDM is not applicable. A hard scattering takes place between a parton from the photon and one from the proton (Figure 1.8c). The final state then contains the proton remnant, a photon remnant, and two jets from the hard scattering process.

1.4 Beyond the Standard Model

HERA presents a unique opportunity for the study of ep collisions at unprecedented energies, and is therefore a natural environment in which to search for physics processes beyond the Standard Model. Perhaps the most obvious exotic states for which to search are leptoquarks and leptogluons. Excited lepton production is also a process to which

HERA has competitive sensitivity. While a discussion of this sector is beyond the scope of this thesis, it is interesting to note the recent observation by both H1 [37] and ZEUS [38] of an excess of DIS events at extremely high Q^2 ($> 15000 \text{ GeV}^2$). An estimate of the combined significance of these results places the probability of the signal being due to fluctuations in the Standard Model DIS predictions at $\sim 1\%$. Both experiments expect to double the integrated luminosity of their data samples during the 1997 running period, which may enable the present observations to be either confirmed or denied. While these analyses cannot yet make any discrimination between possible processes which could cause the observed signal, they present perhaps the first tantalising indication of physics beyond the Standard Model.

Chapter 2

Diffractive Deep-Inelastic Scattering

This chapter presents the theoretical basis and motivation for measuring the diffractive proton structure function. The concepts of Regge theory, which has been successful in describing most features of hadron-hadron interactions, are discussed. The role of the pomeron and diffractive interactions in Regge theory is outlined. The observation by the HERA experiments of DIS events with rapidity gaps [2, 3] has been interpreted as a consequence of diffractive interactions between the virtual photon and proton mediated by pomeron exchange. In an attempt to understand the partonic nature of the pomeron, the HERA experiments have measured a diffractive structure function of the proton. Recent results from such analyses are presented.

2.1 Hadron-Hadron Interactions and Regge Theory

Hadron-hadron collisions have played a central role in the development of particle physics. When these collisions, mediated by the strong interaction, take place at low momentum transfers, the absence of a hard scale means that the strong coupling constant, α_s , is large and perturbative QCD approaches are not applicable. In this non-perturbative regime, the phenomenological approach of Regge theory [39, 40] has to date provided the best description of the data.

The Regge approach makes predictions about the t channel process $A\bar{C} \rightarrow \bar{B}D$ by analytic continuation of the amplitude for the s channel process, $AB \rightarrow CD$, generalised forms of which are shown in Figure 2.1. s and t are the usual Mandelstam variables, defined in the s channel as

$$s = (A + B)^2 = (C + D)^2 \quad (2.1)$$

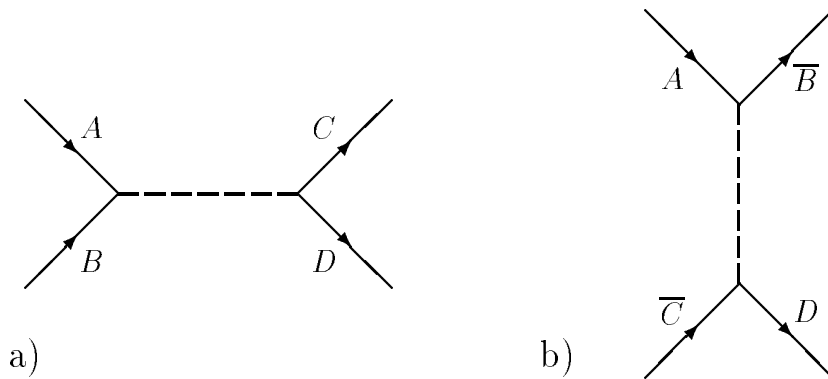


Figure 2.1: *Illustration of generalised a) s and b) the equivalent crossed t channel processes.*

$$t = (A - C)^2 = (B - D)^2 \quad (2.2)$$

where A , B , C and D denote the four-momenta of the hadrons involved in the scattering process. Crossing symmetry implies that s channel resonance production can be described by the same amplitude as the t channel exchange mechanism, providing that the variables s and t are interchanged on crossing. In the s channel, all the possible resonances which can be produced by the interaction of A and B and conserve quantum numbers (parity, charge etc.) are linked by a linear trajectory in a two-dimensional space defined by mass squared and angular momentum. In Regge theory, angular momentum is treated as a continuous, complex variable, $\alpha(t)$. The observable s channel resonances only occur at physical values of spin, such that $\mathcal{R}e[\alpha(t)]$ is an integer or half-integer, known as Regge poles. The extrapolation of this trajectory from the s channel region (positive mass-squared, $M^2 = s$) into the t channel region governs the energy dependence of the t channel process. The linear trajectories¹ can be parameterised as

$$\alpha(t) = \alpha(0) + \alpha' t. \quad (2.3)$$

A prediction can then be made, based on the parameterisation of the trajectory, of the elastic and total cross sections. The Minimal Regge Hypothesis states that the elastic amplitude for $AB \rightarrow AB$, T_{el} , has the form

$$T_{el}(s, t) \propto s^{\alpha(t)} \quad (2.4)$$

from which the differential elastic cross section can be derived, at fixed t with $t \ll s$, as

$$\frac{d\sigma_{el}}{dt} \propto s^{2\alpha(t)-2} \quad (2.5)$$

¹In general, the trajectories could have any shape. However, for mesons they are linear, which can be qualitatively understood in QCD if the mesons are considered to be rotating pairs of massless quarks bound together by a gluon flux tube. See, for example [41].

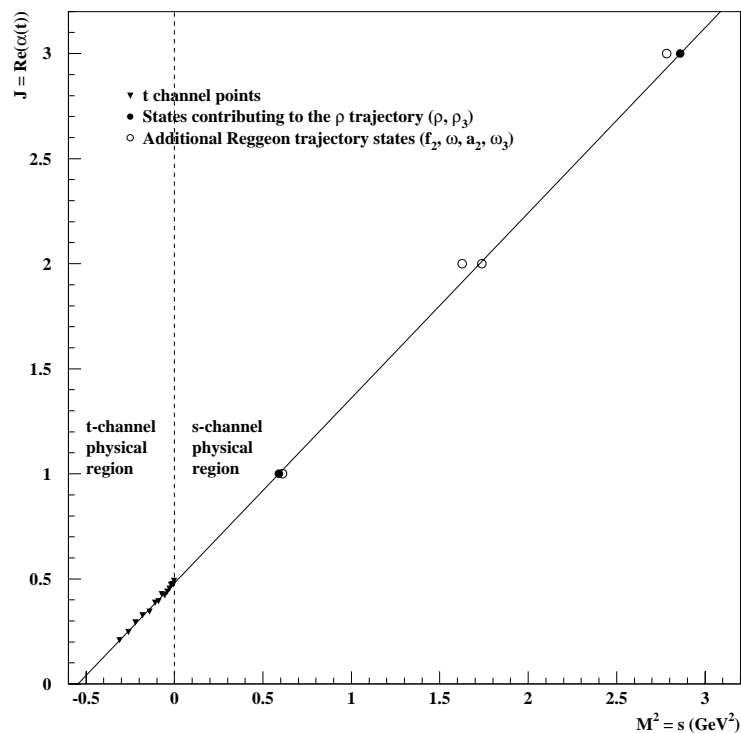


Figure 2.2: Chew-Frautschi plot of the ρ trajectory, $\alpha_\rho(t)$, taken from [33].

The Optical Theorem relates the total cross section to the forward ($t = 0$) elastic amplitude via the following:

$$\sigma_{tot} \sim \frac{1}{s} \mathcal{I}m(T_{el})_{t=0} \quad (2.6)$$

giving, for the total cross section in the limit $t \rightarrow 0$,

$$\sigma_{tot} \propto s^{\alpha(0)-1} \quad (2.7)$$

Regge theory thus makes predictions about the energy dependence of the total cross section for a process based on the *intercept* of the associated trajectory. While this is a purely phenomenological prescription, with no firm theoretical basis in the subsequent developments of QCD, it is able to predict accurately the energy dependence of soft hadronic interactions.

An example of a Regge trajectory is shown in Figure 2.2, plotted as $\text{Re}[\alpha(t)]$ versus $M^2 = t$; this is known as a Chew-Frautschi plot. The physical states in the s channel are the ρ and ρ_3 . A linear fit to these points gives the trajectory $\alpha(t) = 0.480 + 0.881t$. Extrapolated into the negative t region, this gives a good description of the t channel points. These were measured in the charge exchange reaction $\pi^- p \rightarrow \pi^0 n$ [42] which is

dominated by ρ exchange. A more general trajectory, known as the reggeon², $\alpha_{\mathcal{R}}(t)$, is formed by the inclusion of a number of additional physical states (f_2 , ω , a_2 and ω_3) which have degenerate trajectories.

2.2 The Pomeron Trajectory

All of the observed meson trajectories have intercepts in the region of $\alpha(0) \lesssim 0.5$. Thus the cross section of the processes associated with these fall rapidly with increasing centre of mass energy, as indicated by Equation 2.7. This is contradicted by the total and elastic cross sections observed in pp and $p\bar{p}$ scattering, which display a slow rise with \sqrt{s} at high energies. In the language of Regge theory, the trajectory responsible for high energy elastic scattering must therefore have an intercept slightly greater than one and must have the quantum numbers of the vacuum (zero charge, isospin and baryon number, positive parity and C-parity) in order to mediate elastic scattering. The trajectory needed to describe total cross sections at high \sqrt{s} is known as the pomeron, $\alpha_{\mathcal{P}}(t)$, after Pomerončuk.

The pomeron intercept was extracted by Donnachie and Landshoff from the total cross section in pp and $p\bar{p}$ collisions [43] using a fit which was the sum of contributions from the pomeron and from the exchange degenerate reggeon mentioned above:

$$\sigma_{tot}(s) = A_{\mathcal{P}} s^{\alpha_{\mathcal{P}}(0)-1} + A_{\mathcal{R}} s^{\alpha_{\mathcal{R}}(0)-1} \quad (2.8)$$

where the normalisations, $A_{\mathcal{P}}$, $A_{\mathcal{R}}$ and intercepts $\alpha_{\mathcal{P}}$, $\alpha_{\mathcal{R}}$ of the pomeron and reggeon respectively were free parameters. The intercepts were found to be:

$$\alpha_{\mathcal{P}}(0) = 1.08 \quad (2.9)$$

$$\alpha_{\mathcal{R}}(0) = 0.55 \quad (2.10)$$

These values were then constrained and a fit performed to $\pi^{\pm}p$ and γp data where an excellent description of the behaviour was also observed. This indicated that the pomeron/reggeon model was able to describe a wide range of hadron-hadron cross sections. The reggeon coupling is larger than that of the pomeron, and dominates at low energy. However, it falls off as $s^{\frac{1}{2}}$ and the pomeron component, which behaves like $s^{0.08}$, begins to dominate at high energies, where the cross section rises slowly with s . At first sight, this would seem to violate unitarity at extremely large \sqrt{s} . However, it is assumed that the effective intercept, $\alpha_{\mathcal{P}}(0)$, falls slowly with energy due to multiple pomeron exchange thereby preventing any violation. This effect is, however, not relevant at the energy scales encountered at HERA.

²Strictly, the reggeon refers to any Regge trajectory. It is, however, usual to consider the reggeon as any trajectory other than that of the pomeron.

Processes that involve pomeron exchange are known as diffractive. The pomeron trajectory has proven to be a vital tool in the phenomenological description of total and elastic cross sections at high energies, describing well the features of t channel processes. However, no known physical particle has been observed which would lead to a pole in the s channel region of the pomeron trajectory. There is, therefore, considerable motivation for attempting to understand the pomeron in the framework of QCD by investigating its partonic structure.

2.3 Diffraction in Deep-Inelastic Scattering

The observation of a class of DIS events at HERA which contain large rapidity gaps [2, 3] can be interpreted as being due to pomeron exchange between the virtual photon and the proton. In a standard DIS process, such as that shown in Figure 1.1, the hadronic final state is populated by two jets resulting from the hadronisation of the struck (current) parton and the proton remnant. The current jet is typically contained within the detector, while the remnant jet remains close to the initial proton direction and goes largely unobserved into the beam pipe. There is colour flow between the current and remnant jets, which causes hadronisation in the region between the two.

Diffractive exchanges, such as that shown in Figure 2.3, may be viewed in terms of the photon interacting with a colourless component of the proton, for instance a pomeron. The proton remains intact, or is excited into a low-mass state which conserves quantum numbers (e.g. N^*). There is no colour flow between the proton remnant and the current jet region, resulting in a large rapidity gap in the hadronic final state. This is therefore the primary experimental signature for the detection of events mediated by colourless exchange.

2.3.1 The Kinematics of Diffractive DIS

Figure 2.3 illustrates a diffractive DIS process, under the assumption of pomeron exchange. In addition to the usual kinematic variables appropriate to the characterisation of DIS (described in Section 1.1.2), a number of additional invariants are defined:

$$M_X^2 = X \cdot X \quad (2.11)$$

$$W^2 = (q + P)^2 \quad (2.12)$$

$$M_{eX}^2 = (X + k')^2 \quad (2.13)$$

$$t = (P - P')^2 \quad (2.14)$$

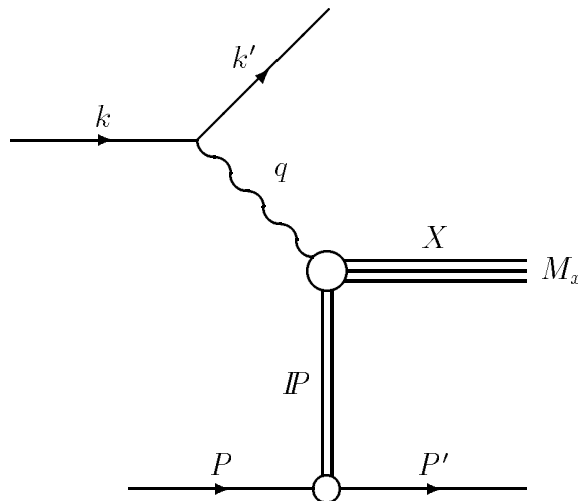


Figure 2.3: A diffractive DIS process, showing the four-momenta used in the construction of the invariants describing diffractive kinematics.

$$x_P = \frac{q \cdot (P - P')}{q \cdot P} \quad (2.15)$$

$$\beta = \frac{Q^2}{2q \cdot (P - P')} \quad (2.16)$$

M_X^2 is the invariant mass squared of the hadronic system, X , arising from the photon-pomeron interaction, W^2 is the mass squared of the photon-proton system, M_{eX}^2 is the invariant mass squared of the final state including the scattered electron but excluding the proton, and t , the usual Mandelstam variable, is the momentum transfer at the proton vertex. x_P and β can be expressed in terms of the other invariant quantities as

$$x_P = \frac{Q^2 + M_X^2 - t}{Q^2 + W^2 - m_p^2} \simeq \frac{Q^2 + M_X^2}{Q^2 + W^2} \quad (2.17)$$

and

$$\beta = \frac{Q^2}{Q^2 + M_X^2 - t} \simeq \frac{Q^2}{Q^2 + M_X^2} \quad (2.18)$$

If t is small and the centre of mass energy is much greater than the proton mass, β may be identified as the analogue of the scaling variable x in inclusive DIS, that is, the fraction of the longitudinal momentum of the pomeron which is carried by the parton interacting with the photon. x_P can be identified in a similar way to y , which describes the fraction of the incoming electron momentum carried by the photon; x_P is, in the limit $t \rightarrow 0$, the fraction of the incoming proton momentum carried by the pomeron. It can be seen from Equations 1.6, 2.15 and 2.16 that the Bjorken scaling variable, x , is related to β and x_P by

$$x = \beta x_P. \quad (2.19)$$

x therefore retains its usual interpretation in diffractive DIS as the fraction of the longitudinal momentum of the proton carried by the struck parton in the pomeron.

A consideration of the process $ep \rightarrow epX$ in a Regge framework leads to the prediction that the differential cross section has the behaviour

$$\frac{d^2\sigma(ep \rightarrow epX)}{dt dM_{eX}^2} \propto \left(\frac{s}{M_{eX}^2}\right)^{2\alpha(t)-2} \quad (2.20)$$

Using the fact that $x_P = M_{eX}^2/s$, Equation 2.20 may be written as

$$\frac{d^2\sigma(ep \rightarrow epX)}{dt dx_P} \propto \left(\frac{1}{x_P}\right)^{2\alpha(t)-1} \quad (2.21)$$

For pomeron exchange, where the trajectory intercept $\alpha_P(0) \simeq 1$ and t is small, the behaviour of the cross section is therefore approximately $d\sigma/dx_P \sim 1/x_P$. In contrast, the expected dependence from other Regge trajectories would lead to a cross section which is flat or rising with increasing x_P . Thus pomeron exchange becomes the dominant mechanism for the production of rapidity gap events in diffractive DIS as x_P falls.

2.3.2 The Diffractive Structure Function

Diffractive DIS is an ideal regime for investigating partonic interpretations of the pomeron because the hard scale arising from the virtual photon gives the possibility of probing substructure. This is formalised by defining diffractive structure functions [44, 45], in analogy with the fully inclusive case (Equation 1.12), such that:

$$\frac{d^4\sigma(x_P, t, x, Q^2)}{dx_P dt dx dQ^2} = \frac{4\pi\alpha_{em}^2}{xQ^4} \left(1 - y + \frac{y^2}{2[1 + R^D]}\right) F_2^{D(4)}(x_P, t, x, Q^2) \quad (2.22)$$

where contributions from F_3^D have been neglected. R^D is defined in the same way as the photo-absorption ratio in inclusive DIS (Equation 1.11) but there is no reason why the two should be simply related, as the defined cross sections are different. Just as F_2 is the usual quantity in which non-diffractive DIS is investigated, F_2^D is the primary method of exploring diffractive DIS.

There is considerable theoretical support [45, 46] for the hypothesis of factorisation, namely that the diffractive structure function may be split into two terms describing the pomeron-proton vertex and the pomeron-photon interaction. The diffractive structure function is then expressed as

$$F_2^{D(4)}(x_P, t, x, Q^2) = f_{P/p}(x_P, t) F_2^P(\beta, Q^2) \quad (2.23)$$

where $f_{\mathbb{P}/p}(x_{\mathbb{P}}, t)$ is the pomeron flux factor, and describes the dynamics of the production of pomerons from the proton. The structure function, $F_2^{\mathbb{P}}(\beta, Q^2)$, describes the partonic structure of the pomeron in exactly the same way that $F_2(x, Q^2)$ describes that of the proton. The factorisation hypothesis assumes that the pomeron emission process and the interaction of the pomeron with the photon are independent. This may be justified by considering the very different time scales on which each occurs; the momentum transfer, t , at the pomeron-proton vertex is generally much smaller than that at the pomeron-photon vertex. Thus the structure function can be factorised into large time-scale, non-perturbative ($f_{\mathbb{P}/p}(x_{\mathbb{P}}, t)$) and short time-scale, perturbative ($F_2^{\mathbb{P}}(\beta, Q^2)$) parts. In the following section the predictions of various models of the pomeron are discussed in which factorisation does and does not hold.

At HERA, measuring t requires detection of the final state proton or its remnant in the forward region, which is technically difficult. It is therefore usual to calculate a three-dimensional structure function, $F_2^{D(3)}(\beta, Q^2, x_{\mathbb{P}})$, which is derived from an implicit integration over t of $F_2^{D(4)}(x_{\mathbb{P}}, t, x, Q^2)$. The triple-differential cross section is defined in terms of this structure function as

$$\frac{d^3\sigma(x, x_{\mathbb{P}}, Q^2)}{dx dx_{\mathbb{P}} dQ^2} = \frac{4\pi\alpha_{em}^2}{xQ^4} \left(1 - y + \frac{y^2}{2(1 + R^D)}\right) F_2^{D(3)}(\beta, Q^2, x_{\mathbb{P}}). \quad (2.24)$$

All of the measurements of diffractive deep-inelastic scattering described in this thesis are based on this definition.

2.3.3 Models of the Pomeron in Diffractive DIS

Forms of the pomeron flux factor, $f_{\mathbb{P}}(x_{\mathbb{P}}, t)$, have been suggested in various factorisable models. Donnachie and Landshoff [47], using Regge theory and an elastic form factor for the proton, propose that

$$f_{\mathbb{P}/p}(x_{\mathbb{P}}, t) = \left(\frac{31.5}{4\pi^2}\right) \left(\frac{4m_p^2 - 2.8t}{4m_p^2 - t}\right) \left(\frac{1}{(1 - t/0.7)^2}\right) \left(\frac{1}{x_{\mathbb{P}}}\right)^{2\alpha_{\mathbb{P}}(t)-1} \quad (2.25)$$

where the pomeron trajectory is

$$\alpha_{\mathbb{P}}(t) = \alpha_{\mathbb{P}}(0) + \alpha'_{\mathbb{P}} t = 1 + \epsilon + 0.25t. \quad (2.26)$$

The parameter $\epsilon = 0.085$ gives the pomeron intercept determined from the fit to $p\bar{p}$ data described in Section 2.2. Ingelman and Schlein [48, 45] derive a flux factor using fits to CERN SPS $p\bar{p}$ data at $\sqrt{s} = 540$ GeV to determine the t and $x_{\mathbb{P}}$ dependence, and Regge theory only for normalisation to the data, giving

$$f_{\mathbb{P}/p}(x_{\mathbb{P}}, t) = 3.4 \left(e^{5.6t} + 0.04e^{2t}\right) \frac{1}{x_{\mathbb{P}}} \quad (2.27)$$

Finally, Berger et al [49] and Streng [46] suggest that

$$f_{\mathbb{P}/p}(x_{\mathbb{P}}, t) = \frac{100}{16\pi} e^{-R_N^2 |t|} \left(\frac{1}{x_{\mathbb{P}}} \right)^{2\alpha_{\mathbb{P}}(t)-1} \quad (2.28)$$

where $R_n^2 = 4.7 \text{ GeV}^{-2}$. It can be seen that all of these models predict an approximate $1/x_{\mathbb{P}}$ dependence of the flux, differing only in their overall normalisation and t dependence.

The simplest partonic picture of the pomeron is that its valence structure consists of a colour singlet combination of either a quark-antiquark or a two gluon pair; QCD pair production mechanisms subsequently produce a mixture of quarks and gluons at low β . The large momentum transfer, Q^2 , provides a hard scale for the pomeron-photon interaction and a perturbative QCD interpretation of the pomeron structure function, $F_2^{\mathbb{P}}(\beta, Q^2)$ may become applicable. In analogy with the proton, one can write the pomeron structure function in terms of parton density functions, $f_i(\beta, Q^2)$, as

$$F_2^{\mathbb{P}} = \beta \sum_i e_i^2 f_i(\beta, Q^2). \quad (2.29)$$

The analogy can be taken further to determine whether the partonic pomeron obeys the momentum sum rule:

$$\sum_i \int_0^1 x_p f_i(x_p) dx_p = 1 \quad (2.30)$$

where x_p is the momentum fraction of the pomeron carried by the parton p . Donnachie and Landshoff argue that, since the pomeron is not an on-shell particle, derivation of a momentum sum rule for its structure function is not valid.

There is no theoretical consensus on whether the pomeron structure is quark or gluon dominated. If the pomeron consists of just two gluons then a natural gluon momentum distribution, which fulfils the momentum sum rule, is

$$x_g g(x_g) = 6x_g(1 - x_g) \quad (2.31)$$

This represents a hard gluon distribution; Streng suggests that additional gluons arising from evolution soften the distribution, with a possible form similar to that of the gluon sea in the proton:

$$x_g g(x_g) = (1 - x_g)^5. \quad (2.32)$$

The real gluon distribution might reasonably be expected to lie somewhere between the two.

Donnachie and Landshoff propose a quark-dominated structure with the density function

$$x_q q(x_q) = \frac{1}{3} C_i \pi x_q (1 - x_q) \quad (2.33)$$

where $C_i \approx 0.2$ for u and d quarks, and ≈ 0.1 for s quarks. Summation over these flavours gives a total momentum sum of ≈ 0.2 , in support of their hypothesis of violation of the momentum sum rule.

Genovese, Nikolaev and Zakharov propose a model [50] in which the photon fluctuates to a quark-antiquark pair which then interacts with the proton via the exchange of gluons. The gluons may couple to different quarks, and the interaction is no longer point-like. In this model, factorisation is broken, and the valence and sea quark distributions within the pomeron have different dependences on x_p .

At high β , there is a contribution to diffractive DIS from direct processes, where the photon interacts with the pomeron as a whole and produces final states consisting of light vector mesons. The x_p dependence of such interactions can be handled using pure Regge theory, since the pomeron structure is not probed. The Q^2 dependence is not predicted, and is input from previous measurements. The Regge predictions are made through the Vector Dominance Model (VDM), mentioned in Section 1.2.5.

The gluon ladder diagram shown in Figure 1.5 can be considered as a perturbative model of pomeron exchange. The prediction of the BFKL evolution formalism of the structure function dependence $F_2(x, Q^2) \propto x^{-\lambda}$ can be understood in the language of Regge theory, where the exponent λ is related to the pomeron intercept by

$$\lambda = \alpha_p(0) - 1 \quad (2.34)$$

giving an intercept

$$\alpha_p(0) \sim 1.4; \quad (2.35)$$

this is known as the BFKL or hard pomeron. It has a larger intercept than that of the soft pomeron of Donnachie and Landshoff ($\alpha_p(0) = 1.085$) discussed in Section 2.2. A fit to the H1 F_2 measurements of the form $F_2 \sim x^{-\lambda}$ has been made [13] as discussed in Section 1.2.5. This shows a growth in λ as a function of Q^2 indicating an intercept consistent with the soft pomeron at low Q^2 rising to a value which is consistent with the BFKL prediction at large Q^2 . This evolution of the intercept gives the Regge description of the rise of the structure function at low x .

It can be seen that there are a number of predictions for the structure and behaviour of the pomeron in diffractive DIS. The questions of whether the pomeron has a partonic substructure, and whether the diffractive structure function can be factorised are therefore of considerable interest. In the next section, the existing measurements of the diffractive structure function by H1 and their interpretation are described.

2.4 Measurements of Diffractive DIS at HERA

The diffractive structure function $F_2^{D(3)}(\beta, Q^2, x_{\mathbb{P}})$ has been measured by H1 from the 1994 data sample of approximately 2 pb^{-1} [51]. The measurement was performed in the kinematic region $2.5 < Q^2 < 65 \text{ GeV}^2$, $0.01 < \beta < 0.9$ and $0.0001 < x_{\mathbb{P}} < 0.05$. Figure 2.4 shows the measured $F_2^{D(3)}$, multiplied by $x_{\mathbb{P}}$ in order to reveal the detail of the structure function.

As discussed in Section 2.3.3, Regge theory predicts a behaviour of the form $F_2^{D(3)} \propto x_{\mathbb{P}}^{-n}$ where $n \simeq 2\alpha_{\mathbb{P}}(t) - 1$. A phenomenological fit to the data of the form $F_2^{D(3)}(\beta, Q^2) = A(\beta, Q^2) \cdot x_{\mathbb{P}}^{-n}$ was therefore performed. A fit where n was independent of β and Q^2 was found to be inconsistent with the data. n was then allowed to vary separately with β (shown in Figure 2.4) and Q^2 in two independent fits. In all fits, the normalisation $A(\beta, Q^2)$, was allowed to vary with both β and Q^2 . Figure 2.5 shows the values of n extracted from these fits as a function of β and Q^2 ; there is a clear dependence on β but no evidence for any dependence on Q^2 . Significant deviations from the hypothesis of a universal factorisation of the diffractive structure function, described in Section 2.3.2, are therefore observed.

There are a number of possible explanations for the variation of n with β . One possibility is the contribution to the diffractive exchange of a meson trajectory having $n \sim 0$, such as the f_2 , ρ , a_2 or ω . Meson structure functions have a much softer β dependence than that of the pomeron, and so would contribute most to the observed structure function at low β . A fit to the data was therefore made in which two individually factorisable components from the pomeron, $F_2^{\mathbb{P}}(\beta, Q^2)x_{\mathbb{P}}^{-n_{\mathbb{P}}}$, and a meson, $C_M F_2^M(\beta, Q^2)x_{\mathbb{P}}^{-n_M}$, contributed. The meson structure function was taken from the GRV parameterisation of the pion. $F_2^{\mathbb{P}}(\beta, Q^2)$, $n_{\mathbb{P}}$, n_M and the normalisation of the meson component, C_M were left as free parameters. The fit gave an equally good description as the phenomenological fit with $n = n(\beta)$. After correction for the integration over t , the intercepts of the pomeron and meson trajectories were extracted and found to be $\alpha_{\mathbb{P}}(0) = 1.18 \pm 0.02(\text{stat}) \pm 0.04(\text{syst})$ and $\alpha_M(0) = 0.6 \pm 0.1(\text{stat}) \pm 0.3(\text{syst})$ respectively. The value of the pomeron intercept, $\alpha_{\mathbb{P}}(0)$ determined by this method is somewhat larger than that of the soft pomeron described above. Figure 2.6 shows the result of the two component fit superimposed on the measured points.

As discussed in Section 2.3.3, there are other models of diffractive DIS in which factorisation is broken, such as that of Genovese, Nikolaev and Zakharov. Comparison of the data with such a model indicated good agreement for $x_{\mathbb{P}} < 10^{-2}$, surprising given the large uncertainty in the gluon distribution of the proton. However, in the region of low β and

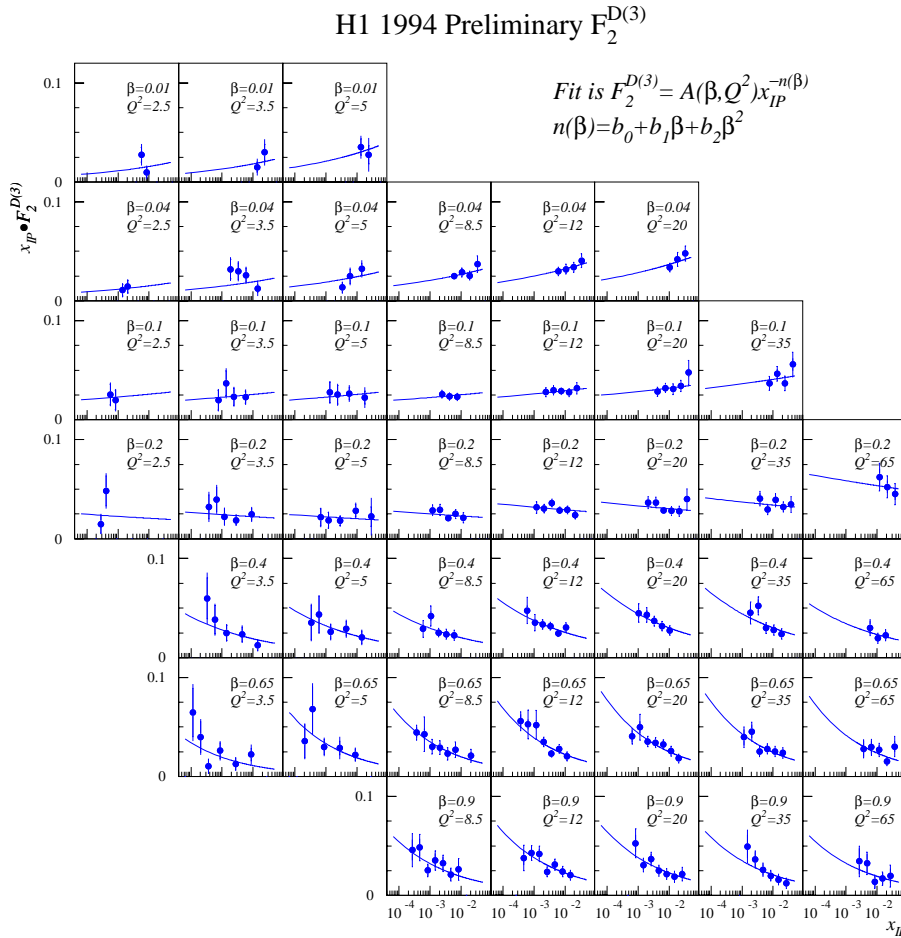


Figure 2.4: $x_{IP} \cdot F_2^{D(3)}(\beta, Q^2, x_{IP})$ from analysis of 1994 data including the result of a phenomenological fit $F_2^{D(3)} = A(\beta, Q^2) x_{IP}^{-n(\beta)}$ (taken from [51]).

H1 Preliminary 1994

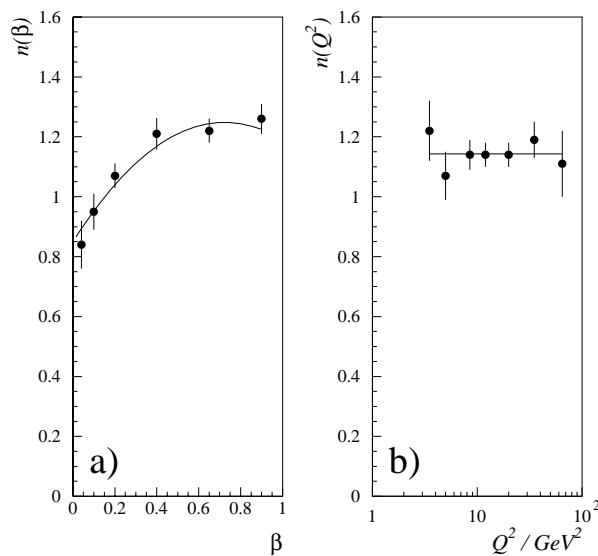


Figure 2.5: Variation of n as a function of a) β and b) Q^2 from phenomenological fit to 1994 data.

H1 Preliminary 1994

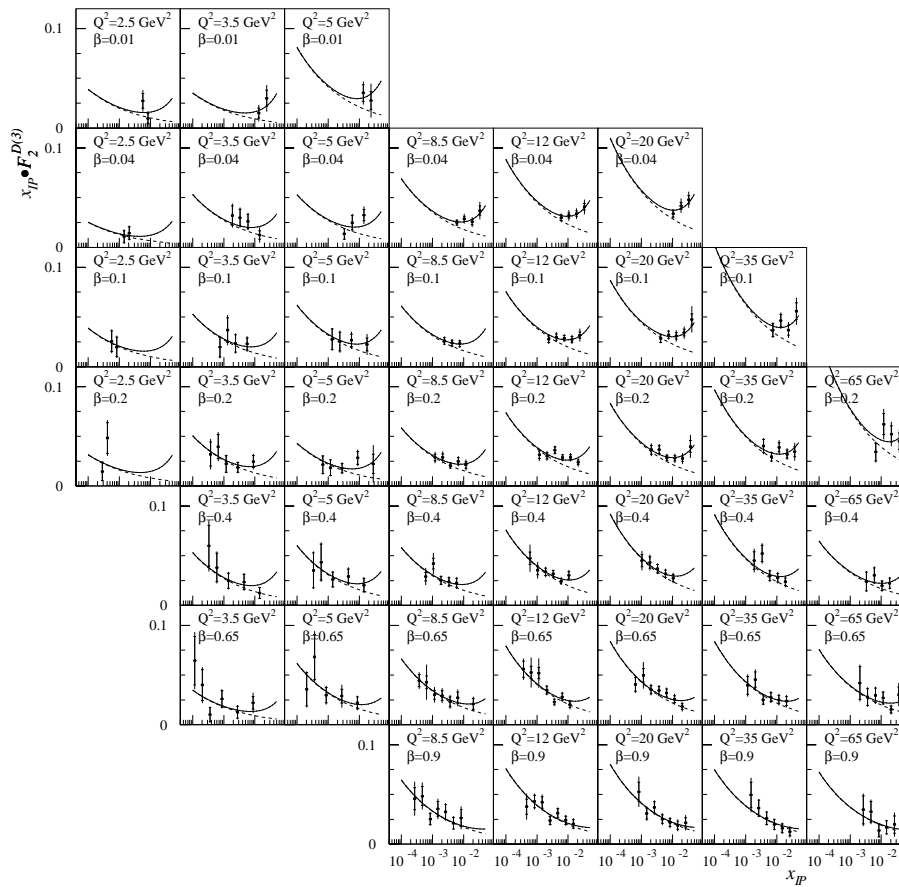


Figure 2.6: $x_P \cdot F_2^{D(3)}(\beta, Q^2, x_P)$ from analysis of 1994 data including fit with pomeron and meson contributions (taken from [51]). The dashed line shows the contribution from the pomeron trajectory; the solid line shows the total from the sum of both contributions.

high x_P where the phenomenological fits described above suggest that meson exchange becomes important, there are significant deviations.

The partonic structure of diffractive exchange has been investigated by defining

$$\tilde{F}_2^D(\beta, Q^2) = \int_{x_{P_{low}}}^{x_{P_{high}}} F_2^{D(3)}(\beta, Q^2, x_P) dx_P \quad (2.36)$$

which, under the assumptions of factorisation and a single trajectory (the pomeron) being exchanged, is proportional to $F_2^P(\beta, Q^2)$ irrespective of the normalisation of the pomeron flux factor, $f_{P/p}$. Despite the observation of factorisation breaking, integrating $F_2^{D(3)}$ over x_P still provides a measurement of the average structure of the diffractive deep-inelastic exchange. In the analysis discussed here, the integration was performed over the range $0.0003 \leq x_P \leq 0.05$.

Figure 2.7 shows $\tilde{F}_2^D(\beta, Q^2)$ as a function of Q^2 for fixed β and as a function of β at fixed Q^2 . There is little variation of \tilde{F}_2^D with β , and therefore no evidence for a structure

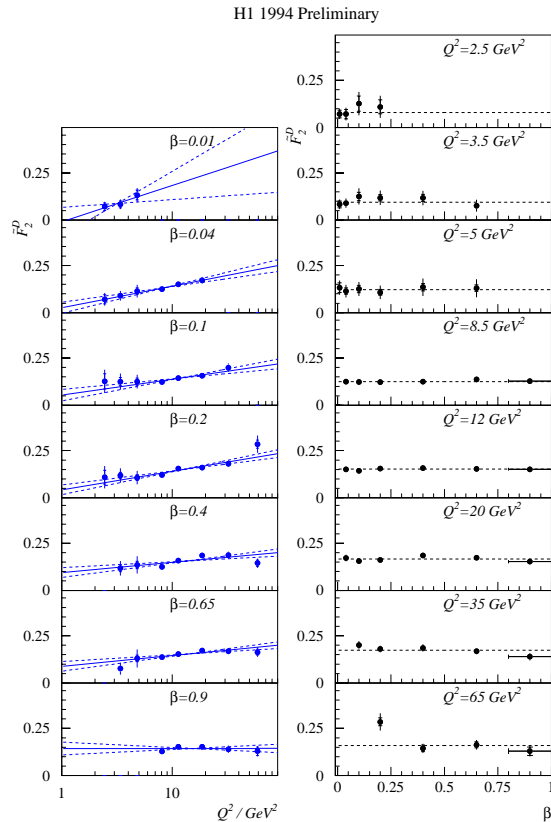


Figure 2.7: $\tilde{F}_2^D(\beta, Q^2)$ as a function of Q^2 for fixed β (left) and as a function of β for fixed Q^2 (right), taken from [51]. The lines shown are from a linear fit to the Q^2 dependence (continuous) and $\pm 1\sigma$ (dashed) and a constant fit to the β dependence (dashed).

function which falls with increasing momentum fraction as is typical of hadrons. There is no large variation with Q^2 , but scaling violations are clearly observed. The rise of \tilde{F}_2^D with $\log Q^2$ persists up to large values of β , which is in marked contrast to the structure function of the proton, where the slope becomes negative at $x \simeq 0.15$. These results are taken as evidence of a substantial gluon component in the structure of the diffractive exchange. The quantity \tilde{F}_2^P was determined from an integration over x_P of the pomeron structure function determined in the two component fit described above. This was found to be in good agreement with \tilde{F}_2^D , reproducing the observed scaling violations. The hypothesis of a pomeron structure dominated by gluons is therefore unaffected by the presence of subleading trajectories.

A QCD analysis of $\tilde{F}_2^D(\beta, Q^2)$ has been performed. The quark singlet (with u, d and s contributions) and gluon distributions were parameterised at a starting scale of $Q_0^2 = 2.5 \text{ GeV}^2$ as

$$x_{i/P} f_i(x_{i/P}) = A_i x_{i/P}^{B_i} (1 - x_{i/P})^{C_i} \quad (2.37)$$

where $i = q, g$ for the quark and gluon distributions and $x_{i/P}$ is the fractional momentum

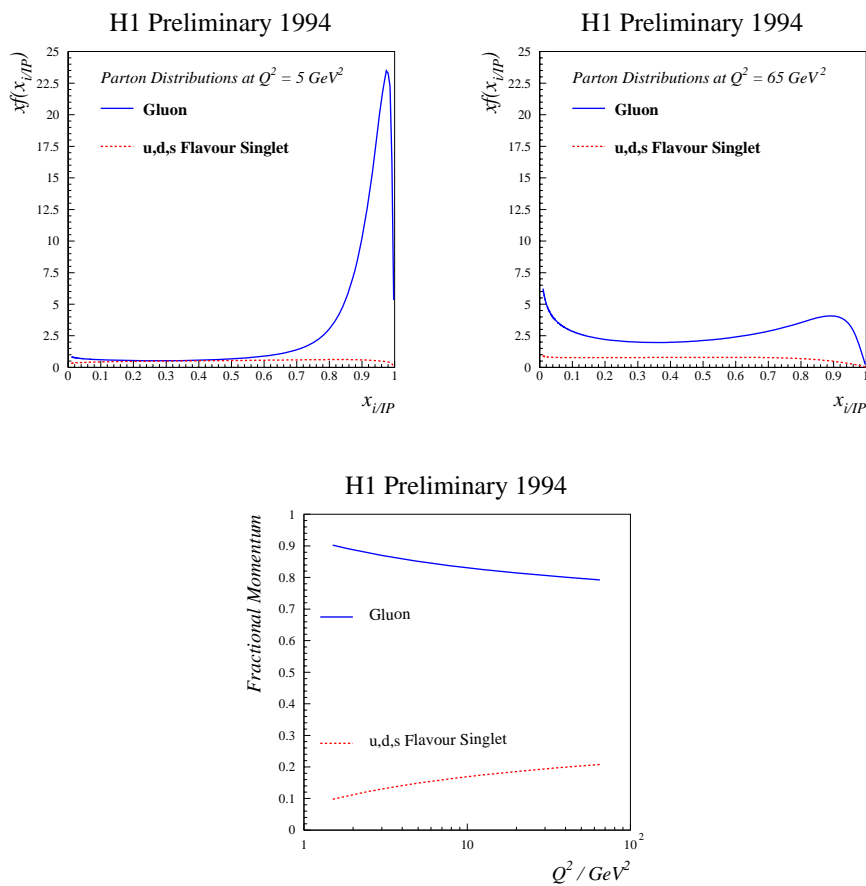


Figure 2.8: Parton momentum distributions from a QCD fit to the integrated structure function \tilde{F}_2^D (taken from [51]): distributions at a) $Q^2 = 5 \text{ GeV}^2$ and b) $Q^2 = 65 \text{ GeV}^2$ as a function of the fractional momentum $x_{i/PP}$. The fraction of the total momentum carried by the quarks and gluons is shown in c).

of the parton i . The distributions were then evolved from the starting scale using the DGLAP formalism (Section 1.2.1) to $Q^2 > Q_0^2$, with the values of A_i , B_i and C_i as fit parameters. In accordance with the argument of Donnachie and Landshoff described in Section 2.3.3, no momentum sum rule was imposed. Good agreement with the data was only obtained when the gluon density was allowed to be non-zero at the starting scale; a fit with A_g constrained to be zero did not describe the scaling violations observed in \tilde{F}_2^D . Figure 2.8 shows the parton distributions at $Q^2 = 5 \text{ GeV}^2$ and $Q^2 = 65 \text{ GeV}^2$. Also shown are the integrated momentum fractions carried by the quarks and gluons as a function of Q^2 . At $Q^2 = 5 \text{ GeV}^2$ the exchange is observed to be dominated by gluons carrying fractional momentum $x_{g/PP} > 0.9$. As Q^2 increases, the DGLAP evolution softens the gluon distribution to lower values of β . It can be seen that the gluons carry in excess of 80% of the exchange momentum over the whole Q^2 range. These results are therefore consistent with the qualitative conclusion, made directly from Figure 2.7 and described above, that the diffractive exchange is dominated by gluons. A similar prescription applied

to \tilde{F}_2^P yielded consistent results.

2.5 Summary

In this chapter the basic concepts of Regge theory, and their applicability to diffractive deep-inelastic scattering, have been presented. It is clear that the use of Regge theory to describe the features of elastic and total cross sections in the low Q^2 regime can successfully be extended to describe features of the high Q^2 HERA data.

The formalism frequently used to describe diffractive DIS, namely the diffractive structure function $F_2^{D(3)}$, has been discussed. The use of $F_2^{D(3)}$ to extract information about the structure of the pomeron in a perturbative, partonic way has been described, and measurements made by the H1 collaboration presented. The hypothesis of factorisation of the diffractive exchange into a non-perturbative flux and a perturbative structure function has been shown to be violated, which may be interpreted as evidence that contributions from both pomeron and meson trajectories are present. Extraction of the structure function of the diffractive exchange, \tilde{F}_2^D , yields evidence of a gluon dominated pomeron.

The trajectory intercept determined in diffractive DIS is smaller than with that predicted by the BFKL formalism for the hard pomeron, and substantially larger than that of the soft pomeron which describes hadron-hadron collision data so well. Clearly, there must be some transition between the two regimes. Analysis of further data from HERA, particularly in the low Q^2 region, may therefore help to answer a number of questions regarding the relationship between the non-perturbative regime and the perturbatively calculable QCD picture of the strong interaction.

Chapter 3

The H1 Detector at HERA

H1 is one of two general purpose detectors situated at the HERA accelerator, designed to study many aspects of ep interactions. The H1 detector consists of a number of complementary subdetector systems, each optimised to provide specific types of information about collision events. The high collision rate and large backgrounds at HERA present significant challenges to the experiment, which are met through the use of sophisticated triggering and data acquisition systems.

In this chapter the motivation and design of the detector are described. The principal subdetectors are described in some detail, with an indication of their performance. An overview of the triggering, acquisition and reconstruction of data is given.

3.1 The HERA Accelerator

HERA (Hadron Electron Ring Accelerator) [52] is the first facility to provide colliding beams of electron and protons. Situated at the DESY laboratory in Hamburg, Germany, it resides in a tunnel of 6.3 km circumference and consists of two accelerators which produce counter-rotating beams of 30 GeV electrons and 820 GeV protons. HERA provides a centre of mass energy of 314 GeV, equivalent to a 50 TeV electron beam incident on a fixed nuclear target. This provides an extension of two orders of magnitude in the accessible kinematic range in Q^2 and x compared to fixed target experiments. A schematic layout of the accelerator complex at DESY is shown in Figure 3.1. The pre-existing chain of accelerators is used to inject beams into HERA at low energies.

The high energy of the proton beam requires a bending field of 4.6 T, which is well in excess of the magnetic saturation of iron. Superconducting magnets are therefore em-

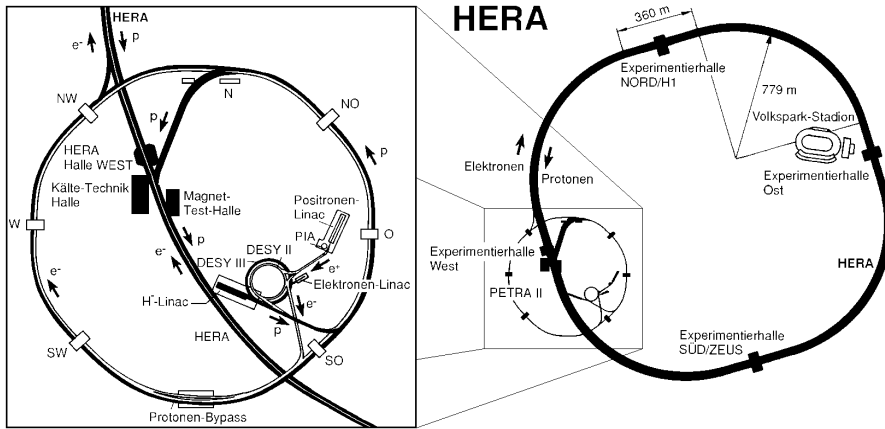


Figure 3.1: *Schematic layout of the HERA accelerator, showing the pre-existing accelerator complex used to inject beams into HERA.*

employed for the proton machine, immersed in liquid helium at a temperature of 4 K. The magnets are designed with an integral cryostat housing which carries the cryogenic and electrical infrastructure required. The proton beam is accelerated from 40 GeV at injection to peak energy by a series of ambient-temperature radio frequency cavities operating at 52 and 208 MHz. The electron beam is steered by conventional magnets, and accelerated from injection at 11 GeV to peak energy by a mixture of ambient-temperature and superconducting RF cavities operating at 500 MHz.

At full design specification, HERA provides 60 mA of electrons and 160 mA of protons in 210 bunches per beam, with a bunch crossing rate of 10.4 MHz. The beam structure is such that not all the bunches are brought into collision. The non-colliding, or pilot bunches are useful for studying beam-induced backgrounds. The electron and proton beams are brought into collision at two interaction points on opposite sides of the HERA ring, where the electron beam is bent upwards into the plane of the proton beam, resulting in a zero crossing-angle of the beams. The interaction points are surrounded by the two general purpose experiments at HERA; H1 (at the North Hall) and ZEUS (at the South).

The design luminosity of HERA is $1.5 \times 10^{31} \text{ cm}^{-2} \text{ s}^{-1}$. Operational since 1992, the currents and integrated luminosity delivered by HERA to the experiments have risen each year resulting in a total, at the end of the 1996 run, of about 30 pb^{-1} . The peak currents so far observed are $I_{p_{max}} = 77.9 \text{ mA}$ and $I_{e_{max}} = 43.3 \text{ mA}$; the maximum luminosity attained was $8.37 \times 10^{30} \text{ cm}^{-2} \text{ s}^{-1}$. It can be seen that the performance is considerably below the design values, but improvements are made each year as understanding of the behaviour of this complex machine increases.

Since the middle of 1994 HERA has accelerated positrons instead of electrons¹. This was due to an effect of the distributed getter pump which maintains a high vacuum in the electron ring. The getter pump generates positive ions which caused the emittance of the electron beam to grow, reducing the lifetime. A positron beam repels the ions, and therefore has a higher lifetime.

HERA is equipped to exploit polarised electron beams. Transverse polarisation builds up naturally in electron storage rings, due to the interaction of the electron beam with synchrotron radiation in the bending magnets (the Sokolov-Ternov effect [53]); a polarisation of about 80% builds up over a period of approximately 30 minutes. Specially designed magnet insertions are used to rotate the spin axis from transverse to longitudinal with respect to the beam direction [54]. These spin rotators are installed around the East Hall, where the HERMES experiment is situated. The longitudinally polarised beam is collided with a polarised gas target to enable measurement of the spin structure of the nucleon. The proton beam is unused by HERMES, but passes through the detector. HERMES has been operational since 1995.

A fourth experiment, HERA-B is located at the West Hall. This collides protons from the extremities of the beam with wire targets, producing b quarks via a gluon-gluon fusion process, with aim of the experiment of studying CP violation in the B system. HERA-B was installed during 1996.

3.2 Overview of the H1 Detector

The H1 detector [55] is designed to study many aspects of ep scattering and therefore consists of a number of subsystems providing complementary information, from which the properties of the collision processes can be reconstructed. In order to exploit fully the physics potential at HERA, the detector has to fulfil a number of major roles, which are:

- **Electron detection:** identification and energy measurement of scattered electrons is vital for the study of neutral current DIS events, particularly in the backward (electron) direction, where the final state electrons at moderate Q^2 are detected.
- **Hadron detection:** calorimetry with good resolution and fine granularity is needed for characterising the hadronic final state in many processes. The calorimeter must be hermetic in order to measure the transverse energy balance; charged current DIS events, where the final state neutrino is undetected, exhibit an imbalance.

¹Throughout this thesis, the beam lepton is referred to as an electron, independent of the charge.

HERA Experiment H1

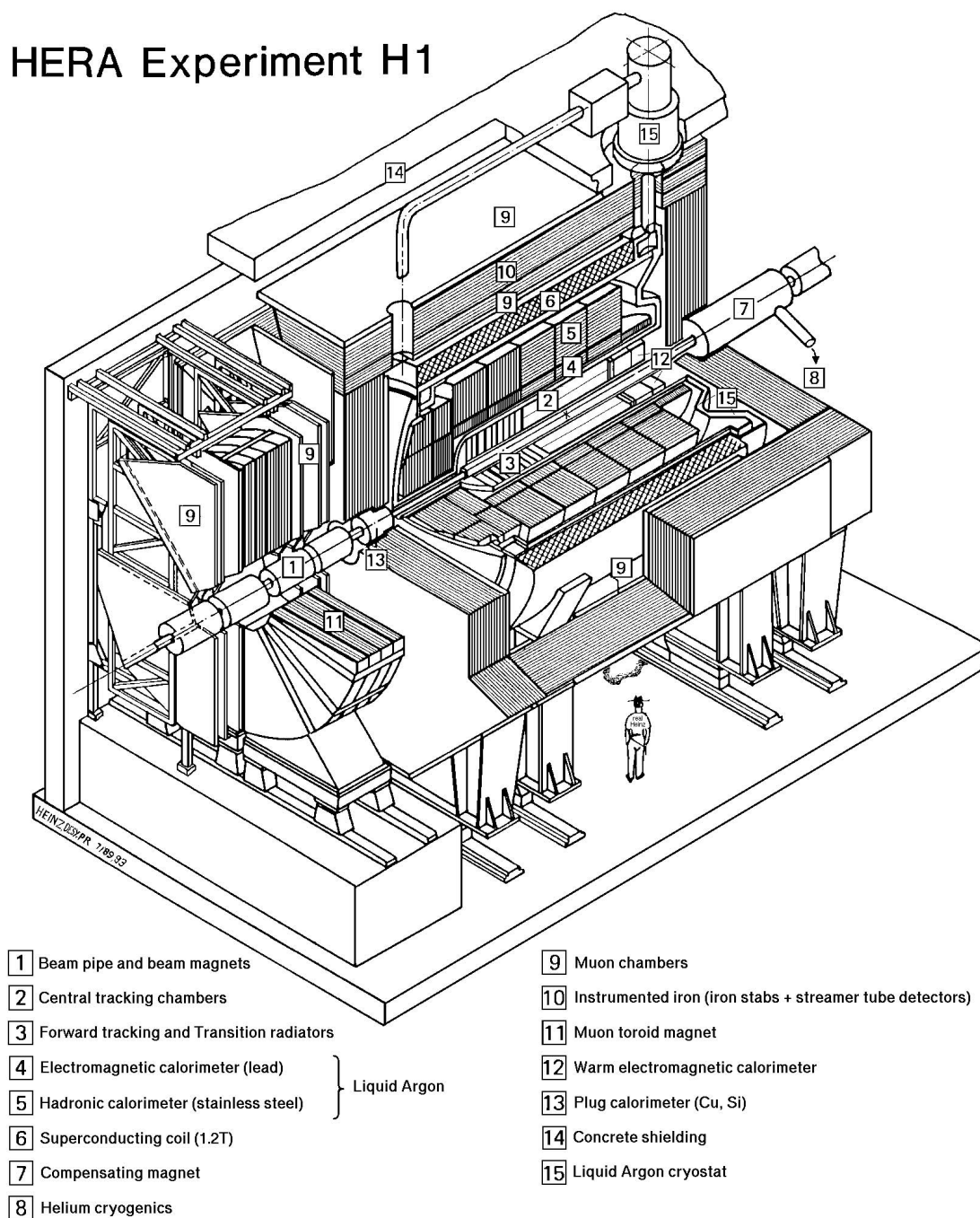


Figure 3.2: A cut-away view of the H1 detector, showing the major components. The proton beam enters from the top right, the electron beam from the bottom left.

- **Charged particle tracking:** charged particle momentum measurement and identification is required for the investigation of many processes at HERA. This is provided by tracking detectors covering a large solid angle. A magnetic field curves the tracks and allows the momentum to be determined, while energy loss measurements enable particle identification.
- **Muon identification:** heavy flavour, rare Standard Model and exotic physics processes are detected through the production of muons in the final state.
- **Luminosity measurement:** accurate determination of the luminosity delivered to the experiment is vital for calculation of cross sections.
- **Triggering and readout:** the high bunch crossing rate at HERA (10.4 MHz) and the very high backgrounds from beam-gas and beam-wall interactions means that the detector must be able to identify physics processes from the background, digitise and read out a large number of detector channels ($> 250,000$) while minimising dead time. A fast, pipelined, multi-level trigger system, in combination with high-speed digitisation and readout, is therefore employed.

Figure 3.2 shows a cut-away view of the H1 detector. In this view, the electron beam enters at bottom-left, the proton beam at top-right. The coordinate system of H1 is right-handed and defined with the z axis parallel to the proton direction, the y axis vertical, and the x axis mutually perpendicular to the others. The origin is defined as the nominal interaction point. In spherical polar coordinates, θ is the polar angle, defined with respect to the proton direction, and ϕ is the azimuthal angle, defined with respect to the x axis. The beam energy asymmetry at HERA means that many particles are produced in the forward ($+z$) direction; more extensive tracking, calorimetry and muon detection system are therefore provided in this region.

Starting from the interaction point, the principle subdetectors are as follows. Silicon trackers surround the beam pipe [1] in the central and backward regions (not shown due to the scale). The central [2] and forward [3] trackers enclose the central silicon tracker and the beam pipe in the forward region. In the backward region, the SPACAL electromagnetic and hadronic calorimeter [12] surrounds the beam pipe. The Liquid Argon (LAr) electromagnetic [4] and hadronic [5] calorimeters are situated outside the trackers, mounted in a large cryostat [15]. A superconducting solenoidal coil [6] of radius 3 m surrounds the cryostat, generating a uniform magnetic field of 1.2 T. A superconducting compensator magnet [7] in the backward region corrects the orbital distortion of the beams created by the main magnet. The large iron return yoke [10], which completes the magnetic circuit of the solenoid, is instrumented with muon detectors [9] and also

serves as a tail catcher to detect hadronic showers not contained by the liquid argon calorimeter. Additional muon detectors in the forward region [9], in combination with a toroidal magnet [11], provide identification and momentum measurement of muons. The plug calorimeter [13] surrounds the beam pipe in the forward region. The whole detector is shielded by concrete [14] to minimise radiation levels in the experimental hall. Additional detectors, including the luminosity system, are situated in the accelerator tunnel forward and backward of the main detector.

In the following sections, the principal subsystems that comprise H1 are presented.

3.3 Tracking

The tracking system of H1 is shown in Figure 3.3 and is split into two major components; the central tracker, covering the region in polar angle $15 < \theta < 165^\circ$, and the forward tracker, covering the region $7 < \theta < 25^\circ$. Each of these is further divided into a number of detectors which provide complementary measurements of charged tracks, and are discussed below. In addition, the backward region is covered by the backward drift chamber (BDC) which is mounted on the front of the SPACAL calorimeter and covers the region $151 < \theta < 177.5^\circ$. The central and backward silicon trackers (CST and BST) provide precision measurements of tracks close to the interaction vertex. The silicon trackers were partially installed during 1995 and not routinely included in the readout of the detector; for this reason they will not be discussed further.

The forward and central trackers contain both drift chambers and multi-wire proportional chambers (MWPCs). The drift chambers are used for precision measurements of track segments; hits can be located to $\sim 150 \mu\text{m}$ in the drift direction. The coordinate perpendicular to the wire can be determined by charge division of the pulses recorded at each end of the wire, to a precision of $\sim 1\%$ of the wire length. The MWPCs have an intrinsic spatial resolution which is limited by the wire spacing and is worse than that of the drift chambers. However, they have rapid response times to the passage of charged particles, and are therefore useful for triggering purposes.

3.3.1 The Central Tracker

The central tracker consists of a number of interleaved drift chambers and MWPCs; a section through the tracker is shown in Figure 3.4. Reconstruction of tracks in the central region is based mainly on two concentric drift chambers, CJC1 and CJC2. These have

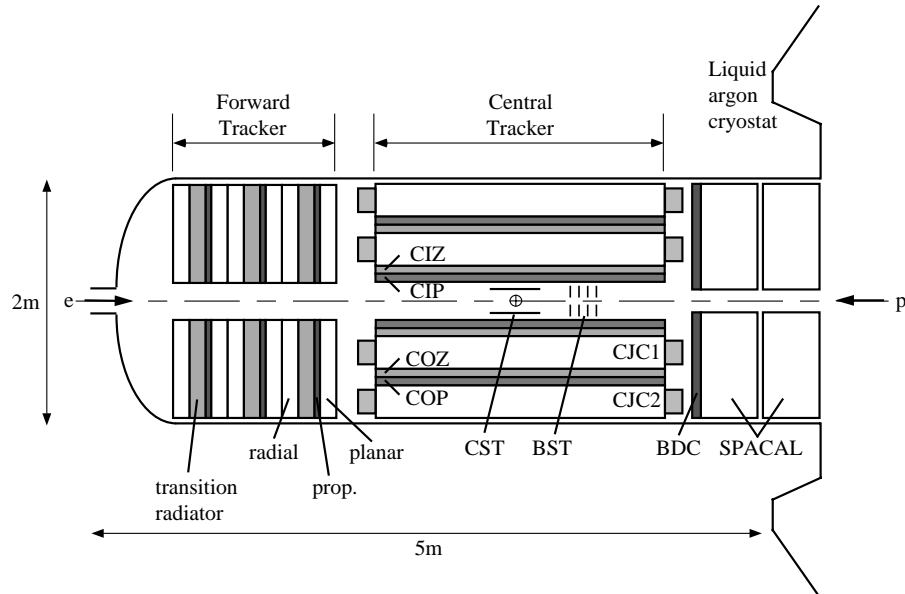


Figure 3.3: Side view of the H1 tracking system.

drift cells defined by 2.2 m long wires strung along the beam direction and inclined by about 30° with respect to the radial direction, so that the drift direction is approximately perpendicular to high momentum tracks. The cell orientation and the segmentation into two chambers mean that tracks are sampled a number of times. Furthermore, inclined cells allows easy resolution of the problem of ghost tracks, where the signal observed in a given cell could come from either side of the wire. The geometry is such that track segments defined by hits from the incorrect side of the wire do not match segments in the other chamber and can therefore be rejected. The inner chamber, CJC1, has 30 cells with 24 sense wires each, and the outer chamber, CJC2, has 60 cells with 32 wires each. A space point resolution of $170 \mu\text{m}$ in the $r - \phi$ plane and 2.2 cm in z has been measured. The particle momentum is reconstructed from the curvature of the track caused by the magnetic field. Particle identification is assisted by measurement of the specific energy loss, dE/dx , along a track, with a typical resolution of 10%.

Two thin drift chambers with sense wires strung perpendicular to the beam axis enable a better measurement of the track position in the z coordinate than is possible from charge division of the CJC signals. The inner z chamber (CIZ) is located inside CJC1, and the outer chamber (COZ) lies between CJC1 and CJC2. They provide track elements with typically $300 \mu\text{m}$ resolution in z and about 2% in ϕ .

The combined track measurements of these four chambers give a design resolution on the momentum of charged tracks of $\sigma(p)/p^2 \approx 3 \times 10^{-3} \text{ GeV}^{-1}$ and on the polar angle of

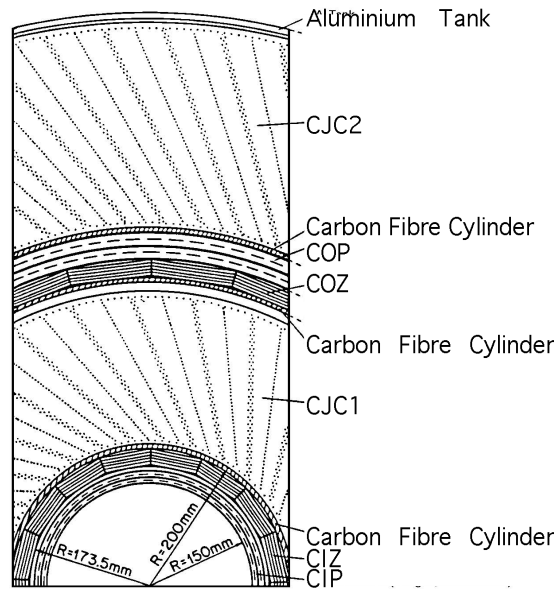


Figure 3.4: An $r - \phi$ section of the central tracker.

$\sigma(\theta) \approx 1$ mrad.

Two MWPC chambers are also included in the central tracker. The inner chamber (CIP) lies inside CIZ and the outer chamber (COP) is located between COZ and CJC2. The CIP and COP both consist of double cell layers, with wires parallel to the z -axis. The signals are read out from the charge induced on cathode pads; the CIP has 60 pads in z and 8 in ϕ and the COP has 18 in z and 16 in ϕ . The fast signals from these chambers are used to define vertex-pointing tracks for the purposes of triggering, with sufficiently good time resolution (for CIP, $\sigma(t) \approx 21$ ns) to enable identification of the bunch crossing in which the track occurred; this is known as a t_0 measurement.

3.3.2 The Forward Tracker

The forward tracker consists of three identical parts, known as supermodules, which contain planar drift chambers, MWPCs, a transition radiator and radial drift chambers.

Each planar module contains three drift chambers oriented at 0° , $+60^\circ$ and -60° with respect to the vertical. Each chamber consists of four wire planes in the z direction with 32 wires per plane. This design enables a space point to be reconstructed in the $x - y$ plane of each module with a spatial resolution of $\sigma_{xy} \simeq 160 \mu\text{m}$.

The transition radiators (TR) consist of a passive array of 400 layers of polypropylene film.

Charged particles passing through the transition in refractive index between the films emit soft X-rays, with a probability proportional to their Lorentz factor γ ; transition radiation can therefore be used to aid particle identification by separating electrons and pions. The soft X-rays cause ionisation in the subsequent drift chambers of each supermodule.

Immediately beyond (in z) the TR modules are the radial drift chambers. These contain wires strung along the radial direction, such that the maximum drift length increases with the distance from the beam axis. The radial chambers thus provide an accurate measurement of the azimuthal angle of the tracks. A coarse measurement of the radial coordinate is available using charge division. Each radial chamber has 48 cells in ϕ with 12 sense wires each in the z direction. The front window of the radial chambers is constructed from Mylar, which is transparent to the soft X-rays from the transition radiator. The X-rays deposit ionisation within in short distance in the gas volume of the radial chambers, and transition radiation is therefore detected as an enhanced charge deposition on the first few wires of a track in the radial chamber.

The forward MWPCs are located between the radial and transition radiation chambers in each supermodule, and consist of a double layer of wires strung along the vertical (y) axis. The readout pads are ring shaped and cover an azimuthal angle of 22.5° in the inner region and 11.25° in the outer. The radial width increases geometrically as a function of radius from 18 to 37 mm. The MWPCs in the first supermodule are used in conjunction with the CIP and COP to provide a trigger on vertex-pointing tracks. All three modules are used to define a trigger on tracks in the forward region. The timing resolution of hits in the forward MWPCs has been determined to be 20 ns, again sufficient for a t_0 identification of the correct bunch crossing.

3.3.3 The Backward Drift Chamber

The Backward Drift Chamber (BDC) [56] is mounted on the front surface of the SPACAL calorimeter. It is designed to provide track segments for final state electrons that enter the backward region, thus providing a better measurement of the electron angle than is possible with SPACAL alone.

The BDC is shown schematically in Figure 3.5 and consists of four double layers of drift chambers in eight octants with sense wires strung parallel to the radial direction. The width of the inner 16 drift cells is 10 mm, increasing to 30 mm in the outer 16 cells. Each double layer is staggered in order to resolve the ambiguity of the track position in the drift coordinate. The double layers are rotated with respect to one another by 11.5° in

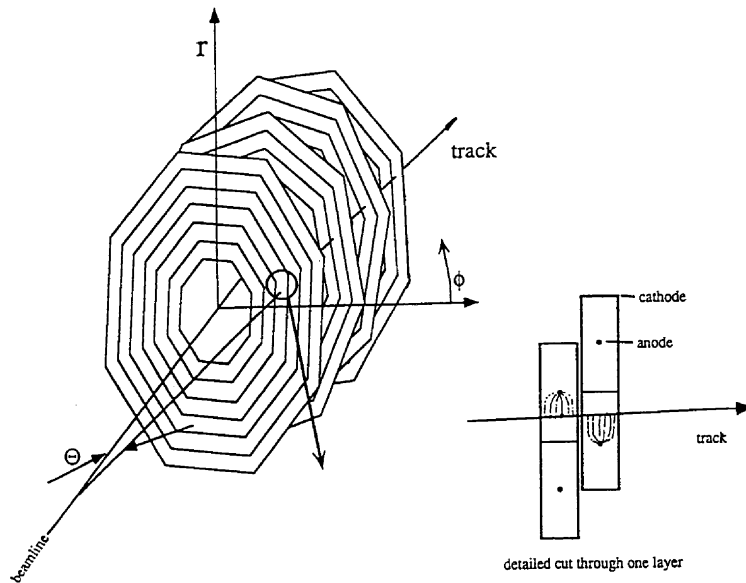


Figure 3.5: *Schematic depiction of the backward drift chamber (BDC), indicating the rotation of the double layers in ϕ . The staggering of the drift cells in one double layer is also shown.*

ϕ to enable track segments to be constructed from the intersection of hits in the layers. The BDC is designed to provide space points on tracks with a resolution in the radial coordinate of $\sigma(r) = 0.4$ mm and in the $r - \phi$ coordinate of $\sigma(r\phi) = 0.8$ mm.

3.4 Calorimetry

There are four subdetectors which provide energy measurement at H1; the Liquid Argon, SPACAL, tail catcher and plug calorimeters. The SPACAL calorimeter is described in detail in Chapters 4 and 5 and will not be mentioned here. Figure 3.6 shows the configuration of the H1 calorimeters in the $r - z$ plane.

3.4.1 The Liquid Argon Calorimeter

The Liquid Argon (LAr) calorimeter [57] provides the primary measurement of hadronic energy in H1. Above $Q^2 \simeq 100$ GeV², the scattered electron in DIS is also detected in this device. The liquid argon technique was chosen on the grounds of good stability, ease of calibration, fine granularity and homogeneity of response.

The LAr covers the polar angle region $4 < \theta < 154^\circ$ and is housed in a large cryostat

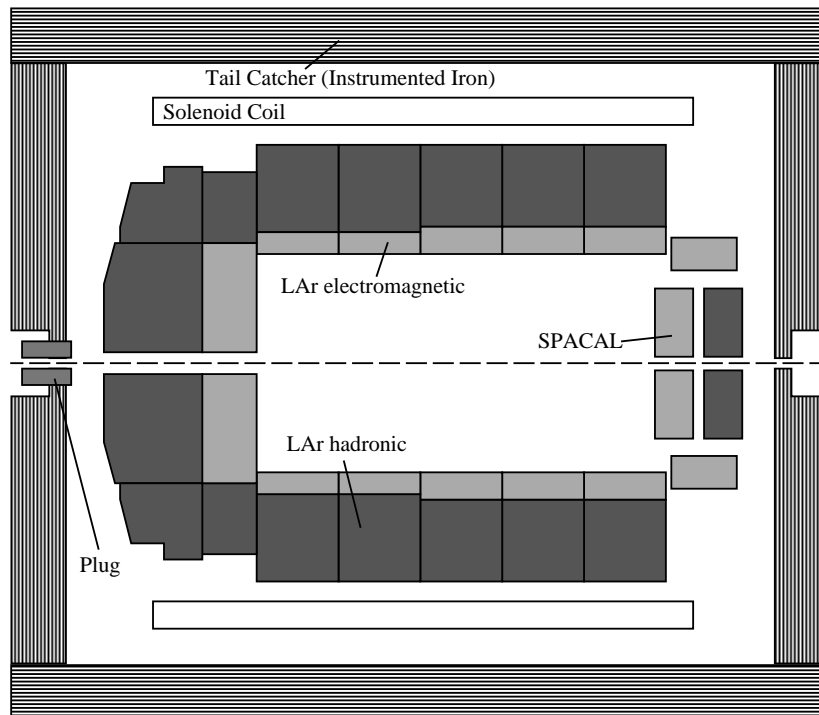


Figure 3.6: *Schematic $r - z$ view of the H1 calorimeters.*

inside the magnet solenoid. Placing the cryostat inside the magnet has the advantages of reducing both the size and weight of the calorimeter and the amount of dead material through which particles must pass. The LAr is divided into inner electromagnetic and outer hadronic sections², and is segmented into wheels which sit on rails inside the cryostat, allowing easy construction and handling. Each wheel is further segmented in ϕ into eight identical octants. The geometry of the octants and wheels is designed to avoid cracks pointing to the interaction vertex.

The electromagnetic section consists of 2.4mm thick lead absorber plates interleaved with similar size gaps flooded with liquid argon as the sampling medium. Energetic photons and electrons produce a shower of lower energy particles due to bremsstrahlung and pair production processes. This shower deposits ionisation in the active medium which is collected onto readout plates by application of a high voltage across the sampling layers. The total thickness of the electromagnetic section varies between 20 and 30 radiation lengths.

The hadronic section is constructed from 16 mm thick stainless steel plates with double gaps of 2.4 mm interleaved with 3 mm steel readout plates; high voltage is applied across

²In the backward region, space limitations allow only an electromagnetic section of the LAr to be installed.

the gaps. Energy is deposited in a hadronic calorimeter by inelastic collisions of the incident particles with nuclei in the absorber material. Ionisation is collected in the same way as in the electromagnetic section. The total depth of the LAr section is between 4.5 and 8 interaction lengths.

The LAr calorimeter is highly segmented in both sections, with a total of approximately 45000 cells. The orientation of the absorber plates is such that the angle of incidence of particles is always greater than 45° . The plates are therefore stacked parallel to the beam axis in the central wheels, and perpendicular to the beam in the forward and backward regions.

The energy resolution of the electromagnetic section has been measured in beam tests to be $\sigma_{em}(E)/E \simeq (12\%/\sqrt{E}) \oplus 1\%$, where E is in GeV. The resolution of the hadronic section was determined to be $\sigma_{had}(E)/E \simeq (50\%/\sqrt{E}) \oplus 2\%$. The hadronic calorimeter is non-compensating, resulting in a response to hadrons that is about 30% smaller than for electrons of the same energy. An energy-dependent weighting factor is applied offline to correct for this effect. The very fine granularity of the LAr allows the longitudinal shower development to be used for efficient e/π separation, with an observed contamination of less than 10^{-3} . The overall energy scale in the electromagnetic section is known to 3%, and in the hadronic section to approximately 4%.

3.4.2 The Tail Catcher

The tail catcher (TC) uses the instrumented iron of the return yoke to provide a coarse measurement of the energy of hadronic showers leaking out of the LAr. The iron itself forms the absorber, and ionisation is detected by analogue readout of eleven of the sixteen layers of limited streamer tubes which populate the iron. The TC covers almost the entire 4π solid angle and is divided into central barrel and forward and backward endcap regions.

The energy resolution of the TC has been measured at beam tests with pion beams to be $\sigma(E)/E \simeq 100\%/\sqrt{E}$. The overall energy scale is determined from calibration with cosmic muons and is known to approximately 35%.

3.4.3 The Plug Calorimeter

The plug calorimeter (PLUG) covers the extreme forward direction $0.6 < \theta < 3^\circ$ and is designed to close the gap in acceptance for energy flow measurements between the beam pipe and the most forward part of the LAr calorimeter. Its primary task is to minimise

the loss in transverse momentum due to hadrons emitted close to the beam pipe. The PLUG consists of nine copper absorber plates interleaved with up to eight active layers of large-area silicon detectors. The PLUG inhabits a high radiation environment close to the beam pipe and so, in order to preserve the operating life of the available silicon detectors, not all the layers are instrumented each year. The resolution of the PLUG is strongly limited by leakage, owing to size constraints from the limited space available in the return yoke, coarse sampling and the large amount of dead material in front of the device; the design value is $150\%/\sqrt{E}$.

Activity in the PLUG is also used in the selection of diffractive events with large rapidity gaps. This is discussed in more detail in Section 6.7.2.

3.5 Muon Detection

Detection of muons, the only observable particles capable of fully penetrating the inner material of the detector, is provided at H1 by two systems. The Central Muon System exploits the instrumentation of the iron return yoke, and the Forward Muon Detector measures the momenta of muons at small angles in the forward direction.

3.5.1 The Central Muon System

The Central Muon System consists of limited streamer tubes interleaved with the iron plates of the return yoke, as described in the context of the Tail Catcher in Section 3.4.2. Signals from the LSTs are read out digitally from the chamber wires and from strip detectors (17 mm wide on 20 mm centres) on the surface of the layers. Signals from pad detectors mounted on some of the layers are read out in analogue for the TC, and integrated into the data acquisition of the calorimeter system. On the inner and outer surfaces of the iron, there are three chamber planes; two with strips perpendicular to the wire direction and a third with pads. The layers with strip readout can therefore be used to determine space points on muons passing through the iron. There are a total of sixteen layers of LSTs, arranged in the barrel region to define a geometry for the readout pads which points to the event vertex. Five of the layers are used to generate muon trigger information, by requiring hit coincidences in a number of layers to define track segments.

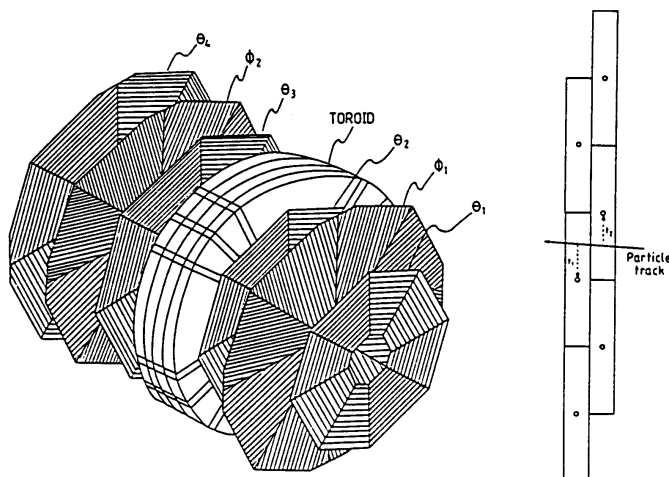


Figure 3.7: *Schematic view of the Forward Muon Detector (FMD), showing the six layers of drift chambers with the iron toroidal magnet and the cell structure of the double layers.*

3.5.2 The Forward Muon Detector

In the forward region, detection of muons is complicated by the high levels of activity. Furthermore, momentum measurement is degraded by the fact that, at small polar angles, particles do not have much transverse motion with respect to the field from the main solenoid. For these reasons, an additional system is provided; the Forward Muon Detector (FMD) [58].

The FMD consists of six double layers of drift chambers and an iron toroidal magnet which generates a field of 1.6 T and enables measurement of the momentum of muons. The configuration of the FMD is shown in Figure 3.7. The drift chambers are arranged in octants, with the configuration of the cells such that four of the layers are optimised for measurement of the polar angle, θ , of muon tracks (sense wires tangential to beam axis), and two for measurement of the azimuthal angle, ϕ (sense wires parallel to the radial direction). The approximate diameter of the chambers increases from 4 m for the first θ layer closest to the interaction vertex, to about 6 m for the farthest layer. The double layers are staggered, as in the BDC (Section 3.3.3), to enable resolution of left-right ambiguities in the drift direction. The sum of the drift times in two cells through which a muon passes is constant; this enables a t_0 to be determined for forward muons.

The FMD covers the polar angle region $5 < \theta < 17^\circ$ and is designed to measure the momentum of muons in the range $5 < p_\mu < 200$ GeV, the lower limit being set by the amount of material the muons have to penetrate and the influence on the momentum

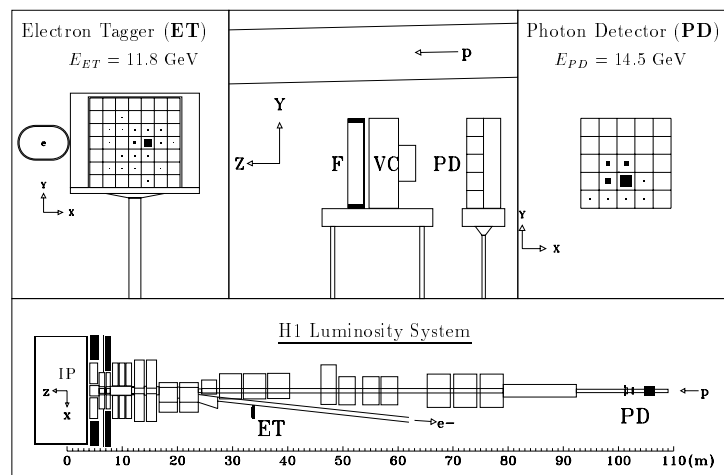


Figure 3.8: The layout of the luminosity system, showing a detected Bethe-Heitler event, $ep \rightarrow ep\gamma$. a) Plan view of the location of the electron tagger (ET) and photon detector (PD) with respect to the magnet elements close to the interaction point, b) front view of the ET, c) side and d) front views of the PD.

measurement of multiple Coulomb scattering in the iron toroid. The upper limit is set by the field strength of the toroid and the spatial resolution and alignment of the drift chambers. The resolution has been measured to be $\sigma(1/p)/(1/p) \simeq 18\%$ for 5 GeV tracks, rising to 50% at 100 GeV.

3.6 The Luminosity System

An accurate determination of the luminosity is vital for measurement of the cross section of physics processes. Installed in the accelerator tunnel in the direction of the outgoing electron beam, the luminosity system [59] provides this information. In addition, the system detects and triggers on scattered electrons at very low Q^2 ($< 10^{-2}$ GeV²) which are scattered through very small angles and therefore pass out of the main detector in the beam pipe. The luminosity is calculated in real time and used by the HERA operating team to steer the beams into collision at the start of each machine fill.

The luminosity system consists of a number of detectors mounted close to the beam pipes, as shown in Figure 3.8. The detectors are mounted on movable platforms which are retracted during beam injection and ramping to minimise radiation damage. There are two principle components of the system; the Electron Tagger (ET), positioned at $z = -33.4$ m adjacent to the electron beam pipe, and the Photon Detector (PD) at

$z = -102.9$ m next to the proton beam pipe. The ET detects electrons scattered at small angles which are deflected by the electron beam magnets, and consists of 49 crystal calorimeters with a depth of 22 radiation lengths read out by photomultipliers. The PD contains a number of components. A lead filter (F) protects the photon detector proper from the high synchrotron radiation flux. The filter is followed by a water Čerenkov Veto Counter (VC) which rejects events with photons originating from interactions in the filter. The PD consists of 25 crystals of the same design as the electron tagger.

The luminosity is measured using the Bethe-Heitler process, $ep \rightarrow ep\gamma$, the cross section of which can be calculated precisely in QED. Corrected for background and the acceptance of the system, the rate of Bethe-Heitler events can then be used to determine the luminosity. The online measurement is made using a coincidence method, which requires the simultaneous detection of the electron and photon. The total energy of the e and γ are constrained, in the limit $Q^2 \rightarrow 0$, to sum to the electron beam energy, $E_e = E_{e'} + E_\gamma$. Events are selected online with the requirement $23 < E_{e'} + E_\gamma < 30$ GeV and thresholds are applied at 5 GeV to both energies to remove noise and trigger threshold effects.

Offline, the method used is somewhat different, relying solely on the detection of the scattered photon. The rate of photons above a threshold of 8 GeV is determined and used to derive the luminosity. Corrections are applied for the acceptance of the detectors and energy leakage at the edges of the detectors. A contribution to the measured rate comes from proton satellite bunches, which appear at 5 ns intervals and arise from protons escaping from bunches into adjacent RF buckets during injection. Proton satellites can contain up to 10% of the total proton current. The principal source of background to the measured process is bremsstrahlung from residual gas in the beam pipe, $eA \rightarrow eA\gamma$. This is subtracted from the rate using data from the electron pilot bunches. The final uncertainty on the luminosity measurement after all corrections is approximately 3%.

3.7 The Very Forward Detectors

A number of detectors are situated in the accelerator tunnel in the proton beam (very forward) direction. These are used principally for the detection of the final state or its remnant. Two such systems are in place; the Proton Remnant Tagger (PRT) and the Forward Proton Spectrometer (FPS).

The PRT surrounds the beam pipe in the very forward direction at $z = 26$ m. It is a simple device, consisting of layers of scintillator sandwiched between layers of lead shielding and read out by photomultipliers. The PRT detects particles originating from fragmentation

of the final state proton remnant in the rapidity region $6 \lesssim \eta \lesssim 8$ and is therefore useful in the selection of diffractive events. Such use of the PRT is discussed in Section 6.7.2.

The FPS [60] makes use of the HERA magnets close to the interaction point as a spectrometer, enabling a measurement of the momentum of final state protons. Two stations at $z = 81$ m and $z = 90$ m are equipped with scintillating-fibre hodoscopes to provide space points on proton tracks. This information can be used to determine the curvature of the proton in the magnetic field of the beam magnets, and therefore the momentum. The hodoscopes are mounted on Roman Pots, which allow the sensitive parts of the system to be retracted during beam injection and ramping when the background is bad. The Roman Pots are subsequently driven to a position close (~ 4 mm) to the circulating beam. A resolution of approximately 4 GeV has been obtained for 650 GeV protons, with a overall scale uncertainty of 3%. The FPS was partially installed for testing during 1995, and therefore not used in the analysis described in Chapters 6 and 7. During the 1996/97 winter shutdown, two additional stations were installed closer to the interaction point, before some of the beam magnets. These will increase the momentum acceptance of the FPS and provide an improved position measurement of the track before the bending magnets.

3.8 Time-of-Flight Detectors

There are a number of relatively simple, but vital, systems included in H1 which reject backgrounds on the basis of time-of-flight (ToF). The path length, and therefore the flight time, of interaction particles arriving at various parts of the detector differs from that of particles arising from beam-induced background, providing a useful method of discriminating between the two. The SPACAL calorimeter, which is close the beam pipe in the direction of the incoming protons, is used in this role; a detailed discussion of this is presented in Chapter 4.

The other ToF systems make use of plastic scintillator which has a good intrinsic time resolution. Such devices mounted between the backward endcap of the return yoke and the beam pipe (BToF), within the unused gaps of the PLUG absorber (PToF) and around the beam pipe in the region of the FMD (FToF) are used to veto triggered events which have a time signature indicating that they arise from background. In addition, a double wall of scintillators is positioned backward of the return yoke at $z = -6.5$ m and $z = -8.1$ m. This is known as the Veto Wall and detects particles, mostly muons, from the proton beam halo, which are generated by inelastic collisions of protons with residual gas molecules and accelerator hardware.

3.9 Triggering and Data Acquisition

The HERA bunch crossing rate of 10.4 MHz is the highest of any collider yet operated, and as such presents a novel challenge to the experiments. In order to be able to select interesting physics processes from a large background, H1 is equipped with a trigger system which processes signals from the detector and makes a selection decision based on them. The philosophy of the trigger is to minimise the dead-time of the experiment, which is the time following a trigger in which the detector subsystems are being read out and are insensitive to new events. The H1 trigger [61, 62] is of a multi-level design, with each successive level processing more detailed data and taking longer to make a more refined trigger decision than the last. Most subsystems in H1 have trigger processors which generate trigger information based on their data. The trigger information is coordinated by the Central Trigger Logic (CTL) which makes a global decision based on combinations of all subsystem trigger information.

The bunch crossing interval of 96 ns is short when compared with the response times of many subdetectors, in particular the drift chambers where the maximum drift time is of the order of 1 μ s. The front-end system of each subdetector therefore pipelines data (for example, pulse digitisations or discriminated hits) in synchronisation with the HERA clock (HCLK)³ for at least 24 bunch crossings. The trigger subsystems are required to send information, in the form of trigger elements, to the first level of the central trigger (CTL1) within 22 bunch crossings. CTL1 resynchronises the trigger elements to the same bunch crossing and then creates logical combinations of them, known as subtriggers. If a subtrigger condition is satisfied then a counter is incremented. Predefined prescale values determine how many times a subtrigger must be set before it can contribute to the level 1 trigger decision. This approach allows the total CTL1 trigger rate to be controlled, and prevents high rate subtriggers from swamping those which fire less frequently. A logical-OR of all subtriggers passing the prescale condition is used to generate the Level 1 Keep (L1K) signal. This is broadcast to the front-end subsystems, at which point the data pipelines are frozen and readout is initiated. The pipelining approach makes the operation of CTL1 free from dead-time.

CTL1 triggers are derived from a number of subsystems in H1. The types of information from which trigger elements are created include:

- **Time-of-flight:** the ToF systems described in Section 3.8 and the SPACAL trigger processor (Section 4.3) generate triggers for in-time events. Other subtriggers can

³The HCLK is a 10.4 MHz frequency standard broadcast by the accelerator to the experiments, providing a timing reference which has a constant relationship with the bunch crossings.

also be vetoed using trigger elements which indicate flight times consistent with background activity.

- **Z-vertex:** information from the central and first forward MWPCs is used to determine the position of the event vertex from tracks in the z -direction.
- **Calorimeter energy:** signals in the LAr are summed in towers defined with a vertex-pointing geometry and compared with thresholds. Candidate electrons in SPACAL are triggered on in a similar way.
- **Muon tracks:** the central muon system (Section 3.5.1) information is used to trigger on muons in the iron return yoke. The FMD data is processed by a sophisticated trigger system [63] which extracts a t_0 and pointing track candidates from the drift chamber signals.

Two subsequent levels of the trigger (CTL2 and CTL3) operate synchronously during the primary dead time of the readout initiated by CTL1. These systems make decisions based on more detailed information generated by the trigger subsystems than is available to CTL1. CTL2 has a latency time of 20 μs , during which time two independent systems evaluate the complex correlations between detector signals. The systems are based on neural network technology [64] and a topological array [65], both of which are suited to making decisions based on correlations in a multi-dimensional space. If CTL2 decides to reject an event, a fast clear signal is sent to the front end systems which then reset and begin to acquire data once more. A decision to keep the event (L2K) extends the dead-time and time-consuming tasks such as zero-suppression begin. During this time, the CTL3 [66], based on a RISC processor, calculates a decision in software based on detailed trigger information. The CTL3 decision is available after typically a few hundred μs ; in the case of a rejected event, the readout is aborted and the front-end systems are alive again within a few μs .

From a background rate in excess of 10 kHz, the trigger is able to reduce the event rate to approximately 50 Hz with a dead time of about 10%. Events which pass the three trigger levels described above are read out in full; the total dead-time for a such an event is 1-2 ms, depending on the level of activity in the detector. The front-end systems of all subdetectors format and place the data in a buffer, tagged with a common reference number. A dedicated processor, the Central Event Builder (CEB), collects the formatted data from each system asynchronously and constructs the full event data. The subsystems communicate with the CEB via a fibre-optic ring [67] capable of a sustained data transfer rate of 55 Mbyte/s with a maximum error rate of 1 in 10^{13} . The buffering in the front-end subsystems and the CEB is sufficient for the asynchronous event building to not contribute

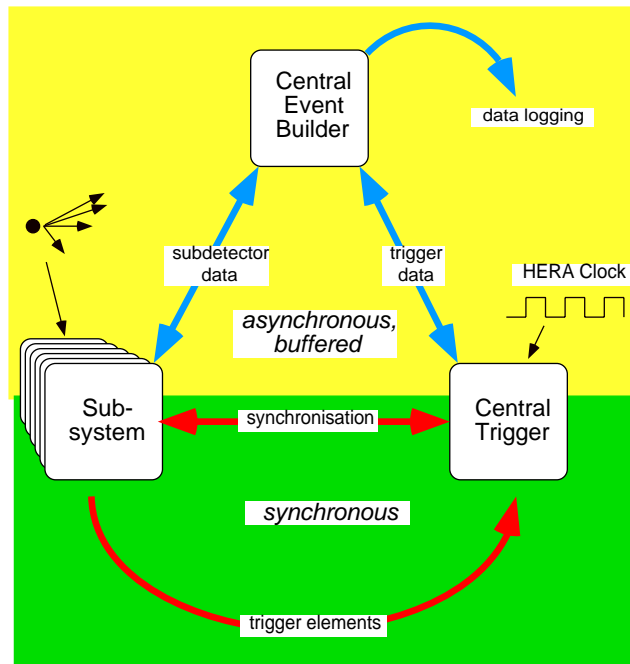


Figure 3.9: *The three components of the trigger and data acquisition system, showing the relationship between and information flow between them (taken from [62]).*

to the dead time of the readout. The relationship between the subsystems, the CTL and the CEB is shown in Figure 3.9.

Once events have been built by the CEB, they are passed to the fourth level (L4) of the trigger system. This is based on a farm of approximately 30 RISC processors running a limited reconstruction of the full-event data in parallel. Each processor reconstructs a complete event to which it applies a series of complex selection criteria which are dependent on the subtriggers which passed the event. L4 rejects the majority of the remaining beam-gas and cosmic events, and those resulting from trigger noise. Events which pass the L4 cuts are written to tape at a typical rate of 10 Hz. After the L4 reconstruction, the events are on average 130 kBytes in size. Separate streams of events are also created by L4 for the purposes of monitoring and calibration of certain subdetectors. A small fraction of the events rejected by L4 are streamed off and written to tape to allow monitoring of the effects of the L4 cuts.

Full reconstruction of the events is performed, typically within a day of data-taking, by a dedicated workstation. After linking of information between all the subdetectors, the events are classified into different physics classes; this can be considered as the fifth level (L5) of the H1 trigger system. The full events are written to Production Output

Tapes (POTs) and stored. The dynamic memory management system BOS [68] is used to format the events in convenient manner. At the end of each year of data taking, after the calibration of each system has been fully determined, events are reprocessed with the reconstruction software. The output of this stage are the data summary tapes (DSTs) which contain compressed data that reflects objects in the events, such as tracks and calorimeter clusters, rather than raw and reconstructed subdetector data. The DSTs are sufficiently compact to be stored on disk, enabling easy and rapid access for analysis.

Chapter 4

The SPACAL Calorimeter and TDC System

This chapter describes the motivation for and the design of the H1 SPACAL calorimeter, electronics and the TDC system. A glossary of frequently used abbreviations can be found on page 166.

4.1 The SPACAL Calorimeter

4.1.1 Physics Motivation

The low- x regime of deep-inelastic scattering is characterised by events with boosts in the backward direction. In addition, low values of x at a given centre of mass energy imply low Q^2 , requiring detection of scattered electrons close to the beam pipe. The need, therefore, to measure both the electron and the hadronic final state in the backward region and also to reject photoproduction, beam-gas and beam-wall backgrounds has led the H1 collaboration to upgrade its detector [56]. Central to this upgrade is a new backward calorimeter, complemented by the backward drift chamber (BDC), which is discussed in Section 3.3.3.

The required features of the new calorimeter are as follows:

- **Extension of kinematic range at low x and Q^2 :** This is achieved by extending the angular coverage for electrons to $\theta \leq 177^\circ$.
- **High resolution in θ_e and E_e :** At 30 GeV the design resolutions are $dE/E \leq 2\%$ and $d\theta_e \leq 1$ mrad (with a matched BDC track). In addition, an absolute energy

calibration of better than 1% is needed to keep the systematic uncertainties in F_2 and F_2^D measurements in the range of 5 – 10%.

- **Reliable electron identification:** The probability of misidentifying a pion as an electron should be less than 1 in 100 at 5 GeV. This is required to suppress photoproduction background which is several orders of magnitude larger than DIS.
- **Good coverage and containment for hadronic energy flow:** This is required to measure the hadronic final state and to determine y without using electron information. In the limited space available a compact and fine-grained calorimeter is therefore needed.
- **Good time resolution** A resolution of better than 1 ns for electrons, pions and minimum-ionising particles is needed to allow rejection of out-of-time backgrounds originating mainly from upstream proton beam-gas and beam-wall interactions. This capability is needed at the first trigger level (L1).

Given these requirements, two designs were considered: lead fluoride crystal and lead-scintillator spaghetti (SPACAL) calorimeters. Both types were prototyped and investigated [69, 70]; the SPACAL design was chosen based on the results and the anticipated high cost and limited hadronic response of crystal calorimetry. The SPACAL design offers a fast signal response and good energy resolution, shower containment and position resolution due to the high sampling frequency achievable with small fibre diameters. There are also the attractive possibilities of hermeticity arising from the high effective density and homogeneity since the optical readout is distributed over the volume of the detector.

4.1.2 SPACAL Construction

The active region of a spaghetti calorimeter consists of lead sheets with grooves into which scintillating fibres are laid. Incident particles shower in the lead, and the products of the shower cause the fibres to scintillate. This light is then collected at the one end of the fibres and measured by a light sensitive device, typically a photo-multiplier. The other ends of the fibres can be mirrored to increase the light output.

The H1 SPACAL implementation [71, 72] was constrained by the practical limitations of the detector; the depth is limited by the distance between the end of the central tracker and the iron return yoke, and the maximum weight that the inner rails of the cryostat can support is 8 tonnes in the backward region. A two part design was chosen, consisting of inner electromagnetic (EM) and outer hadronic (HAD) sections. The total depth of the

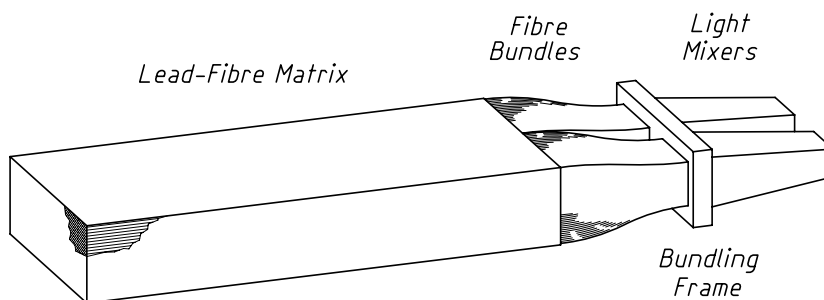


Figure 4.1: An H1 SPACAL EM module.

calorimeter is two interaction lengths which limits hadronic performance but is nonetheless an improvement over the previous BEMC. The acceptance of the HAD section is increased to 178.7° by a backward plug section (BPLUG) located in the return yoke¹. The general design parameters are shown in Table 4.1. The EM section is segmented into cells of side 40.5 mm (120 mm for the HAD section). The EM cells are built up in pairs from 52 lead sheets and 4680 Bicron BCF-12 fibres [73] to form submodules, as shown in Figure 4.1. Eight of these pairs are combined to form a supermodule, which is held together by two layers of $60 \mu\text{m}$ tape and a cushioned $50 \mu\text{m}$ steel cap to protect the front of the lead/fibre matrix. A schematic view of an EM supermodule is shown in Figure 4.2. The construction of the HAD section is similar but the cells are assembled individually. The BPLUG consists of twelve cells of trapezoidal cross-section which are arranged in a ring surrounding the beam pipe.

	Electromagnetic	Hadronic
Pb/Fibre Ratio	2.3:1	3.4:1
Fibre Type	Bicron BCF-12	Bicron BCF-12
Fibre Diameter	0.5 mm	1.0 mm
Cell Size	$40.5 \times 40.5 \text{ mm}^2$	$120 \times 120 \text{ mm}^2$
Number of Cells	1192	136
Angular Coverage	$\leq 177.5^\circ$	$\leq 178^\circ$
Active Length	25 cm	20 cm
Radiation Length	0.91 cm	–
Interaction Length	25 cm	20 cm
Molière Radius	2.55 cm	–

Table 4.1: H1 SPACAL Parameters.

The fibres exiting the lead matrix from each cell are bundled together, glued and mounted

¹The BPLUG was installed one year later than EM and HAD SPACAL, during the 1995/96 shutdown.

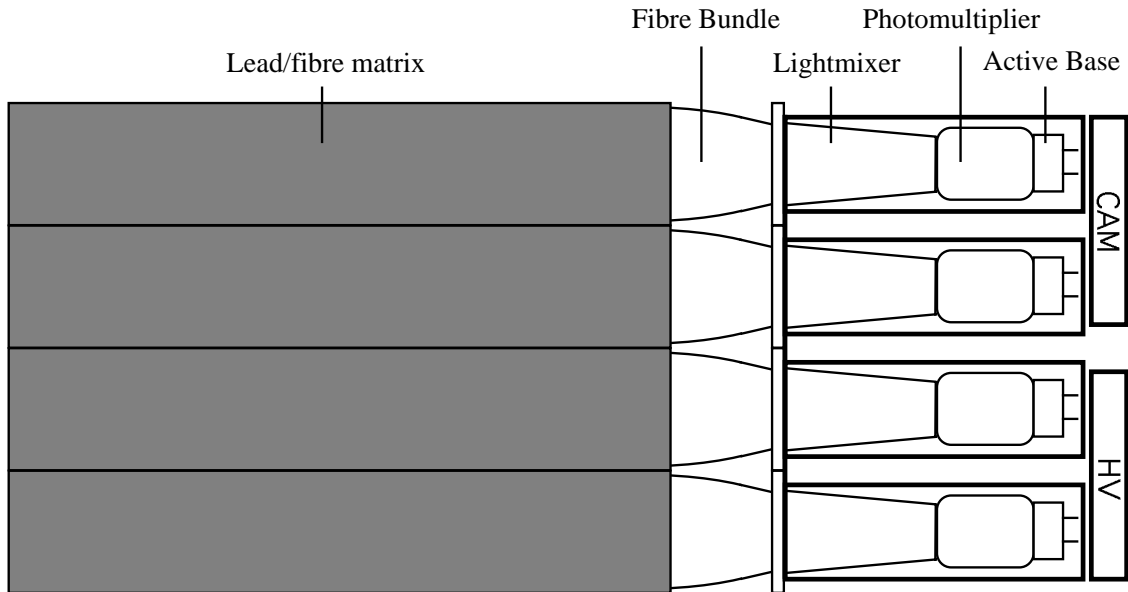


Figure 4.2: *Schematic side view of an H1 SPACAL EM supermodule.*

in a frame. The face of the bundle is machined to give a flat optical surface, to which a light mixer is coupled by a 0.3 mm air gap. The mixer spatially randomises and concentrates the light onto the photocathode of a 1 inch (2 inch for HAD) photomultiplier (PMT). This is glued to the light mixer to ensure the best transmission along the optical path. For each EM supermodule, the sixteen light mixers and PMTs are contained within a light-tight aluminium housing mounted on the rear of the detector. The larger cell geometry of the HAD section means that the light mixers and PMTs are individually mounted.

The PMTs have to operate in the 1.2 T magnetic field of H1 and so Hamamatsu mesh-dynode types were chosen [74]. These provide a typical gain of 10^4 , a factor of 100 smaller than with no field. They are mounted on active bases which provide high-voltage division and pulse integration by a preamplifier. Each supermodule is furnished with a high-voltage (HV) distribution module which, by means of a serial bus, is capable of adjusting the relative voltages applied to the PMTs on a submodule by ± 400 V. This scheme has the advantage of reducing the number of HV cables which have to be brought out of the detector to 75.

There is a calibration module (CAM) [75] attached to the rear of each supermodule. This contains control electronics and two pulsed LEDs which feed light through fibres (not shown in Figure 4.2) into the light mixers. Photodiodes measure the light output of each LED to monitor any instabilities in intensity. The CAM modules are connected via a serial bus to an external module which controls the firing patterns of the LEDs. They are

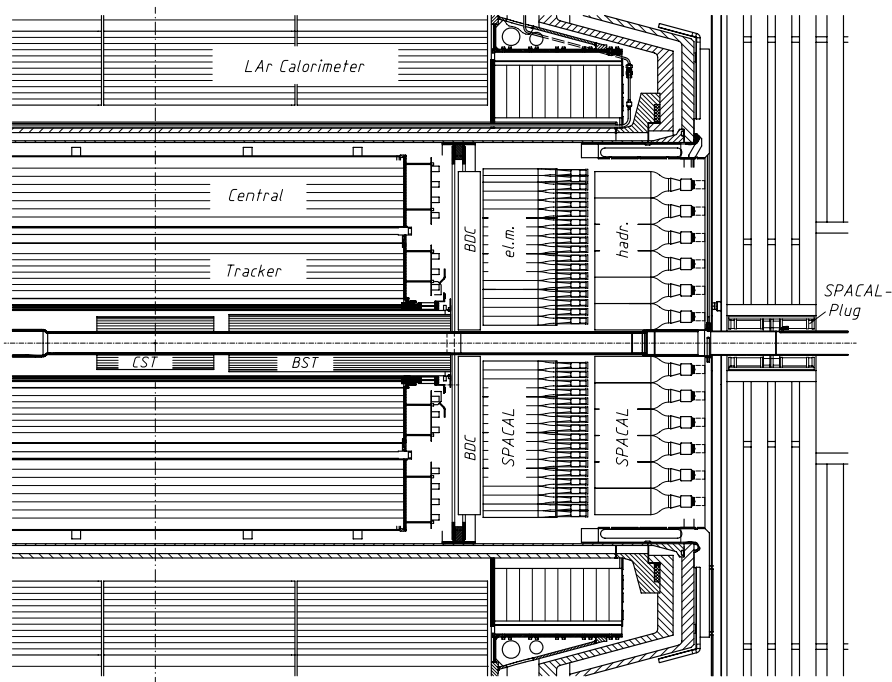


Figure 4.3: Side view of part of the H1 detector showing the location of the SPACAL sections.

typically pulsed at a rate of 1 Hz, synchronised to empty HERA bunches. These pulses are used to monitor the stability of the photomultiplier gains and therefore in the calibration of the calorimeter².

The supermodules for each section are mounted in a circular aluminium vessel of about 1.6 m diameter. The location of the SPACAL detectors within H1 is shown in Figure 4.3. An intrinsic effect common to all scintillating fibre calorimeters is channelling, where particles traversing the active region at some angles encounter significantly more (or less) fibre than lead, leading to anomalous energy depositions. This is avoided by rotating the lead matrix in some submodules in such a way that critical angles are avoided. Specially shaped modules have been constructed for the outer borders of SPACAL and the region surrounding the beam pipe is filled by an insert module with non-standard cell geometries. The insert also includes a 2 mm thick tantalum shield designed to protect the insert cells from synchrotron radiation and a 8 mm lead/fibre veto layer which allows identification of energy leakage from insert cells into the beam pipe. SPACAL lies in the only access path to the central trackers and so, in order to facilitate removal without withdrawing the beam-pipe, a special ‘chimney’ of supermodules above the beam pipe in each section can be removed from the rest of the calorimeter. The chimneys are supported by four

²The calibration of SPACAL is discussed in Chapter 6.

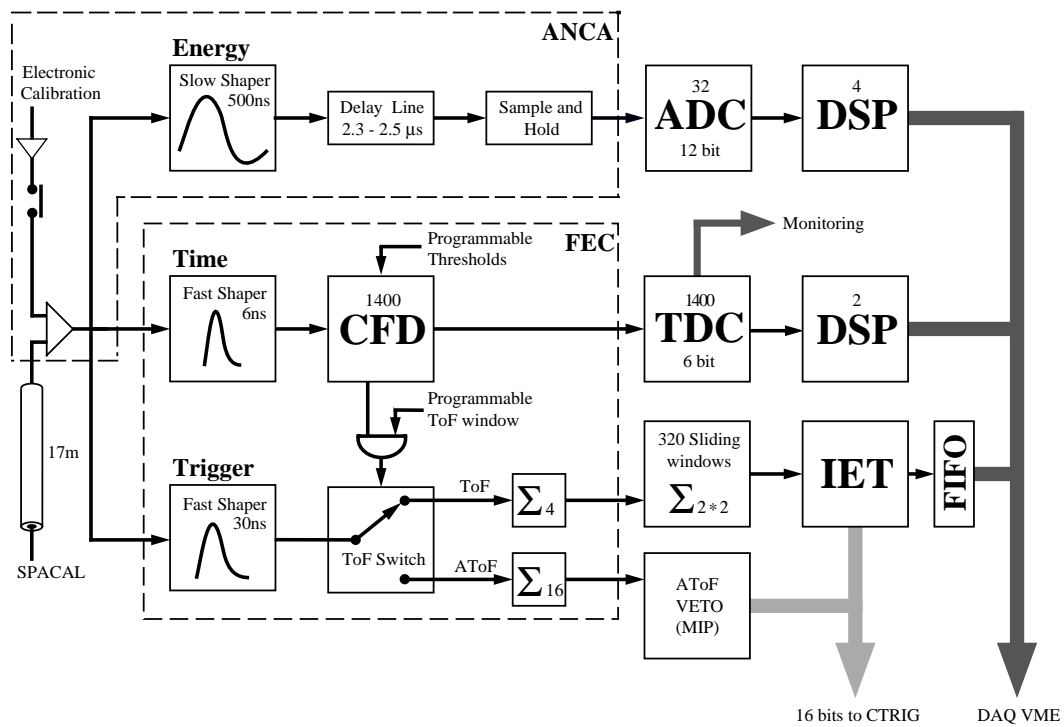


Figure 4.4: Block diagram of the SPACAL electronics chain.

$2 \times 25 \mu\text{m}$ steel bands anchored at the top of the section. This design also prevents a large weight from resting on the insert and hence the beam pipe.

4.2 The SPACAL Electronics Chain

Signals from the active bases are brought out of the detector on 17.5 m long, 50Ω cables to the analogue boxes (ANBXs), mounted next to the iron yoke of the detector. This location, plus a careful shielding and grounding scheme, is designed to minimise environmental noise pickup. The cable terminations are impedance matched to reduce unwanted signal reflections. An ANBX contains eight pairs of analogue cards (ANCAs) and front-end cards (FECs), each of which serves sixteen channels, effectively splitting the SPACAL signals into three branches; energy, timing and trigger. The advantage of this design is that the signal treatment for each measurement can be individually optimised. A block diagram of the electronics chain is shown in Figure 4.4. The readout and trigger systems are situated on the roof of the electronics trailer, some 20 m distant from the ANBXs. Between these two locations, all signals are in differential ECL format, carried by shielded, twisted-pair cables.

The ANCA provides 12V power for the active bases (along the signal cables) and processing for the sixteen signal inputs. Each channel consists of three sub-modules, mounted on daughter boards:

- A shaper module which provides unit-gain buffering, a signal output for the FEC and an RC-CR shaping filter with a time constant of 180 ns.
- A delay line, adjustable between 2.3 and 2.5 μ s in 20 ns steps. This allows the shaped signal to be aligned with the L1K signal for digitisation.
- A sample and hold module which stores the pulse height at the time of the L1K. This is in a increased-bandwidth version of the liquid argon electronics design, so that the same readout electronics can be used.

The mother board provides 16 – 1 signal multiplexing and double outputs with a gain ratio of 4. To allow checking and alignment of channels, two additional daughter boards supply electronic calibration signals of similar amplitude and shape to the PMT outputs. These are inhibited during normal data acquisition to prevent noise pickup.

The outputs of the ANCAs are digitised by H1 calorimeter analogue-to-digital converter (ADC) modules [76]. These consist of eight identical channels equipped with 12bit ADCs. With the multiplexing provided by the ANCAs, each ADC module is therefore capable of converting 1024 channels. The dual gain outputs are separately digitised, increasing the dynamic range by effectively encoding 14 bits. The digitised data are read out from the ADC memory by H1 custom Digital Signal Processors (DSPs) [77], which also provide zero-suppression and channel numbering. Additional service modules (MDS) [78] provide interfacing of central trigger and clock signals, and the fanout of synchronisation and sequencing signals to the ANCAs, ADCs and DSPs. All readout modules are mounted in VME crates and the SPACAL readout is integrated into the full calorimeter DAQ branch. The HCLK, trigger (L1K etc.) and other signals are received from the Central Trigger by the SPACAL subsystem trigger crate (STC) where they are distributed to the individual processors.

The FEC provides two branches handling signals for the TDC system time measurement (described in Section 4.4) and the SPACAL trigger (Section 4.3). In the timing branch, a fast shaper produces short unipolar pulse of about 6 ns length. This is fed to a Constant Fraction Discriminator (CFD). The CFD is designed to reduce the problem of trigger walk in constant threshold discriminators, where pulses of different sizes cross threshold at different relative times (see Figure 4.5). In a CFD the trigger occurs at a constant

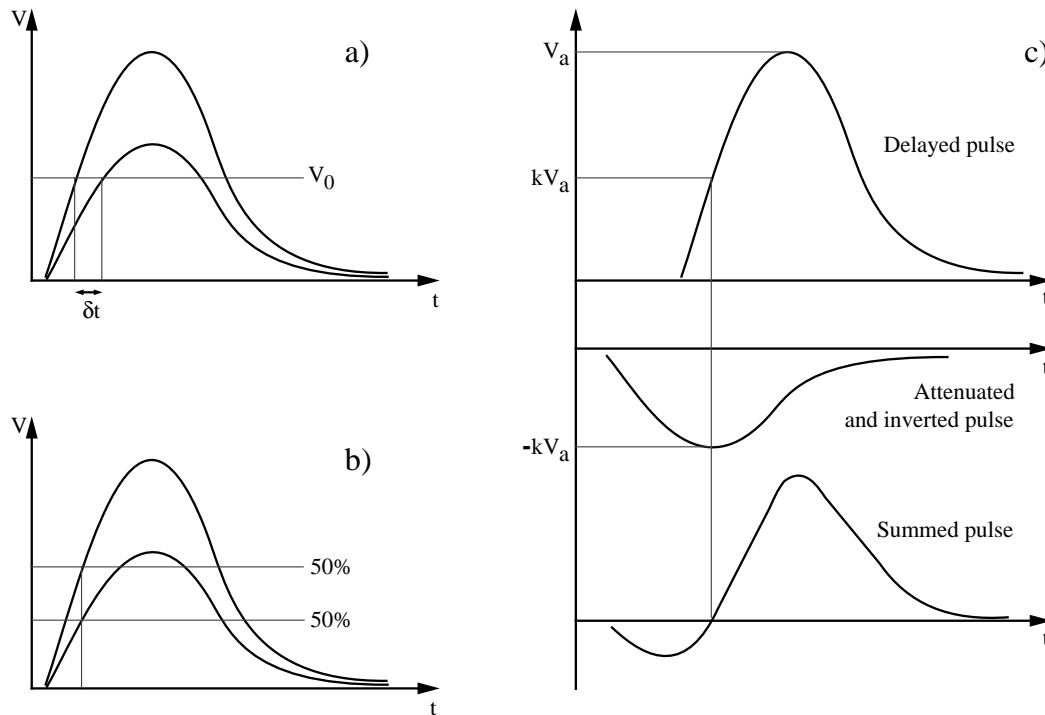


Figure 4.5: Comparison of signal discrimination techniques: a) Constant threshold, showing trigger walk due to different pulse heights, b) Constant fraction, showing independence from pulse height, c) Implementation of a CFD using pulse summation.

fraction of the pulse height, so, providing the pulse rise time is constant, the trigger time is the same for all pulse heights. This is achieved by splitting the pulse into two, with one part delayed by the time taken for the pulse to reach the desired fraction k of its peak level. The other part is attenuated by a factor k and inverted, and the two are added, giving a bipolar pulse. The point at which the resultant pulse crosses zero is then a constant fraction of the original. In practice, detecting the zero-crossing is hampered by residual noise, so the trigger can be validated by requiring the amplitude of the original pulse to be greater than a certain threshold. In the SPACAL CFDs, however, this amplitude validation is not possible. This is because the CFD output drives the ToF logic (discussed below) and is therefore required earlier than is possible with validation. The zero-crossing detection is therefore biased away from the noise by applying a threshold to the summed signal, from which the discriminated output is derived. This has the effect of introducing a trigger walk effect for very small pulse heights. The threshold of each CFD can be individually adjusted with a programmable 8 bit DAC, and is typically set to 4σ above the RMS noise level.

The CFD output signals are fed to the TDC system in differential ECL, and also used in the ToF switching logic. The HERA clock (HCLK) is used to generate a synchronised ToF

window for each channel, which defines times-of-flight consistent with energy deposition from interaction products³. Programmable delays define the start (for each channel) and the stop (common to all sixteen channels) of the ToF window with respect to the HCLK, adjustable in steps of 0.4 ns. When the leading edge of a CFD output pulse occurs within the ToF window, the ToF logic switches from out-of-time (anti-ToF or AToF) to in-time (ToF). The ToF state is held for 150 ns to avoid multiple triggers in a single HCLK cycle. In the absence of a ToF-validated CFD pulse, the logic remains in AToF mode.

In the trigger branch of the FEC, a unipolar pulse of 30 ns length is produced from the input by a shaper and integrator. This is fed into a switch controlled by the ToF logic which outputs the signals into either ToF or AToF lines. The operation of the switch can be controlled by two programmable bits, allowing a free mode controlled by the ToF logic, forced ToF and AToF modes, and a common ground-shortened mode. In the ToF lines, four analogue sums of 2×2 channels are created ($\Sigma_4 TOF$). In the AToF lines, all sixteen channels are summed ($\Sigma_{16} ATOF$). These five sums are fed in differential ECL to the trigger processor, which is described in the following section.

4.3 The SPACAL Trigger

The SPACAL trigger, in replacing the previous BEMC and ToF triggers, has to provide two functions within H1; a trigger for events containing electron candidates and a veto of events originating from beam-induced background which constitute 99% of potential L1 triggers. The design of the system therefore follows this dual requirement, and consists of the Inclusive Electron Trigger (IET) for the EM section, plus AToF veto and ToF/AToF total energies (E_{tot}) for both EM and HAD. These are described in the following sections. The number of bits sent to the L1 central trigger is shown in Table 4.2

Class	EM		HAD	
	Trigger	Bits	Trigger	Bits
TOF	IET	2	-	-
	E_{tot}	1	E_{tot}	2
ATOF	Veto MIP	1	Veto MIP	1
	E_{tot}	1	E_{tot}	2

Table 4.2: *SPACAL L1 triggers.*

³The time signature of SPACAL depositions is discussed in Section 4.4.

4.3.1 The Inclusive Electron Trigger

The IET [79, 80] is designed to trigger on SPACAL electron candidates by comparing the deposited energy in groups of cells with three thresholds, providing the following triggers:

- T1: 50 – 100 MeV : minimum-bias at the MIP level
- T2: 3 – 5 GeV : low- x DIS physics
- T3: 15 GeV : selection of kinematic peak events for SPACAL calibration.

It is inclusive in the sense that no additional criteria are required to provide the trigger decision.

The inputs to the IET are the 2×2 ToF-gated analogue sums generated by the FECs ($\Sigma_4 TOF$). These are then combined again to give a 4×4 cell summation in which most of the energy deposited by a showering electron is likely to be contained. The sums are performed by sliding window logic so that each sum overlaps the adjacent windows in both dimensions by two cells. This technique guarantees that there is no trigger inefficiency arising from electrons with an impact point close to the edge of a group of 4×4 cells. Each sliding sum is then compared with three thresholds, which are programmable via a serial bus. The output signal from each comparison is synchronised to the HCLK, and is known as a cluster bit. Sixteen sliding sums are handled by one trigger card, and are also ORed together to produce local-IET (LIET) bits for each threshold.

The LIET bits from all cards are fed to a further module, where they are resynchronised and ORed together. This produces three global IET (GIET) bits which represent the presence of one or more cluster anywhere in the EM section with an energy above each threshold. These are encoded on two bits and sent to the L1 central trigger processor.

The cluster and LIET bits are also sent to first-in first-out (FIFO) memory store cards, where they can be held until the L1K and read out in the calorimeter data. The store cards are implemented in the H1 PQZP standard [81], and are interfaced to the L2/3 trigger systems, allowing more detailed trigger information to be used at these levels. All T2 cluster bits are sent to L2/3 and, for the central region, T1 and T3 information is also included. All LIET bits are also sent for all three thresholds. In addition, the LIET bits in the adjacent bunch crossings are read out for offline checks of pile-up and trigger timing alignment.

4.3.2 The ToF/AToF Trigger

The ToF/AToF trigger processing for SPACAL is separated into two distinct branches for both EM and HAD sections; the AToF veto which is designed to reject out-of-time background events at the MIP level, and the ToF/AToF energy sums which generate trigger information from the global energies in SPACAL.

The AToF veto for the EM section takes the Σ_{16} *ATOF* signals provided by the FECs and discriminates them against a single threshold, using the same electronics as the IET but without the sliding windows. This provides AToF cluster bits, which are logically ORed together on each AToF card to produce local AToF bits known as Big Towers. A global OR of the AToF Big Towers generates a global AToF bit which is sent to the L1 trigger. The cluster and big tower bits are read out by the PQZP system (including the adjacent bunch crossings) and also sent to L2/3. For the HAD section, a single AToF card discriminates four ‘pre-sums’ of the Σ_{16} *ATOF* signals which are subsequently ORed together to provide a global AToF bit sent to L1. The full information is read out and sent to L2/3.

The energy sums are created by adding the signals in the big towers (provided by the LIET and AToF cards) to give ‘big sums’. For each SPACAL section there are two such big sums for AToF, representing inner and outer regions, and eight for ToF, which are arranged in inner and outer quadrants. These energies are read out to assist in trigger verification. The big sums are added to give total energies which are discriminated by CFDs to generate four E_{tot} bits (ToF/AToF for EM and HAD) sent to L1. In order to ensure that physics events with a small AToF contribution are not vetoed and background events with a small ToF contribution are not triggered, the E_{tot} triggers are validated by comparing the magnitude of the ToF and AToF energies. This is done by calculating $E_{tot}(ATOF) - E_{tot}(TOF)$ and $E_{tot}(TOF) - E_{tot}(ATOF)$ before discrimination of the big sums.

4.4 The SPACAL TDC System

The SPACAL trigger electronics are complex and critical to the efficient operation of H1. It was therefore decided to construct a separate time-to-digital conversion (TDC) and monitoring system to generate timing information for offline analysis and to allow easy setup and maintenance of the performance of the electronics. The TDC system [82, 83] provides the following functions:

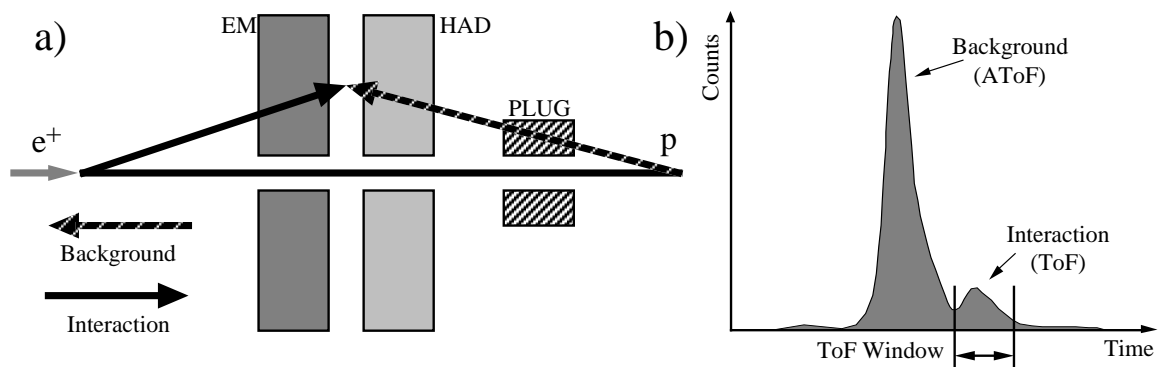


Figure 4.6: *Times-of-flight for SPACAL energy depositions: a) schematic showing the different path lengths for proton-induced background and physics interaction products. b) ToF histogram showing early background and later interaction peaks.*

- **TDC information:** Timing information for all SPACAL channels to a precision of ≤ 1 ns sent to DAQ for triggered beam crossings.
- **SPACAL monitoring:** Monitoring of the SPACAL trigger electronics performance by histogramming times according to trigger information.
- **Beam condition monitoring:** Presentation of visual information in near-real time to enable shift crews to assess background rates and beam quality.

Figure 4.6a shows the different path lengths of SPACAL energy depositions which arise from upstream proton-induced beam-gas and beam-wall backgrounds and physics interaction products. This leads to two distinct peaks in a histogram of SPACAL timing information with respect to the HERA clock (Figure 4.6b), in which the early peak is due to the shorter path length for background, and the late peak contains the physics interactions. The full width of the distribution is typically 30 ns, with the peaks separated by approximately 10 ns for the EM section (more for HAD and BPLUG); a precision of 1 ns is therefore considered sufficient to provide a useful measurement.

The TDC system must cover the entire timing distribution and the data have to be pipelined for the duration of the L1 trigger latency of 23 beam crossings (BCOs). To satisfy these constraints while providing the necessary resolution a semi-custom pipelined device was chosen, a full description of which is given in Section 4.4.2.

In order to trigger successfully on physics events, the ToF window of the SPACAL front-end electronics has to be aligned around the interaction peak. This alignment can be checked by filling a time histogram for events that SPACAL triggered as containing ToF

energy, which should be only physics interactions. The action of the AToF veto can be monitored in a similar way. The TDC system is therefore designed to generate two classes of histogram. The first is for triggered physics events that are sent to DAQ at readout, and the second is a set of unbiased global histograms that use data from as many beam crossings as possible and which can then be classified according to the SPACAL trigger decision. The latter set requires the system to receive the SPACAL trigger bits and generate the histogram information before the L1 trigger decision (L1K signal), otherwise the pipelines will be frozen, or, in the absence of an L1K, the data will ‘fall off’ the end of the pipeline, causing the histograms to become biased. The classification process is based on SPACAL trigger bits, but is completely programmable using a RAM-based look-up table (LUT) which allows sixteen histogram classes to be generated from any combination of the input bits (see Section 4.4.1 for further details).

A schematic layout of the TDC system is shown in Figure 4.7. The system is housed in three VME crates (one 6U high, the other two 9U) and is monitored by an Apple Macintosh computer situated in the H1 control room. The 6U crate is of a standard H1 calorimeter configuration and contains the following modules; a VME branch receiver (VBR) which links to the calorimeter DAQ system via a VME-vertical bus (VMVbus), a vertical interconnect card (VIC) to link the two TDC and other calorimeter control crates via a local VMVbus, two digital signal processor cards (DSPs) that acquire TDC data over a private bus, which they zero-suppress, number and feed into the calorimeter DAQ, and a DSP service module (MDS) that drives the DSPs. A processor running the OS9 operating system [84] is included in the crate for stand-alone operation of the SPACAL DAQ.

The 9U TDC crates are of a custom design and have five 6U slots for standard VME cards. The rest of the slots are 9U high and, in addition to the VMEbus, are serviced by a custom backplane which handles the DSP acquisition bus, signal inputs and control lines. One of the 6U slots in each crate contains a VIC linked to the local VMVbus, over which the system configuration is downloaded during a calorimeter warm-start. The bandwidth of this bus is filled by the calorimeter systems, so the crates are linked to the Macintosh using MacVEE [85] modules. These are interfaced to the Mac using a Micron card [86] which maps the VME address space of up to three crates into the memory of the computer. This link is used to control the monitoring aspects of the system and acquisition of histograms for processing and display in the control room. The design of the system is such that the TDC data acquisition and monitoring tasks, while being performed by the same modules, are interfaced and controlled separately, allowing independent operation during data-taking.

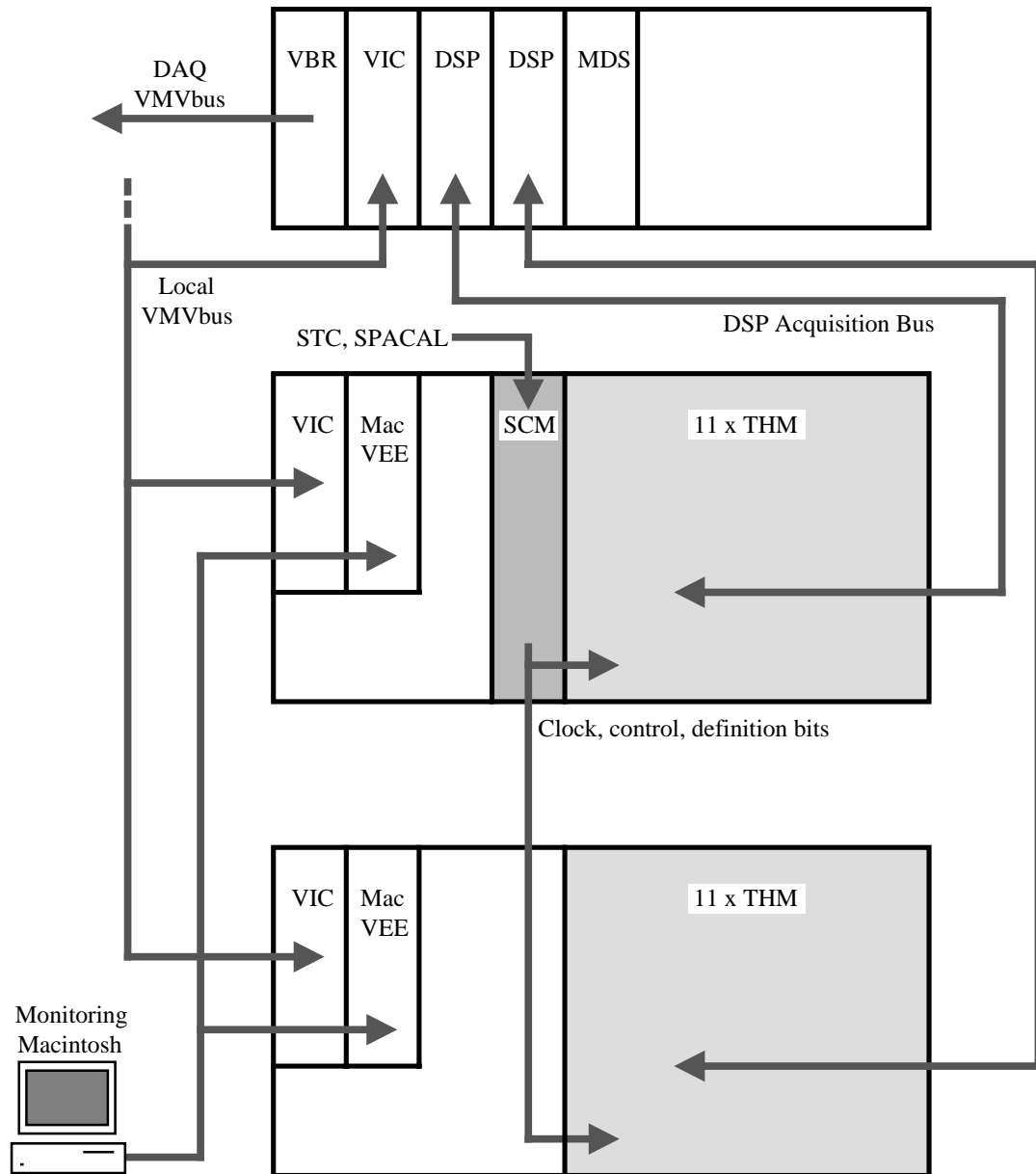


Figure 4.7: *Schematic layout of the SPACAL TDC System.*

There are two types of custom module which comprise the TDC system: the System Controller Module (SCM) and the TDC and Histogrammer Module (THM). Both types are controlled by 16 bit registers mapped into the VME address space; each module has a unique base address and is identifiable by a read-only register containing bits representing module type, revision and serial number. The following sections describe these devices in more detail.

4.4.1 The System Controller Module

The System Controller Module [87] provides overall control, monitoring and signal distribution functions for the TDC system. There is one SCM which serves the THMs in both crates. A schematic of the SCM functionality is shown in Figure 4.8.

The SCM receives HERA clock (HCLK), pipeline enable (PE) and four ‘slow’ signals from the SPACAL STC crate. Two slow signals are also driven back to the STC under the control of bits in a register, for test purposes. The HCLK and PE signals are delayable over a range of 32 ns in steps of 0.25 ns to adjust the phase of the HCLK with respect to the input timing signals. The HCLK and PE are delayed by the same amount as they are required to have a specific phase relationship which is set by the STC. The HCLK is fed into a phase-locked loop (PLL), mounted on a removable daughter board, which allows the frequency to be multiplied by an integer in the range of one to five, in order to generate a suitable clock signal for the TDC devices (TMCCLK). All of the above can be substituted with local signals for test purposes. A local 10MHz source replaces the HCLK, or single clock pulses can be generated. The latter mode of operation prevents the PLL and hence the TDC devices from functioning, but allows other parts of the system to be checked step by step.

Eight 32 bit scalars are provided on the SCM for use by the monitoring software. These scale the following signals:

- Number of PE assertions
- Number of HCLK cycles
- Number of HCLK cycles gated by an active PE
- The four slow signals from the STC
- A user-configurable signal, strobed by the HCLK, which may be the number of assertions of other SCM control signals, or a special register bit which can be used

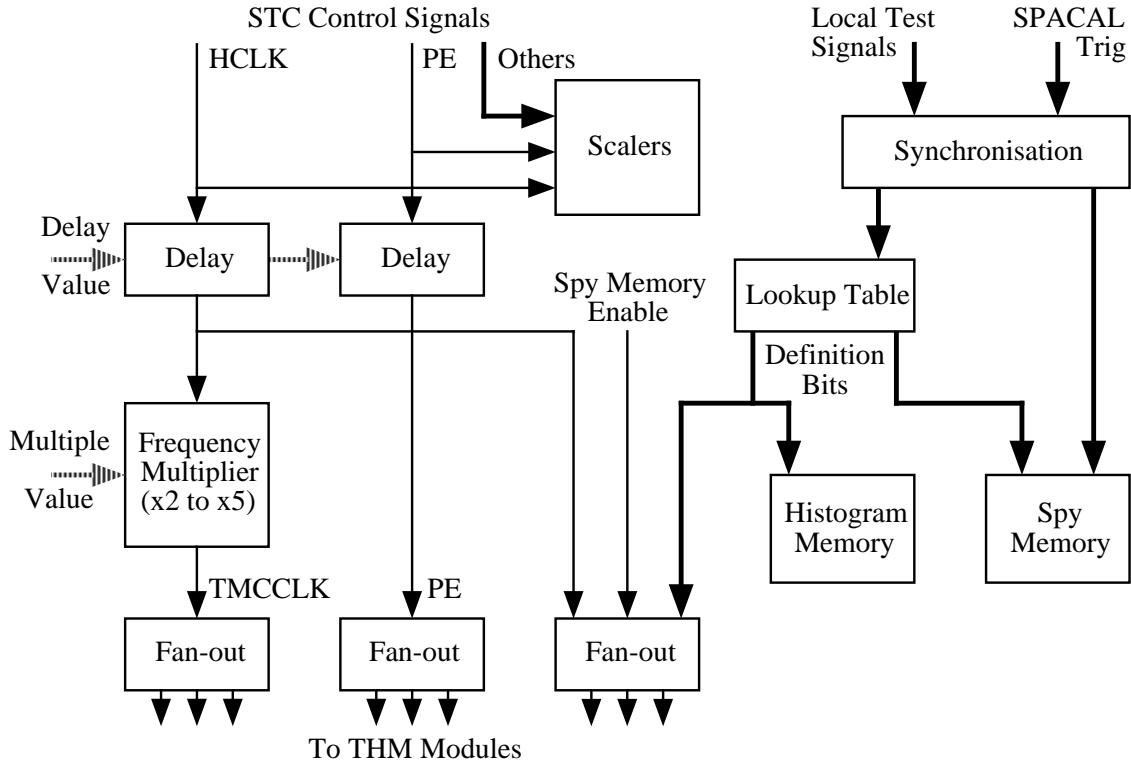


Figure 4.8: Block diagram of the SCM.

to time software monitoring operations.

Additional scalers count the number of HCLK cycles for which THM histogramming of each channel per group of sixteen is active (see Section 4.4.2). This allows the monitoring software to normalise the histograms, thus enabling a quantitative comparison to be made. To achieve this, a copy of the active channel number is stored on the SCM and incremented in step with the THMs, either when the PE is re-asserted after event readout, or by the monitoring software.

The unbiased monitoring relies on the SCM receiving up to sixteen trigger elements from the SPACAL trigger sufficiently in advance of the L1K assertion for the THMs to histogram TDC data. The signals are therefore sent direct to the SCM from the SPACAL trigger processor, where they are first resynchronised to the local HCLK. The bits are then used to form the input address of a 6 kB RAM-based programmable lookup table (LUT), the output of which is four bits that define up to sixteen histogram classes for the THMs. The trigger element input can be simulated with a 2 kB programmable RAM (SIMRAM), whose address is synchronised to the HCLK. This allows a changing pattern of predetermined trigger elements to be fed into the LUT for testing purposes. A further

sixteen scalers count the number of occurrences of each histogram definition.

The SCM (and THM) contains memory which allows the monitoring to ‘spy’ on the events read out by DAQ. This is filled when the software explicitly requests that the next event be stored by setting a register bit. When the pipelines are next enabled, the SCM spy memory is filled with the resynchronised SPACAL trigger elements and the histogram definition bits output by the LUT. The SCM signals to the THMs to fill their memories for the same event, then sets a flag when the data are available. In this way the monitoring is able to acquire information and generate histograms for triggered events.

The SCM fans out the HCLK, PE, TMCCLK, spy memory enable and histogram definition bit signals to the THMs in differential ECL. This is done on individual, equal length cables to avoid signal degradation and unequal delays.

4.4.2 The TDC and Histogrammer Module

The TDC and Histogrammer module [88] provides the following functions:

- Digitisation of time-of-flight information for 64 input signals from the SPACAL FECs.
- Interfacing logic to enable TDC data to be read out by the DSPs for triggered events.
- Accumulation of unbiased histograms of TDC data of each channel, classified according histogram definitions from the SCM.
- Spy memory to enable triggered events to be captured for online monitoring.

A block diagram of the module is shown in Figure 4.9. There are 22 such modules in the TDC system, split evenly between the two crates.

The CFD outputs from the FECs are received in differential ECL over shielded twisted-pair cables. There are 16 channels in each, reflecting the FEC structure, leading to a total requirement of 88 cables. Since H1 is in a radiation-controlled underground environment, they are required to be halogen free and so are stiffer than is typical. For this reason the cables are connected to the TDC system via patch panels mounted on the rear of the crates; this allows the use of lockable connectors, easy access and prevents strain on the backplane.

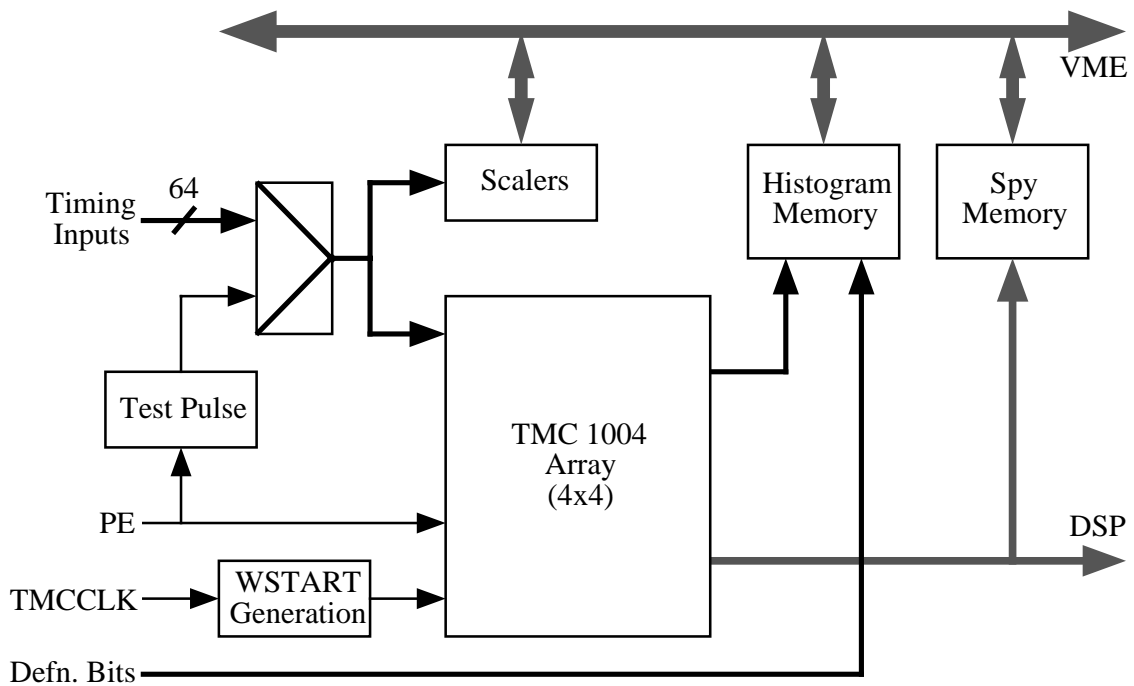


Figure 4.9: Block diagram of the THM.

The signal inputs can be replaced by a local test signal, which is the HCLK divided by four. This is delayable over a range of 128 ns in steps of 0.25 ns. Four copies of the test signal are separately distributed around the board in order to reduce systematic fan-out delays.

The THM receives HCLK, TMCCLK, PE, spy memory enable and histogram definition bits from the SCM. These can also be substituted with local versions, the clocks being derived from a local 32 MHz oscillator (direct for TMCCLK, divided by three for HCLK). The other signals are simulated by setting appropriate bits in control registers.

The TDC function of the THM is handled by the TMC 1004 [89, 90], a semi-custom CMOS device designed for use on detectors at the now cancelled Superconducting Super Collider. The TMC contains four channels, each of which measures the time difference between a signal input and a common clock. The layout of the channel can be considered as an array of 32×32 memory cells, configured in such a way that a timing digitisation can be stored in each row, providing a pipeline depth of 32 such measurements. A schematic diagram of the TMC concept is shown in Figure 4.10. The timing input is connected to the data input of all memory cells in the selected row. The clock (TMCCLK) is fed into chain of voltage-controlled delay elements whose outputs are also connected sequentially to the write input of the memory cells in the row; as a clock pulse propagates down the

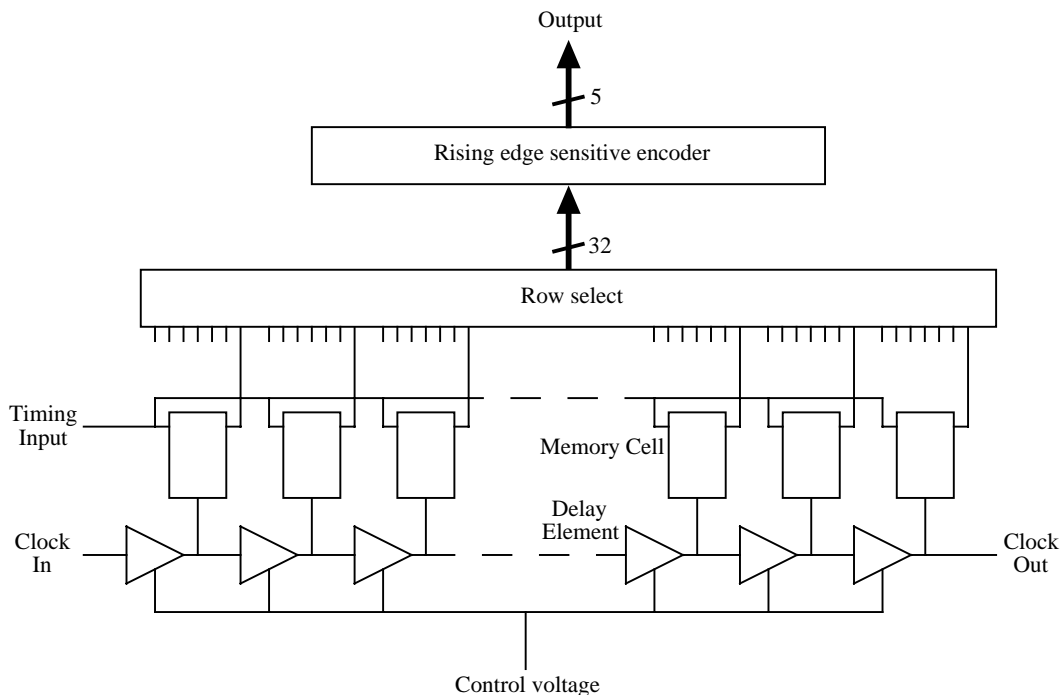


Figure 4.10: Schematic of the TMC device. The memory cells and delay lines of one row only are shown.

delay line it successively enables each cell in turn. Thus cells which were enabled while the signal input was set will store a value of one. The zero-to-one transition along the row therefore encodes the time of the rising edge of the input with respect to the clock.

In order to reduce the number of pins required on the package, the TMC encodes the output of each channel in six bits as a binary representation of the position of the zero-to-one transition and therefore the rising edge of the input signal. Five bits are needed for the full range of 32 bins in each row, and the sixth bit is used to flag if the input pulse was active when the TMC began acquiring data (known as the pile-up flag). This edge-sensitive encoding means that the TMC cannot be sensitive to more than one input pulse in a row.

A phase-lock loop on the TMC measures the relative phase of the clock at the input and output of the delay line. If they are not in phase the control voltage of the delay elements is adjusted appropriately. This feedback mechanism ensures that each memory cell is enabled for $1/32$ of the clock period. The time width of the row, and hence the precision of the device, is therefore determined by the clock frequency. The TMC is specified to operate over a clock range from 25 to 50 MHz, providing bin widths from 1.25 to 0.6 ns. The increased precision at higher clock frequencies is balanced against a shorter window

in which a measurement can be made per row. This window varies from 40 to 20 ns across the specified range. For the nominal 1 ns bins desired in for the SPACAL TDC system, the TMCCLK frequency must be 31.2 MHz, which is conveniently the HCLK multiplied by three. The SCM provides the TMCCLK as HCLK multiples in the range from one to five. The lowest two TMCCLK frequencies are not strictly in range (initial tests have shown that the response of some TMC samples is not monotonic) but can be useful for testing.

At the nominal TMCCLK of 31.2 MHz the pipeline depth of the TMC is $32 \times 32 \text{ ns} = 1.02 \mu\text{s}$. This is insufficient for the L1 trigger latency of $2.2 \mu\text{s}$ so the TMC cannot acquire data continuously. The THM therefore contains logic which, when the PE signal is asserted, generates from the TMCCLK a pulse sequence fed to the write-enable to the TMC (WSTART). If this is configured to enable the TMC for one TMCCLK cycle in three, the pipeline depth becomes $3.1 \mu\text{s}$ which is ample for L1 requirements. This mode of operation gives the TMC a 32 ns active window within each HCLK cycle (and therefore bunch crossing). In order to achieve this, the WSTART generator is fully programmable to account for different clock frequencies and to allow choice of the active TMCCLK cycle. In conjunction with the HCLK delay on the SCM this allows the active window to be aligned such that it contains the full time distribution from background and physics.

Data are acquired by the rows of the TMC array in a circular fashion, according to the value of a write pointer (WPTR). This is automatically incremented (modulo 32) during normal data acquisition by the WSTART sequence. A read pointer on the TMC (RPTR) selects the TMC row which is currently available to read on the output of each channel. When the PE signal is de-asserted by the L1 trigger the TMCs are frozen and the WPTR points to the ‘top’ of the pipeline (the most recent data). The data from the triggered bunch crossing lie at some fixed offset behind this value, corresponding to the L1 trigger latency. In order to access these data, an external shadow pointer is incremented in step with the WPTR, and its value loaded into the TMC RPTR when the PE is de-asserted. The offset that this external pointer has with respect to the TMC WPTR, and therefore the pipeline depth, is configurable in a register on the THM.

The TMC is equipped with four control and status registers (CSRs) which contain the read and write pointers, serial input and output (SIO) bits, and a field which specifies the operating mode. During data taking the TMCs are set to stand-alone mode, which allows acquisition of data and the read and write pointers to auto-increment. During readout the TMCs are set to a slave mode, where the array output is controlled by the value of the RPTR. A test mode is also available, in which the array can be written to and read from via the SIO bits, in which case the row and column of the cell to be addressed is

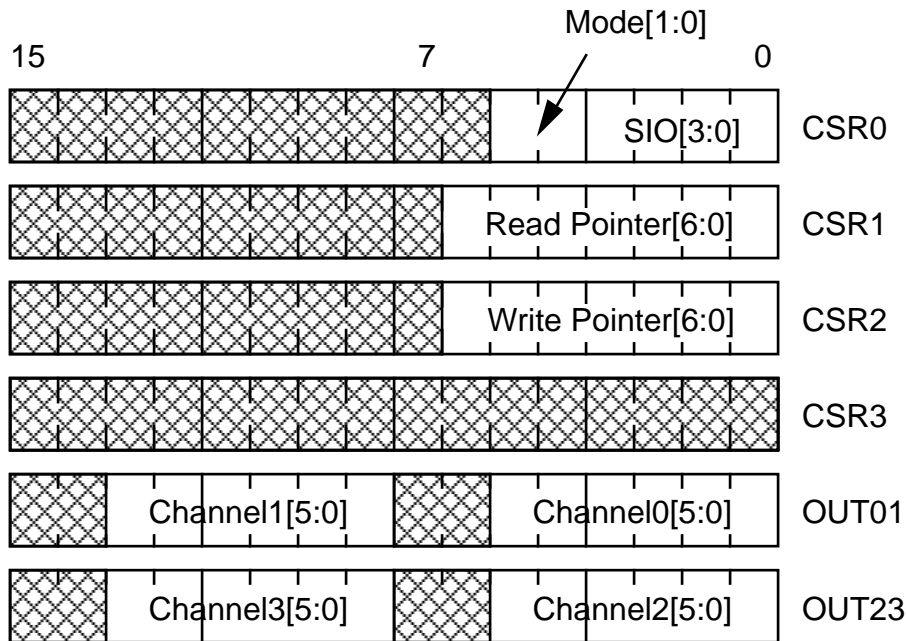


Figure 4.11: *VME memory mapping of the TMC registers.*

specified by the RPTR and WPTR values respectively. This allows the function of the array and the output encoder to be extensively tested.

The CSRs and encoded outputs of each TMC are mapped onto VME registers as indicated in Figure 4.11 (taken from [88]). The DSP readout accesses the output registers directly, thus packing two channels into each sixteen-bit word. For each event the DSPs read three bunch crossings; the triggered bunch and one either side of this. This enables offline monitoring of the TDC alignment, event pile-up and the trigger performance. The DSP readout sequence and the management of the TMCs during data taking is performed by a controller on the THM.

It is possible to lengthen the pipelines of the TMCs without reducing the available precision by chaining together two, or all four, of the channel arrays in each TMC. This is at the expense of the number of available channels per TMC and therefore requires more devices and hence a larger system to cover all the SPACAL channels. The cost of such an option proved to be prohibitive, but the THMs can be configured to operate in this mode. Under these circumstances, it is possible to create a logical OR of one or more channels using jumpers on the board, in order to make full use of the THM signal inputs. In order to function in the nominal mode, each THM is equipped with sixteen TMCs, arranged in a 4×4 array on the board. The clock and control signals are fanned out to the TMCs individually and along different axes of the array, in order to minimise any effects due to delay.

The THM is equipped with four 32 bit scalers, each of which is connected to the sixteen inputs from one FEC. The inputs can be ORed in any combination, under the control of a VME register. Individual channels can be scaled allowing, for example, monitoring of the rate when the CFD threshold is being set. Groups of channels can be scaled together to produce global rates, while masking dead or noisy channels. An additional register allows the instantaneous state of the inputs to be read which assists in the diagnosis of bad channels. A latch is provided which allows the inputs to be frozen; this is vital to prevent the scaler value being corrupted during a read access. This is especially important since the scaler is read in two sixteen bit words.

256 kB of memory is provided on the THM to fulfil the histogramming requirements of the system. There is insufficient space on the module to provide histogramming logic for each channel, so only one channel out of sixteen in each column of four TMCs can be histogrammed at any one time. The active channel is selected by a register, which can be incremented automatically each time the PE is re-asserted after readout, or left static to focus on one channel in each column. This register is mirrored on the SCM which can then scale the number of HCLK cycles for which each channel on the THM is histogrammed, thus enabling a meaningful normalisation between histograms to be made. Each location in the histogram memory is a 32 bit count of how many times a given TMC code has been observed in the channel for a given set of definition bits supplied by the SCM. The address of the location is therefore the channel number, TMC code and definition bits packed together. The TMC data used to form the histograms are required to be unbiased by triggered events, and so must be acquired during the normal running of the TMCs (while the PE is asserted) without affecting the readout cycle. In order to achieve this, the TMC internal RPTR is set in such a way that the data appearing on the output coincide with the arrival of the relevant histogram definition bits from the SCM. Since this occurs much sooner than the L1 trigger, unbiased histograms from as many bunch crossings as possible can be made. The setting of the internal RPTR offset is overwritten by the shadow readout pointer for the acquisition of triggered events, and so is reloaded by the controller each time the PE is asserted from a register on the THM (histogram read pointer).

As on the SCM, provision is made to allow online monitoring of TDC data for triggered events. Spy memory captures and buffers TMC data read by the DSPs. This is filled during DSP readout following reception of the spy memory enable signal from the SCM. The number of words generated per event is

$$\frac{64 \text{ channels} \times 3 \text{ BCOs}}{2 \text{ channels per word}} = 96 \text{ words} \quad (4.1)$$

which is well contained within the 2 kB of memory provided and allows the possibility of multi-event buffering. A pointer maintained in a register and incremented after each word is written points to the end of the most recent event, and can be used to access the relevant data. Combined with the trigger and definition bits stored in the SCM spy memory, these data can then be used to generate histograms for triggered events based on the same classifications as used for the global versions. The spy memory has an identical format to that of the DSP readout (two TMC channels per sixteen bit word) and can be ‘turned around’ to provide a source of data in place of the TMCs. This is purely a test feature and is useful for checking DSP readout sequencing, zero-suppression and channel numbering.

4.4.3 Online Monitoring

The online monitoring is performed on a Macintosh computer located in the H1 Control Room and provides the most visible aspects of the TDC system. It is designed to simplify the major tasks associated with managing the large number of channels in SPACAL; setup and monitoring of the SPACAL analogue electronics (CFD thresholds, channel timings, ToF window settings) and trigger operation. More general information is of use to the shift crews in assessing the quality of the HERA beams using timing and rate information. Finally the management and monitoring of the TDC system itself is necessary.

The number of channels, and the concomitant volume of online data generated by the system (the SCM has 40 scalars and 2 kB of spy memory, the 22 THMs have a total of 352 channel scalars, 44 kB of spy memory and 5.6 MB of histogram memory), means that the monitoring application must be able to process and present a large amount of detailed information while encapsulating more critical aspects in a visual and accessible manner. The graphical user interface of the Macintosh is ideally suited to this task.

The monitoring application [91] provides a number of key features designed to fulfil the required role:

Histogramming: Channel histograms are acquired from the THMs, normalised using SCM information, stored and displayed. These are shown on a channel by channel basis, classified according to the histogram definitions. Histogram sums are defined in software, which are combinations of the stored THM histograms designed to reflect the broad trigger types (for instance: global, all ToF, all AToF). Summary plots are also calculated, which are the histogram sums totalled over all channels in each SPACAL section, enabling the global distributions to be shown.

Rate information: The scaler information from the THMs is used to generate input rates for individual cells or FECs. These are displayed on a two-dimensional representation of the SPACAL sections using colour maps, which provide a rapid means of assessment. History plots are also created for rate information from ANBXs, FECs, and user-defined channels. The SCM scalers are used to determine the occurrence rate for the histogram definitions, which are also shown on history plots. Beam current information, sent from the Central Trigger, is also displayed.

Analyses: Calculations are performed on the histograms to extract global features such as peak position and width, mean time and distribution edges. Applied to the appropriate histogram definitions, these analyses can be used to calculate background and physics peak times and widths and the position of the ToF window for each channel. The results are displayed in summary histograms for each SPACAL section, and also as colour maps, allowing channels with bad timing or ToF window configuration to be identified rapidly.

System management: Parameters such as the SCM clock delay and WSTART sequence can be modified (in an expert mode) allowing the system to be set up while observing the histograms. The LUT can be programmed and downloaded to provide the histogram definition bits. Since such operations can disrupt, and be disrupted by, the normal TDC configuration performed by the calorimeter OS9 processor, unused bits in the SCM registers are used to provide handshaking information. This prevents the application from attempting to access scalers or download parameters while the TDC system is in use. The histogram sums and analyses performed in software can also be directly configured.

The rate maps and histograms can be saved and displayed using the application at a later time. A network interface allows the display aspects of the application to be run remotely.

4.4.4 Offline Reconstruction

TDC data read by the DSPs are passed to the calorimeter event builder and written to the full-event data in the SRTE (SPACAL Response to Time Event) BOS bank. This contains a column identifying THM, channel and bunch crossing, and a data column, formatted as described in Section 4.4.2, with two channels per sixteen-bit word. The data for each event include three bunch crossings and the channel ordering does not reflect the geometry of SPACAL in a natural manner, since the electronics are mapped in groups of sixteen while the basic shape of the detector is circular. There is also a dispersion in

timing response due to differences in cable lengths, signal propagation and paths in the electronics and the variation of transfer function in the TMC devices.

To address the above difficulties a module, SPTIME [92], has been written within the H1REC event reconstruction framework. The module reads the raw TDC data from the SRTE bank, unpacks and corrects them, and creates output banks parallel to those created by the energy reconstruction modules [93]. Figure 4.12 shows the routines and data flow which make up the TDC reconstruction code.

The main routine SPTIME provides the H1REC standard module declaration and dependencies and declares the output bank formats. This calls in turn SPTCAL which provides most of the processing and takes as its input the SRTE and SNGR banks. The latter, created by the energy reconstruction module, is a list of channels having energy deposits above the DSP zero-suppression threshold, numbered in a continuous spiral starting at the centre of SPACAL (referred to hereafter as geometrical numbering) and is parallel to the reconstructed energy bank, SE0R⁴, meaning a given row in each bank refers to the same channel. The data are separated into individual channels, the pile-up flags stripped off and the correct bunch crossing selected (usually the centre of the three). The channel information is passed to a further routine NSGEOM which makes use of database banks describing the mapping of TDC channels to SPACAL cells to derive the correct geometrical number. The time values are corrected using a database bank containing offsets for each channel. The output is the STER bank which is parallel to SNGR and SE0R and contains the corrected TDC times. Channels which have an energy value but no time (when the energy deposited is sufficient to exceed to DSP suppression threshold but not to pass the CFD) are flagged as such. There also exists the possibility that channels have timing but no energy information, in which case it is not possible to include them in STER since there is no corresponding entry in SNGR. Two additional parallel ‘overflow’ banks are therefore produced; SNOR is a list of geometrical channel numbers and STOR contains the corresponding time. A further bank, SNPU, contains a list of channels for which the pile-up flag was set in the selected bunch crossing.

The operation of SPTIME is steered by information stored in the H1 database which flags if the overflow and pile-up banks are to be written. Additional information specifies global time offsets to be applied to the channels in each SPACAL section, allowing the timing distributions to be aligned such that the peak from physics interactions lies at a particular time value (typically zero). Since database information can be run-dependent,

⁴This bank contains the so-called zeroth energy scale, which is after calibration has been applied. Subsequent corrections for dead material in front of SPACAL and variations in response at module boundaries (cracks) give rise to the first energy scale bank, SE1R. A final bank, SEFR, results from corrections to the energy scale of hadronic activity in SPACAL.

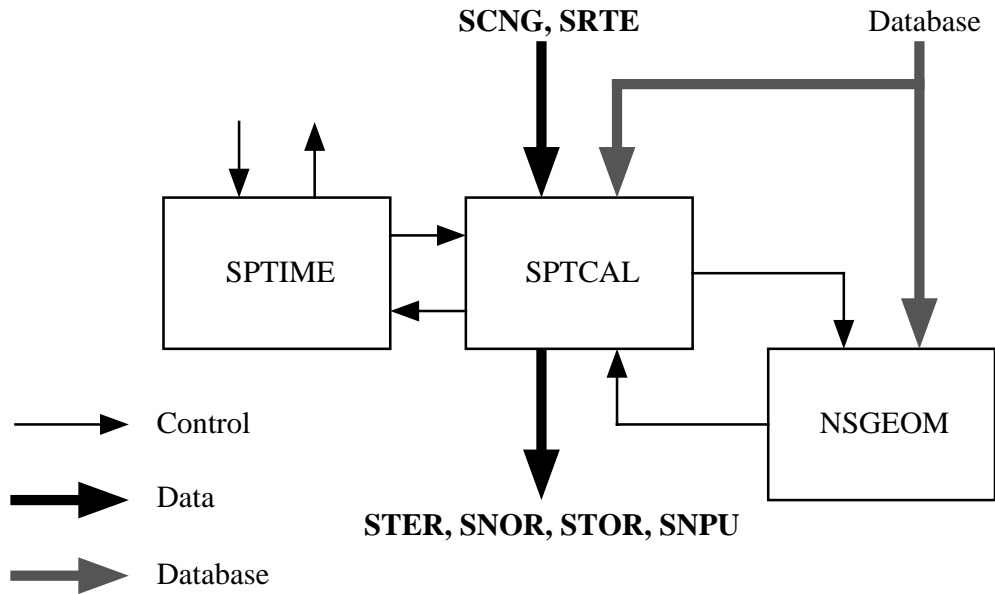


Figure 4.12: Schematic of the TDC reconstruction mode *SPTIME*, showing flow of control between routines, data banks and database information.

this feature enables any shifts in timing that arise from variations in operation of HERA to be corrected, simplifying use of TDC data in analysis.

The process described above potentially generates a substantial amount of data, and is performed during full reconstruction to generate POTs. Since this volume is incompatible with the bank scheme and consequently smaller event size in the DST datasets, the TDC information has to be compressed. This is achieved by writing timing information only for channels with energy into a word of the DST cell (DCEL) bank, which contains information for all calorimeter cells. The format of this bank constrains the time to only eight bits which, given the need to represent the full range of possible timings after correction and also to include the pile-up flag, means that TDC data can only be stored with a precision of 0.5 ns. Code has been written and integrated into the DST production modules of HIREC which packs the TDC values in the specified manner. An additional routine can be employed to uncompress the information and dynamically recreate the STER bank at analysis time.

Chapter 5

Performance of SPACAL and the TDC System

Prototypes and final designs of the SPACAL calorimeter modules and electronics were extensively tested during 1994 at the CERN Proton Synchrotron (PS) and Super Proton Synchrotron (SPS), at DESY and at ITEP, Moscow. Elements of the TDC system were tested during the design phase, and also at the PS. This chapter describes key results from these tests and the commissioning and initial use of the TDC system within H1.

5.1 SPACAL Electromagnetic Section Performance

The SPACAL EM section was tested with electron beams in the range 2 to 60 GeV [94, 95]. At the CERN SPS and DESY, three supermodules plus one quarter of the special insert modules were tested, while at the CERN PS four complete supermodules were investigated. In order to measure the basic performance of the calorimeter, standard readout electronics were used in place of those designed for use at H1. The modules were rotated with respect to the beam axis (3° and 4.5° for the SPS/DESY and PS tests respectively) to avoid channelling effects.

Calibration of the cells tested was achieved by firing electrons of a fixed, well-determined energy into the centre of each cell. From this a relative cell-to-cell calibration of better than 2% was obtained. The average response was used in combination with knowledge of the beam energy to fix the overall energy scale.

The SPACAL lead/fibre matrix is a naturally homogeneous medium for calorimetry; the main contribution to inhomogeneity arises due to variations in structure at submodule

boundaries where the lead sheets are discontinuous. This effect was measured by scanning the impact point of a 4 GeV electron beam across a number of module boundaries and measuring the summed output from the cells involved. The maximum deviation from a uniform response was found to be 8% at the boundary between two submodules; no significant effect was observed between cells in the same submodule. The effect was also seen to be strongly dependent on the cells measured, and is thought to be due to damage to the fibres at the edges of lead sheets which occurs during the stacking process. During this procedure a total pressure of 1.5 tonnes is applied to press the modules to their nominal dimensions, which is equivalent to that caused by the weight of the fully-assembled calorimeter. It is possible that the lack of support at the edges of the modules causes the lead to deform and squeeze the fibres which has an effect on their properties. The assembly procedure for the final calorimeter was therefore modified in an attempt to mitigate this effect.

The linearity of the EM section was measured by fitting a straight line to the energy response as a function of beam energy between 10 and 60 GeV. The maximum deviation from linearity was found to be 1.3%, which is within the non-linearity of the readout electronics used.

Data from the SPS and DESY tests were used to obtain the energy resolution. Super-modules with small inhomogeneities were used for this purpose. The energy in a region of 3×3 cells was summed, in order to maximise the containment of the electron shower. At each energy point a Gaussian fit to the energy sums was performed to extract the mean value, giving the energy, and the resolution was obtained from the width of the fit. For the DESY points the estimated beam resolution of 85 MeV was subtracted in quadrature while the smearing in the SPS beam energy contributes to the determined resolution. In Figure 5.1 (taken from [94]) the normalised resolution σ_E/E is plotted as a function of $1/\sqrt{E}$. A fit to this plot of the form

$$\frac{\sigma_E}{E} = \frac{a}{\sqrt{E}} \oplus \frac{b}{E} \oplus c \quad (5.1)$$

was used to parameterise the energy resolution. The result of the fit demonstrates that the noise term is negligible, and gives a resolution of

$$\frac{\sigma_E}{E} = \frac{(7.1 \pm 0.2) \%}{\sqrt{E/\text{GeV}}} \oplus (1.0 \pm 0.1) \%$$

This gives a resolution of better than 2% for 30 GeV electrons which satisfies the design requirement and is in good agreement with expectations from Monte Carlo simulations. The constant term will be larger than that shown above, due to the inhomogeneities at submodule boundaries. A pessimistic simulation which parameterises the signal fluctuations at all boundaries to be 5% predicts the constant term to be 2.2%. A complementary

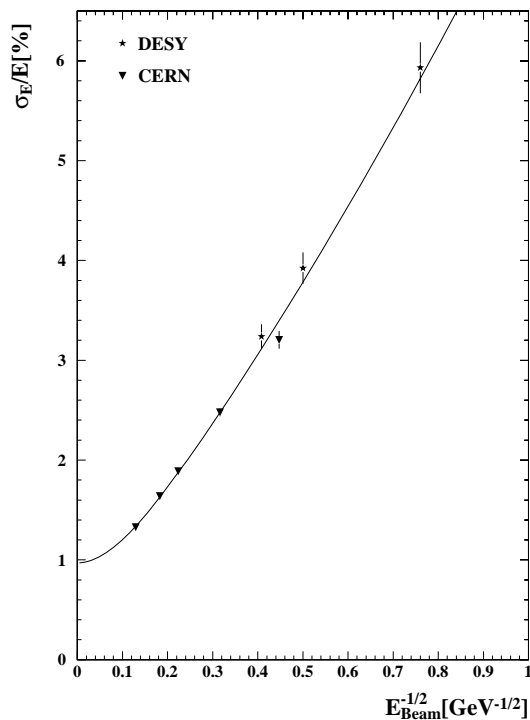


Figure 5.1: *SPACAL EM section energy resolution as a function of $1/\sqrt{E}$, including the fitted parameterisation.*

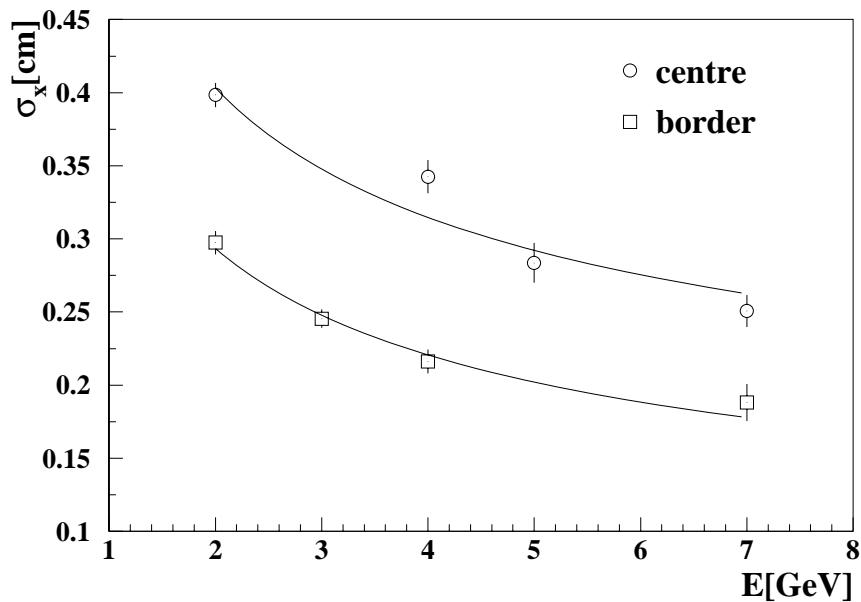


Figure 5.2: *SPACAL EM section spatial resolution as a function of energy for two impact positions, including the fitted parameterisations.*

measurement at the CERN PS using electrons in the range 1 to 7 GeV gives a resolution of

$$\frac{\sigma_E}{E} = \frac{(7.6 \pm 0.2) \%}{\sqrt{E/\text{GeV}}} \oplus (1.2 \pm 0.3) \%$$

and a linearity of better than 1%, both of which are consistent with the higher energy results.

The spatial resolution for electromagnetic showers was measured using 4 GeV electrons at the PS. The impact point of the shower, \bar{r} , in each coordinate was reconstructed using a logarithmic weighting method

$$\bar{r} = \frac{\sum_i w_i r_i}{\sum_i w_i} \quad (5.2)$$

where r_i is the centre coordinate of cell i and the weight w_i is derived from the cell energy E_i using the following formula:¹

$$w_i = \max(0, w_0 + \ln(E_i / \sum_j E_j)). \quad (5.3)$$

The cutoff parameter w_0 controls the sensitivity to the fluctuations in the shower tails and the optimal choice is dependent on the energy, cell size and impact angle. Since the cell size and impact angle were fixed, and the dependence on energy is only weak, the value was determined to be 4.3 at 4 GeV by optimising the spatial resolution, and used for all energies. This agrees well with Monte Carlo predictions. The resolution is then determined by comparing the calculated impact position with the extrapolation of a track measured in a wire chamber (which has a resolution of 200 μm in both coordinates) positioned in front of the calorimeter. A Gaussian fitted to the distribution of difference in the two positions gives the resolution. This is done at a range of energies and for two impact points; the centre of a cell and close to the border between two cells. Figure 5.2, taken from [94], shows the results. A fit to these data as a function of energy gives a spatial resolution of

$$\sigma_x = \frac{(4.4 \pm 0.4) \text{ mm}}{\sqrt{E/\text{GeV}}} + (1.0 \pm 0.2) \text{ mm}$$

for impact points at the centre of cells, and

$$\sigma_x = \frac{(3.8 \pm 0.4) \text{ mm}}{\sqrt{E/\text{GeV}}} + (0.3 \pm 0.2) \text{ mm}$$

for impact points at the border of two cells. The reason for this difference is that, when the shower centre is at a border, the energy is more equally shared between the cells, improving the impact point calculation.

¹A linear weighting method $w_i = E_i$ is currently used in H1, as this has proven to give a better response.

The time resolution of the design was also determined at the SPS tests, by comparing the time of the SPACAL signal with that from coincidence scintillators mounted upstream in the beam. The resolution of the scintillators is well-known and was subtracted in the analysis. The time of the SPACAL signal was not measured with the new TDC system but with standard modules. The result obtained was

$$\sigma_t = (0.38 \pm 0.03) \text{ ns.}$$

This value contains the intrinsic resolution of the calorimeter and also that of the photo-multipliers used, and is within the acceptable limit for H1.

The response of the EM section to MIPs was measured at the PS using mixed electron, pion and muon beams. It was not possible to select muons offline effectively, so punch-through pions (those that do not interact inelastically within the volume of the detector) were used. The peak of the punch-through energy distribution was taken as the MIP response. The measurements show a strong dependence on impact position, which is due to the influence of the fibre bundle at the rear of the active region. The varying cross section of the bundle means that the path length through the sensitive volume of the calorimeter, and hence the amount of energy deposited by MIPs, changes with impact position. The response was observed to vary by as much as 50% across cells; this is well-reproduced by Monte Carlo simulation. Taking this effect into account, the e/MIP ratio was measured, which reflects the relative response to electromagnetic showers and MIPs. The ratio was found to be 0.87 ± 0.03 . Similarly, the e/π ratio, which demonstrates the differing response to electrons and pions for this non-compensating design of calorimeter, was measured [96] and found to range from 2.15 at 1 GeV to 1.97 at 7 GeV. Pions interacting the EM section were also analysed. The active region of this section (one interaction length) means that 63% of pions should interact inelastically. A Gaussian fit to the energy distribution at a range of beam energies (2 to 7 GeV) gives a resolution of

$$\frac{\sigma_\pi}{E} = (36 \pm 4) \%$$

and the linearity of response was measured to be better than 2%.

Shower profiles for electrons and interacting pions were investigated by measuring the energy sharing between cells to the left and right of a fixed reference plane, as a function of impact position. This was performed with 4 GeV beams scanned over a distance of 4 cm each side of the reference plane. From the resulting distribution, a characteristic transverse shower scale, R_0 can be extracted. This is related to the Molière radius and defines the region in which 95% of the energy of a shower is contained. For electrons the result of the fit gave $R_0 = (2.1 \pm 0.1) \text{ cm}$, while for pions the result was $R_0 = (7.5 \pm 0.5) \text{ cm}$. Lack of statistics at higher beam energies meant that the evolution of R_0 with energy could

not be investigated in detail, but a general trend could be extracted. This showed that the transverse scale of electron-induced showers is largely independent of energy, whereas in the case of pions, it grows with increasing energy. These trends are in agreement with expectations from simulation, and indicate that the shower radius is a useful estimator for selection of electrons in SPACAL.

5.2 SPACAL Hadronic Section Performance

The hadronic section was tested at ITEP and at the CERN PS, using similar methods to those presented above for the EM section [72, 95]. As at CERN, the ITEP tests were carried out with the modules rotated by 4° with respect to the beam axis. Upstream scintillators were used to trigger on particles.

At ITEP an electron beam in the range of 1 to 3 GeV was used to measure the electromagnetic response. A fit of the type described in Equation 5.1, with the beam energy smearing of 1% subtracted, gives

$$\frac{\sigma_E}{E} = \frac{(12.5 \pm 3.0) \%}{\sqrt{E/\text{GeV}}} \oplus (3.8 \pm 2.2) \%.$$

A measurement at 2 GeV at the CERN PS of 10% is consistent with this. The linearity in the above energy range was estimated to be better than 5%.

The response to interacting pions was measured at the PS with a 4 GeV π^- beam. Since both calorimeter sections were mounted in the beam, a MIP signature of less than 500 MeV in the EM cells was required. The energy deposited by the MIP in the EM section (typically 350 MeV) was subtracted from the beam energy in the analysis. The results show that the energy response is linear to better than 5%, with a resolution of

$$\frac{\sigma_\pi}{E} = (39 \pm 4) \%.$$

The time resolution was also determined with a pion beam and found to be $\sigma_t = 0.83 \pm 0.3$ ns. The spatial resolution was not measured, as this is not a critical function of the hadronic section.

5.3 Combined Performance

The PS tests were also used to measure the combined response of the EM and HAD sections. Using the π^- component of the beam, the energy resolution for pions interacting

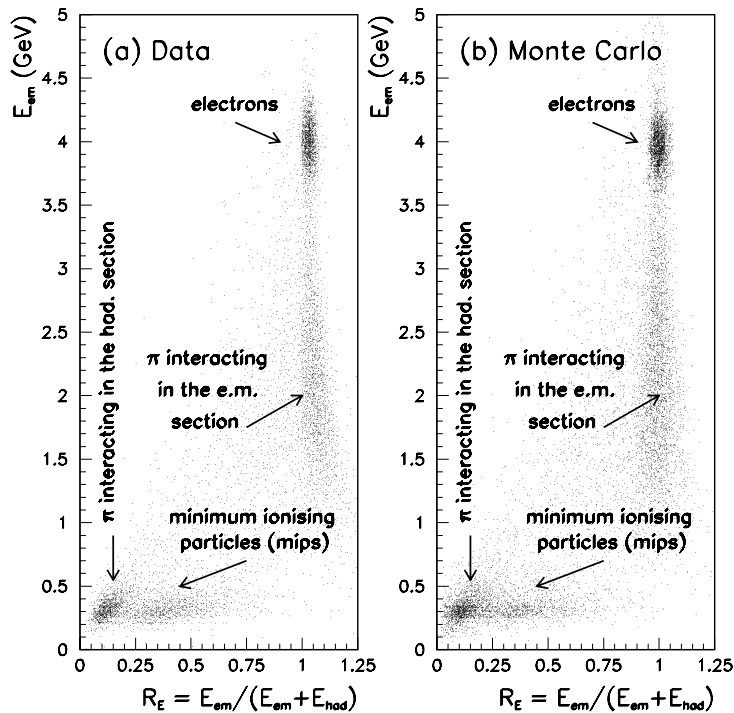


Figure 5.3: Electromagnetic energy E_{em} distribution as a function of R_E for data and Monte Carlo with 4 GeV beam energy.

in either detector volume was determined by comparing the beam energy with the total calorimeter energy $E_{em} + E_{had}$. The resulting response was found to be linear to better than 5% and the resolution was

$$\frac{\sigma_{\pi}}{E} = (29 \pm 2) \%$$

which is a considerable improvement over the individual measurements detailed above.

The combined measurements in SPACAL were also used to separate electrons and pions. The longitudinal energy sharing ratio, R_E , defined as

$$R_E = \frac{E_{em}}{E_{em} + E_{had}} \quad (5.4)$$

is a suitable estimator for rejection of pions. Figure 5.3 (taken from [95]) shows the energy deposited in the EM section versus R_E . It can be seen how electrons, which leave all their energy in the EM section and give values of R_E peaked at one, can be separated from MIPs by a suitable cut in this ratio. The optimal choice of cut was found to increase with energy, due to residual noise in the hadronic section. At 4 GeV a cut at $R_E = 0.95$ leads to an efficiency for selecting electrons of 97%. The rejection factor $R_{e/\pi}$, defined as the electron detection efficiency divided by the probability of misidentifying a pion as an

electron, was found to range from 2 to 4 in the beam energy range from 2 to 7 GeV for 97% electron efficiency.

Given this method for efficiently rejecting the MIP signature of punch-through pions, it is necessary to determine estimators which can reject the interacting pions based on the properties of the shower in the electromagnetic section. The properties of the showers can conveniently be parameterised in terms of the moments of their energy distributions about the impact points. The k -th moment of the shower (in each coordinate) is defined as

$$\mu_k = \left(\frac{\sum_i w_{ik} (x_i - \bar{x})^k}{\sum_i w_{ik}} \right)^{1/k} \quad (5.5)$$

where x_i is the coordinate of the i -th cell and \bar{x} is the impact point of the shower, which is can be calculated using equation 5.2. The weights of the k -th moment are calculated in the same way as for the shower impact point, shown in equation 5.3. The second moment, μ_2 , defines the lateral spread of the shower and was found to be the best estimator for e/π separation. The optimal cutoff parameter for this moment, w_2 , was found to be 4.85. Based on this, pion rejection was performed by cutting on the combination of x and y components of the second moment, added in quadrature:

$$\mu_2 = \sqrt{\mu_{2x}^2 + \mu_{2y}^2}. \quad (5.6)$$

Values of μ_2 above the cut are then considered as pions, those below as electrons. The cut value was determined for an electron detection efficiency of 90%, and found to be dependent on energy, ranging from approximately 4 at 1 GeV to 3.2 at 7 GeV. The resulting e/π rejection factors depend on both the energy of the pion and the energy of the electron that the pion fakes. Typical values range from 20 (for 2 GeV pions faking 1 GeV electrons) to 860 (for 7 GeV pions faking 6 GeV electrons). The probability of a pion of any energy being misidentified as an electron of energy 4 GeV is 1/300. These figures show that SPACAL has the required capability for separation of DIS electrons from photoproduction background, even for energies of a few GeV.

Table 5.1 summarises the key results from the SPACAL beam tests. These show that the SPACAL calorimeter meets the specified design criteria and is capable of providing the necessary measurements within H1.

5.4 Inclusive Electron Trigger Performance

The IET processors of the trigger were investigated as part of the SPACAL test program at the CERN PS [79]. The testing of HCLK-synchronous components under these conditions

	Electromagnetic	Hadronic	Unit
Energy Resolution, σ_E/E	$7.1/\sqrt{E} \oplus 1.0$ (e^-) 36 ± 4 (π^\pm)	$12.5/\sqrt{E} \oplus 3.8$ (e^-) 36 ± 4 (π^\pm)	%
Combined:	29 ± 2 (π^\pm)		
Spatial resolution, σ_x/E	$4.4/\sqrt{E} + 1.0$ centre $3.8/\sqrt{E} + 0.3$ border	Not measured	mm
Time resolution, σ_t	0.38 ± 0.03	0.83 ± 0.02	ns
e/π separation	20 (2 GeV π faking 1 GeV e) 860 (7 GeV π faking 6 GeV e)		

Table 5.1: Results of SPACAL beam tests.

was complicated by the fact that the PS beams are delivered in continuous spills of 0.5 s duration, separated by 19 s. This is a very different environment from that of HERA, where particles arrive at well-defined times relative to the HCLK phase. In order to simulate this to some extent, a local 10.4 MHz clock was distributed around the systems under test. A 20 ns wide ToF window was then set arbitrarily with respect to this clock. The triggering, as mentioned above, was performed with scintillators in the beam, and the IET operated and read out independently of this.

In order to measure the IET efficiency, the ToF sums performed by the LIET cards (Σ_{ToF}) were digitised by a separate ADC system. The IET trigger bits were also read out, and an offline comparison of the two performed. Figure 5.4, taken from [79], shows in the left column Σ_{ToF} energy distributions with and without the requirement of the trigger bit for each threshold (shaded and open histograms respectively)². The response to MIPs, interacting pions and electrons can be clearly seen; the thresholds were set to trigger on each of these components. The T1 threshold was set at 5 mV, which corresponded to an energy of approximately 30 MeV, given PMT gains set to match those expected in H1 with magnetic field. The output noise of the sliding window summations (which therefore includes contributions from all the preceding parts of the signal chain) was measured to be 500 μ V, some 10σ from the threshold, demonstrating the ability to set T1 well below the MIP peak.

The right column in Figure 5.4 shows the ratio of the energy spectra for each threshold, which is a measure of the efficiency of each trigger bit. Above threshold, the total efficiencies have been measured to be $\varepsilon_{T1} = 99.2\%$, $\varepsilon_{T2} = 99.1\%$ and $\varepsilon_{T3} = 99.1\%$. Also

²The T2 distribution explicitly requires that only the T2 bit is set, hence the lack of response above the T3 threshold.

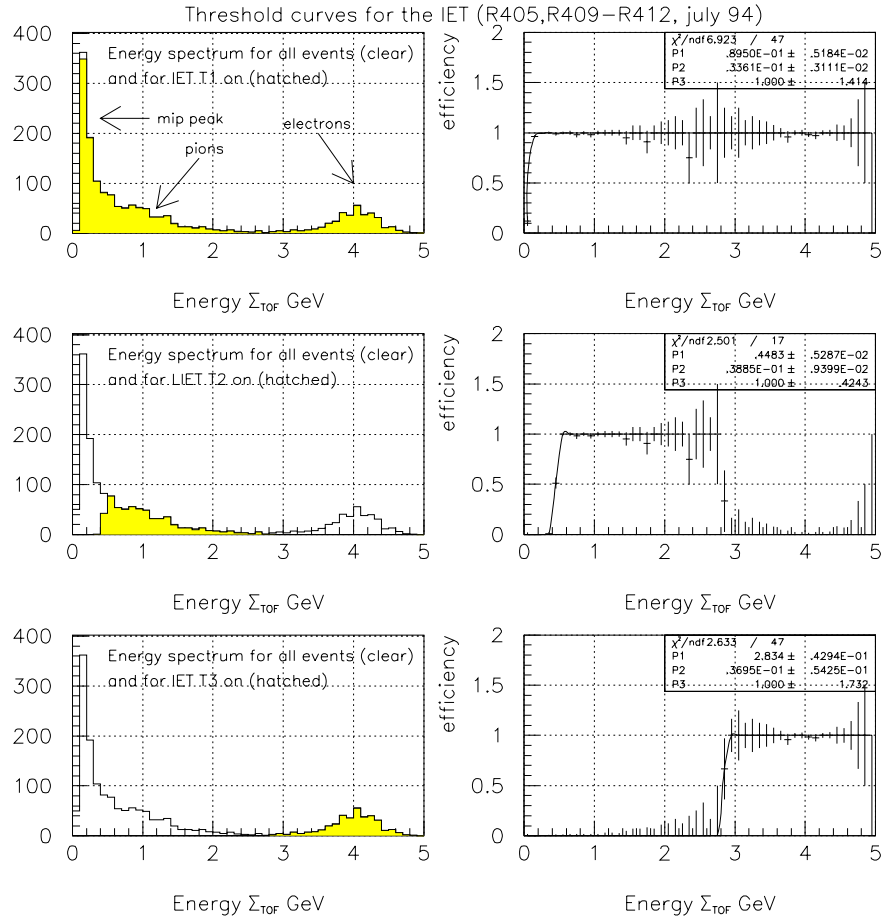


Figure 5.4: Performance of the IET processor at the CERN PS beam tests. The left-hand histograms show the ToF energy sums without (open) and with (shaded) the IET trigger bit set at each threshold. The right-hand plots show the efficiencies of each threshold as a function of energy.

shown are fits to the threshold function of each distribution; these indicate a width of approximately 35 MeV for each. These results were derived from data taking with the beam fired into the centre of one cell, but it is also important to quantify the efficiency for other impact positions; data taken with the beam impinging on the boundary of four cells gave a T2 threshold efficiency of 99.8%.

The detailed operation of each stage of the IET was also tested; the LIET and GIET bits were found to be 100% efficient with respect to the cluster bits. The synchronisation of the trigger bits to the HCLK was also found to be correctly functioning. These results prove the IET to be capable of meeting the specified design criteria.

5.5 The TDC Pre-Prototype Module

During the design phase of the TDC system, a pre-prototype module (PPM) [97] was constructed. This was designed as a test-bed for aspects of both the SCM and THM, and was equipped with a full VME interface, the signal handling and PLL of the SCM and input scalars, control logic, input receivers, test signal substitution and sixteen TMCs from the THM. Histogramming was not implemented due to lack of space and no DSP acquisition interface was provided meaning that readout of TMC data had to be performed via the VMEbus.

This module was used to prove the design viability and operation of key parts of the system, as target hardware for early software development and to test the TMCs before final installation. The PPM was also used during the early beam test period before the SCM and THM designs were finalised.

5.6 Acceptance Testing of the TMCs

The complete TDC system (including three spare THMs) contains 400 TMC devices. In order to check the operation of the delivered batch of TMCs prior to installation, a Macintosh application (TMCaccept [98]) was written which enabled the rapid testing of groups of sixteen chips on the PPM.

The application first tests the digital performance of the TMCs. This involves exercising the CSR registers (writing all possible values to the register and verifying the result), loading and reading the TMC array via the SIO bits, and checking the encoder output with a known test pattern loaded into the array. Devices which fail this step are not tested further.

TMCs passing this phase are then tested for TDC performance by applying a local test pulse to the timing input. The TMC output data are averaged over a large number of acquisitions and the measurement repeated at successive delays of the test pulse in 1 ns steps over a range of 64 ns. All cycles in the WSTART sequence are enabled so that the TMC acquires data continuously. The test is performed at each clock multiple available from the PLL (10 to 50 MHz). The response of one channel to this test is shown in Figure 5.5. As the delay is increased the TMC output increases linearly, until the end of the row when the output value moves into the next (i.e counting modulo 32). The slight rounding at the edges of each slope is an artifact of jitter in the test pulse; at such positions the output time may occasionally appear in the adjacent row, causing the

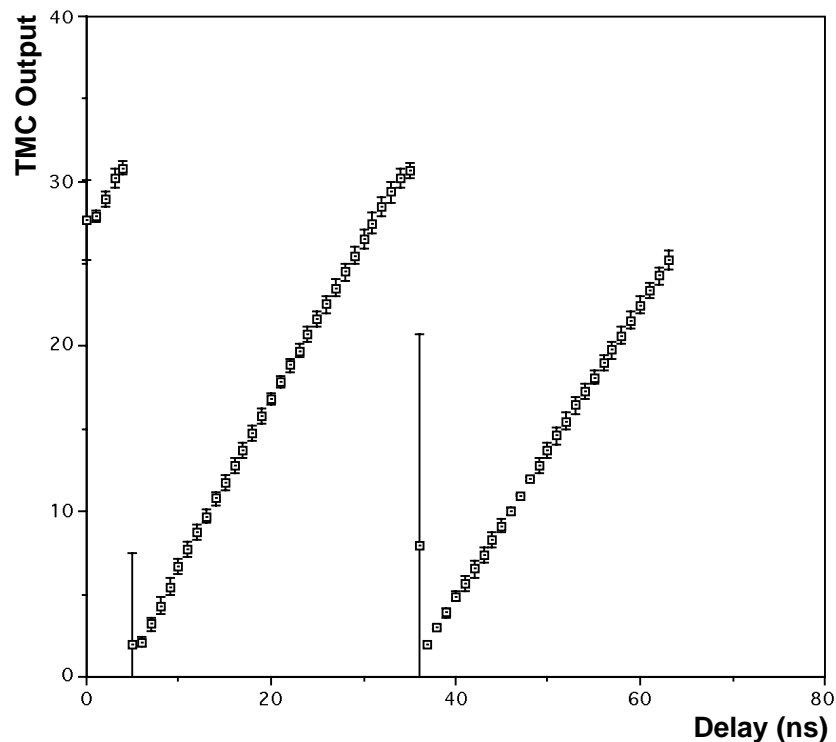


Figure 5.5: *TMC single channel response to a delay-scanned test pulse input.*

mean value to be biased slightly. The large errors on points lying in the edges of this sawtooth distribution are also attributable to this effect. The TMC transfer function is then characterised in terms of this response. A least-squares fit to the linear portion of the distribution is performed, excluding the end values where the rounding effect occurs. The gradient, intercept and χ^2 of the fit are then compared to pre-determined acceptable ranges to generate a pass/fail decision for the device. The clock frequencies of 10 and 20 MHz are not within the specified operating range of the TMC and are therefore ignored in the decision, although the results are still useful in characterising the operating potential of the device. The gradient of the fit calibrates the bin width of the TMCs, while the intercept has a more arbitrary significance and reflects the detailed timing of the input signal with respect the TMC clock.

From the full batch, four TMCs were found to fail at the digital test stage and were returned to the manufacturer for replacement. The remaining chips were all found to have satisfactory performance in the TDC test. A global analysis of the test data showed that the fit gradients for a clock frequency of 30 MHz (closest to the nominal operating conditions) have a mean value of 1.02 ± 0.04 , demonstrating that the spread in performance of the devices is small. The mean gradients for 40 and 50 MHz were found to be consistent with this result to within 1σ . The error on the mean intercept is larger (typically 18%),

which is interpreted as arising from the topology of the PPM; the TMCs are laid out, as on the THM, in a square array with the clock and control signals fanned out along one axis and the signal inputs along the other. This causes a systematic shift in the relative phase of clock and test pulse. However, this effect was considered to be small relative to potential timing shifts arising from other components in the signal path, and therefore of no significance.

5.7 TDC Beam Test Results

The TDC system was tested with the other SPACAL electronics at the CERN PS. During the initial tests in May and July 1994 early prototypes of the ANCA and FEC were used, equipped with CFDs and output drivers for only two channels. The TDC function was provided by the PPM, using VME readout under the control of an OS9 data acquisition system to access the TMC data.

As mentioned in Section 5.4, the non-synchronous nature of the PS beams complicates the investigation of the HCLK-driven parts of the electronics. The TDC system was fed the local 10.4 MHz HCLK; the phase of this clock was also measured with respect to the time-of-arrival of the beam particles, defined by a coincidence in the beam scintillators, using a dedicated VME TDC module. This information can then be used to correct the TDC times in the following way; if the TDC system measures the time of the TMC input signal with respect to the HCLK, $\Delta_{\text{TMC}} = t_{\text{TMC}} - t_{\text{HCLK}}$, and the beam TDC measures the time of the HCLK with respect to the beam arrival, $\Delta_{\text{HCLK}} = t_{\text{HCLK}} - t_{\text{beam}}$, then the sum of the two, $\Delta_{\text{TMC}} + \Delta_{\text{HCLK}} = t_{\text{TMC}} - t_{\text{beam}}$, is a measurement of the TDC time with respect to the beam.

Figure 5.6 shows results from one of these runs, taken with a 4 GeV mixed electron, pion and muon beam. The DSP energy for one channel (in ADC counts) versus the HCLK-corrected TMC time is shown in the upper plot. The increased density of the plot at an ADC count of 1500 corresponds to electron showers and the pion tail and MIP peak (approx. 320 counts) can be seen at lower energies. The discriminator can be seen to work satisfactorily down to approximately 400 ADC counts, but below this value the trigger walk arising from small pulse heights can be seen to have a large slewing effect in time. This occurs above the MIP level and was therefore not considered to be satisfactory performance. In order to estimate the resolution of the TDC system, a cut was therefore applied to the energy distribution at 400 ADC counts. A fit to the resulting corrected time distribution yielded a resolution of 0.99 ns. It is important to note that this contains a contribution from HCLK TDC module which had a resolution of $\simeq 0.7$ ns. Subtracting

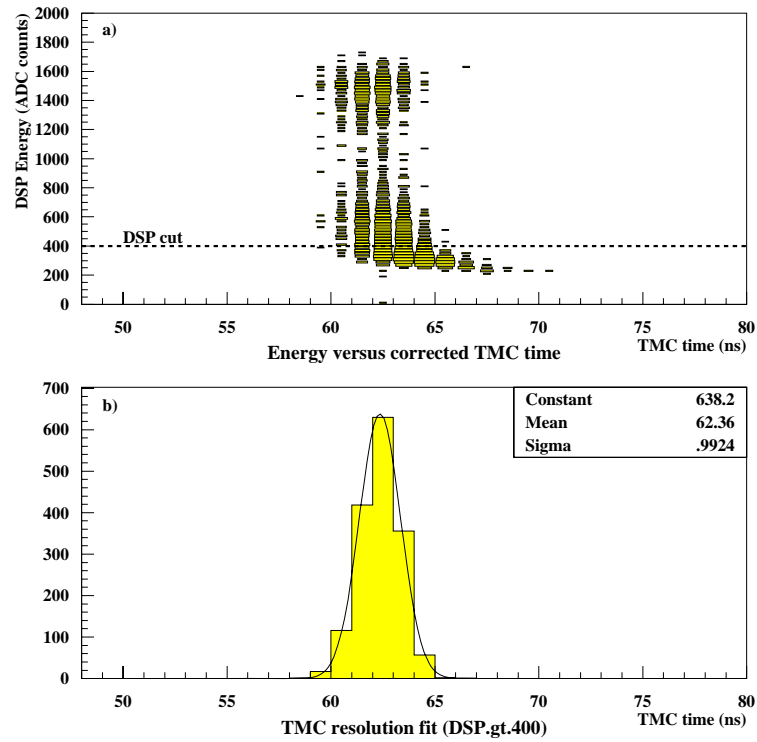


Figure 5.6: *a) Energy-time correlation and b) resolution fit for one TDC channel. The DSP energy cut is shown.*

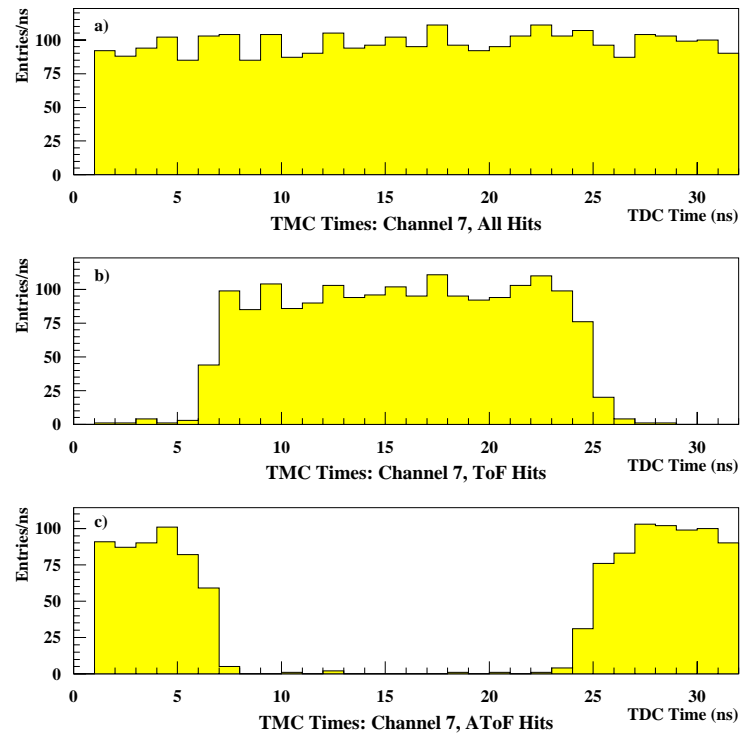


Figure 5.7: *Raw TDC time distributions for ToF/AToF selections: a) all triggers, b) ToF triggers only, c) AToF triggers only.*

this in quadrature gives an estimated resolution for the TDC system of $\sigma_t \simeq 0.7$ ns, which also includes the inherent resolution of the calorimeter and electronics, but indicates that the desired resolution is achievable.

Since the TDC system plays an important role in the setting of the ToF window, a check was performed on the alignment of the window with the active TMC cycle. For this analysis, no HCLK correction of the TDC times was made; this removes the correlation between the TDC measurement and the beam timing and should have the effect of filling the TMC window with a uniform distribution of events. In the early beam tests the IET trigger was not fully functional, so the discrimination between ToF and AToF events was made using the energy sums, by cutting on the following quantity:

$$S = \frac{\Sigma_{\text{ToF}} - \Sigma_{\text{AToF}}}{\Sigma_{\text{ToF}} + \Sigma_{\text{AToF}}} \quad (5.7)$$

The cut was made at $S = -0.8$, with events having values greater than this classed as ToF (in the final implementation, when the ToF and AToF summations are correctly calibrated, the cut is at $S = 0$). Figure 5.7 shows the raw TDC distributions for all hits, and for ToF and AToF only hits. The extent of the ToF window can clearly be seen, correctly aligned and well contained with the active TMC cycle. The edges of the window are smeared by the time slew effect and dispersion in the position of the ToF windows for the cells which entered into the energy sums.

For the final test beam period in October 1994, more advanced versions of the electronics were available for testing. The TDC system was populated with prototype version of the SCM and THM, allowing the DSP readout and histogramming functions to be tested. In the ANBX, 32 channels were equipped with the final design of the CFD, allowing TDC measurement for two of the EM supermodules under test. The HAD section was not connected to the TDC system.

The HCLK TDC module was replaced with one capable of measuring times to $\simeq 100$ ps precision. In order to use data from this to correct the TDC times in the manner described above, it was first necessary to calibrate the module to extract the appropriate step size. A set of runs were taken with increasing delay between the start and stop inputs of the TDC (corresponding to the beam trigger and HCLK signal), and the mean values of the HCLK times in these runs fitted with a straight line as a function of delay, yielding the factor by which the HCLK TDC raw data must be divided to give correct times. The correction factor was found to be 13.22; this was confirmed by measuring the TDC resolution as a function of this value, the results of which are shown in Figure 5.8, where it can be seen that the TDC resolution is optimised by this choice; values greater or less than this have

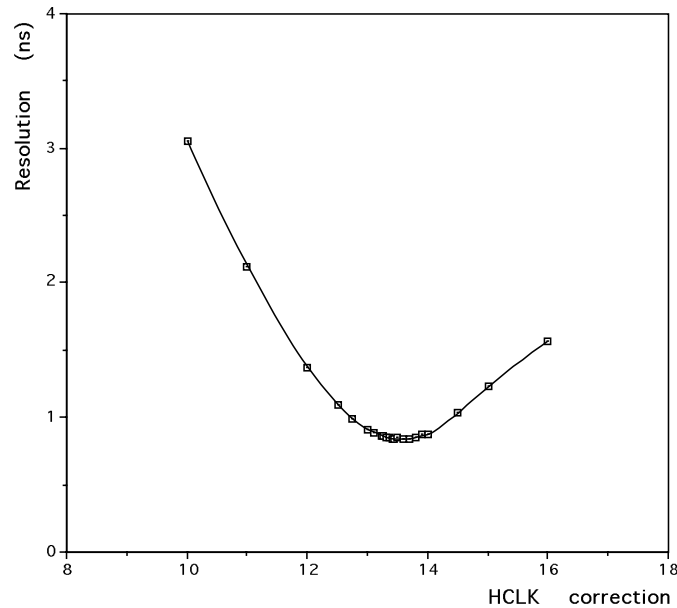


Figure 5.8: *TDC resolution dependence as a function of the HCLK correction factor.*

the effect of de-correlating the HCLK and TDC times, thus degrading the measured TDC resolution.

Data were taken at a number of beam energies, providing the opportunity for extensive testing of the TDC system. The resolution has been measured for runs with mixed beams at energies of 2, 4 and 7 GeV, as shown in Figure 5.9. The energy versus time scatter plots show that the performance of the CFD was significantly improved over earlier tests, with only a small amount of trigger walk at very low pulse heights. The resolution histograms were made without DSP energy cuts and have bin widths of 0.1 ns, reflecting the increased precision of the HCLK TDC measurement. Gaussian fits to the resolution plots are shown and yield a typical resolution of $\sigma_t = 0.8$ ns, demonstrating that the specified resolution can be achieved. These results, and detailed investigations of the acquired TDC data, indicated that the DSP readout was also functioning correctly.

The histogramming function of the THM was also tested, with the data being processed by a prototype development of the online software, described in Section 4.4.3. Figure 5.10 shows two histograms created during the test runs, with definition bits generated from a limited number of trigger elements received from the IET processor. Since there was no correction made online to the HCLK time digitisation, the unbiased histogram shows the expected flat distribution across the active TMC window. The requirement of an IET trigger shows a distribution consistent with the ToF window configured with this run

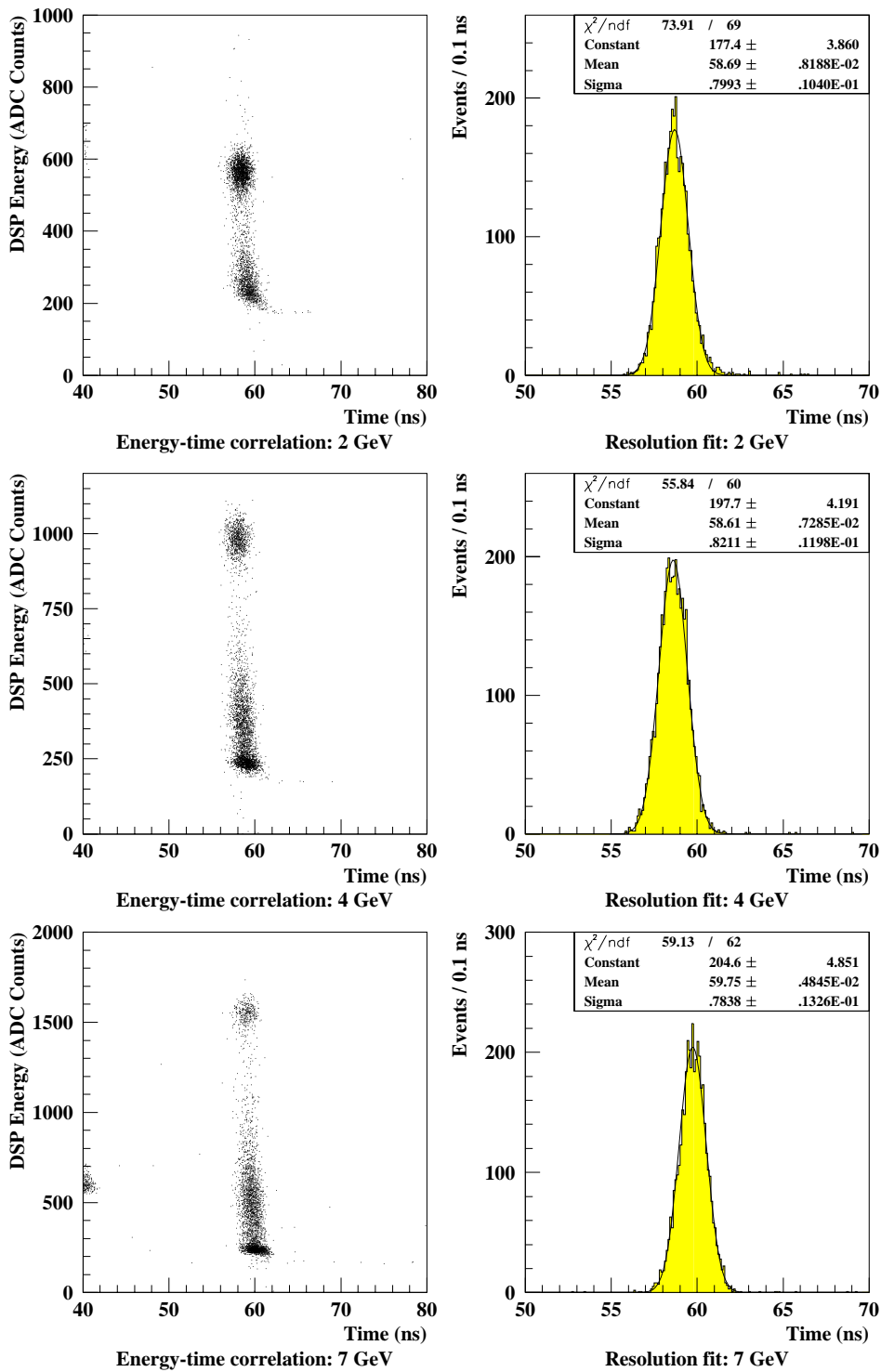


Figure 5.9: TDC energy-time correlations and resolution fits for beam energies of 2, 4 and 7 GeV. The hits in the 7 GeV correlation plot at $t = 40$ ns are from the LED calibration system. The mean times are arbitrary.

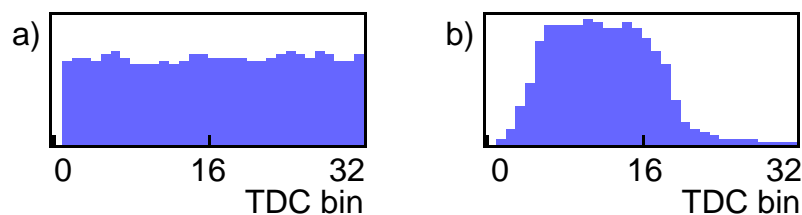


Figure 5.10: *Online histograms from a beam test run for a) unbiased events and b) with an IET trigger bit required.*

which was 14 ns wide, starting at a TDC time of 5 ns. These results indicated that the basic operation of the histogramming logic was correct.

In summary, the test beam results demonstrated that the SPACAL TDC system is capable of delivering the desired performance. The timing resolution measured during the tests of $\sigma_t \simeq 0.8$ ns, including contributions from the calorimeter and front-end electronics, exceeds the design criteria by a significant margin and indicates that the TMC1004 was an appropriate choice of device. The data acquisition and monitoring aspects of the system were also shown to function correctly, with the latter showing the feasibility of using the SPACAL trigger information for producing unbiased histograms of TDC data from as many bunch crossings as possible.

5.8 Commissioning and use of the TDC System in H1

The TDC system was installed, with the SPACAL calorimeter and electronics, into H1 during the Winter 1994/95 shutdown. During the time leading up to luminosity running extensive tests were performed to ensure that the modules were correctly functioning after transit, and to verify the integrity of the signal paths from the front-end electronics. Integration of the TDC system into the warm-start and DAQ systems of the calorimeter was also tested; the DSP readout was verified by loading the TMCs and spy memory with test patterns and analysing the resulting data.

The first stable beams of the 1995 run were used to time the TDC system in. This procedure had two stages; first the TMC active window had to be adjusted to contain the full distribution from background and interactions, then the DSP readout was aligned with the correct bunch crossing. The first step was achieved by adjustment of the SCM clock delay and THM WSTART sequence, as discussed in Section 4.4.2. The results of these adjustments were observed using the online monitoring and later verified in the offline

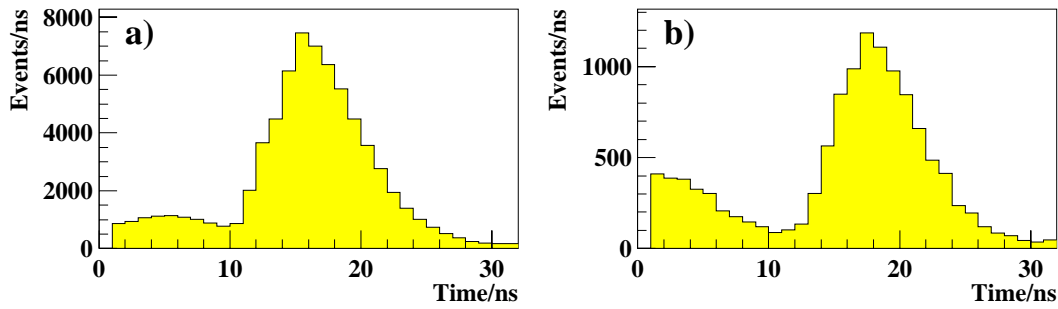


Figure 5.11: *Raw timing distributions from the SRTE bank for a) all EM channels and b) all HAD channels, showing the correct alignment of the TMC active window around the interaction peak.*

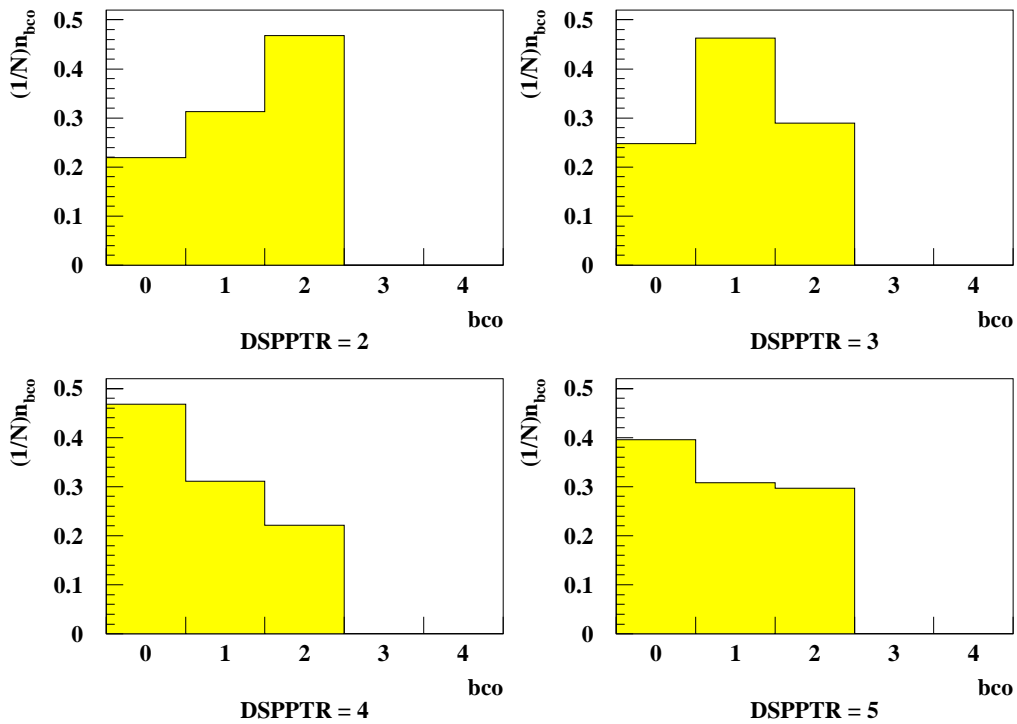


Figure 5.12: *Fraction of SRTE time hits per bunch crossing, for four DSPPTR values. For DSPPTR=3, more hits are in the central bunch crossing indicating correct alignment of the DSP readout with the TDC data.*

data. The HAD section has a broader distribution of times, with an earlier background peak, than that from the EM cells. In order to contain fully the interaction peak from both sections it was therefore necessary to sacrifice the leading edge of the background in the window alignment for HAD cells. This setup can be seen in Figure 5.11, which shows SRTE times for cells in each section. It should be noted that the background is suppressed relative to the interaction peak since these data are for triggered, and therefore predominantly ToF validated, events.

The second step in the setup procedure was to align the DSP readout with the bunch containing the correct TDC data for the triggered event. This was done by taking a series of CDAQ runs with SPACAL triggers during stable beam time, with the DSPPTR value incremented for each run. The TDC input rate per channel is significantly lower than the bunch crossing rate, so events triggered by the SPACAL processor have on average a larger number of cells hit than other events. One would therefore expect to see more TDC data in the central bunch crossing of the three read out when the DSPPTR value is correct. This is shown in Figure 5.12 where the fraction of hits per bunch crossing is plotted for four DSPPTR values. It can be seen that for a value of 3, there are more hits in the central bunch crossing ($BCO = 1$) than the other two. For DSPPTR values of 2 and 4 there are more hits in the later and earlier bunch crossings respectively, which is consistent with the observation that the correct value is 3. This indicates that the time between the input signal arriving at the TDC system and the THM pipelines being frozen is 29 bunch crossings, or $2.8 \mu\text{s}$, which was confirmed by a manual measurement of signals on a THM.

In order to produce online histograms classified by SPACAL trigger decision it was first necessary to define the histogram classifications used to generate the LUT load (described in Section 4.4.1). This was done in such a way as to allow individual elements to form histogram definitions independent of the others. A global histogram for all trigger patterns was also included. The alignment with the trigger information sent directly from the SPACAL trigger processor was achieved by setting the histogram read pointer to various values. This sets the TMC internal pointer for the time that the pipelines are enabled, and hence can be used to adjust which bunch crossing appears on the TMC output, and therefore to align the data with the correct trigger information. When the pointer is correct and the data match the trigger, there is a clear correlation between histogram type and content. The histograms were observed for each setting, until the expected correlation was observed, especially an unambiguous separation between different definitions. Figure 5.13 shows typical output from the monitoring; for a single EM cell, global, AToF and ToF classified histograms are shown, and summary plots of all cells in the EM section for ToF and AToF histogram sums. These show a clear isolation of the two types

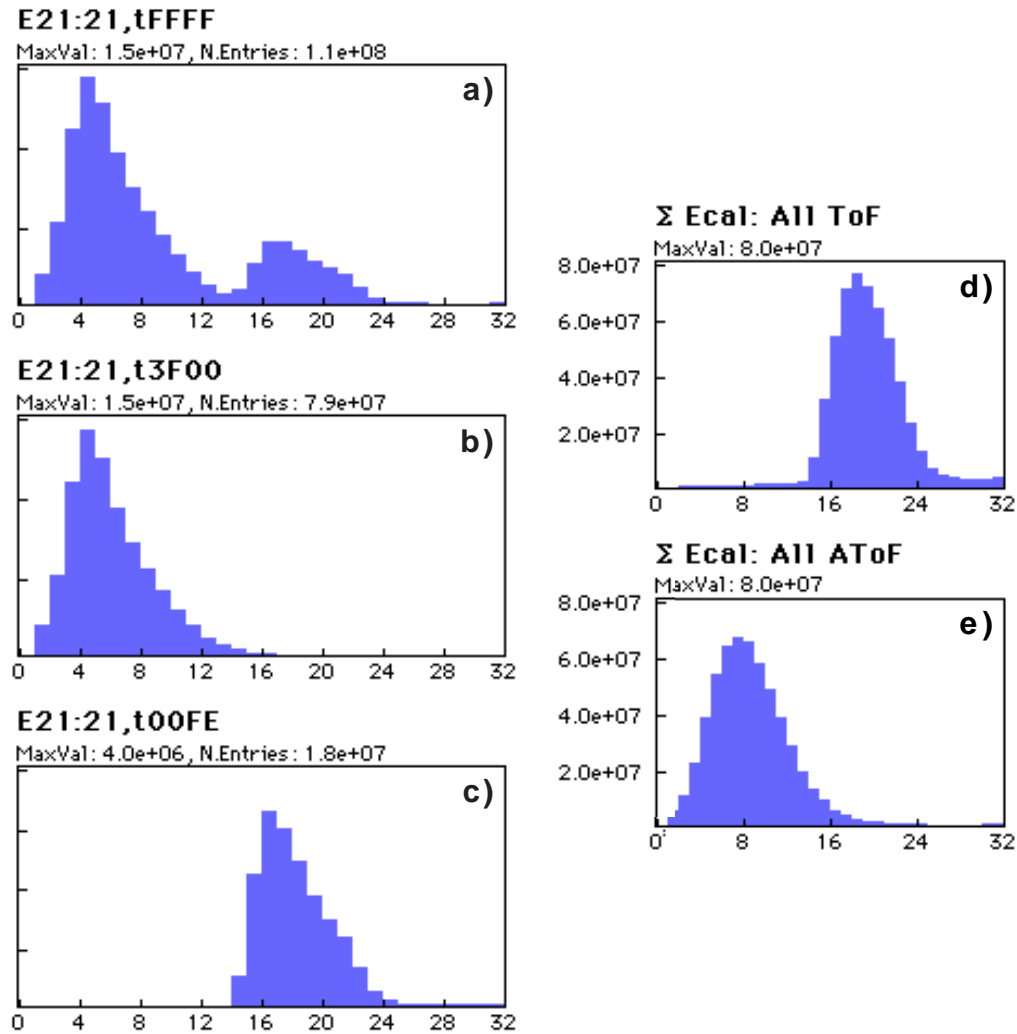


Figure 5.13: Online TDC histograms from luminosity running. For one EM cell: a) global histogram, b) AToF only, c) ToF only. Global summaries for all EM cells: d) all ToF trigger definitions and e) all AToF.

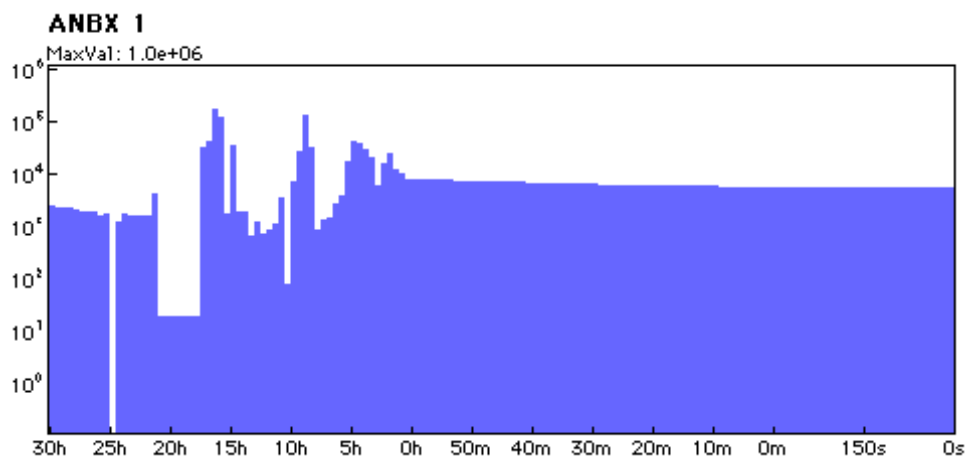


Figure 5.14: Rate history for all cells in one ANBX during luminosity running, showing varying rates during to injection and luminosity fills. Note that the time scale is compressed in three stages.

of events, indicating both the TDC system and the trigger to be correctly configured. It can be seen that this information can be readily used to identify channels with a bad ToF window setup, where events from the interaction peak appear in histograms classified as background and vice versa.

The rate information derived from the THM scalers has also proven to be very useful in the setup and monitoring of SPACAL. Figure 5.14 shows a history plot of the rate in all cells of one ANBX during luminosity running. Note that the time scale is compressed twice across the plot; from right to left the past five minutes are shown, then the last hour, then the last 30 hours. Peaks in the distribution corresponding to beam injection and periods of bad background can clearly be seen as can the gradual decrease in rate during a luminosity fill as the beam currents decay. In addition to providing this sort of information which is useful to the shift crew, the scalers are also used by the SPACAL OS9 system during an automated procedure to determine optimal CFD thresholds. The CFD threshold is ramped down in steps, and the rate determined at each; once the noise floor is reached there is a marked increase in rate. The noise level for each channel can be rapidly determined in this manner and used to set the threshold accordingly.

Offline data generated by the TDC system were also used in the setup and monitoring of both the TDC system and SPACAL as a whole. Such analysis can take advantage of the data generated by the energy readout for both beam and LED system events to derive useful information. One of the primary tasks during the commissioning of SPACAL was to identify noisy or dead channels. While the TDC rate information alone provides an initial indication of such problems, precise location of the fault requires more investigation. Given the large number of channels and the limited access to the analogue electronics, this type of work is vital.

Figure 5.15 shows the number of hits per channel for one luminosity run as a function of geometric channel number, derived from the energy and time banks; this is simply a count of how frequently a given channel appears in the SNGR and STER banks. The plots shows an overall structure which decreases with increasing channel number, repeating at $N_{geom} \simeq 1200$ for the hadronic section, which reflects the spiral geometry of the numbering scheme and the SPACAL rate which has a strong radial dependence. The periodic structure overlaid on this is due to the fact that the spiral actually follows the square shape of the cells, and so sweeps in and out of regions of equal rate as it rotates around the calorimeter. In the energy data derived plot a small number of channels can be seen with reduced or zero hits; these can be attributed to problems with the PMT, HV, cabling or ADC/DSP readout. In the timing data plot, there are more channels. Some have reduced rate which was found to be due to an excessive CFD threshold. The channels which are completely

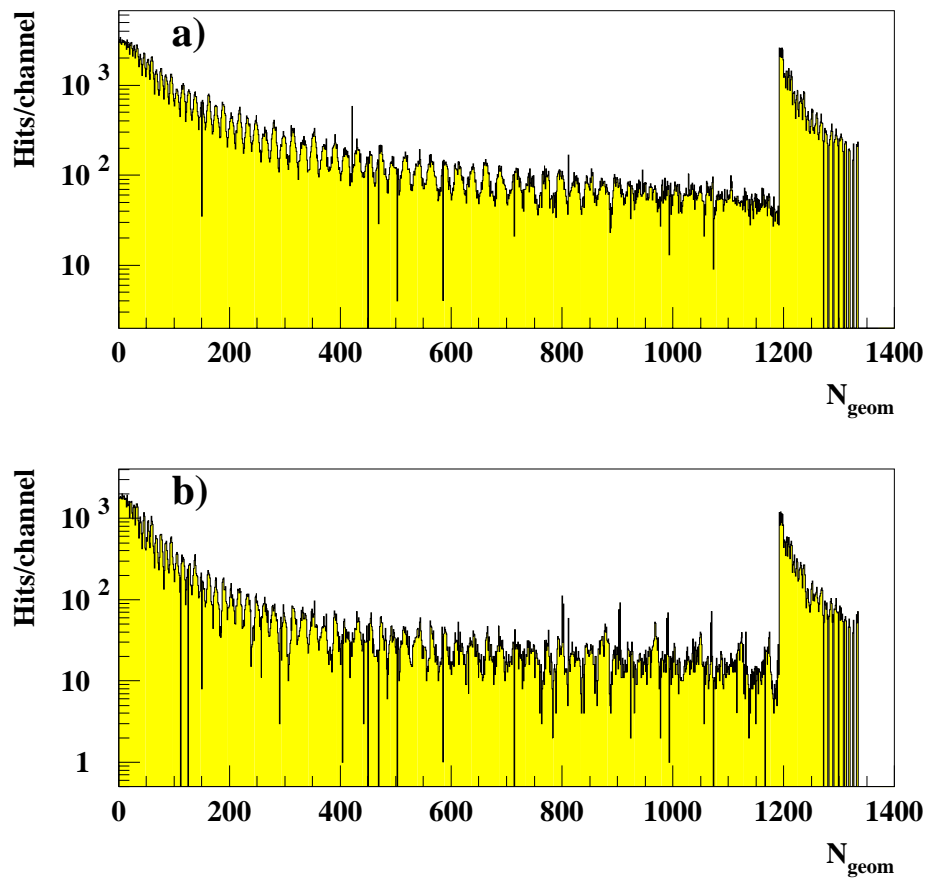


Figure 5.15: *SPACAL* activity as a function of geometrical channel number derived from a) energy and b) timing data banks.

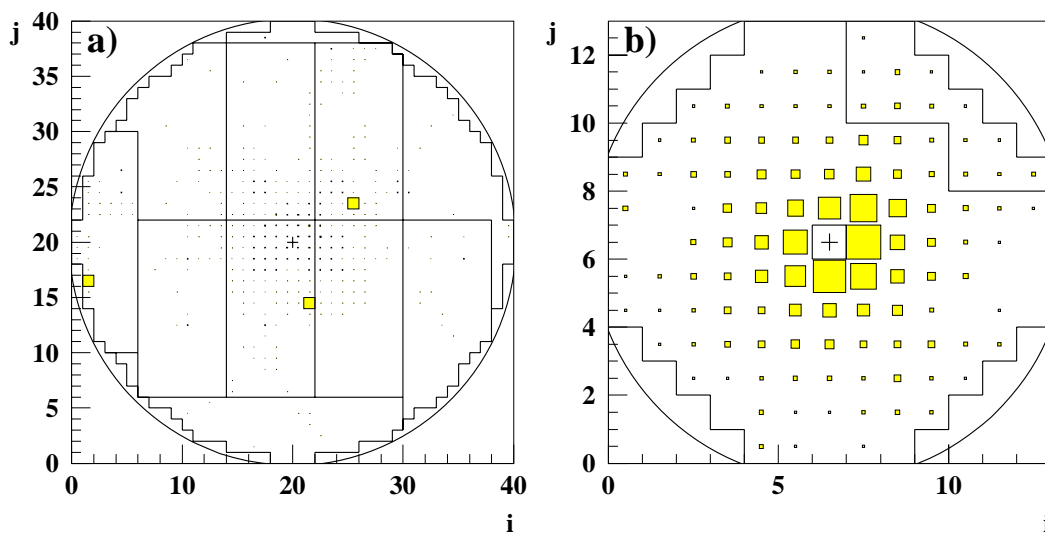


Figure 5.16: *Hit maps* from the *SNPU* pile-up bank for a) *EM* and b) *HAD SPACAL* sections. The size of the box in each cell indicates the number of entries.

dead were investigated further; a number were due to faults in the FEC or CFD and fixed during access time. Three EM channels were found to have no activity in the TDC system, but appeared on each event in the SNPU bank. This was detected using hit maps of the type shown in Figure 5.16, which shows the number of SNPU entries in one run, mapped out for each SPACAL section. It can be seen that in the EM section three channels dominate the plot (large boxes) whereas in the HAD map, no channel is dominant and the distribution of hits reflects the random occurrence of pile-up events. This indicated that the TDC input of the three cells was high before each triggered event, and was traced to a failure in the driver circuitry which feeds the CFD output to the TDC system.

The CFDs play a dual role in SPACAL; they provide discriminated signals for the TDC system and also, by validating the ToF/AToF decision, have a direct influence on the trigger performance. Determination of the optimal setting is therefore a compromise between TDC input efficiency and trigger rate. In order to assess the effect of the CFD thresholds on the TDC system, it is necessary compare timing data with information from the energy readout, which is independent of the CFD. Figure 5.17 a) and b) show energy spectra from the SE0R bank for EM and HAD channels without (shaded histogram) and with (points) the requirement of a matched time present in the STER bank. The sharp lower edge in the distributions is the result of the noise cut applied to SPACAL data at 15 MeV. The effect of the CFD threshold can clearly be seen in the STER matched points where the number of hits relative to the full SE0R distribution is reduced below an energy of about 70 MeV. The ratio of the two distributions for each section is therefore a measure of the TDC input efficiency and is shown in Figure 5.17 c) and d) for each section. This is effectively due to the average CFD threshold behaviour for each section but also contains potential contributions from other losses in the system, such as bad channels or hits outside the TMC active window. The width of the transition in each plot, and the non-zero efficiency below threshold is due to dispersion in the setting of the CFD thresholds. The efficiency above threshold is typically 90% (80%) for the EM (HAD) section, and the ratio of the number of hits in the matched to non-matched distributions for each section, which is a measure of the acceptance of the TDC system for the total energy spectrum in SPACAL, was found to be 39% (37%). These figures can clearly be improved by lowering thresholds, but at the expense of increased trigger rates, and so were deemed to be acceptable.

An investigation into the trigger walk behaviour of the CFDs was also made; the effect can be seen in Figure 5.18 which shows SPACAL SE0R energies versus STER times for EM and HAD channels. A two band structure is observed, with the earlier arising from residual AToF activity left in triggered events. Below 1 GeV, there is significant slewing in

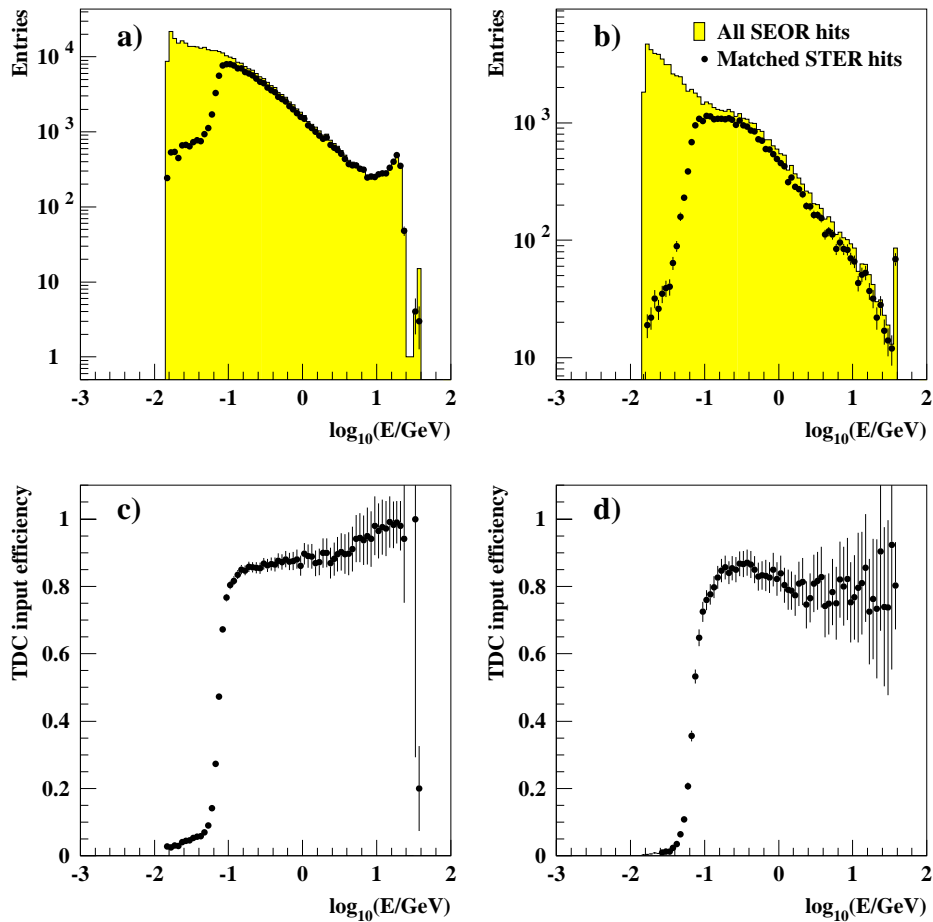


Figure 5.17: *SPACAL* energy spectra and TDC input efficiency: SEOR energy spectra without and with matched STER time for a) EM and b) HAD channels. The ratio of the two is a measure of the TDC input efficiency and is shown for c) EM and d) HAD sections..

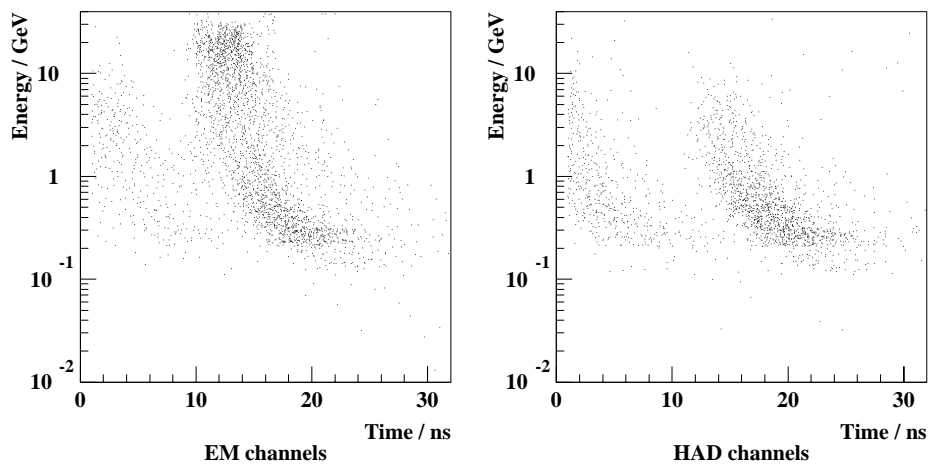


Figure 5.18: *SPACAL* energy versus time plots for a) EM and b) HAD sections, showing the effect of trigger walk at low energies.

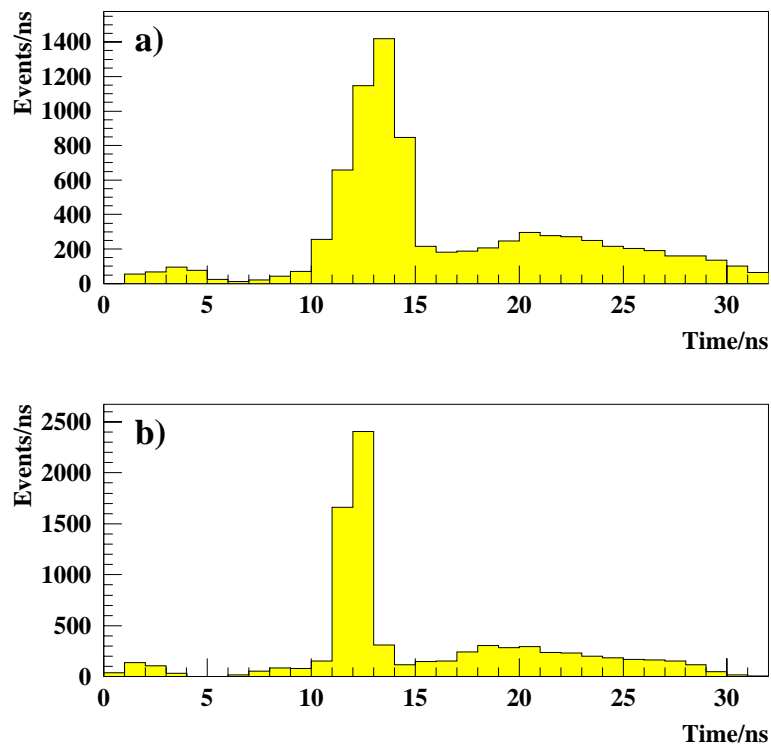


Figure 5.19: *Effect of offset correction of TDC data: time spectrum for EM cells a) before and b) after application of offsets. A cut at 0.9 GeV is applied to the data.*

the time distribution due to trigger walk, causing the times to be delayed by up to 8 ns with respect to the nominal time. This is contrary to the observations made at the final beam tests, discussed in Section 5.7, due to the difference in particle energy spectra created in the CERN PS and HERA beams. At the PS, there was no energy below the MIP peak, the thresholds were set very low and so the slew effect occurred in region of no activity and was hence not significant. At H1, where the spectrum reaches down to much lower energies and the thresholds have to be set higher to manage the rate, the effect is clearly observable. The slew can also be seen in the online histograms shown in Figure 5.13, where the single channel AToF and ToF peaks, expected to be Gaussian from the beam structure and intrinsic resolution of the timing measurement, in fact have a skewed upper tail arising from low energy deposits. This effect sets a serious performance limitation on the TDC system, especially online where energy data are not available to correct the times. Offline, there is the prospect of characterising the slew curve of each channel and, using the matched energy, correcting the time. However, this analysis requires the accumulation of large statistics for each channel, and was not performed for 1995 data. The use of TDC data is therefore limited in typical physics analyses to the selection of electrons by, in addition to other cuts, discrimination on the basis of the time in the most energetic cell of the candidate cluster.

As discussed in Section 4.4.4, the TDC reconstruction allows the possibility of correcting data offline to account for the time dispersion in each channel. This correction takes the form of offsets, and is generated by measuring the mean time of the interaction peak in each channel, and deriving a constant to shift them to the same value [99]. For 1995 data, this was done for the innermost 500 cells of the EM section; the remainder were not analysed due to lack of statistics. The effect of applying the corrections can be seen in Figure 5.19, which shows the TDC spectrum for EM channels before and after correction. In order to remove the effect of slew from the CFD trigger walk, a cut was applied to the cell energy at 0.9 GeV. The dominant interaction peak can be seen in each plot, with smaller contributions from residual AToF energy (at $t < 5$ ns) and from the late satellite bunch ($t > \sim 20$ ns), which was large in the run investigated here. A significant reduction in width of the peak can be seen after correction, from approximately 1.3 ns to 0.7 ns, indicating that this is a useful method, and showing the typical distribution which can be cut on in selection of SPACAL-based physics.

Chapter 6

Event Reconstruction and Selection

This chapter describes the selection of DIS and diffractive events used for the analysis presented in this thesis. The reconstruction of the kinematic variables and the energy calibration of SPACAL, which is vital to keep systematic errors on the measurement under control, are discussed. The criteria applied to select appropriate runs and DIS and diffractive candidate event samples are discussed. A comparison of the data with the Monte Carlo models used in this analysis is presented.

6.1 Reconstruction of Kinematic Variables

The kinematic variables Q^2 , y and x , defined in Section 1.1.2, can be expressed in terms of the four vectors of the scattered electron¹ or the hadronic final state. Since both are in principle well measured at H1, it is possible to reconstruct the event kinematics using either, or a combination of the two. A number of methods have been investigated which are designed to optimise the resolution of x and Q^2 and are discussed in detail in [100]. For the purposes of this analysis, the electron and sigma methods have been used; these provide complementary measurements, the advantages of which are discussed below.

The electron method calculates the kinematic variables solely from the initial electron energy, E , and the energy, E' , and polar angle, θ_e , of the scattered electron, giving:

$$y_e = 1 - \frac{E'}{E} \sin^2 \frac{\theta_e}{2} \quad (6.1)$$

$$Q_e^2 = 4EE' \cos^2 \frac{\theta_e}{2} \quad (6.2)$$

¹Throughout 1995 HERA collided positrons and protons; the term electron is therefore used generically.

$$x_e = \frac{Q_e^2}{sy_e} \quad (6.3)$$

where s is the square of the centre of mass energy. This method has the advantage of being experimentally simple and independent of any assumptions regarding the hadronic final state. Good resolution in Q_e^2 is obtainable over the region of interest. The resolution in y_e is good at high values but degrades rapidly with decreasing y_e due to the $(1 - y_e)/y_e$ term in the propagation of the error:

$$\frac{dy_e}{y_e} = \frac{1 - y_e}{y_e} \left(\frac{dE'}{E'} \oplus \frac{d\theta}{\tan \theta/2} \right) \quad (6.4)$$

In order to reduce smearing at low y to an acceptable level the energy resolution is required to be typically better than 2%. An important source of error in the measurement of structure functions is the energy scale of the calorimeter which measures the final state electron energy. A 1% systematic error in the energy calibration generates a shift in the differential cross section rising as the inverse power of y which is 10% at $y \simeq 0.1$. Similarly, the θ_e resolution is required to be approximately 1 mrad in order to control smearing.

At high y the electron method is sensitive to contributions from initial state QED radiation (ISR), which modify the incoming electron energy entering into the calculation. This leads to the need for large radiative corrections to the measured cross section. The implementation of these corrections in this analysis is discussed in Section 7.2.

The sigma method [101] addresses these difficulties by combining electron and hadronic final state information in such a way as to improve the resolution at low y while reducing sensitivity to ISR at high y . The initial electron energy E is replaced by E_{rec} , determined from the complete final state. From energy-momentum conservation the following can be written:

$$\begin{aligned} 2E_{rec} &= \sum_h (E_h - p_{z,h}) + (E' - p_{z,e}) \\ &= \Sigma + E'(1 - \cos \theta_e) \end{aligned} \quad (6.5)$$

where $\Sigma = \sum_h (E_h - p_{z,h})$ is a summation over all reconstructed hadrons. The quantity Σ has the advantage of being insensitive to losses of the hadronic final state in the forward ($+z$) beam pipe direction, where the values of $E_h - p_{zh}$ are small. Substituting E_{rec} for E in equations 6.1 - 6.2 gives the following expressions for the kinematic variables:

$$y_\Sigma = \frac{\Sigma}{\Sigma + E'(1 - \cos \theta_e)} \quad (6.6)$$

$$Q_\Sigma^2 = \frac{E'^2 \sin^2 \theta_e}{1 - y_\Sigma} \quad (6.7)$$

$$x_\Sigma = \frac{Q_\Sigma^2}{sy_\Sigma} \quad (6.8)$$

The error of y_Σ is therefore

$$\frac{dy_\Sigma}{y_\Sigma} = (1 - y_\Sigma) \left(\frac{d\Sigma}{\Sigma} \oplus \frac{dE'}{E'} \oplus \frac{d\theta}{\tan \theta/2} \right) \quad (6.9)$$

which avoids the divergence at low y . At high y the error is, in principle, reduced by the term $(1 - y_\Sigma)$, but in this region it is dominated by the experimental uncertainty in the measurement of Σ .

The sigma method is less sensitive to ISR since the radiated photon, which is generally lost down the beam pipe, does not enter into the calculation. E_{rec} is therefore closer to the energy of the electron which interacts with the proton and the calculated Q^2 and y better reflect the ‘true’ values. This leads to a reduction in the overall radiative corrections required, from typically 20% for the electron method in region of high y , to typically 3% for the sigma method.

The variables β and x_p which are used in measurements of diffractive DIS (see Section 2.3.1) are determined from the variables described above and from the invariant mass, M_x , of the hadronic component of the final state observed in the main detector components. M_x is calculated from the four-momentum of this system, determined from the energy of active cells in the LAr and SPACAL calorimeters, as

$$M_x^2 = E_{had}^2 - \mathbf{p}_{had}^2. \quad (6.10)$$

Where the momentum transfer at the proton vertex, t , is small compared to Q^2 , β may be reconstructed using

$$\beta \simeq \frac{Q^2}{Q^2 + M_x^2} \quad (6.11)$$

and x_p is then calculated using the relation

$$x_p = \frac{x}{\beta}. \quad (6.12)$$

6.2 Calibration of SPACAL

From the discussion on kinematic variable reconstruction, it can be seen that a precise knowledge of the energy scale is required for the measurement of the scattered electron. For the low Q^2 region of DIS, the electron is detected in SPACAL and therefore a considerable effort was made to provide a good calibration of this detector.

The primary step in the calibration of SPACAL was achieved by adjustment of the high voltage settings to equalise the gain of the cells [102] using data taken during the initial

running period of 1995. The corrections to the HV were derived from analysis of photo-electron statistics and from the MIP signature of cosmic muons passing vertically through the detector [103], giving a coarse, initial cell-to-cell equalisation of approximately 15%.

As discussed in Section 4.1, LED pulses generated by the CAM system were used to monitor short-term variations in the photomultiplier gains due to, for example, temperature fluctuations. Corrections derived from the LED events were stored in the H1 database and used in the reconstruction of SPACAL energies. The LED calibration gives an arbitrary energy scale which is, in principle, constant in time. Since the LED system feeds pulses into the light-mixers of each cell, this calibration is not sensitive to aging effects in the active regions of SPACAL. For 1995 nominal vertex data, this effect was investigated and corrected for offline, using the results of the improved calibration described below. The 1995 shifted vertex data, taken at the end of the running period, showed no such time dependence.

It was then necessary to determine an equalisation more accurate than that provided by the initial HV adjustment described above. This was done with the kinematic peak (KP) methods which offered the best potential for a precise calibration. The single-cell KP method [104] required at least $2/3$ of the energy of a cluster in the kinematic peak to be in one cell. The mean energy in the peak region of the resulting energy distribution was compared with that found in Monte Carlo samples to derive a calibration constant for each cell. An alternative method [105] was also used, in which constants for the cells in a 4×4 sliding window (which fully contains the electron cluster) are simultaneously determined by a maximum log-likelihood fit to a parameterisation of the shape of the peak determined from Monte Carlo. The final constants used for the 1995 calibration were derived from the former method, since the latter is more complex and required more development time. KP methods work well, but are strongly limited by the $1/Q^4$ behaviour of the DIS cross section, which reduces the statistics available in the outer regions of SPACAL. For the 1995 run, the data sample size limited KP calibration to the cells within a radius of 35 cm about the beam axis, for which a spread in relative equalisation of less than 1% was achieved. In the outer region and for the HAD section, where there is no kinematic peak, the MIP signatures from cosmics and beam halo muons were used, giving an equalisation to within 3%. In the inner region of the EM section, the relative scales of the two methods were checked and found to agree to within errors.

The KP method is not optimal for a determination of the absolute energy scale, since it is dependent on Monte Carlo simulations to correct for effects such as dead material. The absolute scale was therefore determined with a method which is less sensitive to these effects, using QED Compton events [106, 107], $e + p \rightarrow e + \gamma + X$, in which the

electron and photon are detected in SPACAL and the hadronic final state or elastic proton X , which has very small transverse momentum, remains in the beam pipe and therefore escapes detection. The energies in the electron and photon cluster are constrained to a high degree of accuracy to sum to the incoming electron beam energy, and the expected energies can also be calculated from the polar angles of the clusters. It was therefore possible to derive the absolute energy scale from this method, the error on which was determined to be 1%.

Additional calibration methods have been used to validate the above procedure. A log-likelihood procedure similar to that used for the KP method was used to determine calibration constants from the π^0 peak. This method is useful because the π^0 is produced in abundance in photoproduction, has a well determined mass, and provides a low-energy cross check of the calibration determined at the kinematic peak. At the same time, it is less useful for providing a calibration suitable for application to high energy electrons.

The absolute scale for hadrons in SPACAL was determined by adjusting the energy spectrum for data after calibration to that of Monte Carlo [108]. The uncertainty in this scale has been determined to be 7%.

6.3 Final Electron Energy Reconstruction

A detailed analysis of the kinematic peak position was used to investigate the homogeneity of response in the inner region of EM SPACAL. This showed fluctuations in response of 4–5% in the cracks between the main body of SPACAL and the insert (which is a separate construction). A correction map for this has been determined using a 5 mm grid, leading to a corrected overall homogeneity in the inner region of better than 2%.

6.4 Monte Carlo Models

In this analysis, non-diffractive neutral and charged current DIS events were modelled using the DJANGO [109] generator, which is based on HERACLES [110] for effects from QED radiation, and LEPTO [111] for simulation of the hadronic final state. The input structure function was a parameterisation of the GRV94 parton distributions [112]. The sample used corresponded to an integrated luminosity of 218.23 nb^{-1} , approximately twice the size of the data sample.

The photoproduction background was modelled with the PHOJET [113] generator, in

which the total cross section is parameterised in terms of a superposition of pomeron and reggeon components. A sample corresponding to an integrated luminosity of 304.20 nb^{-1} was used. The PHOJET sample was tuned by comparison with a sample of tagged photoproduction events where a cluster faking and electron in SPACAL was observed [13]. The energy spectra of the electron tagger and of the leading SPACAL cluster (faked electron) were found to be in good agreement.

Diffractive DIS events were simulated using RAPGAP [114]. This generator uses a perturbative model of diffractive hard scattering in which the pomeron has a partonic substructure. Standard DIS, QED-Compton and boson-gluon fusion subprocesses are also included. Higher order QED radiative processes are included in RAPGAP using HERACLES. Fragmentation to create the hadronic final state is provided by either matrix elements and parton showers (MEPS) as in LEPTO, or via the colour dipole model (CDM) implemented in ARIADNE [115]; in this analysis the MEPS option was used. The input structure function was derived from the parameterisation of the phenomenological fit to the 1994 $F_2^{D(3)}$ measurement, described in Section 2.4. The integrated luminosity of the sample employed for this analysis was 905.36 nb^{-1} (eight times the data sample size).

Simulation of the detector response was performed with the GEANT program [116]. The Monte Carlo samples were reconstructed and analysed using the same chain as was employed for the data.

6.5 Run Selection

The data sample used for this analysis was the 1995 shifted vertex (SVX) data, where the collision point of the electron and proton beams within the detector is moved. With the nominal vertex shifted to +70 cm, the angular acceptance of SPACAL is extended to $\theta < 178.5^\circ$, enabling detection of DIS electrons down to $Q^2 \simeq 0.3 \text{ GeV}^2$. During this period of data taking the SPACAL readout was fully operational, and the IET trigger settings and prescales stable.

Runs selected for analysis during the SVX period were recorded in trigger phase 2, in which beam conditions were sufficiently good for all relevant subdetector high voltages to be on, and for the appropriate subtriggers to operate with little or no prescale. Several indicators of data quality were also examined for each run in the period. The number of events per unit of integrated luminosity should be relatively stable over time; a significant deviation (more than 3σ) from the nominal value indicates problems with triggering or data acquisition, and a number of runs were rejected on this basis [117]. The position of

the kinematic peak for SPACAL electrons was also monitored; a number of runs where the peak was shifted due to a high voltage or readout fault were rejected [118]. A total of 79 runs passed all criteria, giving an event sample with an integrated luminosity of 121.2 nb^{-1} .

6.6 DIS Event Selection

The primary selection of DIS events in this analysis was made on the hypothesis that the highest energy cluster in the SPACAL EM section, in coincidence with a matching BDC track, was the scattered electron. Additional selection criteria, or cuts, were imposed to enhance the purity of the DIS sample by rejecting backgrounds originating largely from photoproduction events and beam-gas/beam-wall interactions.

The BDC track associated with the cluster was determined in the following way. A straight line was extrapolated from the event vertex through each BDC track, onto the z coordinate of the cluster. The track with the smallest distance from the extrapolation to the cluster barycentre in the xy plane was then considered to be a match. For electron candidates of high enough energy to be of interest in this analysis, the curvature of tracks in the magnetic field is sufficiently small for the linear track extrapolation to be a good approximation to the true path. The coordinates of the matched track in the cluster plane were then used for any calculations requiring the cluster position. In addition to providing a good spatial reconstruction, the requirement of a track also has the advantage of reducing the photoproduction background in which a π^0 fakes an electron in SPACAL but leaves no track in the BDC.

The cuts applied to select DIS candidate events are listed below. An acronym is given for each for the sake of future brevity.

- **TRIG:** subtrigger ST0 requirement; SPACAL IET threshold 2 trigger (4 GeV) in anti-coincidence with BToF and FToF veto conditions. This is a loose selection of a high energy cluster. The prescale of ST0 during the shifted vertex running was one, making this subtrigger particularly suitable.
- **ECLU:** energy of cluster, $E_{clus} > 8 \text{ GeV}$. This cut rejects low-energy clusters from beam-induced events, and suppresses a significant amount of the photoproduction background, as shown in Figure 6.1a. Monte Carlo studies have shown that above this energy, the probability of the hypothesis that the highest energy cluster is the

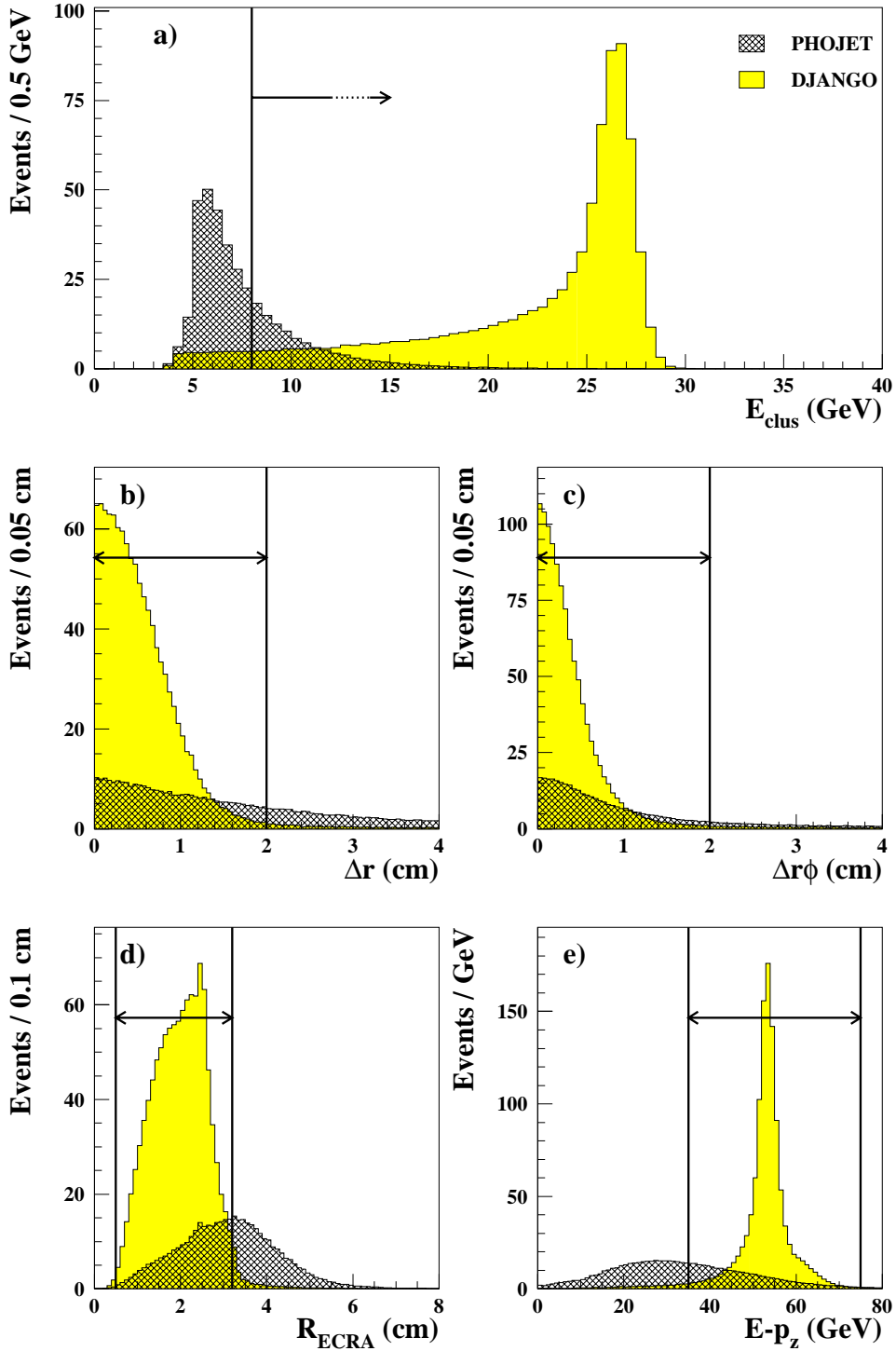


Figure 6.1: *DJANGO* (DIS) and *PHOJET* (γp) comparisons for DIS selection criteria: a) energy of electron candidate (E_{CLU} cut), b) Δr and c) $\Delta r\phi$ (DBDC), d) cluster radius ($ECRA$) and e) $\sum(E - p_z)$ (EMPZ). The regions selected for DIS events are indicated. The distributions are normalised to equal luminosity.

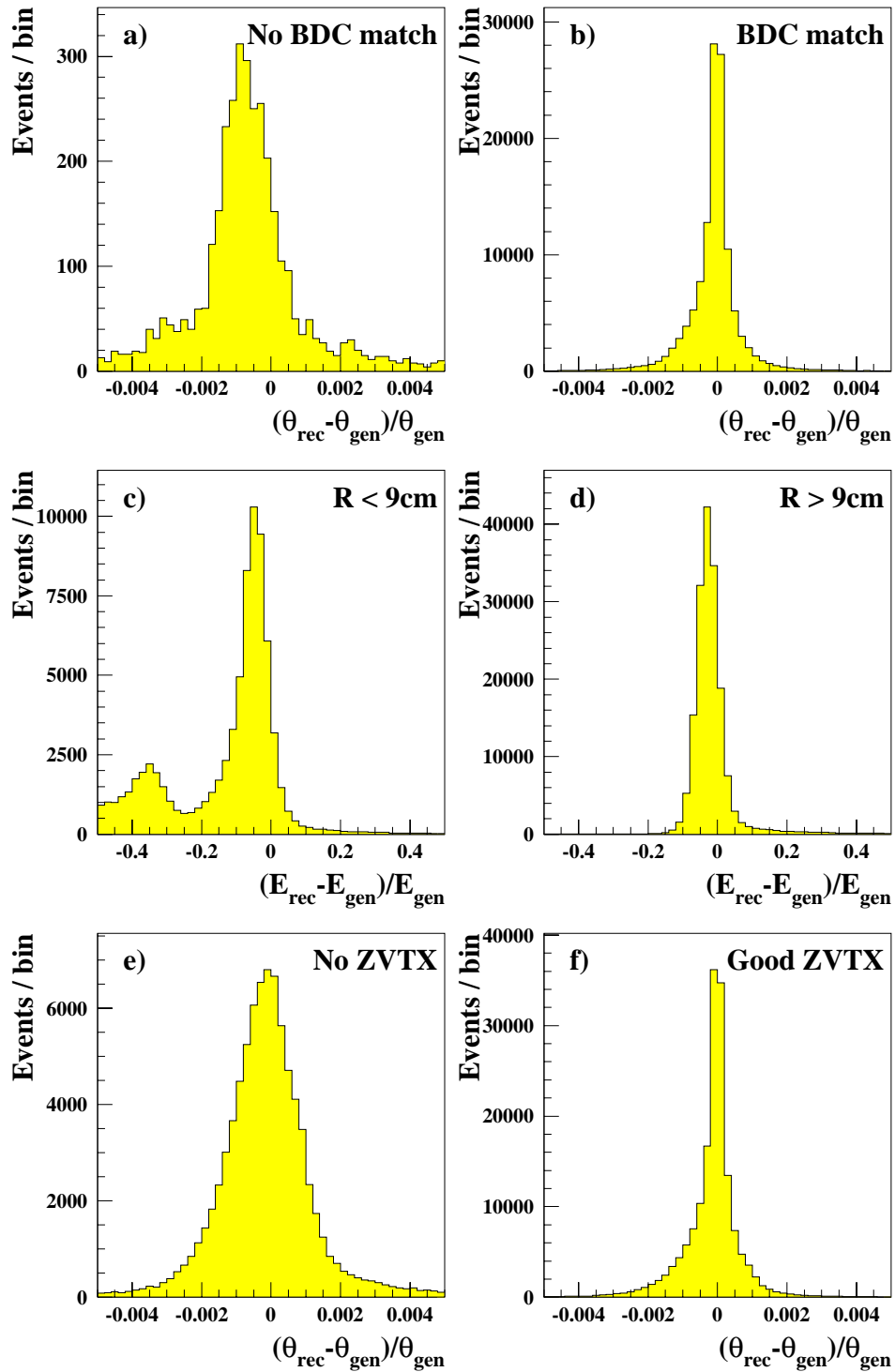


Figure 6.2: Effect of DIS cuts on reconstruction of electron candidate in DJANGO: $(\theta_{\text{rec}} - \theta_{\text{gen}})/\theta_{\text{gen}}$ a) without and b) with a track passing DBDC cut, $(E_{\text{rec}} - E_{\text{gen}})/E_{\text{gen}}$ for c) $R < 9\text{ cm}$ and d) $R > 9\text{ cm}$ (RCLU), and $(\theta_{\text{rec}} - \theta_{\text{gen}})/\theta_{\text{gen}}$ e) without and f) with a well-reconstructed vertex passing the ZVTX cut.

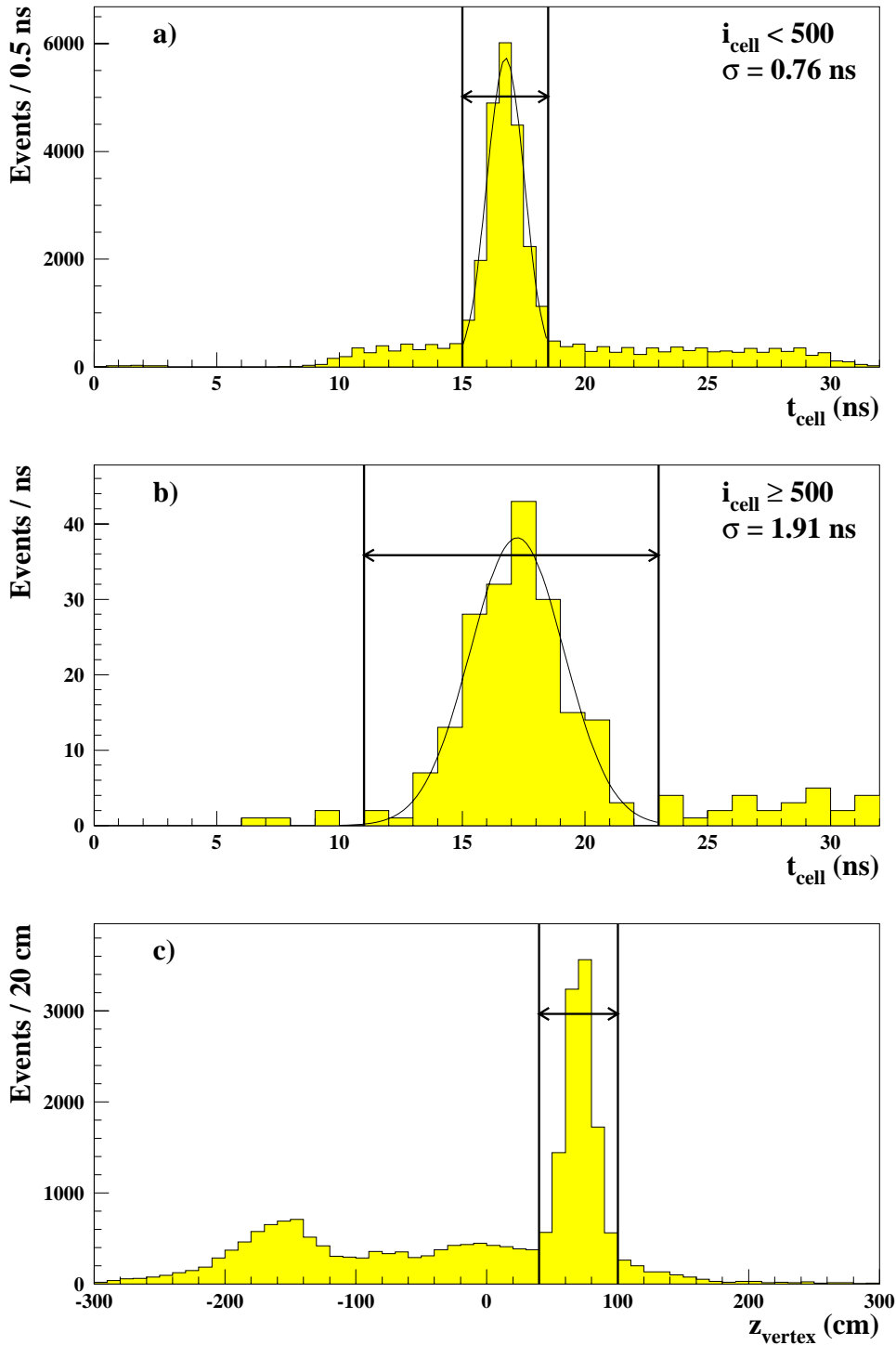


Figure 6.3: Shifted vertex data distributions for the DIS selection: TDC time of hottest cell in cluster, t_{cell} for a) $i_{\text{cell}} < 500$ and b) $i_{\text{cell}} \geq 500$, and c) z_{vertex} showing peaks from collisions, satellite bunches and beam-induced backgrounds. The regions selected for DIS events are indicated.

electron being correct is greater than 99%. Furthermore, above 8 GeV the ST0 trigger requirement is $\simeq 100\%$ efficient.

- **DBDC:** for the BDC track closest to the cluster, cuts are made individually on the track-cluster separation in r and $r\phi$; $\Delta r \leq 2$ cm, $\Delta r\phi \leq 2$ cm, reflecting the geometry and resolution behaviour of the BDC. This ensures that the track and cluster are associated with the same particle and also rejects part of the photoproduction background, where hadronic clusters in SPACAL have poor track matches (Figure 6.1b,c), or where, as mentioned above, π^0 faking electrons are associated with tracks from other particles. The use of the BDC track significantly improves reconstruction of the electron polar angle; Figure 6.2a and b show $(\theta_{rec} - \theta_{gen})/\theta_{gen}$ for events without and with a track passing this cut. It can be seen, from Figure 6.1c, that the $\Delta r\phi$ cut could in principle be tightened to 1 cm, but this was not done in order to maintain good efficiency.
- **RCLU:** radial position of the cluster barycentre, $R_{clus} \geq 9$ cm. This rejects electron candidates in the insert region of SPACAL, where there is leakage of energy into the beam pipe and difficulty in reconstruction of the cluster energy and position. Figure 6.2c and d show the effect on the reconstruction the electron energy, which is significantly improved by application of the cut.
- **ECRA:** energy-weighted cluster radius, $0.5 \leq R_{ECRA} \leq 3.2$ cm. The radius of clusters induced by electrons is on average smaller than that of hadrons arising from photoproduction events, as shown in Figure 6.1d. The upper cut therefore reduces photoproduction background, while the lower is to reject events where the cluster radius has not been correctly calculated.
- **TIME:** timing of the hottest cell of the candidate is required to satisfy the following: $14.5 < t_{cell} < 18.5$ ns ($i_{cell} < 500$), $11.0 < t_{cell} < 23.0$ ns ($i_{cell} \geq 500$), where i_{cell} is the geometrical cell number which follows a spiral starting at the veto layer cells. The looser cut for the outer cells in SPACAL reflects the fact that there was no timing calibration in this region (see Figure 6.3a,b). This rejects residual out-of-time beam-induced backgrounds.
- **VETO:** energy in the SPACAL veto layer, $E_{veto} \leq 1$ GeV. This is, in addition to the RCLU cut, designed to reject events with leakage of energy into the beam pipe. Beam-wall backgrounds where particles are back-scattered into SPACAL from beam line material close to the interaction (collimators in particular) are also reduced by this cut.
- **ZVTX:** the event is required to have a primary vertex reconstructed from at least

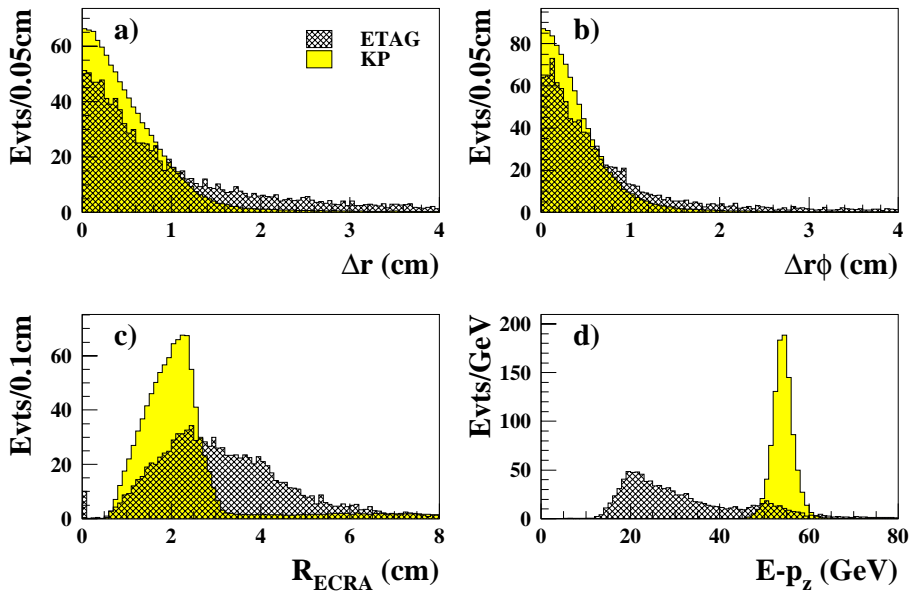


Figure 6.4: *SVX* kinematic peak (*KP*) and electron-tagged (*ETAG*) sample comparisons: a) Δr and b) $\Delta r\phi$ for track-cluster match (*DBDC* cut), c) R_{ECRA} and d) $E - p_z$. The normalisation is arbitrary.

one central or forward track with $|z_{nominal} - z_{vertex}| < 30$ cm, where the nominal interaction z -position, $z_{nominal} \simeq 70$ cm, for the *SVX* data. Satellite bunch collisions and beam-wall interactions lead to a wide distribution of primary vertices (see Figure 6.3c). The cut is set at three times the RMS length of the colliding bunches (3σ) and greatly reduces contamination from such backgrounds. A well-reconstructed vertex within this interval is also important for good reconstruction of the electron polar angle, as shown in Figure 6.2e and f.

- **EMPZ:** $\sum_i (E_i - p_{z,i})$ of all particles measured in the main detector calorimeters is required to be $35 \leq E - p_z \leq 75$ GeV. DIS events, where both the electron and the hadronic final state are contained in the main detector, have a peak in this quantity at twice the electron beam energy, namely 55 GeV. In photoproduction events, the electron is lost down the beam pipe, and does not enter into the sum, and the distribution is broadly smeared out at lower values. This distinction is shown in Figure 6.1e. It is therefore possible to reject some fraction of the photoproduction background with this cut. Radiative events are also partially rejected by this cut, as the loss of the initial state photon in the beam pipe modifies the longitudinal energy-momentum balance.

Figure 6.4, derived from the initial data sample triggered by *ST0*, demonstrates the different signatures generated by DIS and photoproduction events in the relevant cut variables.

A loose DIS sample, selected solely by requiring that the electron energy be in the kinematic peak region (KP), $E_e > 23 \text{ GeV}$, is compared with a photoproduction sample defined by requiring significant energy in the electron tagger (ETAG), $E_{\text{tagger}} > 4 \text{ GeV}$. The longer tail for ETAG events in the distributions of Δr and $\Delta r\phi$, used in the DBDC cut, can be seen. The cluster radius R_{ECRA} has a narrower distribution for KP events, where the hottest cluster is the electron, than for ETAG events. The peak in $E - p_z$ expected for DIS events is clearly visible in the KP sample, but absent for ETAG events.

6.7 Selection of Diffractive Events

The absence of colour flow between the target and current regions in diffractive events leads to large rapidity gaps in the hadronic final state. Since the proton remnant, which usually has low mass, escapes undetected down the beam pipe in H1², the rapidity gap is observed between the hadronic final state from the current interaction and the forward edge of the detector acceptance. Indeed, diffractive events with large rapidity gaps were first observed by the H1 [2] and ZEUS [3] collaborations by analysis of the distribution of the most forward energy deposits in the main calorimeter.

6.7.1 The η_{max} Selection

The primary cut used to select diffractive events is in the variable η_{max} , which is defined as the pseudo-rapidity of the most forward calorimeter energy deposit above a specified energy threshold (to reject noise, typically 400 MeV). Note that in the H1 coordinate system, where the polar angle θ is defined relative to the opposite direction to that of fixed target experiments, the pseudo-rapidity is

$$\eta = -\ln \tan \frac{\theta}{2}. \quad (6.13)$$

Figure 6.5 shows η_{max} distributions for the DIS candidate event sample and for the non-diffractive Monte Carlo (DJANGO). At low values the data have an excess of events which is not described by the MC. This discrepancy is attributed to the presence of diffractive events in the data sample. η_{max} therefore provides a useful method for distinguishing between diffractive and non-diffractive processes. For previous measurements of $F_2^{D(3)}$ at H1 [119], the cut in this variable has been defined as $\eta_{\text{max}} < 3.2$, which is repeated for the purposes of this analysis. Alone, this cut is capable of selecting a clean sample of

²The forward proton spectrometer (FPS) is designed to detect such proton remnants; this was only partially installed for the 1995 running for testing, and was therefore not used in this analysis.

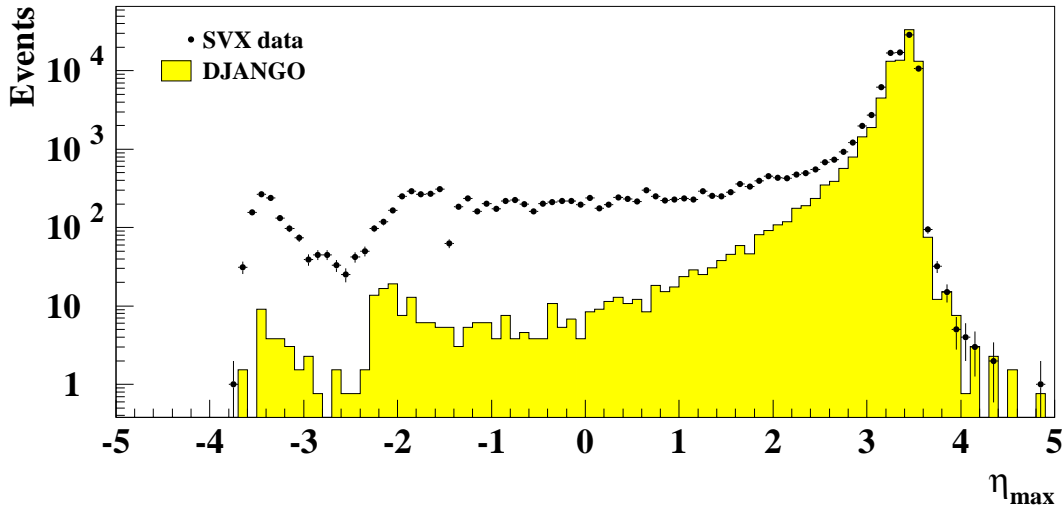


Figure 6.5: η_{\max} distribution for data and the DIS MC model (DJANGO), showing excess events at low values in data. The distributions are normalised to the number of events with $\eta_{\max} > 3.2$.

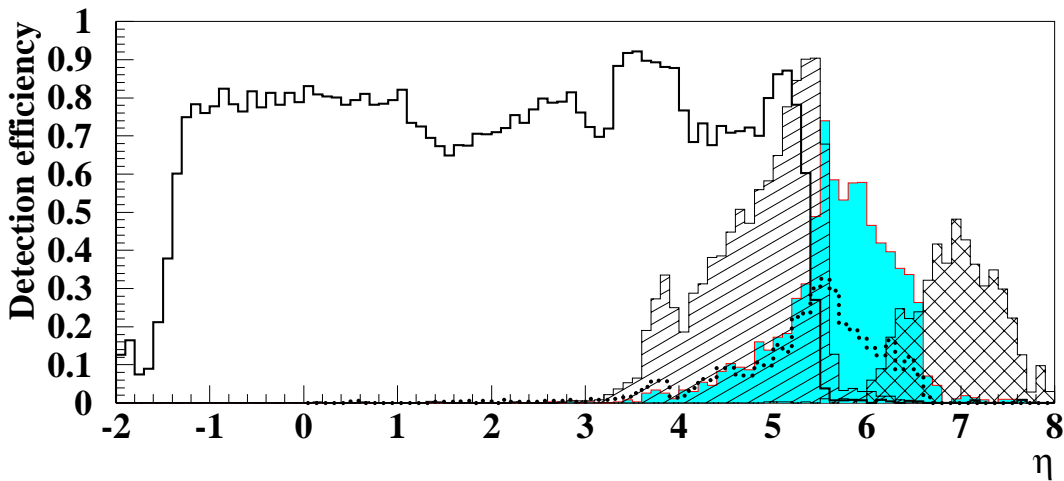


Figure 6.6: Single particle detection efficiency from DJANGO: solid line is the LAr, diagonal lines are the PLUG, shaded region is the FMD, dotted line is the IRON, cross-hatched is the PRT. The IRON is not used in this analysis since it is not described by Monte Carlo.

diffractive events, but has the disadvantage of restricting the available kinematic region in x_p and M_x , due to correlation between the polar angle of the hadronic final state and the values of these variables. It is therefore desirable to extend the range with additional subdetector signals.

6.7.2 Use of the Forward Subdetectors

In order to improve the acceptance at high x_p and high M_x it is necessary to extend the range of particle detection to higher rapidity, using the forward subdetectors. The plug calorimeter (PLUG) described in Section 3.4.3, forward muon detector (FMD) (Section 3.5.2) and proton remnant tagger (PRT) (Section 3.7) allow, in addition to the liquid argon (LAr) and SPACAL calorimeters, coverage of the pseudo-rapidity interval -4 (178°) $< \eta < 7$ (0.1°). The flux of high rapidity particles entering the forward subdetectors arises from two sources. Primary particles from the final state either enter directly or interact with material in the forward region such as the beam pipe wall, focusing magnets or collimator masks. Such interactions produce showers of secondaries, some of which enter the active detectors at large angles to the beam. The forward detectors are therefore sensitive to the presence of primary particles at considerably higher rapidity than is indicated by their geometrical acceptance alone. This is demonstrated in Figure 6.6, taken from [120], which shows the single particle detection efficiency as a function of η calculated with DJANGO Monte Carlo. While this indicates that the single particle detection efficiency is comparatively low in the forward region, most of the final states in which the proton remnant dissociates generate significant numbers of particles; the efficiency of finding any particle from that state is high. Use of the forward subdetectors therefore extends the detection capabilities to $\eta \simeq 7.5$.

Figure 6.7a shows a candidate DIS event without a large rapidity gap. It can be seen that there is significant activity in the forward region arising from secondaries; there are energy deposits in the PLUG and most forward parts of the LAr and a large number of hits in the FMD pre-toroid layers. In contrast, the event shown in Figure 6.7b, a DIS diffractive candidate, has very little activity in the forward region and therefore a large rapidity gap up to the most forward LAr cluster ($\eta = 2.8$).

6.7.3 Reconstruction of Forward Subdetector Signals

In order to use the forward subdetectors in the selection of diffractive events, the signals derived from each must be defined. This was done by consideration of the subdetector

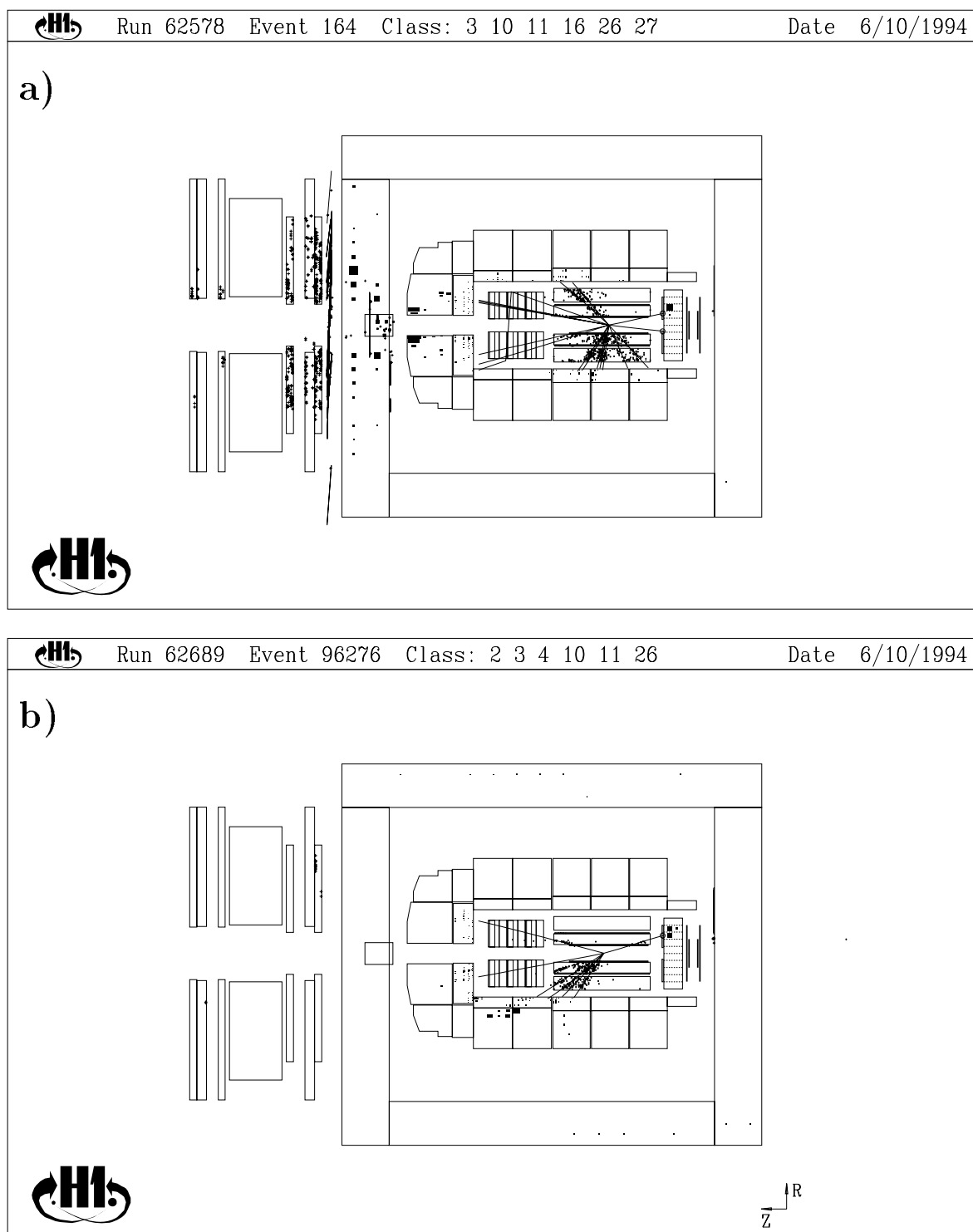


Figure 6.7: Typical DIS events: a) non-diffractive, with considerable activity in the forward subdetectors, and b) diffractive with little forward activity. The events are from data taken before the installation of SPACAL.

geometry, reconstruction and noise levels.

The PLUG suffers from noise due to pile-up of events and the high radiation environment in the forward region close to the beam pipe. The signals used are derived from the standard reconstruction, including a noise threshold cut at 500 MeV, to give an energy measurement in GeV for each channel. Since the PLUG occupies a relatively small region in rapidity, no attempt was made to exploit the segmentation of the device. Instead, the total energy, E_{PLUG} , was calculated and used.

The FMD detects mainly secondaries, as described above, since it is well shielded from the interaction vertex by the LAr and forward endcap of the iron return yoke, and the flux of primary muons originating from ep interactions is small. The post-toroid layers are sensitive to synchrotron radiation from the upstream electron beam, the level of which is strongly dependent on the beam conditions. However, the iron of the toroid magnet absorbs this radiation, and so the pre-toroid layers are relatively free from such background. There is only a small amount of noise in the FMD (typically 0.005 hits per cell per event), originating from the readout electronics. The noise observed in each cell is random, whereas charged particles passing through the subdetector generate hits in each sub-layer, so the pairing algorithm used in the FMD reconstruction is sufficient to effectively reject the noise. For the purposes of detecting secondaries, the pairing algorithm requires the hits in each sub-layer to be within 9 cm in the drift coordinate, which allows for the steep tracks, and each hit can only enter into one pair. As with the PLUG, there is little to be gained from attempting to divide the FMD into regions of rapidity. Taking all the above factors into account, the signal used was the total number of pre-toroid pairs, N_{FMD} .

The noise levels in the PRT are very low, and allow a clean signal to be derived from the single hits in each layer. It was found [121] that the signal in one layer was not well described by the Monte Carlo samples used, and so this layer was excluded. The signal used was therefore the total number of the remaining five PRT layers firing, N_{PRT} .

6.7.4 Forward Subdetector Response and Cuts

The cuts applied to the signals in the forward subdetectors were determined by an analysis of the residual noise in each. This was investigated using random trigger events, which constitute approximately 1% of the data written to tape during normal runs. Such events have no other trigger element requirement and are synchronised to a filled electron and proton bunch. They are therefore an important source of information about noise levels

in the detector and pile-up of events under normal beam conditions. The chance of an ep interaction or beam-gas event occurring in coincidence with a random trigger is small. 21077 such events were used, recorded during the 1995 shifted vertex run period in order to match the noise conditions present in the physics data sample.

Figure 6.8 shows the signals observed in the random events. An analysis of the distributions was made to optimise the cuts used to distinguish residual noise from the interaction particles in the forward region. The definition of the absence of activity in the forward subdetectors, used to select diffractive events, was determined to be the following:

$$E_{PLUG} < 2.5 \text{ GeV}, \quad N_{FMD} < 2, \quad N_{PRT} = 0$$

As can be seen from the random trigger signals, these cuts do not completely remove noise, leading to the possibility of misidentifying an event with no particle in the forward subdetectors. The random event sample was used to quantify this, by determining the fraction of events remaining after each of the cuts. The results are summarised in Table 6.1. The fraction of events remaining after all of the forward cuts is used as a noise correction to the number of diffractive events found in this analysis; this was determined to be $(12.9 \pm 0.3)\%$. This is a relatively large correction, the dominant contribution to which is from the PLUG, but the increased rejection that this subdetector provides was deemed sufficient to justify its inclusion. Furthermore the magnitude of this correction is well-defined and is applied universally across all bins in the measurement, affecting the overall normalisation only.

The Monte Carlo simulations do not include noise in the forward subdetectors, so, in order to achieve a good description of the detector response, noise was included manually. This was performed on an event-by-event basis by adding the signal from a random trigger event to that of a Monte Carlo event.

6.8 Comparison of Diffractive Data and Monte Carlo Samples

In order to model effects such as detector acceptance and resolution, it is necessary to rely on Monte Carlo samples where access to the ‘true’ values of reconstructed variables is available. For the estimation of these effects to be reasonable it is clearly desirable to have a good description of the data at the reconstructed MC level in all respects. In this section, a comparison is therefore made of the diffractive Monte Carlo sample (RAPGAP) and the real data events which are selected as diffractive candidates. The photoproduction

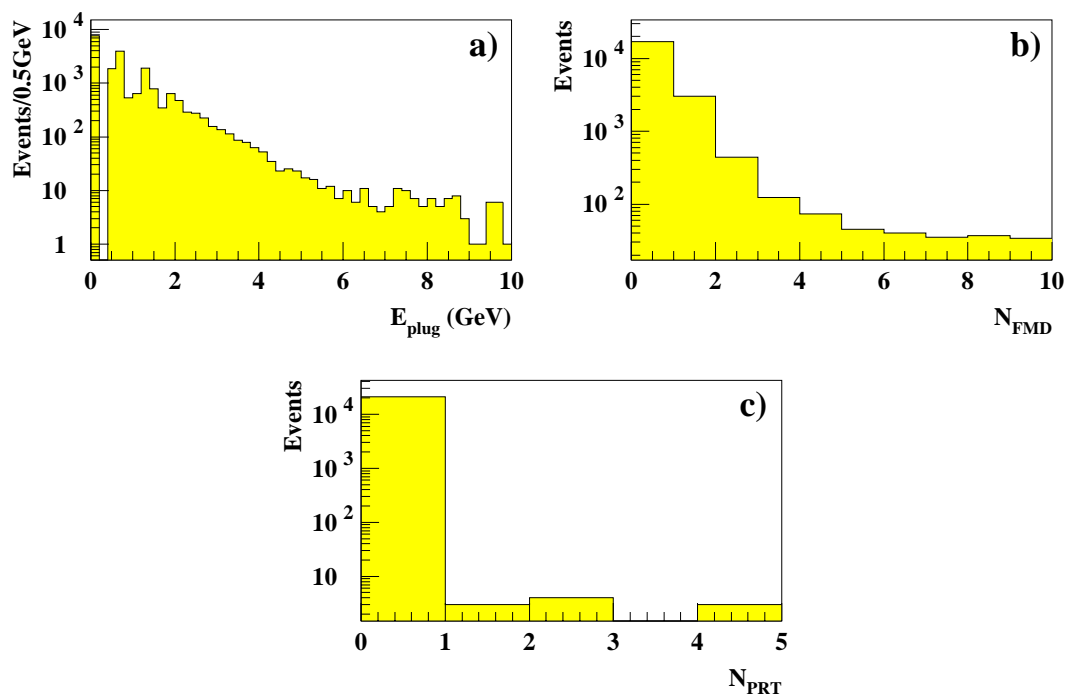


Figure 6.8: Forward subdetector signals observed in random trigger events: a) plug total energy, E_{PLUG} , b) number of FMD pre-toroid pairs, N_{FMD} and c) number of PRT hits.

Forward Cut	Fraction Passing
E_{PLUG}	0.0908 ± 0.0022
N_{FMD}	0.0549 ± 0.0017
N_{PRT}	0.0006 ± 0.0001
All Cuts	0.1288 ± 0.0026

Table 6.1: Fraction of random trigger events passing forward detector cuts.

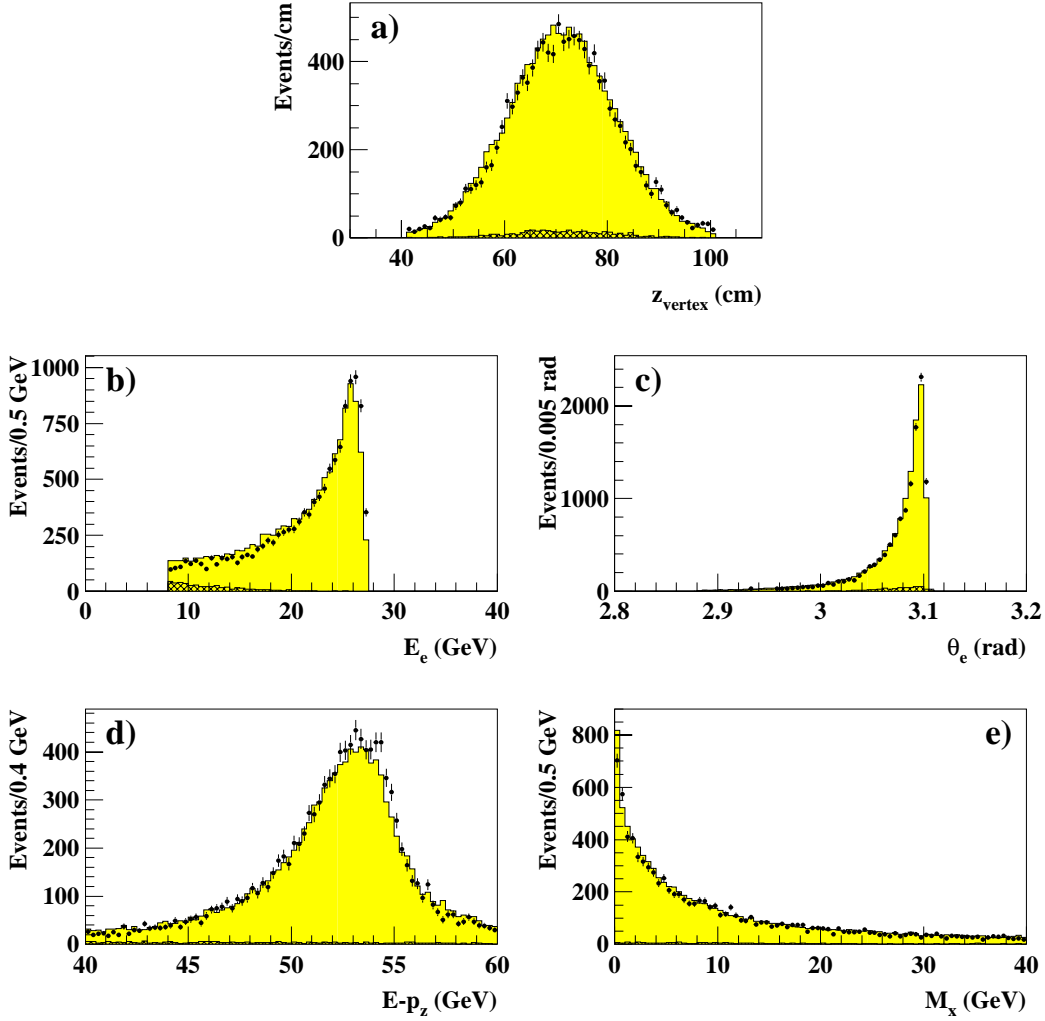


Figure 6.9: Comparison of the diffractive Monte Carlo with data: a) z_{vertex} distribution, b) electron candidate energy, E_e c) electron candidate polar angle, θ_e , d) $E - p_z$ and e) mass of the hadronic final state, M_x . The points are for data, shaded histogram is diffractive MC with photoproduction background added, and the hatched region is the photoproduction background.

background is estimated using PHOJET and added to the MC distributions. Corrections for acceptance effects are not applied.

A good description of the data was obtained by reweighting the generated kinematic variables of the diffractive MC. Discrepancies between data and MC arise from the fact that the structure function in the MC is unknown in the new region of this measurement, and is based on extrapolation of the fit to the 1994 $F_2^{D(3)}$. The Monte Carlo is therefore reweighted iteratively with a parameterisation in β and Q^2 until the generator level MC best matches the new measurement presented in Section 7.6. It was found that, after two iterations, the measurement was not affected by subsequent reweighting attempts.

Figure 6.9a shows a comparison of the z_{vertex} distribution. It was found that the mean

and width of the MC distribution differed somewhat from that observed in the data. A Gaussian fitted to each gave the means and widths as

$$\begin{aligned}\bar{x}_{data} &= 71.2, & \sigma_{data} &= 10.7 \\ \bar{x}_{MC} &= 72.1, & \sigma_{MC} &= 11.4\end{aligned}$$

The MC events were therefore reweighted to correct for this, the weight being derived from the ratio of two fitted Gaussian functions. After this reweighting, a good agreement was observed in the comparison. The photoproduction background was normalised to the integrated luminosity of the data. For the diffractive MC, the reweighting described above alters the overall normalisation. The z_{vertex} distribution was therefore used to derive a normalisation by scaling the number of events observed in the MC distribution (including the background contribution) to the number observed in the data. This was used for all subsequent comparisons.

Figure 6.9b,c show the electron candidate energy and polar angle, the latter being calculated from the matched BDC track. These distributions show reasonable agreement between data and MC. The same is true for $E - p_z$ and M_x , as shown in Figure 6.9d and e respectively.

Figures 6.10 and 6.11 show comparisons of the reconstructed kinematic variables Q^2 , x , β and x_p for the electron and sigma methods respectively. It can be seen that there is an adequate description in all the variables with the exception of x_p calculated by the sigma method. This is due to the increased sensitivity of this method to the reconstruction of the hadronic final state, particularly in the backward region between the LAr and SPACAL calorimeters. This region gives rise to the structure in the distribution at $\log_{10}(x_p) \simeq -3.2$. Evidence for this strong variation in response can also be seen in Figure 6.5 at $\eta_{max} \simeq -2.5$.

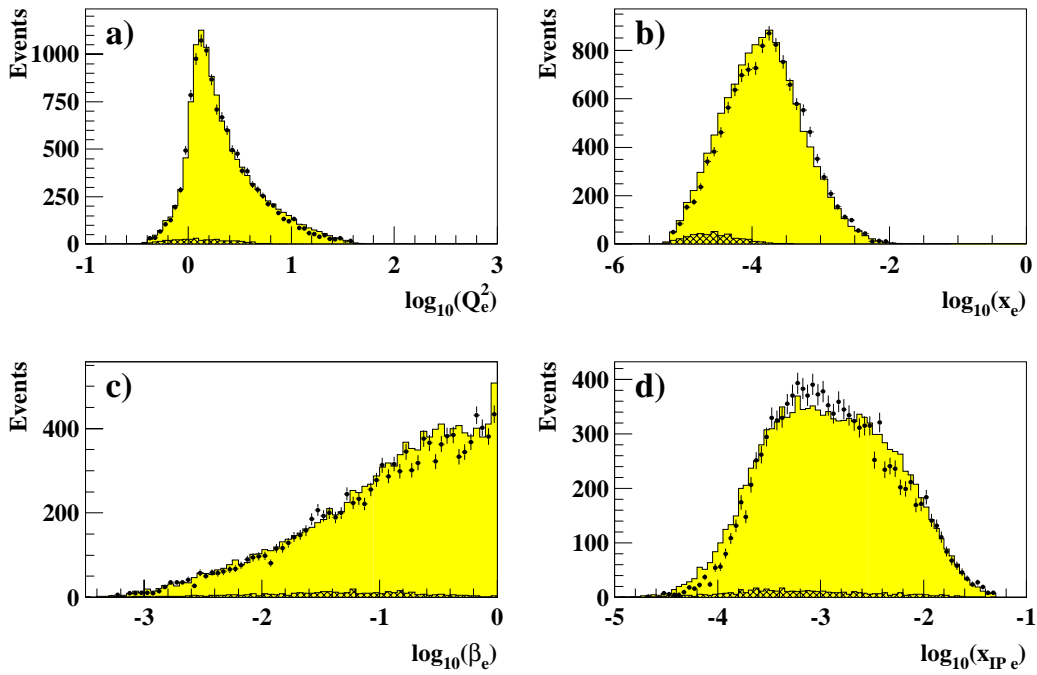


Figure 6.10: Comparison of the diffractive Monte Carlo with data for electron kinematics: a) $\log_{10}(Q^2)$, b) $\log_{10}(x)$, c) $\log_{10}(\beta)$ and d) $\log_{10}(x_{IP\ e})$. The distributions are displayed as in Figure 6.9.

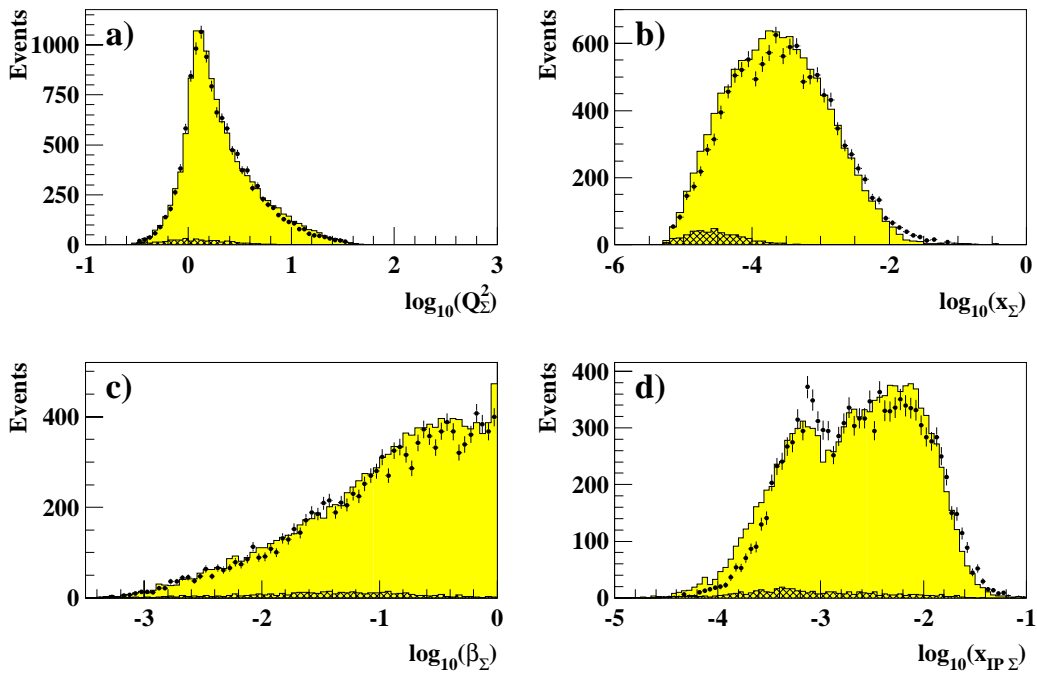


Figure 6.11: Comparison of the diffractive Monte Carlo with data for sigma kinematics: a) $\log_{10}(Q^2)$, b) $\log_{10}(x)$, c) $\log_{10}(\beta)$ and d) $\log_{10}(x_{IP})$. The distributions are displayed as in Figure 6.9.

Chapter 7

Measurement of the Diffractive Proton Structure Function

7.1 Definition of the Diffractive Structure Function

In this analysis the final state proton or its remnant was not detected, so no measurement of t could be made¹. The diffractive proton structure function, discussed in Section 2.4, was therefore measured as a function of three variables by an implicit integration over t :

$$F_2^{D(3)}(x, x_P, Q^2) = \int F_2^{D(4)}(x, x_P, Q^2, t) dt. \quad (7.1)$$

The structure function is determined from the differential cross section for the process $ep \rightarrow eXY$, where the system Y is the proton or its remnant, having a mass $M_Y < 1.6\text{GeV}$, using the following formula:

$$\frac{d^3\sigma(x, x_P, Q^2)}{dx dx_P dQ^2} = \frac{4\pi\alpha^2}{xQ^4} \left(1 - y + \frac{y^2}{2(1 + R^D)} \right) F_2^{D(3)}(x, x_P, Q^2). \quad (7.2)$$

A Jacobian transformation then gives a measurement of the cross section in terms of β rather than x_P :

$$\frac{d^3\sigma(\beta, x, Q^2)}{d\beta dx dQ^2} = \frac{4\pi\alpha^2}{\beta^2 Q^4} \left(1 - y + \frac{y^2}{2(1 + R^D)} \right) F_2^{D(3)}(\beta, x, Q^2). \quad (7.3)$$

R^D has not been measured and is expected to be significant only at high y , while this measurement is predominantly made at low y . Furthermore, there is no theoretical con-

¹In principle, t could be determined from the final state electrons and hadrons. However, the energy loss of the proton is typically less than the energy resolution of the detector, so the accuracy of such a measurement is poor. The FPS provides the possibility of measuring t in the analysis of future data.

sensus on the prediction of this quantity. For these reasons, R^D is set to zero for this analysis.

7.2 Extraction of the Measured Cross Section

As explained in Section 7.1, $F_2^{D(3)}(\beta, x_p, Q^2)$ is extracted from the measured differential cross section. This was determined by counting events in three-dimensional bins in the kinematic variables. For each bin, the Born cross section was measured using the following equation:

$$\frac{d^3\sigma(\beta, x, Q^2)}{d\beta dx dQ^2} = \frac{N_{obs} - N_{back}}{\mathcal{L}'} \frac{1}{\varepsilon_{eff}} \frac{1}{\varepsilon_{acc}} \frac{1}{BCC} \frac{1}{(1 + \delta_{rad})} (1 + \delta_{noise}) \quad (7.4)$$

where the terms are as follows:

N_{obs}	:	number of diffractive candidate events
N_{back}	:	number of background events
\mathcal{L}'	:	integrated luminosity of the data sample
ε_{eff}	:	selection cuts efficiency
ε_{acc}	:	smeared acceptance
BCC	:	bin centre correction
δ_{rad}	:	radiative correction.
δ_{noise}	:	forward subdetector noise correction

Each term is described in more detail below.

N_{obs} - number of diffractive candidate events

This is the number of events in the bin which pass the DIS and diffractive selection cuts, described in Sections 6.6 and 6.7 respectively.

N_{back} - number of background events

A correction is made in each bin to remove possible background events. These arise from photoproduction and non-collision beam backgrounds. The photoproduction background is estimated and subtracted bin-by-bin, using the PHOJET Monte Carlo sample, normalised to the integrated luminosity of the data sample and the signal in the electron tagger. The non-collision background was estimated using proton and electron pilot bunch events, found to be small compared to the statistical errors of the measurement, and therefore neglected.

\mathcal{L}' - integrated luminosity

The integrated luminosity is summed for all runs passing the run selection described in Section 6.5. The final value is corrected for dead-time in the readout of the data, and for a small contribution to the measured luminosity arising from satellite bunch collisions ($\simeq 5\%$).

 ε_{eff} - selection cuts efficiency

Where possible, corrections to the measured cross section to account for event losses are evaluated directly from the data sample. This is possible for the DIS selection cuts, since there is considerable redundancy in the quantities used to select DIS events. This correction is calculated by determining, for each cut i applied, the efficiency

$$\varepsilon_{eff,i} = \frac{\text{Number of events after cut } i}{\text{Number of events before cut } i} \quad (7.5)$$

and taking the product of the efficiencies for all cuts. For each cut efficiency, the remaining cuts are left in place, in order to provide a clean DIS sample with which to make the calculation. Given the above expression for ε_{eff} , which can be written for simplicity as

$$\varepsilon_{eff} = \frac{n}{N} \quad (7.6)$$

we can write the error on this quantity as

$$\delta\varepsilon_{eff} = \sqrt{\frac{n(N-n)}{N^3}} \quad (7.7)$$

However, these expressions are only valid when n , N and $N-n$ are large, which may not be the case for all bins in the analysis. A better prescription for the efficiency and its error is therefore [122]:

$$\varepsilon_{eff} = \frac{n+1}{N+2} \quad (7.8)$$

$$\delta\varepsilon_{eff} = \sqrt{\frac{(n+1)(N-n+1)}{(N+2)^2(N+3)}} \quad (7.9)$$

The error in the final efficiency is propagated from the individual errors in quadrature. The evaluation of the selection efficiency is discussed in Section 7.4.

 ε_{acc} - smeared acceptance

The smeared acceptance corrects the measured cross section for the loss of diffractive events due to detector inefficiencies and the smearing of events from one bin to another due to resolution effects in the reconstruction of the event. Correcting for diffractive event losses cannot be performed directly in the data sample using the efficiency method described above, since there is not enough redundancy in the

diffractive selection cuts. Furthermore, relaxing diffractive cuts to evaluate their efficiency modifies the acceptance for diffractive events as a function of the kinematic variables. The smeared acceptance is determined from the diffractive Monte Carlo from the following expression:

$$\varepsilon_{acc} = \frac{\text{Number of reconstructed events (diff. cuts)}}{\text{Number of generated events}} \quad (7.10)$$

The number of reconstructed events in the numerator has two components; events which were generated and reconstructed (remain) in the bin, N_{rem} , and events which enter the bin due to smearing, N_{enter} . Therefore the acceptance can be written:

$$\varepsilon_{acc} = \frac{N_{rec}}{N_{gen}} = \frac{N_{rem} + N_{enter}}{N_{gen}} \quad (7.11)$$

The statistical error on the acceptance is small relative to that on the number of diffractive events in data, due to the large size of the diffractive MC sample.

BCC - bin centre correction

This term transforms the cross section from a bin-oriented measurement to a value at the specified centre of the bin in the three kinematic variables. It is determined by calculating the following quantity:

$$BCC = \frac{\iiint \frac{d^3\sigma(\beta, x, Q^2)}{d\beta dx dQ^2} d\beta dx dQ^2}{\frac{d^3\sigma(\beta_c, x_c, Q_c^2)}{d\beta dx dQ^2}} \quad (7.12)$$

where β_c , x_c and Q_c^2 are the values of the kinematic variables at the centre of the bin. The integration over the bin volume is performed analytically, taking into account truncation of bins due to the kinematic and fiducial limits applied in the analysis (see Section 7.3), with the cross-section parameterised by the fit to the 1994 $F_2^{D(3)}$ analysis.

δ_{rad} - radiative correction

The number of observed events which enters into equation 7.4 contains a contribution from radiative events. The term containing δ_{rad} corrects the cross section to the Born level, and is determined from a diffractive Monte Carlo sample which does not contain radiative events. The term in the cross section $1/(1 + \delta)$ is calculated as:

$$\frac{1}{1 + \delta} = \frac{\text{Number of events generated (Born level MC)}}{\text{Number of events generated (Born+Rad MC)}} \quad (7.13)$$

δ_{noise} - forward subdetector noise correction

This is the correction described in Section 6.7.4 which takes account of the loss of diffractive candidate events due to noise in the forward subdetectors. The correction is $\delta_{noise} = 0.1288$ and is applied globally to all bins.

7.3 Selection of Bins

The binning used in this analysis was chosen to be consistent with that used in the 1994 $F_2^{D(3)}$ measurement, in order to allow a direct comparison between the two. Defined in terms of the variables Q^2 , x and β , the bins were chosen to minimise smearing effects due to detector resolution, and to ensure that most contained a reasonable number of events. Since the primary goal of this analysis is the extension of the kinematic range available for this analysis using SPACAL, bins at lower Q^2 and β have been included.

Tables 7.1-7.3 present the bins chosen for each variable. The upper and lower limits on each bin and the “centre”, the point to which the measurement in each bin is corrected, are shown. In order to minimise the effect of smearing the resolution in each kinematic variable should be smaller than the width of the bin. Figure 7.1 shows the resolution as a fraction of the bin width, determined using the diffractive Monte Carlo. It can be seen that in Q^2 and $\log_{10}(x)$, the resolution is less than half the width of all bins. The fractional resolution in β is poor in the highest two bins. This is due to the behaviour of β as Q^2 falls where a given bin occupies smaller and smaller regions in M_x , since $d\beta = (\beta^2/Q^2)dM_x^2$ at fixed Q^2 . The resolution is therefore driven by that of M_x when $Q^2 \lesssim 5 \text{ GeV}^2$. While this choice of β bins is less than optimal, it was decided to keep the β binning described, in order to match that used for the previous measurement.

When combined, the bins define a subdivided cube in the three-dimensional kinematic volume in Q^2 , x and β . Not all of the possible bins are physically accessible and additional restrictions were applied to remove regions where the measurement is potentially degraded due to effects such as poor resolution or large radiative corrections.

The range in Q^2 and x was restricted by the geometrical acceptance of the SPACAL, which placed a limit on the polar angle of the candidate electron at $\theta > 165^\circ$. In addition, the RCLU cut on the radial position of the candidate cluster, $R_{clus} > 9 \text{ cm}$ (discussed in Section 6.6), places an upper limit on the angle at $\theta \lesssim 178^\circ$ (the value of theta depends upon the z coordinate of the cluster barycentre, which varies somewhat). The sample size available from the shifted vertex data limited the statistics at high Q^2 ; the maximum value entering into any bin in the measurement was therefore chosen to be $Q^2 = 70 \text{ GeV}^2$. The number of events at low Q^2 , which is restricted due to geometrical acceptance of SPACAL, and the difficulty of making a measurement in this region where the photoproduction background is large necessitated a lower limit at $Q^2 = 0.3 \text{ GeV}^2$. The range in y was limited to avoid regions where the resolution is poor and radiative corrections are large, leading to the requirement $0.01 < y < 0.8$.

Q^2 bin	Low Edge	Centre	High Edge
1	0.3	0.4	0.6
2	0.6	0.8	1.0
3	1.0	1.17	1.33
4	1.33	1.5	2.0
5	2.0	2.5	3.16
6	3.16	3.5	4.22
7	4.22	5.0	6.25
8	6.25	8.5	12.0
9	12.0	20.0	30.0
10	30.0	50.0	70.0

Table 7.1: Q^2 bin centres and boundaries.

$\log x$ bin	Low Edge	Centre	High Edge
1	-5.5	-5.25	-5.0
2	-5.0	-4.75	-4.5
3	-4.5	-4.375	-4.25
4	-4.25	-4.125	-4.0
5	-4.0	-3.875	-3.75
6	-3.75	-3.625	-3.5
7	-3.5	-3.25	-3.0
8	-3.0	-2.75	-2.5
9	-2.5	-2.25	-2.0
10	-2.0	-1.75	-1.5

Table 7.2: $\log x$ bin centres and boundaries.

β bin	Low Edge	Centre	High Edge
1	0.0005	0.001	0.005
2	0.005	0.01	0.023
3	0.023	0.04	0.07
4	0.07	0.1	0.14
5	0.14	0.2	0.3
6	0.3	0.4	0.5
7	0.5	0.65	0.8
8	0.8	0.9	1.0

Table 7.3: β bin centres and boundaries.

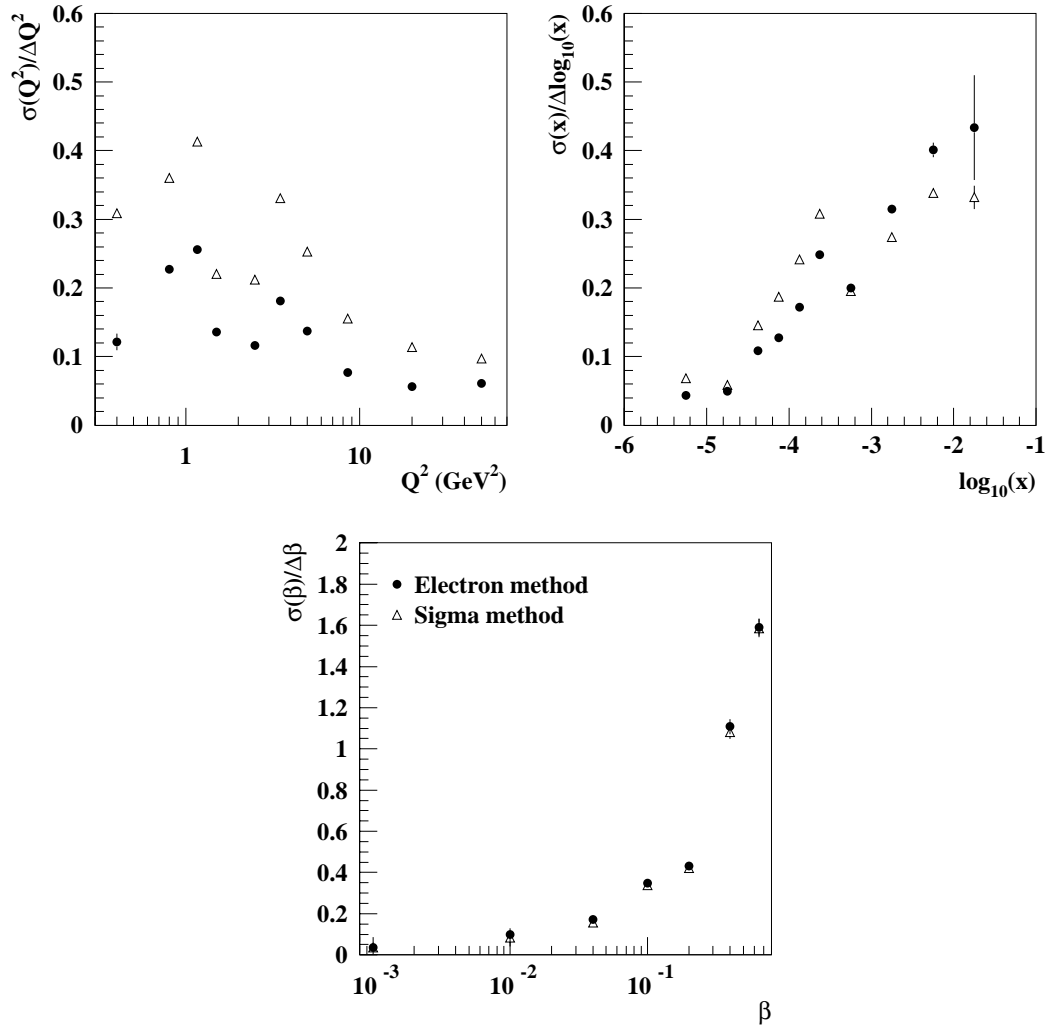


Figure 7.1: Resolution in the kinematic variables as a fraction of bin size, determined using the diffractive Monte Carlo for a) Q^2 , b) $\log_{10}(x)$ and c) β . Closed circles are for electron method kinematics and open triangles for sigma method.

The diffractive selection, described in Section 6.7, has limited acceptance at high x_P . The measurement was therefore restricted to the region $x_P < 0.1$.

In summary, the restrictions applied to the kinematic volume are as follows:

$$0.3 < Q^2 < 70 \text{ GeV}^2 \quad (7.14)$$

$$165 < \theta \lesssim 178^\circ \quad (7.15)$$

$$0.01 < y < 0.8 \quad (7.16)$$

$$x_P < 0.1 \quad (7.17)$$

Figure 7.2 shows the projection of the kinematic volume onto the $x - Q^2$ plane, including the diffractive candidate events reconstructed by electron and sigma methods. Also shown are the cuts described above. The bins which lie outside the selected region, or which

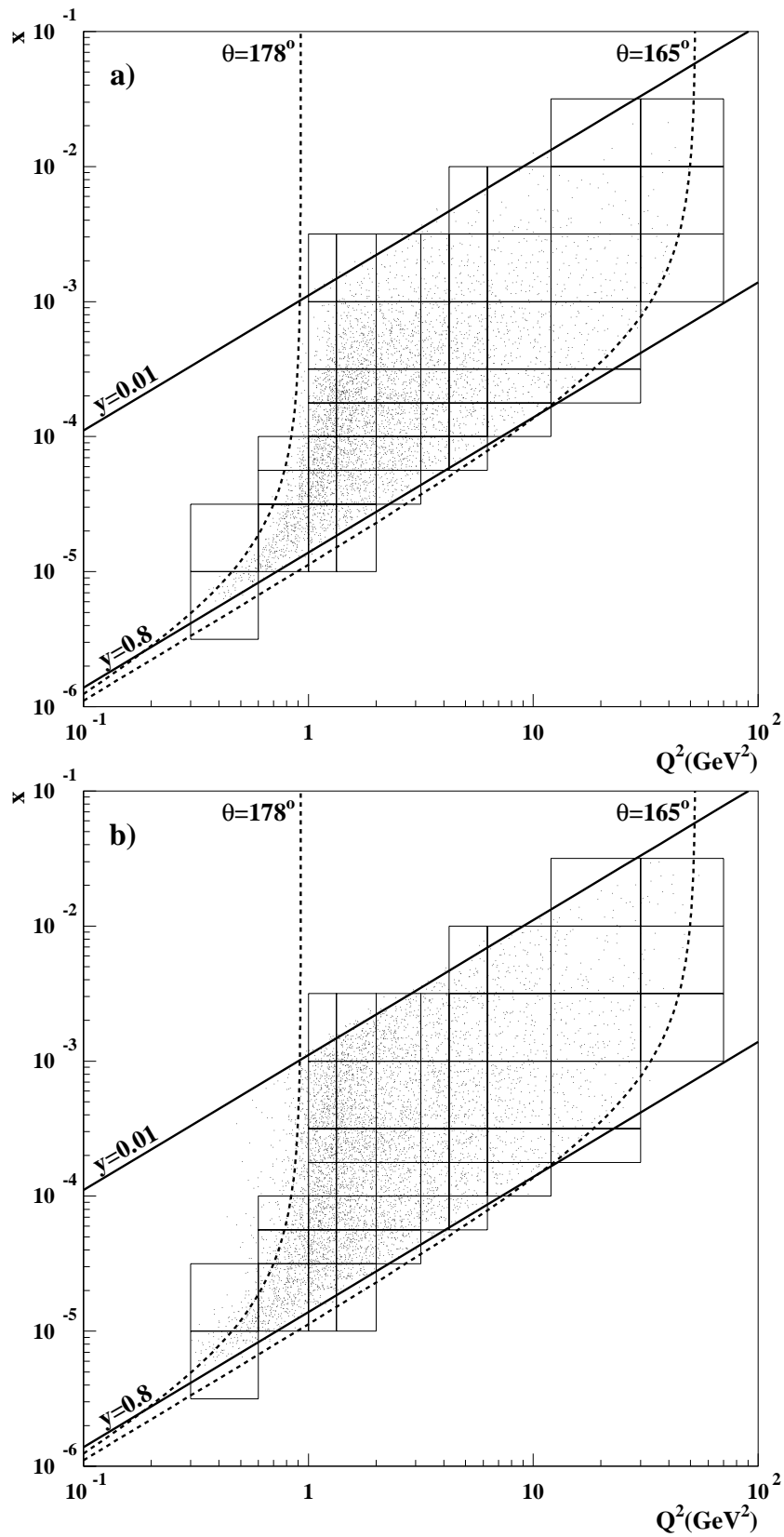


Figure 7.2: The $x - Q^2$ kinematic plane, with diffractive candidate events reconstructed by a) electron and b) sigma methods. Also shown are the kinematic limits and bins used in the analysis.

are highly truncated by the kinematic limits, were excluded from the measurement and are not shown. It can be seen that a number of the remaining bins were truncated by the limits; this is corrected for by applying the limits to the analytic integration used to obtain the bin centre correction, as described in Section 7.2.

7.4 Selection Efficiency

As discussed in Section 7.2, the efficiency of the DIS selection cuts was applied as a correction to the measured cross section. This was evaluated from the data sample, factorised into a product of the efficiency of each cut entering into the selection. The fiducial cuts included in the selection (ECLU and RCLU), described in Section 6.6, restrict the kinematic region rather than enhancing the purity of the sample are therefore not included in the efficiency calculation. The efficiency of the EMPZ cut was also not included since $E - p_z$ is strongly dependent on initial state radiation; the inclusion of this cut would effectively implement a large additional correction dependent on radiative events and therefore increase the error on the measurement.

Evaluation of the ZVTX efficiency is difficult, since removal of the vertex requirement in order to calculate the denominator of Equation 7.5 significantly degrades the estimation of the number of events for the following reasons:

- The vertex requirement plays a major role in the rejection of beam-induced backgrounds which typically lack a reconstructed vertex;
- Removal of the vertex cut allows a significant contribution from the satellite bunches, which artificially decreases the apparent efficiency;
- Calculation of the event kinematics is degraded due to the lack of a vertex to define, with the BDC matched track, the polar angle of the electron candidate.

The ZVTX efficiency was therefore estimated in two ways. Firstly, an alternative vertex can be reconstructed using information from the CIP and BDC subdetectors [123, 124]². However, the geometrical acceptance of the CIP limits this method to the region $Q^2 \gtrsim 5\text{GeV}^2$. Below this, the vertex efficiency was estimated by enhancing the purity of the DIS sample with tighter EMPZ and ECRA cuts ($45 < E - p_z < 70$ and $1.0 < R_{ECRA} < 3.0$). In order to remove the satellite contribution, a loose vertex requirement was applied. Events

²This method was developed with use of the backward proportional chamber (BPC), which was replaced in 1995 by the BDC. However, the principle of the method remains the same.

without a vertex were assigned the default values in order to improve the reconstruction of the kinematics. In spite of these techniques, the calculation of the vertex efficiency was still subject to some background, and suffered from large errors due to the small number of events passing either the CIP requirement or the tighter cuts. A comparison was therefore made with the diffractive MC of the ZVTX efficiency, shown in Figure 7.3, with the diffractive selection applied to both data and MC. It can be seen that there is reasonable agreement between the two, with the MC efficiency somewhat higher at low Q^2 and the extremes of the x distribution. This is due to the absence of background in the MC sample. Furthermore, the errors on the MC efficiencies are smaller due to the considerably larger sample size. Therefore, the MC values were taken for the calculation of the final efficiency.

The final efficiencies of each cut are shown as a function of Q^2 and x in Figures 7.4 and 7.5 respectively, for both the electron and sigma kinematics. It can be seen that there is good agreement between the two methods. The ZVTX efficiency is the combination of the two methods discussed above, and is shown in plot a) of the figures.

The efficiency of the ECRA cut, ε_{ECRA} , is presented in plot b) of each figure and is close to 1 at high x and Q^2 , falling by at most 8% at low values. This is attributable to the growth of the cluster radius at low energies due to the increased significance of noise fluctuations in cells included in the cluster. The trigger requirement efficiency (plot c), ε_{TRIG} , shows a similar behaviour, falling by a maximum of 4%; this is due to the inefficiency of the trigger at low cluster energy. The efficiency of the TIME cut (plot d) shows no strong dependence on either kinematic variable, having an average value of $\varepsilon_{TIME} \simeq 0.98$, which reflects signal losses in the SPACAL analogue electronics and TDC system.

Removal of the BDC track requirement, in order to calculate the efficiency of the DBDC selection (plot e), significantly increases the contamination of the background at low Q^2 and low x . This efficiency was therefore evaluated using a cleaner DIS sample obtained by strengthening the EMPZ and ECRA cuts to the values used for the ZVTX and described above. The remaining inefficiency at low Q^2 and x is due to poor matches between tracks and large clusters at low energy. The slight decrease at high Q^2 and x is due to a number of inefficient layers in the outer regions of the BDC.

The VETO cut efficiency, ε_{VETO} falls at low x and Q^2 (plot f) since this region corresponds to increasing polar angles which place the cluster closer to the SPACAL veto layer. Energy from the electron cluster may then be present in the veto layer, causing loss of events.

For the purposes of the cross section measurement, the efficiency of each cut is calculated bin by bin using the methods illustrated here, and the product is taken to derive to final

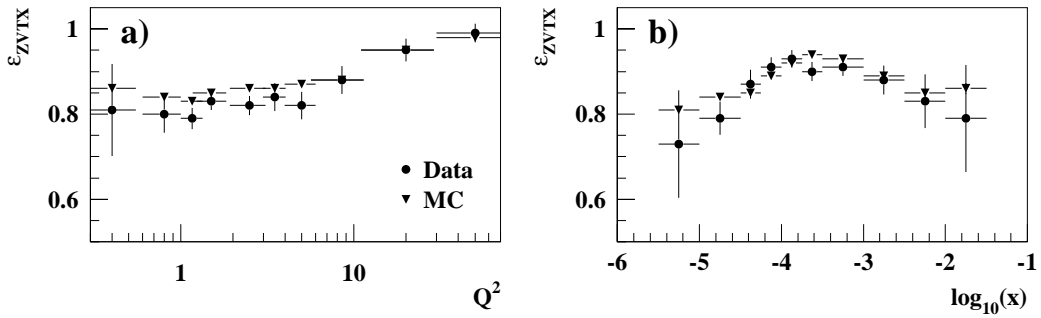


Figure 7.3: Comparison of ZVTX efficiency in data and MC for electron method as a function of a) Q^2 and b) $\log_{10}(x)$.

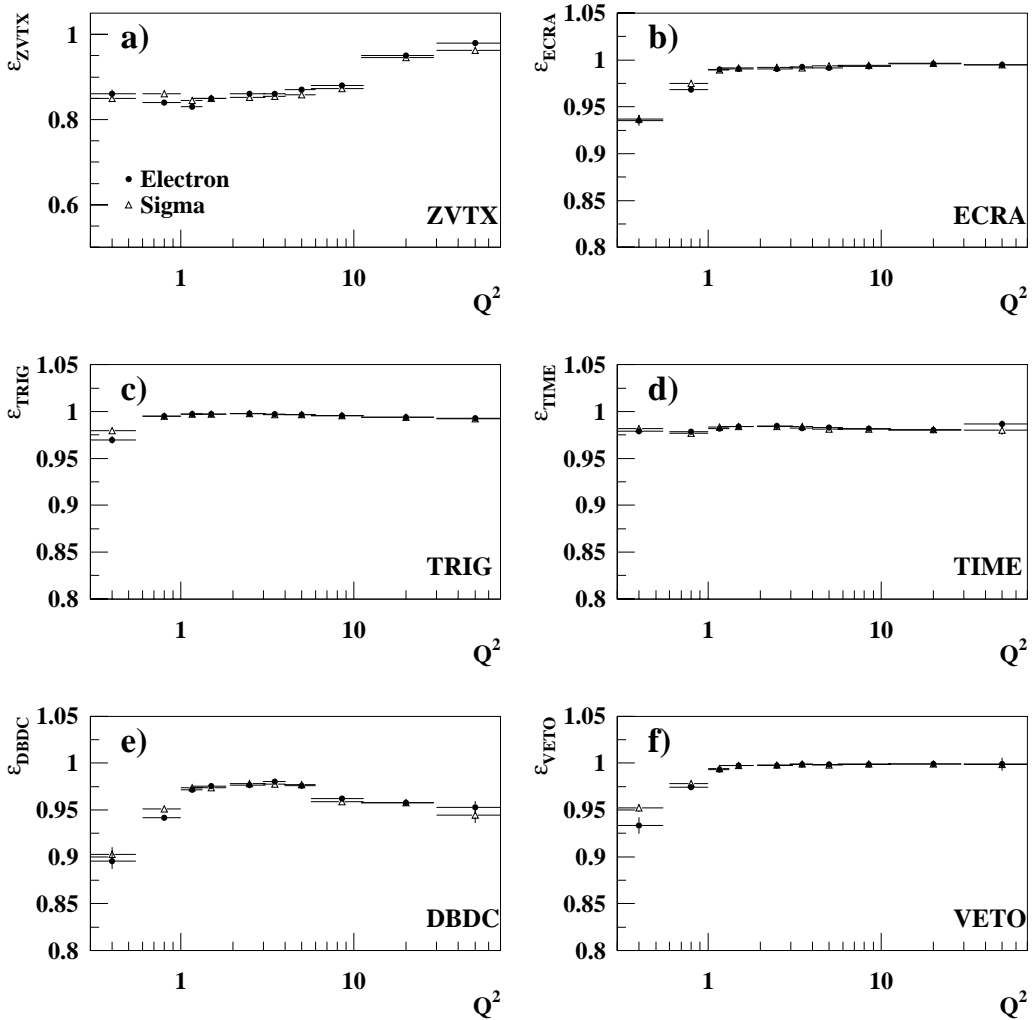


Figure 7.4: Efficiency of the DIS selection cuts as a function of Q^2 : a) ZVTX, b) ECRA, c) TRIG, d) TIME, e) DBDC and f) VETO. Filled circles are for electron method kinematics, open triangles are for sigma method.

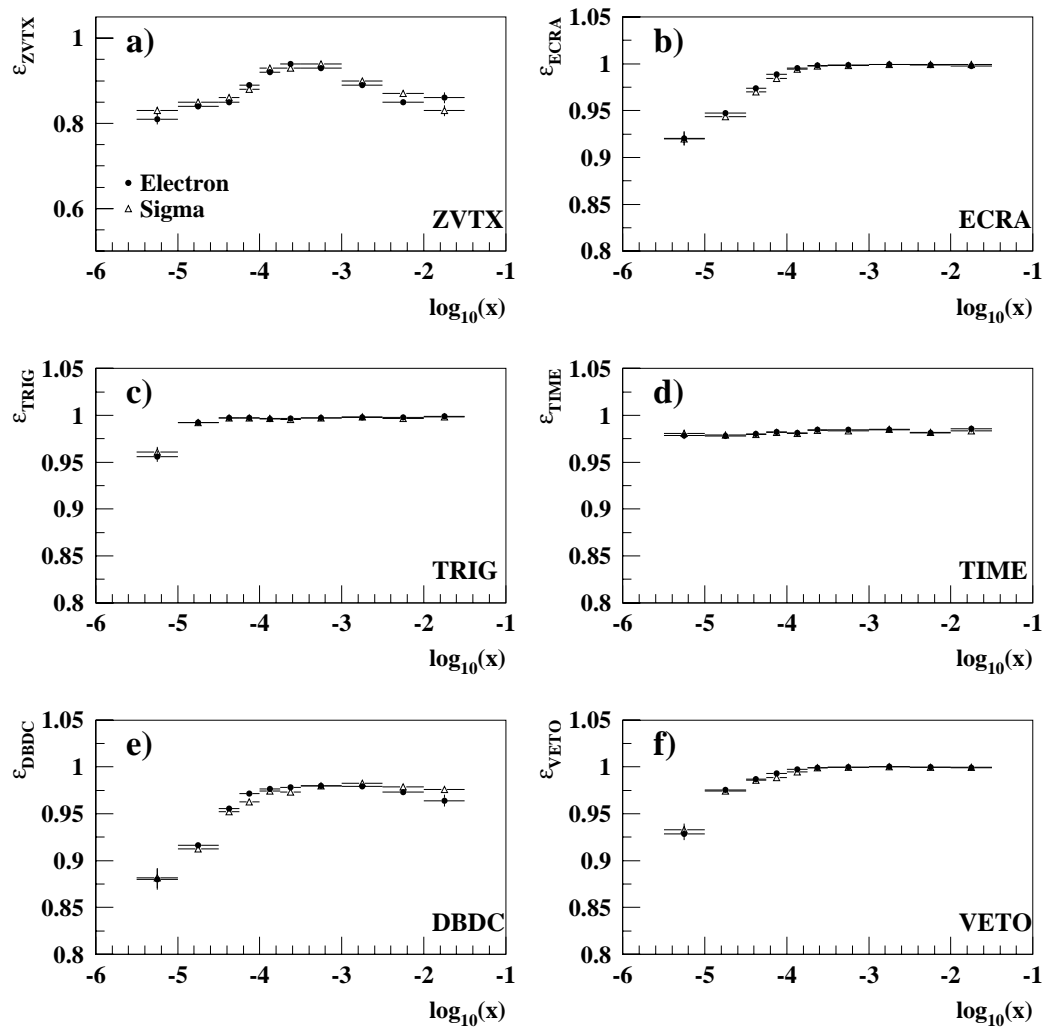


Figure 7.5: Efficiency of the DIS selection cuts as a function of $\log_{10}(x)$: a) ZVTX, b) ECRA, c) TRIG, d) TIME, e) DBDC and f) VETO. Filled circles are for electron method kinematics, open triangles are for sigma method.

value. The errors on each efficiency are added in quadrature.

7.5 Systematic Errors

A number of sources that contribute to the systematic error on the measurement have been considered. These are described below.

- **Electron energy:** the potential miscalibration of the electromagnetic energy scale in SPACAL varies linearly from 3% at 8 GeV to 1.5% at 27 GeV. The effect of this was estimated by shifting the scale for the electron candidate and recalculating the acceptance using the diffractive Monte Carlo. The average of the errors found by shifting the scale up and down was taken.
- **Electron angle:** a shift of up to 1mrad in the electron polar angle. The contribution to the total systematic error from this effect was determined in a similar way as for the electron energy.
- **SPACAL hadronic scale:** a potential error in this scale of 10% was considered. The error was calculated as above.
- **LAr hadronic scale:** a scale error of 4% was assigned, and the error calculated as above.
- **Noise correction uncertainty:** this is the error on the correction applied to account for noise in the forward detectors. From the investigation described in Section 6.7.4, this uncertainty was estimated to be 0.3%.
- **Overall normalisation uncertainty:** this arises from the uncertainty in the total integrated luminosity, and is due to the inherent error in the luminosity measurement and the correction applied for the effect of satellite bunches. The error was estimated to be 3%.
- **Monte Carlo x_P distribution uncertainty:** this is an estimate of the effect on the acceptance of the uncertainty in the input structure function. The acceptance was recalculated after increasing and decreasing the slope of the x_P distribution in the diffractive Monte Carlo with the function:

$$w = \frac{1}{x_P^{\pm 0.2}}. \quad (7.18)$$

The error was taken as the average of the change in acceptance calculated from each of the two slope shifts.

- **Monte Carlo β distribution uncertainty:** in a similar way to the x_P uncertainty, the β distribution was modified using the function:

$$w = \left(\frac{1}{g} - g \right) \beta + g, \quad (7.19)$$

where the distribution was hardened by using $g = 0.5$ and softened with $g = 2$. Again, this contribution to the systematic error was taken as the average in the change of the acceptance calculated from each distribution.

The systematic and statistical errors on the measurement are calculated individually for each bin and added in quadrature to derive the total error.

7.6 The Diffractive Proton Structure Function

The measured $F_2^{D(3)}(\beta, x_P, Q^2)$ values are presented as a function of x_P for each point in Q^2 and β defined by the binning described in Section 7.3. The values calculated by both the electron and sigma methods are shown. The two bins in Q^2 at 20 and 50 GeV² were completely excluded from the measurement due to lack of statistics. Bins where the contribution from events smearing in and out was large were rejected; data points for which the smeared acceptance was too small (< 0.2) or large (> 2.5) or where the purity was small (< 0.2) are therefore not shown.

Figure 7.6 shows $F_2^{D(3)}$ for both electron and sigma methods; it can be seen that there is good agreement between the two across the whole kinematic region shown. In many (Q^2, β) bins, the sigma method covers a wider range of x_P with sufficient purity for the points to be presented. The approximate $1/x_P$ dependence can be seen at all points in Q^2 and β . The final set of values for each measurement can be found in Appendix A.

In order to show the structure function in the finest detail possible, it is usual to present the quantity $x_P \cdot F_2^{D(3)}$. This is shown in Figures 7.7 and 7.8 for electron and sigma kinematic reconstruction methods respectively. Also shown on each are the points determined from the H1 analysis of 1994 data [51] which overlap the kinematic region of this measurement, and the parameterisation of the fit to these points, described in Section 2.4 in which a pomeron and a meson component contribute. The two measurements are in good agreement in the region of overlap. At low Q^2 and β there is a significant deviation of the parameterisation from the points determined in this analysis. The parameterisation was, however, purely phenomenological and it is not surprising that it breaks down in the new kinematic region investigated in this analysis.

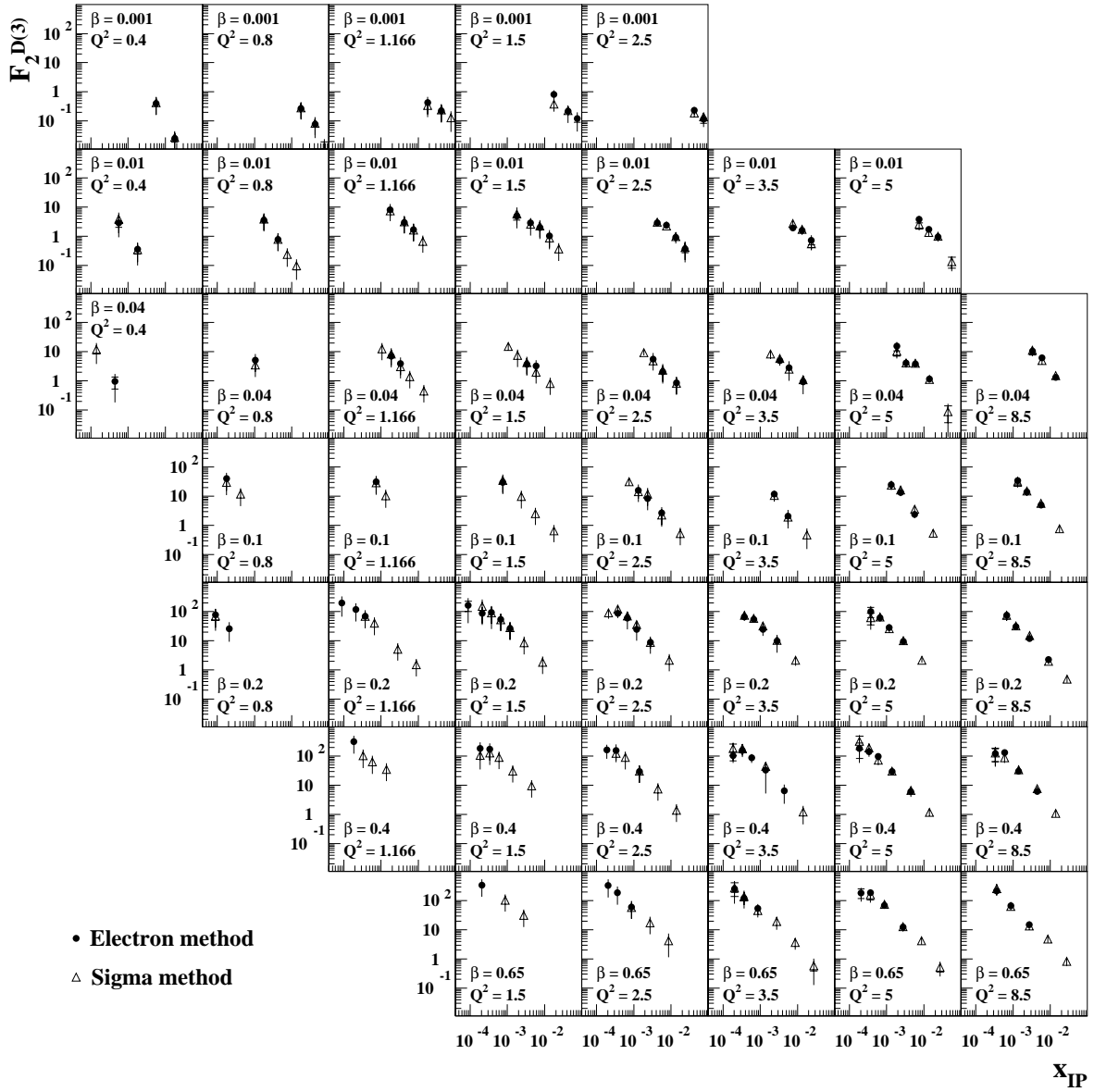


Figure 7.6: Comparison of measured $F_2^{D(3)}$ points for electron (closed circles) and sigma (open triangles) reconstruction methods.

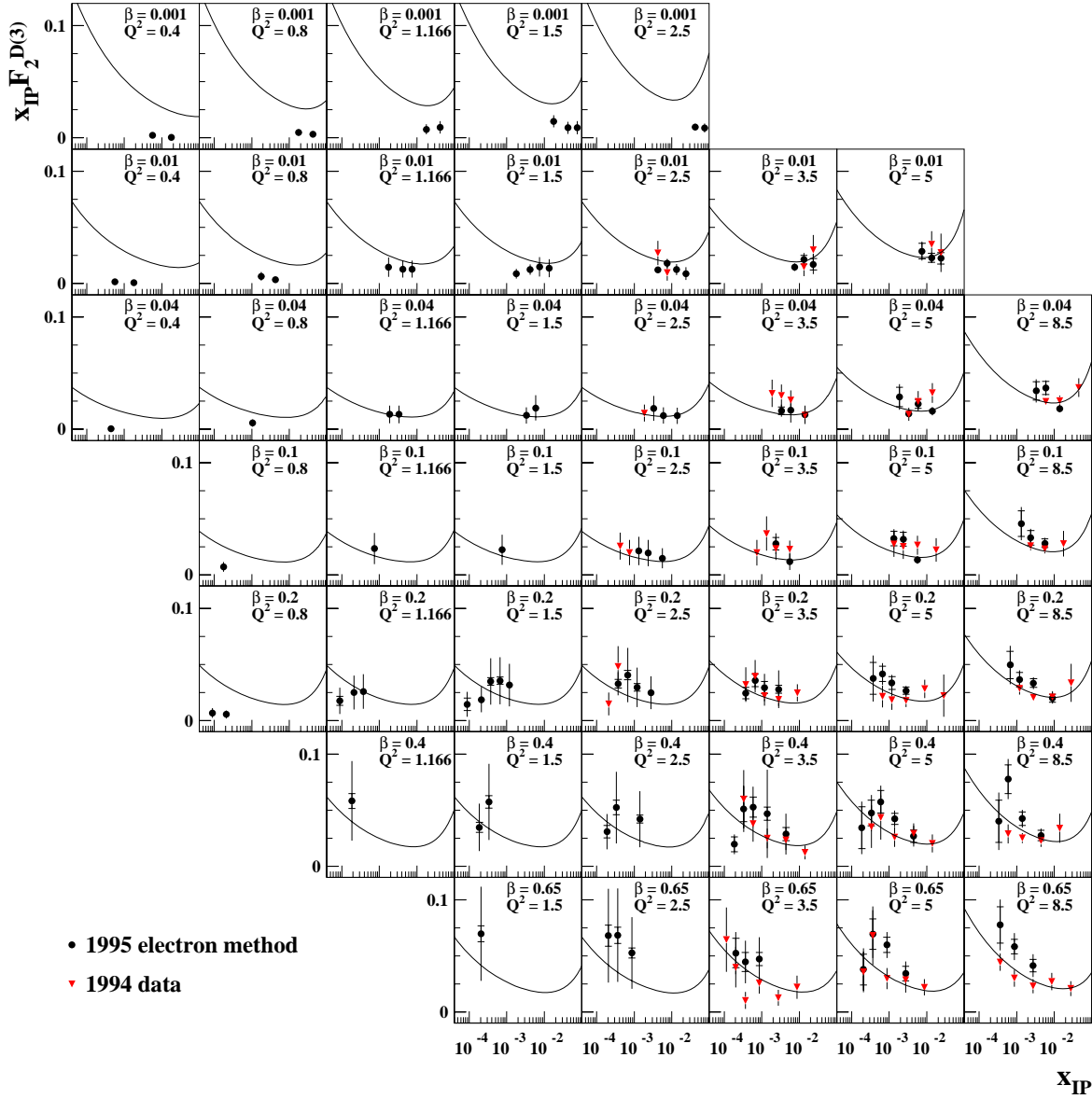


Figure 7.7: Comparison of $x_{\text{P}} \cdot F_2^{D(3)}$ measured by the electron method (filled circles) with the 1994 measurement (filled triangles) and the parameterisation of 1994 fit including pomeron and meson trajectories. Statistical (inner) and total (outer) errors are shown.

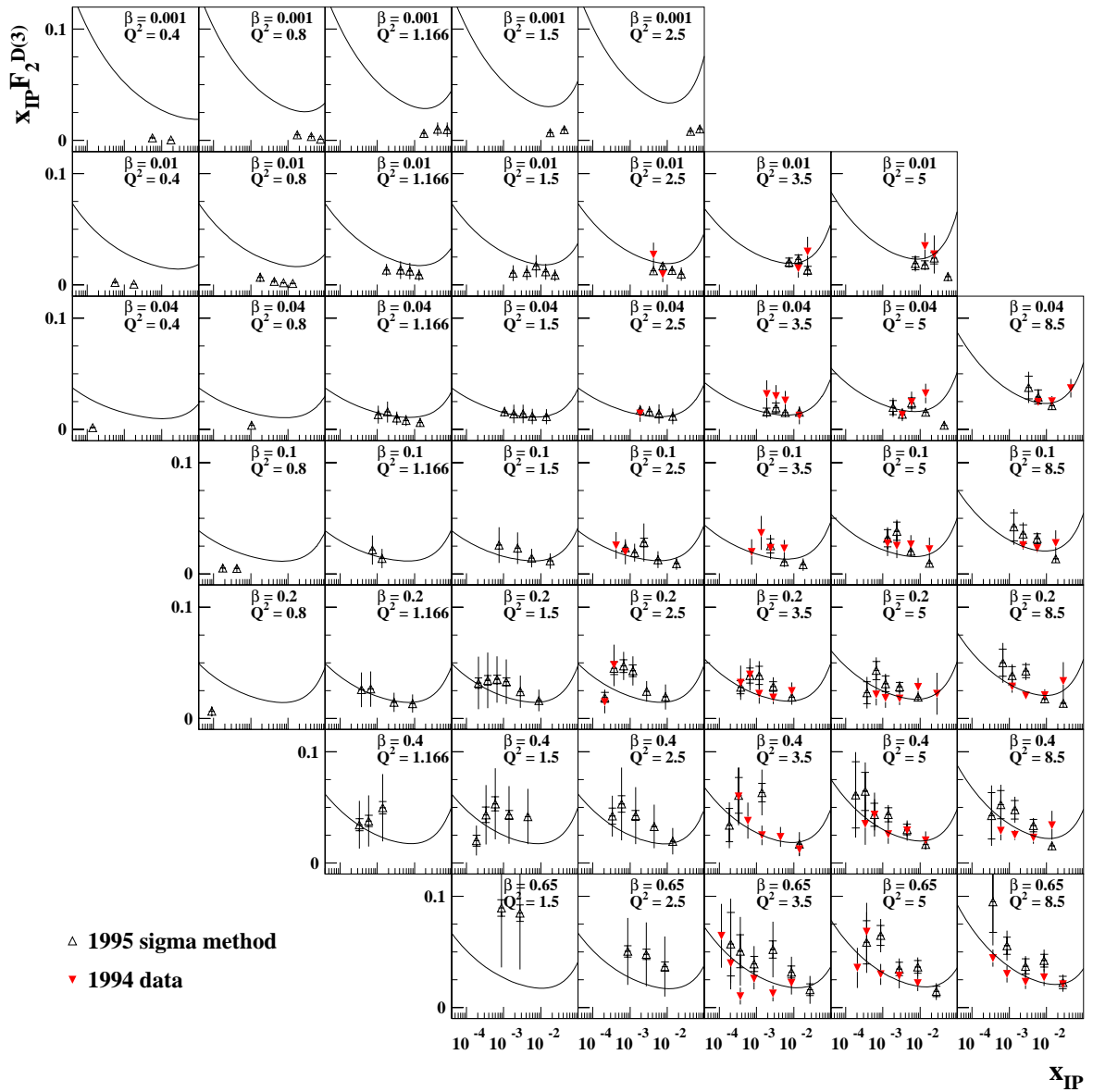


Figure 7.8: Comparison of $x_{IP} \cdot F_2^{D(3)}$ measured by the sigma method (open triangles) with the 1994 measurement (filled triangles) and the parameterisation of 1994 fit including pomeron and meson trajectories. Statistical (inner) and total (outer) errors are shown.

A phenomenological fit to the measurement has been performed. While there is good agreement between the values determined using the electron and sigma kinematic methods, the latter set contains more points in some regions of Q^2 and β and so was used for the fit. The functional form employed was from the Regge-motivated fit presented in Section 2.4, with the behaviour:

$$F_2^{D(3)} = \frac{A(Q^2, \beta)}{x_P^n}, \quad (7.20)$$

where n was allowed to vary as a function only of β and only of Q^2 in two separate fits and the normalisation, $A(Q^2, \beta)$, varied freely in each variable for both. In a Regge interpretation, $n = \langle 2\alpha(t) - 1 \rangle$, with $\alpha(t) = \alpha(0) + \alpha't$. Since the t distribution is expected to be highly peripheral [125], the value of $\langle \alpha(t) \rangle$ obtained from this fit is expected to be slightly ($\lesssim 5\%$) smaller than the intercept of the effective pomeron trajectory, $\alpha(0)$.

Figure 7.9 shows the sigma $x_P \cdot F_2^{D(3)}$ points with both fits superimposed, which were found to be consistent with the data ($\chi^2/ndf = 113/103$ for $n = n(\beta)$ and $\chi^2/ndf = 127/102$ for $n = n(Q^2)$). The values of n determined are shown in Figure 7.10. There is evidence for a variation as a function of both β and Q^2 . n is consistent with the previous measurement [51] at high β , but falls less rapidly with decreasing β . The variation as a function of Q^2 in which n falls steadily with decreasing $\log_{10}(Q^2)$, is contrary to the previous observation. However, at low Q^2 the accessible kinematic region restricts the measurement to low β and the variation of n with Q^2 may be an indirect consequence of the β dependence.

These results support those of the 1994 measurement since there is an unambiguous change in the value of n at low β , giving clear evidence for deviation from the hypothesis of factorisation in the diffractive structure function. This is consistent with the interpretation of the 1994 data in which a contribution is included from the exchange of a subleading meson trajectory with a smaller intercept than that of the pomeron. The meson component has a structure function, $F_2^M(\beta, Q^2)$, which falls rapidly with increasing β and therefore contributes most significantly to $F_2^{D(3)}$ at low β .

The results of the fit presented here contain the first evidence for the variation of n with $\log_{10}(Q^2)$, with the value falling steadily with decreasing Q^2 . This is of particular interest since it is expected that the pomeron intercept at $Q^2 = 0$ should be $\alpha(0) = 1.08$, as determined by from the fit of Donnachie and Landshoff to the total cross section in hadron-hadron collisions [43], while at higher Q^2 the hard pomeron is expected to have an intercept of $\alpha(0) \simeq 1.4$.

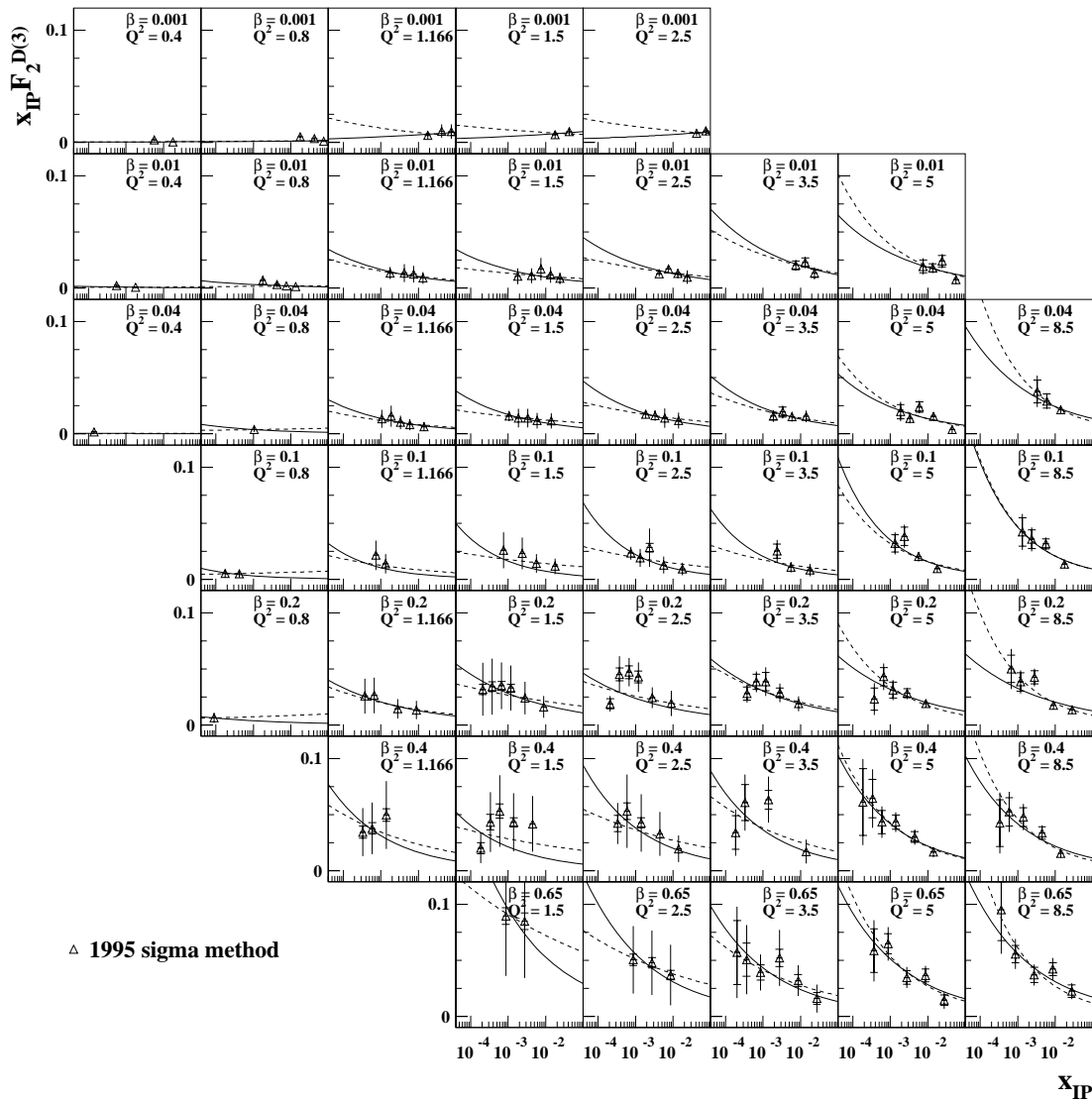


Figure 7.9: $x_{IP} \cdot F_2^{D(3)}$ calculated using sigma kinematics with the phenomenological fits $F_2^{D(3)} = A(Q^2, \beta)x_{IP}^{-n(\beta)}$ (solid line) and $F_2^{D(3)} = A(Q^2, \beta)x_{IP}^{-n(Q^2)}$ (dashed line).

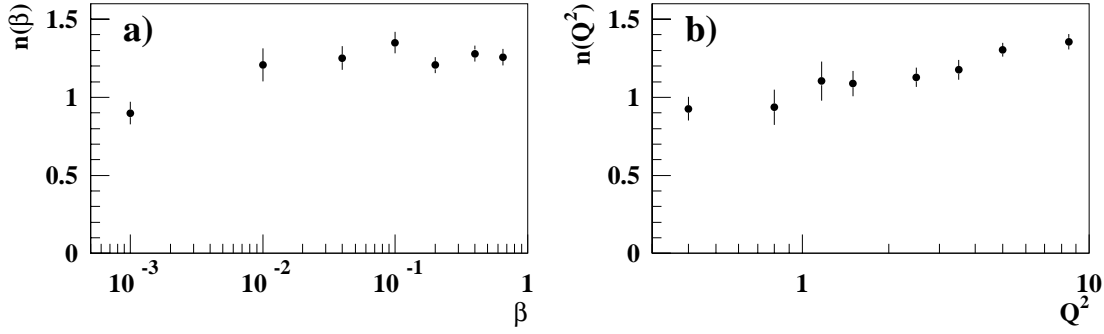


Figure 7.10: Result of the phenomenological fit to $F_2^{D(3)}$: the dependence of the exponent, n , on a) β and b) Q^2 when allowed to vary as a function of each variable.

7.7 Summary

The diffractive proton structure function, $F_2^{D(3)}$, has been measured in a new kinematic region at low β and Q^2 , exploiting the increased geometrical acceptance of the SPACAL calorimeter in the upgraded H1 detector. The use of SPACAL to detect scattered electrons at large angles ($\theta \lesssim 178^\circ$) in the 1995 shifted vertex data has proved to be feasible.

The measured $F_2^{D(3)}$ has been shown to be consistent with the previous measurement from the analysis of 1994 data, in the kinematic region where there is overlap, namely large β and Q^2 . A phenomenological fit to the data points is consistent with the previous measurement at high Q^2 and β and supports the finding that factorisation of the diffractive structure function is broken. The extension of the measurement to low Q^2 provides evidence that the pomeron intercept, $\alpha(0)$, evolves towards the value expected at $Q^2 = 0$ (1.08). Consideration must be taken of the fact that the measurement at low Q^2 is also at low β , where the contribution of meson exchanges becomes important. In order to isolate the two effects, a full fit to the entire range in Q^2 and β will be necessary.

This analysis has been primarily limited by the relatively small statistics available from the 1995 shifted vertex data. Difficulties have been highlighted in making a measurement in the new low Q^2 , high β region, where the resolution in β is dominated by that of M_x and significant smearing in β results. This could motivate an alternative binning method in M_x rather than β , which could then follow the resolution in a more natural way.

Future measurements of diffractive DIS will benefit from increased statistics, including nominal vertex running, allowing measurements to be made across a significantly larger portion of the kinematic plane. The first indications of interesting behaviour found here, particularly at low Q^2 can then be tested in more detail.

Appendix A

Measured Values of $F_2^{D(3)}$

The $F_2^{D(3)}(\beta, x_p, Q^2)$ values measured by electron and sigma methods, and presented in Section 7.6, are shown here. The calculated values and the statistical and systematic errors are listed for each bin presented. The number of observed events, N_{obs} , number of background events, N_{back} and acceptance, ε_{acc} are also shown.

Electron method

Q^2	β	$\log_{10}(x_p)$	$F_2^{D(3)}$	$\delta(\text{stat})$	$\delta(\text{syst})$	N_{obs}	N_{back}	ϵ_{acc}
0.4	0.001	-2.250	0.40	0.06	0.24	59	15.5	1.16
0.4	0.001	-1.750	0.03	0.01	0.02	21	5.2	0.72
0.4	0.010	-3.250	2.93	0.89	1.79	34	23.1	1.88
0.4	0.010	-2.750	0.36	0.11	0.23	16	6.0	0.82
0.4	0.040	-3.352	0.94	0.41	0.64	8	2.8	1.37
0.8	0.001	-1.750	0.27	0.02	0.16	196	45.0	1.35
0.8	0.001	-1.375	0.08	0.02	0.05	19	0.8	0.29
0.8	0.010	-2.750	3.58	0.28	2.08	234	69.3	2.50
0.8	0.010	-2.375	0.80	0.13	0.47	41	4.0	0.93
0.8	0.040	-2.977	5.17	0.68	3.06	63	4.4	1.38
0.8	0.100	-3.750	39.97	5.39	23.96	88	33.1	2.40
0.8	0.200	-4.051	77.00	16.31	45.84	43	20.7	1.05
0.8	0.200	-3.676	26.14	5.15	16.07	29	3.2	1.03
1.2	0.001	-1.750	0.43	0.06	0.25	53	9.2	1.27
1.2	0.001	-1.375	0.22	0.03	0.13	46	2.0	0.72
1.2	0.010	-2.750	8.14	0.89	4.77	97	13.5	2.49
1.2	0.010	-2.375	3.02	0.30	1.76	101	1.6	2.05
1.2	0.010	-2.125	1.71	0.19	1.00	79	0.4	1.25
1.2	0.040	-2.727	7.05	0.71	4.13	98	0.0	2.25
1.2	0.040	-2.477	3.96	0.44	2.31	83	0.4	1.75
1.2	0.100	-3.125	31.30	3.08	18.40	103	0.0	2.21
1.2	0.200	-4.051	197.96	46.62	122.51	26	8.0	1.53
1.2	0.200	-3.676	118.70	13.76	71.14	78	3.6	1.93
1.2	0.200	-3.426	69.02	6.71	40.82	107	1.2	1.93
1.2	0.400	-3.727	310.83	35.65	185.78	76	0.0	1.09
1.5	0.001	-1.750	0.82	0.17	0.25	33	9.2	1.19
1.5	0.001	-1.375	0.21	0.03	0.12	49	4.8	0.90
1.5	0.001	-1.125	0.12	0.03	0.07	17	0.4	0.26
1.5	0.010	-2.750	4.95	1.38	1.96	24	11.2	2.41
1.5	0.010	-2.375	2.92	0.32	1.05	93	8.8	2.13
1.5	0.010	-2.125	1.98	0.20	1.15	96	0.4	1.40
1.5	0.010	-1.875	1.02	0.13	0.60	59	0.0	0.87
1.5	0.040	-2.477	3.69	0.39	2.15	89	0.4	2.00
1.5	0.040	-2.227	3.21	0.33	1.88	96	0.0	1.40
1.5	0.100	-3.125	29.93	3.25	17.69	85	0.0	2.12
1.5	0.200	-4.051	164.06	62.86	106.98	10	3.2	2.32
1.5	0.200	-3.676	88.48	12.04	52.07	64	10.0	2.21
1.5	0.200	-3.426	93.08	8.87	54.62	110	0.0	1.63
1.5	0.200	-3.176	53.43	4.73	31.17	128	0.4	1.67
1.5	0.200	-2.926	26.73	2.30	15.88	135	0.0	1.87
1.5	0.400	-3.727	185.30	24.59	110.84	58	1.2	1.32
1.5	0.400	-3.477	172.17	16.88	100.59	104	0.0	1.28
1.5	0.650	-3.688	340.18	34.26	202.03	99	0.4	1.19

Electron method

Q^2	β	$\log_{10}(x_P)$	$F_2^{D(3)}$	$\delta(\text{stat})$	$\delta(\text{syst})$	N_{obs}	N_{back}	ε_{acc}
2.5	0.001	-1.375	0.23	0.05	0.04	24	5.6	0.93
2.5	0.001	-1.125	0.12	0.03	0.04	14	0.8	0.35
2.5	0.010	-2.375	2.89	0.47	0.32	52	14.7	2.16
2.5	0.010	-2.125	2.40	0.27	0.47	80	3.2	1.64
2.5	0.010	-1.875	0.94	0.14	0.34	45	0.0	1.02
2.5	0.010	-1.625	0.37	0.10	0.23	15	0.0	0.49
2.5	0.040	-2.477	5.60	0.61	3.29	84	0.8	1.82
2.5	0.040	-2.227	2.05	0.29	1.20	50	0.4	1.49
2.5	0.040	-1.852	0.86	0.13	0.50	45	0.0	0.65
2.5	0.100	-2.875	15.98	1.98	9.36	65	0.0	2.15
2.5	0.100	-2.625	8.25	1.13	4.83	54	0.4	1.62
2.5	0.100	-2.250	2.65	0.33	1.58	63	0.0	1.18
2.5	0.200	-3.426	87.72	10.02	25.59	85	8.4	2.02
2.5	0.200	-3.176	60.89	6.24	35.73	96	0.8	1.48
2.5	0.200	-2.926	24.97	2.81	14.62	79	0.0	1.51
2.5	0.200	-2.551	8.82	0.77	5.18	132	0.0	1.33
2.5	0.400	-3.727	164.71	29.11	78.27	34	2.0	1.46
2.5	0.400	-3.477	157.36	19.37	93.91	66	0.0	1.25
2.5	0.400	-2.852	29.91	2.55	17.62	138	0.0	1.28
2.5	0.650	-3.688	331.87	45.59	198.08	53	0.0	0.86
2.5	0.650	-3.438	187.70	19.90	112.52	89	0.0	1.26
2.5	0.650	-3.063	60.93	5.17	36.56	139	0.0	1.32
3.5	0.010	-2.125	1.96	0.38	0.24	31	4.4	2.03
3.5	0.010	-1.875	1.59	0.28	0.36	33	0.8	1.29
3.5	0.010	-1.625	0.72	0.22	0.29	11	0.0	0.47
3.5	0.040	-2.477	4.95	1.00	1.29	26	1.6	1.80
3.5	0.040	-2.227	2.85	0.52	1.78	31	0.4	1.64
3.5	0.040	-1.852	0.93	0.19	0.55	23	0.0	0.73
3.5	0.100	-2.625	11.77	2.35	3.15	25	0.0	1.59
3.5	0.100	-2.250	2.09	0.42	1.23	25	0.0	1.40
3.5	0.200	-3.426	65.42	13.29	11.05	29	4.8	2.45
3.5	0.200	-3.176	53.53	8.34	7.79	44	2.8	1.82
3.5	0.200	-2.926	24.86	4.57	9.24	30	0.4	1.39
3.5	0.200	-2.551	9.90	1.26	5.86	62	0.0	1.40
3.5	0.400	-3.727	104.80	34.92	30.84	11	2.0	1.99
3.5	0.400	-3.477	153.56	33.83	51.73	21	0.4	1.21
3.5	0.400	-3.227	89.15	15.29	26.49	34	0.0	1.38
3.5	0.400	-2.852	33.35	4.17	27.73	64	0.0	1.34
3.5	0.400	-2.352	6.45	1.32	3.90	24	0.0	0.80

Electron method

Q^2	β	$\log_{10}(x_p)$	$F_2^{D(3)}$	$\delta(\text{stat})$	$\delta(\text{syst})$	N_{obs}	N_{back}	ε_{acc}
3.5	0.650	-3.688	255.88	63.96	66.74	18	2.0	0.90
3.5	0.650	-3.438	122.39	23.13	46.74	28	0.0	1.54
3.5	0.650	-3.063	54.65	6.73	21.52	66	0.0	1.46
5.0	0.010	-2.125	3.85	0.93	0.65	19	2.0	1.95
5.0	0.010	-1.875	1.72	0.30	0.20	35	1.2	1.43
5.0	0.010	-1.625	0.95	0.22	0.16	19	0.0	0.65
5.0	0.040	-2.727	15.37	4.63	3.88	13	2.0	1.80
5.0	0.040	-2.477	4.11	0.88	0.58	25	3.2	2.25
5.0	0.040	-2.227	3.82	0.69	0.44	31	0.0	1.37
5.0	0.040	-1.852	1.14	0.22	0.14	27	0.0	0.75
5.0	0.100	-2.875	24.34	4.97	3.93	26	2.0	1.69
5.0	0.100	-2.625	13.40	2.58	1.95	27	0.0	1.44
5.0	0.100	-2.250	2.38	0.50	0.37	23	0.0	1.29
5.0	0.200	-3.426	100.31	37.89	39.66	9	2.0	2.16
5.0	0.200	-3.176	62.44	10.24	10.37	38	0.8	1.88
5.0	0.200	-2.926	28.28	4.81	3.79	35	0.4	1.59
5.0	0.200	-2.551	9.48	1.15	0.90	68	0.0	1.65
5.0	0.400	-3.727	183.35	99.34	76.12	5	1.6	1.39
5.0	0.400	-3.477	142.87	34.45	33.25	18	0.8	1.35
5.0	0.400	-3.227	97.05	16.84	17.88	34	0.8	1.51
5.0	0.400	-2.852	30.12	3.58	3.81	71	0.4	1.61
5.0	0.400	-2.352	6.03	1.23	1.66	24	0.0	0.93
5.0	0.650	-3.688	184.70	66.99	63.32	8	0.4	0.87
5.0	0.650	-3.438	190.35	37.33	44.53	26	0.0	1.08
5.0	0.650	-3.063	69.18	7.78	10.90	79	0.0	1.46
5.0	0.650	-2.563	12.57	2.38	3.11	28	0.0	0.87
8.5	0.040	-2.477	10.26	2.49	1.84	19	2.0	1.80
8.5	0.040	-2.227	6.20	1.00	0.53	39	0.4	1.30
8.5	0.040	-1.852	1.31	0.21	0.11	40	0.0	1.03
8.5	0.100	-2.875	34.31	8.47	7.24	18	1.6	1.97
8.5	0.100	-2.625	13.96	2.77	2.02	27	1.6	1.60
8.5	0.100	-2.250	5.02	0.69	0.47	53	0.0	1.41
8.5	0.200	-3.176	74.37	18.14	18.47	18	1.2	2.18
8.5	0.200	-2.926	30.83	5.48	4.12	32	0.4	1.51
8.5	0.200	-2.551	11.91	1.41	1.22	71	0.0	1.53
8.5	0.200	-2.051	2.26	0.40	0.40	32	0.0	1.01
8.5	0.400	-3.477	120.46	56.16	52.42	5	0.4	1.60
8.5	0.400	-3.227	131.15	21.68	21.16	37	0.4	1.35
8.5	0.400	-2.852	30.25	4.32	3.59	49	0.0	1.34
8.5	0.400	-2.352	6.19	1.03	0.95	36	0.0	1.31
8.5	0.650	-3.438	213.14	44.44	43.48	23	0.0	0.95
8.5	0.650	-3.063	67.43	7.64	11.66	78	0.0	1.60
8.5	0.650	-2.563	15.11	2.02	3.18	56	0.0	1.47

Sigma method

Q^2	β	$\log_{10}(x_P)$	$F_2^{D(3)}$	$\delta(\text{stat})$	$\delta(\text{syst})$	N_{obs}	N_{back}	ε_{acc}
0.4	0.001	-2.250	0.42	0.07	0.25	55	15.5	0.96
0.4	0.001	-1.750	0.03	0.00	0.02	54	12.8	1.51
0.4	0.010	-3.250	3.90	1.14	2.36	38	26.3	1.48
0.4	0.010	-2.750	0.35	0.07	0.21	40	12.8	1.76
0.4	0.040	-3.852	11.96	3.45	7.36	28	15.9	2.20
0.8	0.001	-1.750	0.28	0.02	0.17	173	40.6	1.18
0.8	0.001	-1.375	0.08	0.01	0.05	39	2.0	0.53
0.8	0.001	-1.125	0.01	0.01	0.01	6	0.0	0.30
0.8	0.010	-2.750	3.89	0.34	2.27	195	61.8	2.00
0.8	0.010	-2.375	0.78	0.09	0.46	76	6.4	1.76
0.8	0.010	-2.125	0.24	0.04	0.14	38	0.4	1.61
0.8	0.010	-1.875	0.10	0.03	0.06	14	0.0	0.78
0.8	0.040	-2.977	3.50	0.46	2.08	66	8.0	2.00
0.8	0.100	-3.750	29.57	5.81	17.63	55	29.1	1.89
0.8	0.100	-3.375	11.79	1.58	7.00	64	8.4	2.40
0.8	0.200	-4.051	71.45	21.69	43.99	24	13.2	0.61
1.2	0.001	-1.750	0.35	0.06	0.20	49	11.2	1.34
1.2	0.001	-1.375	0.24	0.04	0.14	43	1.2	0.66
1.2	0.001	-1.125	0.13	0.03	0.08	19	0.0	0.27
1.2	0.010	-2.750	7.55	1.04	2.82	71	17.9	2.04
1.2	0.010	-2.375	3.15	0.38	1.84	71	3.6	1.41
1.2	0.010	-2.125	1.66	0.19	0.97	75	0.0	1.26
1.2	0.010	-1.875	0.67	0.09	0.39	57	0.0	1.20
1.2	0.040	-2.977	12.60	1.42	7.39	81	2.8	2.36
1.2	0.040	-2.727	8.39	0.97	4.92	75	0.8	1.54
1.2	0.040	-2.477	3.04	0.37	1.79	67	0.4	1.84
1.2	0.040	-2.227	1.38	0.18	0.82	62	0.0	1.97
1.2	0.040	-1.852	0.45	0.05	0.26	94	0.0	1.96
1.2	0.100	-3.125	28.76	3.44	17.10	71	1.2	1.61
1.2	0.100	-2.875	10.43	1.41	6.25	55	0.0	1.82
1.2	0.200	-3.426	68.91	8.07	40.71	75	2.0	1.41
1.2	0.200	-3.176	39.68	4.76	23.47	70	0.4	1.20
1.2	0.200	-2.551	5.16	0.45	3.06	129	0.0	2.29
1.2	0.200	-2.051	1.51	0.19	0.89	61	0.0	1.02
1.2	0.400	-3.477	103.20	16.40	62.00	40	0.4	0.89
1.2	0.400	-3.227	63.79	8.52	38.05	56	0.0	1.31
1.2	0.400	-2.852	35.38	3.98	21.06	79	0.0	1.00
1.5	0.001	-1.750	0.38	0.09	0.15	24	7.2	1.49
1.5	0.001	-1.375	0.23	0.04	0.07	41	6.4	0.79

Sigma method

Q^2	β	$\log_{10}(x_P)$	$F_2^{D(3)}$	$\delta(\text{stat})$	$\delta(\text{syst})$	N_{obs}	N_{back}	ε_{acc}
1.5	0.010	-2.750	5.92	1.64	3.67	21	8.0	2.03
1.5	0.010	-2.375	2.63	0.35	1.54	67	11.6	1.69
1.5	0.010	-2.125	2.26	0.24	1.31	87	0.8	1.13
1.5	0.010	-1.875	0.88	0.11	0.51	60	0.0	1.03
1.5	0.010	-1.625	0.36	0.06	0.21	34	0.0	0.73
1.5	0.040	-2.977	15.12	1.74	3.92	82	6.4	2.24
1.5	0.040	-2.727	7.40	0.91	4.34	69	2.4	1.65
1.5	0.040	-2.477	4.21	0.50	2.46	72	1.2	1.45
1.5	0.040	-2.227	1.97	0.23	1.15	76	0.4	1.77
1.5	0.040	-1.852	0.81	0.07	0.47	139	0.0	1.58
1.5	0.100	-3.125	34.73	4.43	20.89	63	1.6	1.38
1.5	0.100	-2.625	9.77	1.11	5.85	77	0.0	1.45
1.5	0.100	-2.250	2.53	0.22	1.48	134	0.0	2.00
1.5	0.100	-1.750	0.65	0.08	0.38	70	0.0	1.28
1.5	0.200	-3.676	151.35	22.12	109.64	52	5.2	1.32
1.5	0.200	-3.426	91.50	11.53	65.34	67	4.0	1.03
1.5	0.200	-3.176	52.63	5.77	30.82	84	0.8	1.08
1.5	0.200	-2.926	27.90	2.96	16.71	89	0.4	1.12
1.5	0.200	-2.551	8.56	0.69	5.15	156	0.4	1.41
1.5	0.200	-2.051	1.82	0.15	1.09	138	0.0	1.75
1.5	0.400	-3.727	107.19	26.96	66.50	17	1.2	0.79
1.5	0.400	-3.477	130.08	20.67	77.65	40	0.4	0.74
1.5	0.400	-3.227	89.81	10.81	52.61	69	0.0	0.94
1.5	0.400	-2.852	30.75	2.91	18.12	112	0.0	0.99
1.5	0.400	-2.352	9.40	0.78	5.52	146	0.0	1.26
1.5	0.650	-3.063	103.55	8.54	61.21	147	0.0	0.85
1.5	0.650	-2.563	31.02	2.69	18.29	133	0.4	1.00
2.5	0.001	-1.375	0.19	0.05	0.03	23	5.6	1.07
2.5	0.001	-1.125	0.14	0.04	0.03	15	1.2	0.34
2.5	0.010	-2.375	3.05	0.53	0.38	44	10.4	2.00
2.5	0.010	-2.125	2.27	0.29	0.27	69	5.6	1.41
2.5	0.010	-1.875	0.98	0.15	0.27	45	0.8	0.99
2.5	0.010	-1.625	0.41	0.08	0.25	29	0.0	0.81
2.5	0.040	-2.727	9.32	1.26	1.43	61	6.4	1.65
2.5	0.040	-2.477	4.85	0.71	1.22	48	1.6	1.35
2.5	0.040	-2.227	2.35	0.31	1.40	59	0.8	1.52
2.5	0.040	-1.852	0.84	0.09	0.49	80	0.4	1.15
2.5	0.100	-3.125	31.15	4.41	6.37	53	3.2	1.95
2.5	0.100	-2.875	14.40	2.51	5.47	33	0.0	1.32
2.5	0.100	-2.625	11.93	1.68	7.03	51	0.8	1.08
2.5	0.100	-2.250	2.27	0.29	1.32	62	0.0	1.38
2.5	0.100	-1.750	0.52	0.07	0.30	50	0.0	1.44

Sigma method

Q^2	β	$\log_{10}(x_P)$	$F_2^{D(3)}$	$\delta(\text{stat})$	$\delta(\text{syst})$	N_{obs}	N_{back}	ϵ_{acc}
2.5	0.200	-3.676	89.77	21.03	25.19	23	4.8	1.80
2.5	0.200	-3.426	120.59	15.12	40.82	68	4.4	1.37
2.5	0.200	-3.176	70.85	8.59	16.78	70	2.0	1.00
2.5	0.200	-2.926	36.19	4.35	10.20	70	0.8	0.89
2.5	0.200	-2.551	8.69	0.84	3.19	107	0.4	1.13
2.5	0.200	-2.051	2.17	0.20	1.26	121	0.0	1.50
2.5	0.400	-3.477	126.62	22.04	50.66	33	0.0	0.79
2.5	0.400	-3.227	89.75	12.54	53.72	52	0.8	0.82
2.5	0.400	-2.852	30.34	3.20	17.93	90	0.0	0.93
2.5	0.400	-2.352	7.39	0.71	4.33	107	0.0	1.30
2.5	0.400	-1.852	1.39	0.20	0.82	49	0.0	1.03
2.5	0.650	-3.063	58.41	5.88	34.24	100	1.2	0.99
2.5	0.650	-2.563	17.49	1.72	10.38	103	0.0	1.05
2.5	0.650	-2.063	4.26	0.49	3.09	77	0.0	1.08
3.5	0.010	-2.125	2.71	0.52	0.35	29	2.0	1.53
3.5	0.010	-1.875	1.71	0.30	0.23	32	0.4	1.09
3.5	0.010	-1.625	0.56	0.15	0.17	14	0.0	0.75
3.5	0.040	-2.727	8.42	1.88	2.00	22	2.0	2.43
3.5	0.040	-2.477	5.80	1.33	1.13	21	2.0	1.14
3.5	0.040	-2.227	2.54	0.52	0.50	25	0.8	1.60
3.5	0.040	-1.852	1.10	0.18	0.33	37	0.0	1.19
3.5	0.100	-2.625	10.64	2.64	3.25	17	0.8	1.14
3.5	0.100	-2.250	1.94	0.40	0.72	24	0.0	1.53
3.5	0.100	-1.750	0.47	0.11	0.29	17	0.0	1.37
3.5	0.200	-3.426	74.90	15.75	14.90	25	2.4	1.93
3.5	0.200	-3.176	58.09	10.24	9.32	33	0.8	1.37
3.5	0.200	-2.926	32.70	6.94	8.14	23	0.8	0.91
3.5	0.200	-2.551	10.25	1.52	2.55	46	0.4	1.10
3.5	0.200	-2.051	2.14	0.33	0.68	43	0.0	1.55
3.5	0.400	-3.727	181.98	79.78	76.33	6	0.8	0.81
3.5	0.400	-3.477	182.36	48.39	57.70	15	0.8	0.69
3.5	0.400	-2.852	45.08	5.97	13.33	57	0.0	0.90
3.5	0.400	-1.852	1.21	0.23	0.73	28	0.0	1.39
3.5	0.650	-3.688	277.92	138.96	142.28	4	0.0	0.38
3.5	0.650	-3.438	138.63	40.70	74.21	12	0.4	0.64
3.5	0.650	-3.063	45.29	8.01	16.85	32	0.0	1.16
3.5	0.650	-2.563	19.07	2.81	8.67	46	0.0	1.03
3.5	0.650	-2.063	3.69	0.62	1.48	35	0.0	1.13
3.5	0.650	-1.563	0.58	0.19	0.41	9	0.0	0.61

Sigma method

Q^2	β	$\log_{10}(x_P)$	$F_2^{D(3)}$	$\delta(\text{stat})$	$\delta(\text{syst})$	N_{obs}	N_{back}	ε_{acc}
5.0	0.010	-2.125	2.58	0.78	0.57	13	2.0	2.01
5.0	0.010	-1.875	1.34	0.27	0.18	25	1.2	1.33
5.0	0.010	-1.625	1.02	0.22	0.16	23	0.8	0.70
5.0	0.010	-1.250	0.14	0.06	0.04	6	0.0	0.29
5.0	0.040	-2.727	10.51	3.43	3.06	11	1.6	2.43
5.0	0.040	-2.477	4.09	1.05	0.77	18	2.8	1.71
5.0	0.040	-2.227	4.02	0.79	0.55	26	0.0	1.14
5.0	0.040	-1.852	1.11	0.18	0.11	36	0.0	1.02
5.0	0.040	-1.352	0.09	0.05	0.06	3	0.0	0.37
5.0	0.100	-2.875	24.08	5.74	4.80	18	0.4	1.32
5.0	0.100	-2.625	16.21	3.41	2.74	23	0.4	1.05
5.0	0.100	-2.250	3.61	0.62	0.40	34	0.4	1.25
5.0	0.100	-1.750	0.55	0.13	0.12	19	0.0	1.39
5.0	0.200	-3.426	61.82	26.59	26.60	7	1.6	2.47
5.0	0.200	-3.176	64.70	12.18	12.85	29	0.8	1.56
5.0	0.200	-2.926	26.30	5.94	4.78	20	0.4	1.09
5.0	0.200	-2.551	10.09	1.45	1.11	49	0.4	1.18
5.0	0.200	-2.051	2.16	0.31	0.23	49	0.4	1.51
5.0	0.400	-3.727	326.43	159.23	129.04	5	0.8	0.82
5.0	0.400	-3.477	193.18	51.63	58.47	14	0.0	0.91
5.0	0.400	-3.227	73.35	17.48	16.05	18	0.4	1.00
5.0	0.400	-2.852	30.91	4.51	4.34	47	0.0	1.11
5.0	0.400	-2.352	6.76	1.08	1.09	39	0.0	1.26
5.0	0.400	-1.852	1.19	0.23	0.22	26	0.0	1.52
5.0	0.650	-3.438	160.69	53.56	52.28	9	0.0	0.46
5.0	0.650	-3.063	74.79	10.37	13.82	52	0.0	0.98
5.0	0.650	-2.563	12.69	2.24	2.62	32	0.0	1.07
5.0	0.650	-2.063	4.23	0.67	0.73	40	0.0	1.06
5.0	0.650	-1.563	0.53	0.17	0.22	10	0.0	0.73
8.5	0.040	-2.477	11.34	3.05	2.93	15	1.2	1.59
8.5	0.040	-2.227	4.92	1.05	0.56	23	1.2	1.00
8.5	0.040	-1.852	1.51	0.21	0.13	54	0.0	1.20
8.5	0.100	-2.875	31.74	9.40	7.48	13	1.6	1.54
8.5	0.100	-2.625	15.07	3.53	2.79	19	0.8	1.24
8.5	0.100	-2.250	5.65	0.79	0.57	51	0.4	1.21
8.5	0.100	-1.750	0.76	0.15	0.10	25	0.0	1.35
8.5	0.200	-3.176	75.19	18.24	19.73	17	0.0	2.27
8.5	0.200	-2.926	32.46	6.98	5.33	22	0.4	1.08
8.5	0.200	-2.551	15.13	2.08	1.85	53	0.0	1.01
8.5	0.200	-2.051	1.97	0.32	0.17	38	0.4	1.33
8.5	0.200	-1.551	0.49	0.10	0.07	23	0.0	1.03

Sigma method

Q^2	β	$\log_{10}(x_P)$	$F_2^{D(3)}$	$\delta(\text{stat})$	$\delta(\text{syst})$	N_{obs}	N_{back}	ϵ_{acc}
8.5	0.400	-3.477	127.46	62.17	52.83	5	0.8	1.26
8.5	0.400	-3.227	88.54	21.35	21.66	18	0.8	1.05
8.5	0.400	-2.852	34.08	5.97	5.91	33	0.4	0.92
8.5	0.400	-2.352	7.57	1.23	0.92	38	0.0	1.13
8.5	0.400	-1.852	1.10	0.22	0.16	25	0.0	1.46
8.5	0.650	-3.438	261.05	75.36	77.33	12	0.0	0.49
8.5	0.650	-3.063	64.32	8.83	12.76	53	0.0	1.13
8.5	0.650	-2.563	13.52	2.47	2.39	30	0.0	1.05
8.5	0.650	-2.063	4.87	0.66	0.94	55	0.0	1.29
8.5	0.650	-1.563	0.82	0.20	0.17	17	0.0	0.78

Glossary

A list of acronyms and abbreviations used frequently during the discussing of SPACAL and the TDC system in Chapters 4 and 5 is given here, for the convenience of the reader.

ADC	Analogue to Digital Conversion
ANBX	Analogue Box
ANCA	Analogue Card
AToF	Anti-Time-of-Flight
BCO	Bunch Crossing
BDC	Backward Drift Chamber
BPLUG	Backward plug SPACAL section
CAM	Calibration Module
CFD	Constant Fraction Discriminator
CSR	Control and Status Register
DAC	Digital to Analogue Conversion
DAQ	Data Acquisition
DCEL	DST cell bank (calorimeter energy)
DSP	Digital Signal Processor
DST	Data Summary Tape
ECL	Emitter Coupled Logic
EM	Electromagnetic SPACAL section
FEC	Front-end Card
FIFO	First-in First-out memory
GIET	Global Inclusive Electron Trigger
HAD	Hadronic SPACAL section
HCLK	Hera Clock
HV	High Voltage
IET	Inclusive Electron Trigger
L1/2/3	Level 1/2/3 Trigger
L1K	Trigger Level 1 Keep

LIET	Local Inclusive Electron Trigger
LUT	Look-up Tables
MDS	DSP Service Module
MIP	Minimum-ionising Particle
PE	Pipeline Enable
PLL	Phase-locked Loop
PMT	Photomultiplier Tube
POT	Production Output Tape
PQZP	Parallel Quickbus Zero-suppression Processor
RPTR	TMC Read Pointer
SCM	System Controller Module
SE0R	SPACAL Energy bank (Zeroth Scale)
SIMRAM	Simulator RAM
SIO	Serial Input-Output
SNGR	SPACAL geometrical numbering bank
SPACAL	Spaghetti Calorimeter
SPTIME	SPACAL TDC Reconstruction Module
SRTE	SPACAL raw time bank
STC	Subsystem Trigger Controller
T1/2/3	IET Thresholds level 1/2/3
TDC	Time to Digital Conversion
THM	TDC and Histogrammer Module
TMC	Time Memory Cell
TMCCLK	TMC clock
ToF	Time-of-Flight
VBR	VME Branch Receiver
VIC	Vertical Interconnect Card
VME	VersaModule Europe bus standard
VMVbus	VME Vertical bus
WPTR	TMC Write Pointer
WSTART	Write Start

References

- [1] R.E. Taylor, Rev. Mod. Phys. **63** (1991) 573.
H.W. Kendall, Rev. Mod. Phys. **63** (1991) 597.
J.I. Friedman, Rev. Mod. Phys. **63** (1991) 615.
- [2] T. Ahmed et al. (H1 Collaboration), Nucl. Phys. **B429** (1994) 477.
- [3] M. Derrick et al. (ZEUS Collaboration), Phys. Lett. **B315** (1993) 481.
- [4] F.E. Close, *An Introduction to Quarks and Partons*, Academic Press, (1979).
- [5] F. Halzen and A. Martin, *Quarks and Leptons* John Wiley (1984).
- [6] A.M. Cooper-Sarkar et al., Proceedings of the Workshop Physics at HERA, eds, W. Buchmüller and G. Ingelman, DESY, **1** (1992) 155.
- [7] M.W. Krasny et al., Proceedings of the Workshop Physics at HERA, eds, W. Buchmüller and G. Ingelman, DESY, **1** (1992) 171.
- [8] J.D. Bjorken, Phys. Rev. **163** (1967) 1767.
- [9] C. Callan, D. Gross, Phys. Rev. Lett. **21** (1968) 311.
- [10] R. Voss, *Deep-Inelastic Lepton Scattering*, Lectures presented in the CERN Summer Student Lecture Programme, 1992.
- [11] C. Adloff, et al. (H1 Collaboration), Phys. Lett. **B393** (1997) 452.
- [12] S. Aid, et al. (H1 Collaboration), Nucl. Phys. **B470** (1996) 3.
- [13] C. Adloff, et al. (H1 Collaboration), DESY-97-042, Submitted to Nucl. Phys. **B**.
- [14] J. Bartels, *Structure Functions at Small- x : New Physics at HERA*, DESY-90-153.
- [15] E.M. Levin, *Parton Density at Small x_B* , DESY-92-122.
- [16] J. Bartels and J. Feltesse, Proceedings of the Workshop Physics at HERA, eds, W. Buchmüller and G. Ingelman, DESY, **1** (1992) 131.

- [17] J. Feltesse, *Low x Physics, Deep Inelastic Scattering and Structure Functions*, Rapporteur talk at 24th International Conference on High Energy Physics, Glasgow, July 1994.
- [18] V. Gribov, et al., Sov. J. Nucl. Phys. **B15** (1972) 438.
- [19] G. Altarelli and G. Parisi, Nucl. Phys. **B126** (1977) 298.
- [20] A. Martin, W. Stirling and R. Roberts, Phys. Lett. **B354** (1995) 155.
- [21] M. Glück, E. Reya and A. Vogt, Phys. Lett. **B306** (1993) 391.
- [22] A. Vogt, *On dynamical parton distributions of hadrons and photons*, Talk at the Workshop on DIS and QCD, Paris, April 1995.
- [23] R. Ball and S. Forte, Phys. Lett. **B225** (1994) 77.
- [24] E. Kuraev, L. Lipatov and V. Fadin, Sov. Phys. JETP. **44** (1976) 443.
- [25] Y. Balitski and L. Lipatov, Sov. J. Nucl. Phys. **28** (1978) 822.
- [26] S. Aid, et al. (The H1 Collaboration), Phys. Lett. **B356** (1995) 118.
- [27] L. Gribov, E. Levin and M. Ryskin, Phys. Rep. **100** (1983) 1463.
- [28] S. Aid, et al. (The H1 Collaboration), Nucl. Phys. **B449** (1995) 2.
- [29] A. Donnachie and P. Landshoff, Z. Phys. **C61** (1994) 139.
- [30] A. Capella, et al., Phys. Lett. **B337** (1994) 358.
- [31] H. Abramowick, et al., Phys. Lett. **B269** (1991) 465.
- [32] B. Badelek and J. Kwiecinski, Phys. Lett. **B295** (1992) 263.
- [33] P.R. Newman, Ph.D. Thesis, The University of Birmingham, 1996.
- [34] J. Storrow, J. Phys. **G19** (1993) 1641.
- [35] S. Aid, et al. (The H1 Collaboration), Nucl. Phys. **B472** (1996) 3.
- [36] S. Aid, et al. (The H1 Collaboration), Nucl. Phys. **B472** (1996) 32.
- [37] C. Adloff, et al. (The H1 Collaboration), DESY-97-024, Submitted to Z. Phys. **C**.
- [38] J. Breitweg, et al. (The ZEUS Collaboration), DESY-97-025, Submitted to Z. Phys. **C**.

- [39] T. Regge, *Nuovo Cimento* **14** (1959) 951.
- [40] T. Regge, *Nuovo Cimento* **18** (1960) 947.
- [41] I.R. Kenyon, *Elementary Particle Physics*, RKP (1987).
- [42] A. Barnes et al., *Phys. Rev. Lett.* **37** (1976) 76.
- [43] A. Donnachie and P. Landshoff, *Phys. Lett.* **B296** (1992) 227.
- [44] G. Ingelman and J. Bartels, *Phys. Lett.* **B255** (1990) 175.
- [45] G. Ingelman and K. Janson-Prytz, *Proceedings of the Workshop Physics at HERA*, eds. W. Buchmüller and G. Ingelman, DESY, **1** (1992) 233.
- [46] K. Streng, *Proceedings of the HERA Workshop*, DESY, ed. R.D. Peccei, **1** (1987) 365.
- [47] A. Donnachie and P. Landshoff, *Phys. Lett.* **B191** (1987) 309.
- [48] G. Ingelman and P. Schlein, *Phys. Lett.* **B152** (1985) 256.
- [49] E. Berger, et al., *Nucl. Phys.* **B256** (1987) 704.
- [50] M. Genovese, N. Nikolaev and B. Zakharov, *J. Exp. Theor. Phys.* **81** (1995) 625.
- [51] The H1 Collaboration, Paper pa02-061, 28th International Conference on High Energy Physics, Warsaw, Poland, July 1996.
- [52] The HERA Proposal, DESY HERA Report 81-10 (1981).
- [53] A. Sokolov and I. Ternov, *Sov. Phys. Dokl.* **8** (1964) 1203.
- [54] D. Barber, et al., DESY 94-171.
- [55] I. Abt, et al. (The H1 Collaboration), *The H1 Detector at HERA*, *Nucl. Instr. Meth.* **A386** (1997) 310.
I. Abt, et al. (The H1 Collaboration), *The Tracking, Calorimeter and Muon Detectors of the H1 Experiment at HERA*, *Nucl. Instr. Meth.* **A386** (1997) 348.
- [56] The H1 Collaboration, *Technical Proposal to Upgrade the Backward Scattering Region of the H1 Detector*, DESY PRC 93/02.
- [57] B. Andrieu, et al., *Nucl. Instr. Meth.* **A336** (1993) 460.
- [58] H. Cronström, et al., *Nucl. Instr. Meth.* **A340** (1994) 304.

- [59] The H1 Collaboration, Paper pa17-026, 28th International Conference on High Energy Physics, Warsaw, Poland, July 1996.
- [60] The H1 Collaboration, Paper pa17-025, 28th International Conference on High Energy Physics, Warsaw, Poland, July 1996.
- [61] E. Elsen, *The H1 Trigger and Data Acquisition*, Proceedings of the International Symposium on Electronic Instrumentation in Physics, Dubna, May 1991.
- [62] F. Sefkow, et al., *Experience with the First Level Trigger of H1*, Proceedings of the IEEE Nuclear Science Symposium, Norfolk, Virginia, July 1994.
- [63] T. Ahmed, et al., Nucl. Instr. Meth. **A346** (1995) 456.
- [64] A. Gruber, et al., *A Neural Network Architecture for the Second Level Trigger in the H1 Experiment at HERA*, Proceedings of the IEEE Conference TAI94, New Orleans, 1994.
- [65] L. Goerlich, et al., *Strategy Studies for the H1 Topological L2 Trigger*, H1 Internal Note H1-01/97-508.
- [66] M. Turiot and C. Vallée, *Implementation of the L3 Trigger at H1*, H1 Internal Note H1-09/94-382.
- [67] W. Haynes, *The Data Acquisition System for the HERA H1 Experiment*, RAL Report RAL-90-039.
- [68] V. Blobel, The BOS System, Fortran 77 Version, DESY, December 1987.
- [69] R.D. Appuhn et al., Nucl. Instr. Meth. **A350** (1994) 208.
- [70] S. Dagoret et al., Nucl. Instr. Meth. **A346** (1994) 137.
- [71] R.D. Appuhn et al., DESY-96-171, submitted to Nucl. Instr. Meth.
- [72] R.D. Appuhn et al., DESY-96-013.
- [73] A. Walther and R. Barschke, Proceedings of the SCIFI 93 Workshop on Scintillating Fibre Detectors, Notre Dame University, Indiana, USA (1993) 253.
- [74] J. Janoth et al., Nucl. Instr. Meth. **A350** (1994) 221-225
- [75] The H1 SPACAL Group, *The LED based Calibration System of the H1 Lead-Scintillating Fibre Calorimeter*, to be submitted to Nucl. Instr. Meth.

- [76] R. Bernard and G. Cozzika, *The ADC board of the H1 calorimeter read-out*, H1 Internal Note H1-10/95-459.
- [77] *Digital Signal Processor Board (DSP8150) User's Manual*, Creative Electronic Systems S.A. Geneva, Switzerland.
- [78] R. Bernard and G. Cozzika, *MDS, a Service Module for the H1 calorimeter DSPs*, H1 Internal Note H1-10/95-458.
- [79] V. Boudry et al., *The Inclusive Electron Trigger for the SPACAL: Design and CERN test results*, H1 Internal Note H1-03/95-430.
- [80] S. Spielmann, Ph.D Thesis, Ecole Polytechnique, Paris, France (1996), (H1 Thesis H1T-0796-029).
- [81] C. Beigbeder and D. Breton, *The H1 PQZP System*, H1 Internal Note H1-02/93-269.
- [82] E. Eisenhandler et al., *H1 SPACAL TDC System Description*, Internal Project Document, RAL Electronics Division, March 1994.
- [83] E. Eisenhandler et al., IEEE Transactions on Nuclear Science, **42** (1995) 688.
- [84] The OS9 Real-time Operating System, Microware.
- [85] B.G. Taylor, *The MacVEE Hardware User Manual*, Rev 5.1, CERN.
- [86] B.G. Taylor, *The Micron User Manual*, Rev 2.4, CERN.
- [87] J. Dowdell, *The H1 SPACAL TDC System Controller Module*, Internal Project Report RAL1157, December 1994.
- [88] J. Dowdell, *The H1 SPACAL TDC System TDC and Histogrammer Module*, Internal Project Report RAL1158, December 1994.
- [89] Y. Arai et al., IEEE Journal of Solid-State Circuits, **27** 359.
- [90] *TMC1004 Specification*, AMSC Co. Ltd., Tokyo, Japan.
- [91] *Timon*, the TDC monitoring application, written by M.P.J. Landon, QMW. Documentation is available via the World Wide Web at:
<http://www-h1.desy.de/~nicholls/SpacalTDC/timon/home.html>
- [92] T.C. Nicholls, *SPTIME, the SPACAL TDC reconstruction scheme*, SPACAL internal project documentation, March 1995.

- [93] S. Schleif, *SPACAL reconstruction technical note*, SPACAL internal project documentation, February 1995.
- [94] T. Nicholls, et al., Nucl. Instr. Meth. **A374** (1996) 149.
- [95] R.D. Appuhn, et al., Nucl. Instr. Meth. **A382** (1996) 395.
- [96] F. Moreau, private communication.
- [97] J. Dowdell, *The H1 SPACAL TDC System Pre-Prototype Module*, Internal Project Report RAL1156, April 1994.
- [98] T. Nicholls and J. Dowdell, *TMCaccept: Testing the TMC1004 ASICs*, Internal Project Document, August 1994.
- [99] P. Bruel, private communication.
- [100] S. Bentvelsen, et al., Proceedings of the Workshop Physics at HERA, eds. W. Buchmüller and G. Ingelman, DESY, **1** (1992) 23.
- [101] U. Bassler and G. Bernardi, DESY 94-231.
- [102] A. Meyer, *Adjustment of the High Voltage for the H1 SPACAL*, H1 Internal Note H1-08/96-486.
- [103] M. Dirkmann, *Calibration of the SPACAL with Cosmics*, H1 Internal Note H1-05/96-477.
- [104] C. Royon, private communication.
- [105] J. Janoth, et al., *An Algorithm to Calibrate the new H1 Backward Calorimeter SPACAL using the Kinematic Peak*, H1 Internal Note H1-11/95/464.
- [106] A. Courau and S. Kermiche, *QED Compton Events in H1*, H1 Internal Note H1-12/92-260.
- [107] R. Maracek, Ph.D. thesis in preparation.
- [108] A. Meyer, Presentation at the H1 SPACAL Meeting, January 1997.
- [109] G. A. Schuler and H. Spiesberger, Proceedings of the Workshop Physics at HERA, eds. W. Buchmüller and G. Ingelman, DESY, **3** (1992) 1419.
- [110] A. Kwiatkowski, et al., Proceedings of the Workshop Physics at HERA, eds. W. Buchmüller and G. Ingelman, DESY, **3** (1992) 1294.

- [111] G. Ingelman, Proceedings of the Workshop Physics at HERA, eds, W. Buchmüller and G. Ingelman, DESY, **3** (1992) 1266.
- [112] A. Vogt, Proceedings of the Workshop on Deep-Inelastic Scattering and QCD, Paris (1995) 261.
- [113] R. Engel and J. Ranft, Phys. Rev. **D54** (1996) 4244.
- [114] H. Jung, Computer Phys. Comm. **86** (1995) 147.
- [115] L. Lönnblad, Computer Phys. Comm. **71** (1992) 15.
- [116] F. Carminati, et al., GEANT User's Guide, CERN Program Library (1987).
- [117] C. Royon, private communication.
- [118] A. Meyer, private communication.
- [119] T. Ahmed, et al. (H1 Collaboration), Phys. Lett. **B348** (1995) 681.
- [120] A. Mehta, Ph.D. Thesis, The University of Manchester, 1994.
- [121] B. List, private communication.
- [122] C. Royon, Ph.D. Thesis, Centre d'Orsay, Université de Paris-Sud, 1994.
- [123] A. Panitch and P. Marage, *Vertex reconstruction using BPC and CIP in DIS events*, H1 Internal Note H1-05/93-397
- [124] A. Panitch, Ph.D. Thesis, Université Libre de Bruxelles, 1996.
- [125] The ZEUS Collaboration, Paper pa02-026, 28th International Conference on High Energy Physics, Warsaw, Poland, July 1996.